Study of quarkonium collectivity in Pb-Pb collisions at 5.36 TeV of LHC Run 3

Chi Zhang

université PARIS-SACLAY

Study of quarkonium collectivity in Pb–Pb collisions at 5.36 TeV of LHC Run 3

Étude de la collectivité de quarkonium dans les collisions Pb–Pb à 5.36 TeV du Run 3 du LHC

Thèse de doctorat de l'université Paris-Saclay

École doctorale n°576, Particules Hadrons Energie et Noyau : Instrumentation, Imagerie, Cosmos et Simulation (PHENIICS)
Spécialité de doctorat: Physique nucléaire
Graduate School : Physique. Référent : Faculté des sciences d'Orsay

Thèse préparée au **Département de Physique Nucléaire (Université Paris-Saclay, CEA)**, sous la direction de **Javier Ernesto CASTILLO CASTELLANOS**, Directeur de recherche

Thèse soutenue à Paris-Saclay, le 19 décembre 2025, par

Chi ZHANG

Composition du jury

Membres du jury avec voix délibérative

Cynthia HADJIDAKIS Directrice de recherche, Université Paris-Saclay, IJCLab	Présidente
Elena GONZALEZ FERREIRO Professeure des Université, University of Santiago de Compostela, IGFAE	Rapportrice & Examinatrice
Emilie MAURICE Professeure de l'École Polytechnique, Institut Polytechnique de Paris, LLR	Rapportrice & Examinatrice
Jean-Yves OLLITRAULT Directeur de recherche, Université Paris-Saclay, IPhT	Examinateur
You ZHOU Professeur associé, University of Copenhagen, Niels Bohr Institute	Examinateur

THESE DE DOCTORAT
NNT : 2025UPASP185

université PARIS-SACLAY

ÉCOLE DOCTORALE
Particules, hadrons, énergie et noyau : instrumentation, imagerie, cosmos et simulation (PHENIICS)

Titre: Étude de la collectivité de quarkonium dans les collisions Pb–Pb à 5.36 TeV du Run 3 du LHC

Mots clés: QGP, Collisions d'ions lourds, Charmonium, Flow elliptique, Quarkonia

Résumé: Quelques microsecondes après le Big Bang, l'Univers se trouvait dans un état de plasma de quarks et de gluons (QGP) où les quarks et gluons sont déconfinés de hadrons. Ce dernier, formé à des températures ou des densités d'énergie très élevées, peut être recréé lors des collisions ultra-relativistes d'ions lourds au LHC. Pour étudier un tel état de matière, les charmonia, états liés des quarks et antiquarks du charm, sont des sondes clés puisque leur production et transport, en particulier ceux du J/ψ hadron, sont modifiés dans le milieu, ainsi révèlent les indices permettant de caractériser le QGP.

Depuis 2022, ALICE a commencé sa nouvelle période d'acquisition des données du Run 3 avec des mises à jour importantes. En ce qui concerne la mesure des quarkonia par la désintégration en paires de muons dans la rapidité forward, le spectromètre à muons nécessitait certaines étapes de commissioning pour atteindre la performance promise en Run 3; parmi lesquelles, une indispensable est l'alignement du système de tracking. Ce dernier, mené dans le travail de la thèse, présente un rôle fondamental pour la reconstruction des signaux de quarkonia, ce qui va permettre la poursuite de l'analyse.

Parmi les signatures du QGP, le flow anisotropique de quarkonia se situe au cœur de nos intérêts; ce dernier, quand il s'agit du flow elliptique, nous fournit des évidences pour comprendre la thermalisation des quarkonia, ainsi le passage dynamique en comparant avec les calculs de transport où le QGP est considéré comme un fluide décrit par l'hydrodynamique. Dans le travail de la thèse, des nouvelles mesures de flow du J/ψ dans les collisions Pb–Pb ont été menées, en mettant en ensemble plusieurs méthodes ainsi avec une meilleure précision et plus grande portée grâce au Run 3.

Title: Study of quarkonium collectivity in Pb–Pb collisions at 5.36 TeV of LHC Run 3

Keywords: QGP, Heavy-ion collisions, Charmonium, Elliptic flow, Quarkonia

Abstract: A few microseconds after the Big Bang, the Universe was in a state of quark-gluon plasma (QGP) where quarks and gluons are de-confined from hadrons. The latter, formed at very high temperatures or energy densities, can be recreated in ultra-relativistic heavy-ion collisions at the LHC. To study such a state of matter, charmonia, bound states of charm quarks and antiquarks, play a crucial role since their production and transport, in particular for J/ψ hadron, are modified in the medium, thus revealing the properties of the QGP.

Since 2022, ALICE has begun its new data acquisition period for Run 3 with important upgrades. With regard to the measurement of quarkonia through muon decay channel in the forward rapidity, the Muon Spectrometer required certain commissioning steps to achieve the promised performance in Run 3; Among these, one essential step is the alignment of tracking system. The alignment of Muon Spectrometer, carried out as part of the thesis work, plays a fundamental role in the quarkonia reconstruction, which will enable the analysis to continue.

Among the signatures of the QGP, the anisotropic flow of quarkonia is of particular interest to us. The latter, when it comes to elliptic flow, provides us with evidence to understand the thermalization of quarkonia, as well as their dynamic evolution compared to transport calculations where the QGP is considered as fluid described by hydrodynamics. In the work of this thesis, new measurements of J/ψ flow in Pb–Pb collisions were carried out, combining several methods with improved precision and range thanks to Run 3.

Acknowledgments

At the moment when I came to ask myself: "How should I start this part?" I've suddenly realized how 3 years went away so quietly and swiftly, then it was as if a small button in my brain was unconsciously pressed and all the memories began to replay – from the very summer of 2020 where the story line has started. If this thesis is to conclude these 3 years of my life, then there is no better way to begin than by expressing my heartfelt gratitude to all those who have shared this path with me.

First and foremost, I would like to sincerely thank my thesis supervisor, Javier, for his unwavering support and patience throughout this journey. Without his guidance, this thesis would not have been possible. I have lost count of the number of times I walked into his office with a flood of questions – many of them stupid or poorly formulated – yet he always made the time to listen, respond thoughtfully, and steer me in the right direction. During the more difficult periods, when I was mentally struggling and navigating moments of immaturity, his patience and understanding meant even more to me than his academic mentorship. I am deeply grateful for both, as I could not have overcome the challenges I faced without his presence and support on the way.

For this special moment, I would like also to express my sincere gratitude to the members of my defense jury for accepting to evaluate this work. I'm deeply thankful for the time and care they devoted to reading the manuscript, and for their insightful comments and questions. Their expertise and critical perspective greatly contributed to improving both the clarity and the rigor of this thesis, and I consider it an honor to have had my work examined by such a distinguished committee.

In classical Chinese literature, the concept of *fate* is often invoked to give meaning to what seems like random. I've come to view life as a collection of delicate threads – sometimes crossing, sometimes running parallel whether near or far. DPhN and LQGP were special to me because it brought together these threads, allowing us to meet, connect, and get to know one another. I would like to begin with Michael, my very first supervisor in LGQP, who has made this *fate* possible; without his kindness and warm support throughout, I wouldn't have come this far. I also owe my heartfelt thanks to Andry, whom I warmly consider my "second supervisor" for all her invaluable help with O2 and alignment during challenging times, as well as for the thoughtful conversations we shared about life

and career. I would like to extend my sincere thanks to all the kind senior physicists in the lab: Alberto for the insightful discussions we shared during coffee time, Andrea for his generous help at P2 and kindly sharing his expertise in detector system, Stéphano whose wit and humor were often a source of inspiration, Benjamin who has been always like our old brother, Hervé for his ever-present kindness. And my PhD/post-doc fellow: Gabriel, Carlos, Alisha, Mostafa, Paul, Carolina, Immanol. I would also like to warmly thank those who supported me during my early days as an intern and have since graduated: Aude, Sébastien, Florian, Robin, Batoul. I feel especially grateful to Mika and Maurice, who have meant far more to me than just teammates; they have become my truly indispensable friends – people with whom I can share my innermost thoughts at any time, without hesitation. My gratitude also goes to those outside LQGP: Hervé and Francesco, for their kindness and support; Isabelle, for her warm help as part of the LQGP family; and Nicolas, for his invaluable technical support. Finally, I would like to thank all the members of DPhN. It has been a great honor to work with you all under the same roof.

I would like to express my sincere gratitude to all my colleagues in the ALICE collaboration, especially the amazing team at P2: Christophe, Livia, Charlotte, Aimeric, and Shreyasi; and the dedicated DQ group: Laure, Biao, Yuan, Zhenjun, Ionut, and many others. I am also deeply thankful to my incredible analysis team: Luca, Maxime, Victor, and Dhananjaya. A special thanks goes to Victor—for the long nights we devoted to our project and the mutual support that helped us navigate the difficult moments together.

Finally, I owe my deepest thanks to my parents, who have always been my greatest source of strength, despite the physical distance that has separated us over the past ten years since I left China. And of course, to Yijun, without her constant support and presence by my side, I could not have imagined completing this work.

To my parents and Yijun

Figure 1: Chiesa di Sant'Ignazio di Loyola, Rome, April 2024.

I have had to experience so much stupidity, so many vices, so much error, so much nausea, disillusionment and sorrow, just in order to become a child again and begin anew. I had to experience despair, I had to sink to the greatest mental depths, to thoughts of suicide, in order to experience grace.

- Hermann Hesse, Siddhartha

Contents

List of Figures

List of Tables

Chapter 1

Introduction

Contents

1.1 A view from above

First and foremost, physics, being a branch of natural philosophy, seeks to understand the external world, this objective reality in which matter appears to interact according to a small set of physical laws that remain consistent across space and time. This constancy feels natural to us, as it forms the foundation of our everyday experience. Yet, it is far from trivial that reality should be structured in such a way that the human mind, through reason, can grasp it with understanding. This mystery provides the enduring motivation for every curious mind to devote their strength and intellect to uncover the truth hidden beneath appearances. Before diving into the details, I find it helpful to think like a philosopher and ask myself a fundamental question whenever I begin investigating a topic in physics: *What is the subject of my study? Why study it?* and *How can I approach it?* These questions shall be very important later on, as they help us stay focused on the core ideas and remain mindful of the concrete steps we might need to take. Following this approach, I will attempt to explore heavy-ion physics by first addressing the aforementioned questions, based on my initial understanding. Adopting this abstract methodological perspective, our initial inquiry may appear as straightforward as asking why an apple falls from a tree. Yet, despite their shared semantic structure, one must not overlook the profound technical differences between the two cases.

In our case, heavy-ion physics, people are interested in a special physical system produced in heavy-ion collisions, the latter is created under extreme conditions. As energy increases, one naturally expects to probe deeper into the fundamental structure of matter. This paradigm has well guided experimental nuclear physics from the early 19th century to the present day with the only significant change being the size, therefore energy scale, of the apparatus. The motivation of such a way aligns closely with the goal of elementary particle physics, which seeks to understand the fundamental building blocks of physical reality at the smallest scales, complementing and in contrast to gravity, which governs the large-scale structure of the universe. Beyond offering a unique opportunity to directly investigate the dynamics of the strong interaction as a fundamental force, this system spans also multiple complexity scales, making it a rich environment where emergent phenomena are expected to occur. In this context, our "apple" is the unique physical system of hot and dense nuclear matter. Rather than posing direct questions such as "Why does it fall?", we aim to study the system across its entire evolution, from its creation to its final stage, in order to gain the deepest possible understanding. And we have the remarkable privilege of being able to create such a system using a giant particle collider and "observe" it through "eyes": particle detectors. Much like creating something and observing how it evolves, this straightforward and practical way of thinking lies at the heart of approaching the subject from a positivist, and therefore experimental perspective.

In the following sections of this chapter, I will develop this picture in greater technical detail. Despite the richness and complexity of the topic, my aim is to offer a rather simple and structured understanding of heavy-ion physics, framed from my own perspective, which represents just one narrow viewpoint within the broader landscape, but one grounded in my experience over the past three years.

In the following discussion, the natural units will be used for convenience:

$$c = k_{\mathrm{B}} = \hbar = 1 \tag{1.1}$$

And Minkowski metric tensor would be taken as $g^{\mu\nu} = \mathrm{Diag}(1, -1, -1, -1)$.

1.2 Introduction to theory of strong interaction

Understanding the nature of matter has been one of the most profound questions since the earliest days of philosophical inquiry and the birth of natural science. This question, closely tied to our direct perception of the world, has historically appeared more accessible through interaction with our surroundings than another equally fundamental question: the nature of time. In the 5th century BC, Leucippus and his pupil Democritus attempted to answer the question: *What is the smallest constituent of matter?*. It was in this context that the term *atom* first entered the human history, referring to the smallest indivisible particles.

From a modern perspective, these thinkers can be regarded as the earliest pioneers of particle physics. This theory of matter being made of atoms was later developed in the modern scientific sense of the basic unit of a chemical element by the British chemist and physicist John Dalton in the 18th century. The remarkable time gap between the original philosophical idea and its concrete formulation within a scientific paradigm highlights the crucial role of technological advancement and experimental methodology in bridging thought and evidence. Then Dmitri Mendeleev pushed one great step with his genius toward the classification of elements into his periodic table. Today, we see how elements like oxygen, carbon, and hydrogen are arranged in an almost magical pattern, which is an abstract yet remarkably readable form that captures the inherent beauty and order of nature. Despite the elegance of Maxwell's equations in describing electromagnetism, a complete picture of matter at the atomic level still required further breakthroughs. It was J. J. Thomson and his team who took the next crucial step, with the discovery of the first elementary particle – electron. Then these elements were put together by Niel Bohr, using early concepts of quantum mechanics, later refined and extended by Arnold Sommerfeld who introduced the fine-structure constant $\alpha = \frac{e^2}{2\pi\epsilon_0 hc}$ – which is a dimensionless quantity – that quantified the spectral lines of hydrogen atom.

Beginning with Rutherford's experiments, it became then evident that atoms consist of a dense nucleus, which is about 1,000 times smaller than the atom itself, but contributes to 99.9% of atomic mass. The nucleus, typically spanning a size of $1\text{-}10\ \mathrm{fm}$, consists of nucleons (positively charged protons and charge neutral neutrons) bound together with energies of $1\text{-}8\,\mathrm{MeV}$ per nucleon. In contrast, even the electrons in the innermost shells of heavy elements are bound by no more than $0.1\,\mathrm{MeV}$ per electron, meaning that electrons can be easily detached from a nucleus with no harm to the nucleus itself. Initial ionization can be experimentally achieved using strong electric fields, then further ionization by accelerating the ions and letting them fly through thin stripping foils. Protons, neutrons and electrons are rather long-living particles. Protons and electrons are stable without the need of staying bound inside an atom (their measured average free lifetime has an upper bound larger than the age of the Universe). While neutrons live about $15\,\mathrm{mins}$ on average before decaying into a proton, an electron and an anti-neutrino – called beta-decay.

From atom to nuclei and nuclei to nucleon, the above described picture seemed satisfying until the measurements of magnetic moment and electromagnetic form factor started to put our initial assumption in question: *"Nucleons seem not to be point-like particles ?"* The latter being the motivation of probing nucleon's inner structure, which became possible with the Deep Inelastic Scattering (DIS) by accelerating electrons as they are elementary particle without inner structure then letting them scatter nucleon. The first DIS experiment was conducted at Stanford Linear Accelerator Center (SLAC) in 1968. Soon, the golden era of particle physics experiment came during 1960-1980s together with the parton theory by Richard Feynman [1] and early quark model by Murray Gell-Mann [2], physicists during that time discovered an extremely rich zoo of short-living particles using electron-positron, proton-electron, proton-proton and other collisions as well as high-energy cosmic rays. In the quest to explore the extremely small, it is reductionism and ontological curiosity that have driven physicists to probe ever deeper, seeking the most fundamental building blocks of reality, without yet knowing whether we will eventually hit a final boundary, or if there is no end at all.

And we will see in the next section how symmetry and a beautiful mathematical framework can help us to bring the rather separate parts together resulting in the so-called Standard Model (SM) of elementary particles. Then, I shall restrict our attention to a special corner on this elementary particle big picture – the world of strongly interacting particles.

1.2.1 . Standard model

Figure 1.1: Paul Dirac, Wolfgang Pauli and Rudolf Peierls in Birmingham, 1953. [3]

The theoretical efforts in physics begin often with intuitions, the latter according to P.A.M. Dirac lie in the inner beauty of mathematical constructions being self-complete and -consistent. And he as well has followed this creed, by putting together the Klein-Gordon

equation being relativistic and Schrodinger equation as defining equation of quantum unitary evolution. Both on the same wave-theoretical scheme, but with two different backbends, Dirac managed to find out a relativistic wave equation being consistent with both relativistic and quantum descriptions, the latter is known as Dirac's equation [4] describing all spin-$\frac{1}{2}$ particles called Dirac particles that obey Fermi-Dirac statistics.

However, this first formulation of Quantum Electrodynamics (QED) has faced several crucial difficulties when it comes to calculate quantities like electron self-energy, the latter has lead to infinities pointing to mathematically undefined terms, hence physically unacceptable. In 1947, Hans Bethe tried to introduce a cutoff in the electron self-energy [5], leading to a finite result for Lamb's shift calculation. The systematic techniques to better formulate the relativistic theory and handle divergences were later developed during late 1940's by Sin-Itiro Tomonaga [6], Julian Schwinger [7] and Richard Feynman [8], where Schwinger introduced the so-called renormalization procedure consisting of dressing up bare parameters by redefinition, so loop divergences will get canceled by corresponding counter-terms. The internal consistency between Schwinger's and Feynman's approaches within this new formulation was then proved by Freeman Dyson [9], therefore renormalization has to be valid to all orders in perturbation theory. The idea of renormalization was further studied deeper and promoted as a powerful tool to access the scale-dependence of physical parameters, the latter become profound in critical phenomena.

Before introducing another crucial theoretical framework, it is worth recalling an important concept: gauge symmetry, first recognized in Maxwell's theory of electromagnetism. Initially, it was understood as a type of symmetry that leaves the system of equations invariant, resulting in a degeneracy of solutions. Later, the physical significance of this symmetry, associated with a complex gauge factor, was demonstrated by the Aharonov–Bohm effect [10]: even in regions where both the magnetic and electric fields vanish, a shift in the complex phase factor can affect the behavior of a charged-particle. These early insights laid the foundation for a gauge theory of electromagnetism, where the underlying symmetry was later formalized as $\mathrm{U}(1)$ symmetry. This concept soon became recognized as a key principle, opening the way to describe fundamental interactions in a unified framework using the language of symmetry and differential geometry. The project was initiated by Hermann Weyl in 1915, in conjunction with Noether's theorem, which relates conserved currents to corresponding symmetries. Weyl then formulated a geometrical theory of symmetry [11].

It soon became clear that the symmetry underlying electromagnetism, described by an Abelian gauge group, was insufficient to account for the strong and weak interactions. To address these forces, one needs instead non-Abelian gauge groups. In 1953, Wolfgang Pauli attempted to extend the gauge-theoretical framework into a non-Abelian Klein-Kaluza model [12]. The decisive breakthrough, however, came shortly after with the work of Chen Ning Yang and Robert Mills [13], who introduced their genius construction of

non-Abelian gauge theories. Their approach relied on the mathematics of fiber bundles, which would later be recognized as the natural language of gauge theory.

An insightful way to visualize this, as suggested by Shiing-Shen Chern, is to imagine assigning a *fiber* to each point in space-time (the base space). These fibers are the spaces in which fields reside. For instance, in the case of electromagnetism, fibers are $\mathrm{U}(1)$ group. Symmetry enters the picture when one considers how these fibers are glued together across the base space, this gluing defines the structure group of the theory, which is also $\mathrm{U}(1)$. Any fiber bundle falls into this type is called *principal bundle*. The dynamics then concern how one moves within this geometrized world of fibers, using the language of differential geometry: connection, curvature, and eventually certain topological invariants. The identification of terms in gauge theory with their twins in differential geometry was later clarified and formalized by Tai Tsun Wu and Chen Ning Yang, known as the "Wu-Yang dictionary" [14].

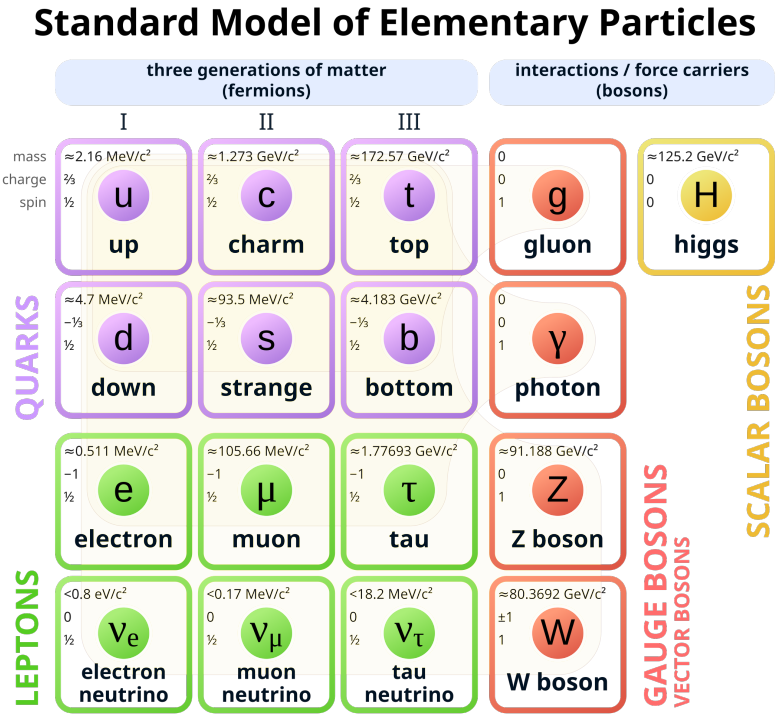

Figure 1.2: Elementary particles with their interactions in the Standard Model.[15]

The framework of Yang-Mills theory provided the last missing piece for the puzzle of non-Abelian theories. The latter, together with the famous *Wu experiment* in 1956 [16], has lead to the unified theoretical description of weak and electromagnetic interactions as electroweak theory $\mathrm{SU}(2)\times\mathrm{U}(1)$ by Sheldon Glashow, Abdus Salam and Steven Weinberg, then also a theory of strong interaction $\mathrm{SU}(3)$ called Quantum Chromodynamics (QCD) by

Harald Fritzsch, Heinrich Leutwyler and Murray Gell-Mann. However, there was a subtlety in developing a unified theory of weak and electromagnetic interaction back then, due to the massive gauge bosons W and Z in mediating weak interaction. The question of *where do their masses come from?* was solved with the idea of Spontaneous Symmetry Breaking (SSB). Although Nambu-Goldstone theorem [17, 18] tell us that a massless Goldstone boson will be generated from spontaneous breakdown of continuous symmetries, in the case gauge theory, Elitzur's theorem [19] actually states that gauge symmetries will never be spontaneously broken. A relativistic model explaining the mass generation problem respecting the gauge-invariance was developed by 3 independent groups in 1964: Robert Brout and François Englert, Peter Higgs, Gerald Guralnik, Carl Richard Hagen, and Tom Kibble. The idea is to introduce a so-called Higgs field which is a complex scalar doublet with 4 components, the latter is added to the electroweak Lagrangian, so 3 of the 4 components in Higgs field are considered as "would-be" Goldstone's bosons after SSB. They will be eaten after SSB induced by a non-symmetric Vacuum Expectation Value (VEV) of Higgs field, hence the longitudinal polarization gives the 3 massive bosons W,Z, leaving one scalar massive component as the physical scalar boson called Higgs boson. Similarly, the mass of fermion can be incorporated into the theory by introducing a Yukawa coupling between fermion fields and Higgs field.

Bringing all these pieces together, we arrive at a theoretical framework of quantum fields as the most powerful tool for describing the fundamental interactions of elementary particles, known as the Standard Model (SM) illustrated in Fig. 1.2. This unified picture represents the culmination of decades of human effort to probe nature at its smallest and most fundamental scale, driven by deep ontological questions about the structure of reality. What were once thought of as indivisible "atoms" are now organized into a simple but profound classification scheme – the Standard Model table. In what follows, we will narrow our attention to a small corner of this vast framework: the realm of the strong interaction.

1.2.2 . Quantum Chromodynamics

During the golden age of particle physics, a particle zoo was formed by so many discovered baryons and mesons in hadron spectroscopy by bubble chamber experiments at Berkeley, Brookhaven and CERN during 1950s-1960s. The underlying symmetry in their quantum numbers and masses was found to be consistent with an internal flavor $\mathrm{SU}(3)$ symmetry according to the famous *Eightfold Way* by Murray Gell-Mann in 1961 [2], with an example of pseudo-scalar meson octet shown in Fig. 1.3. The latter, with an improved version known as quark model by Murray Gell-Mann [20] and George Zweig [21], predicted successfully the discovery of Ω^- in 1964. Within the quark model, baryons are considered as bound states of three quarks and mesons are bound states of pair of quark and antiquark. However, this aforementioned flavor symmetry shall be distinguished from the later discovered color symmetry. For the spin-statistics theorem to hold, it was found that each quark flavor needs instead three varieties as *colors*. These color charges associated

to this gauge symmetry group which turns out to be $\mathrm{SU}(3)$ as well, were later introduced by Oscar Wallace Greenberg, Moo-Young Han and Yoichiro Nambu as a *hidden* quantum number.

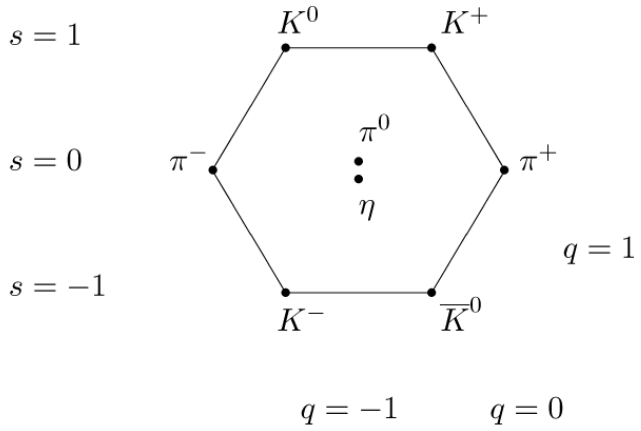

Figure 1.3: The pseudo-scalar meson octet from group representation with quantum numbers of strangeness and electric charge [22].

Formulation of QCD Lagrangian and basic ingredients

By Harald Fritzschm, Murray Gell-Mann and Heinrich Leutwyler in early 1970s [23], a dedicated Yang-Mills theory of $\mathrm{SU}(3)$ gauge symmetry applied to color degree of freedom was then formulated, leading to the so-called QCD Lagrangian that incorporates quark model and solves as well other puzzles involving current algebra and the weak interactions of hadrons. The gauge-invariant QCD Lagrangian in terms of bare quantities is written as [24]:

$$\mathcal{L}_{\mathrm{GI}} = \bar{\psi}_0 \left(i \not{D} - m_0 \right) \psi_0 - \frac{1}{4} \left(G^{\alpha}_{(0)\mu\nu} \right)^2 \tag{1.2}$$

where the first term corresponds to the *minimal coupling* of fermion fields to gauge fields, and the second term is the gauge field interaction term following the Yang-Mills Lagrangian.

The corresponding covariant derivative in eq 1.2 is given by:

$$D_\mu \psi_0 \overset{\mathrm{def}}{=} \left(\partial_\mu + i g_0 t^\alpha A^{\alpha}_{(0)\mu} \right) \psi_0 \tag{1.3}$$

where t^α are the generators of $\mathrm{SU}(3)$, acting on the color indices of quark fields. The gluon field tensor is defined as:

$$G^{\alpha}_{(0)\mu\nu} \overset{\mathrm{def}}{=} \partial_\mu A^{\alpha}_{(0)\nu} - \partial_\nu A^{\alpha}_{(0)\mu} - g_0 f^{\alpha\beta\gamma} A^{\beta}_{(0)\mu} A^{\gamma}_{(0)\nu} \tag{1.4}$$

where $f^{\alpha\beta\gamma}$ is the anti-symmetric structure tensor of gauge group, following $[t_\alpha, t_\beta] = i f_{\alpha\beta\gamma} t^\gamma$.

The Lagrangian is invariant under the following local gauge transformations:

$$\psi_{(0)\,\rho a f}(x) \;\mapsto\; \left[e^{-ig_0\omega_\alpha(x)t^\alpha}\right]_{ab}\,\psi_{(0)\,\rho b f}(x), \tag{1.5a}$$

$$A^\alpha_{(0)\,\mu}(x)t^\alpha \;\mapsto\; -\frac{i}{g_0}\,e^{-ig_0\omega_\alpha(x)t^\alpha}D_\mu e^{ig_0\omega_\alpha(x)t^\alpha}. \tag{1.5b}$$

For the electromagnetic interactions involving quarks, we have their corresponding electric charges: $\frac{2}{3}$ for u, c, t quarks and $-\frac{1}{3}$ for d, s, b quarks.

In practical, this flavor $\mathrm{SU}(3)$ symmetry involving u, d and s fermion fields would be exact if those quarks have the same mass. However, the latter approximation will still be useful as the masses of light quarks are significantly lower than the typical hadronic mass scale, while heavy-quarks c, b, t remain singlets with respect to the flavor symmetry. At the same time, the basic properties of quarks are summarized below in Tab. 1.2.2.

Flavor	Electric charge	Baryon number	Mass
u (up)	$2/3$	$1/3$	$3\ \mathrm{MeV}$
d (down)	$-1/3$	$1/3$	$7\ \mathrm{MeV}$
s (strange)	$-1/3$	$1/3$	$120\ \mathrm{MeV}$
c (charm)	$2/3$	$1/3$	$1.2\ \mathrm{GeV}$
b (bottom)	$-1/3$	$1/3$	$4.25\ \mathrm{GeV}$
t (top)	$2/3$	$1/3$	$175\ \mathrm{GeV}$

Table 1.1: Basic properties of quarks

Gauge-fixing and BRST symmetry

In modern quantum field theory, there is a crucial quantity encoding *all* physics (especially correlation functions) for a given setup, called partition function or generating functional. The latter can be simply defined in the case of no matter fields as an integral over all possible field configurations along a given path [25]:

$$\mathcal{Z} = \int \mathcal{D}A\, e^{iS[A]} \tag{1.6}$$

where A stands for the gauge field.

Since the action $S[A]$ is invariant under local gauge transformation, this integral is actually taking infinitely many equivalent copies of field configurations leading to an ill-defined integral with an infinite "gauge volume". To avoid this ambiguity, one needs to introduce a certain gauge fixing like in the case of QED where we may choose to use Lorentz or Coulomb gauge. The idea is simply to setup a constraint to reduce the double-counting of equivalent gauge states. However, since QCD is a non-Abelian gauge theory, the gauge

fixing procedure is highly non-trivial than a Abelian theory. In 1967, Ludvig Faddeev and Victor Popov proposed a technical solution [26] to fix the issue. This method consists of introducing fermion scalar *ghost* fields, so the original gauge-invariant Lagrangian will be replaced by:

$$\mathcal{L} = \mathcal{L}_{\mathrm{GI}} + \mathcal{L}_{\mathrm{GF}} + \mathcal{L}_{\mathrm{GC}} \tag{1.7}$$

where we add two new terms, $\mathcal{L}_{\mathrm{GF}}$ for gauge-fixing and $\mathcal{L}_{\mathrm{GC}}$ for gauge-compensating:

$$\mathcal{L}_{\mathrm{GF}} = -\frac{1}{2\xi_0}\,(\partial \cdot A_{(0)\alpha})^2, \tag{1.8}$$

$$\mathcal{L}_{\mathrm{GC}} = \partial_\mu \bar{\eta}_{0\alpha}\,\partial^\mu \eta_{0\alpha} + g_0\,\partial^\mu \bar{\eta}_{0\gamma}\,f_{\alpha\beta\gamma}\,A^{\beta}_{(0)\mu}\,\eta_{0\alpha}, \tag{1.9}$$

where the gauge-compensating term involves bare ghost fields η_0 and $\bar{\eta}_0$.

However, this new Lagrangian is actually not gauge-invariant and leads to inconvenient complexities in renormalization and quantization; one needs to use new identities instead of usual *generalized Ward identities*, with a new symmetry. The latter is called BRST transformation introduced by Carlo Becchi, Alain Rouet, Raymond Stora and Igor Tyutin [27, 28]. The BRST symmetry is actually a supersymmetry relating bosons and fermions, it uses an extra parameter $\delta\lambda_0$ taking values in the fermionic part of some Grassmann algebra. The BRST transformation becomes gauge transformation for gluon and quark fields. The linear terms of fields gluons, quarks and ghosts under the variation read:

$$\delta_{\mathrm{BRST}}\psi_0 = -ig_0\eta_{0\alpha}\delta\lambda_0 t^\alpha\psi_0 = ig_0\eta_{0\alpha}t^\alpha\psi_0\,\delta\lambda_0, \tag{1.10a}$$

$$\delta_{\mathrm{BRST}}\bar{\psi}_0 = ig_0\bar{\psi}_0 t^\alpha\eta_{0\alpha}\,\delta\lambda_0, \tag{1.10b}$$

$$\delta_{\mathrm{BRST}}A^{\alpha}_{(0)\mu} = \left(\partial_\mu\eta_{0\alpha} + g_0 f_{\alpha\beta\gamma}\eta_{0\beta}A^{\gamma}_{(0)\mu}\right)\delta\lambda_0, \tag{1.10c}$$

$$\delta_{\mathrm{BRST}}\eta_{0\alpha} = -\tfrac{1}{2}g_0 f_{\alpha\beta\gamma}\eta_{0\beta}\eta_{0\gamma}\,\delta\lambda_0, \tag{1.10d}$$

$$\delta_{\mathrm{BRST}}\bar{\eta}_{0\alpha} = \frac{1}{\xi_0}\,\partial \cdot A_{0\alpha}\,\delta\lambda_0. \tag{1.10e}$$

Regularization and renormalization

After the correct treatment involving gauge-fixing and BRST transformation, one should also deal with the divergences appeared in QCD for both Ultra-violet (UV) and Infra-red (IR) regimes.

- For IR regime, KLN theorem by Toichiro Kinoshita, Tsung-Dao Lee and Michael Nauenberg [29, 30] ensures the cancellation between real and virtual contribution for inclusive cross-sections, the latter solves soft-divergences from soft gluons. On the

other side, Collinear divergences will be factorized into Parton Distribution Function (PDF) and fragmentation functions. For large logarithms, a proper resummation is needed using renormalization-group equations.

- For UV regime, the divergences are from large loop momenta i.e. when interaction vertices get close to each other in space-time. This can be fixed by regularization and renormalization procedures. The first consists of introducing a regulator like non-zero lattice spacing or dimensional regularization [1]. Then the next step is to dress-up bare quantities fields and parameters by introducing counter-terms to cancel the divergences, using a certain renormalization scheme. In QCD perturbative calculations, it is convenient to use the so-called Modified Minimal Subtraction ($\overline{\mathrm{MS}}$) scheme in contrast to the usual Minimal Subtraction (MS) scheme where only $\frac{1}{\epsilon}$ poles from dimensional regularization are removed, in addition to $\frac{1}{\epsilon}$ poles, a rescaling of renormalization scale with the Euler–Mascheroni constant γ_{E} is also implemented.

Running coupling and asymptotic freedom

The renormalization procedure in UV regime leads to two important features of QCD, namely *running coupling* and *asymptotic freedom*.

In the procedure of renormalization, the coupling constant g is dressed-up and becomes a function of a certain relevant scale $g(\mu)$. In quantum field theory, n-point Green's functions $G^{(n)}(x_1, x_2, \ldots, x_n; M, g) = \langle\phi(x_1)\phi(x_2)\cdots\phi(x_n)\rangle$ need to be dressed-up as well, and their evolution with the variation of scale follows the Callan-Symanzik equation [31–33] where the β-*function* is defined by:

$$\beta(g) = \mu\frac{dg}{d\mu} \tag{1.11}$$

Hence the running coupling $\alpha_{\mathrm{s}=} = \frac{g^2}{4\pi}$ in perturbative regime can be solved with the above differential equation using series expansion of β-*function*:

$$\beta(g) = -\beta_0\,\frac{g^3}{16\pi^2} - \beta_1\,\frac{g^5}{(16\pi^2)^2} + \cdots \tag{1.12}$$

At leading order:

$$\beta_0 = 11 - \frac{2}{3}n_f \tag{1.13}$$

where n_f is the number of effective quark flavors. And the corresponding solution to α_{s} reads [34]:

$$\alpha_{\mathrm{s}}(Q^2) = \frac{g^2}{4\pi} = \frac{4\pi}{(11 - \frac{2}{3}n_f)\,\ln(Q^2/\Lambda^2_{\mathrm{QCD}})}\,, Q^2 \gg \Lambda^2_{\mathrm{QCD}} \tag{1.14}$$

[1] Define dimension as $d = 4 - \epsilon$ and let ϵ go to 0.

where $Q^2 = -p^2$ and $\Lambda_{\mathrm{QCD}} \sim 200\mathrm{MeV}$ is the fundamental QCD energy scale depending on the renormalization scheme.

This term will be always positive as $n_f \leq 6$, leading to a negative coefficient at leading order [2]. Since one can read $\alpha_s \to 0$ as $M \to \infty$, this implies that gluons and quarks interact weakly at very high energies (or equivalently at very short distances), the latter is called *asymptotic freedom*. An example of experimental result of running strong coupling measurements from CMS is shown in Fig. 1.4.

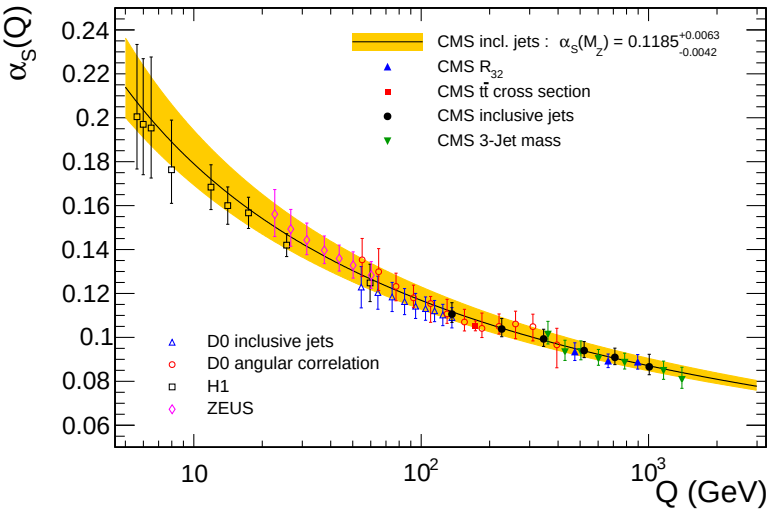

Figure 1.4: The strong coupling α_s as a function of the respective choice for the scale Q from different analyses.[35]

1.2.3 . Color confinement and hadrons

From Deep Inelastic Scattering (DIS) experiments at SLAC, internal structure of protons was first revealed as they contain point-like constituents (parton degrees of freedom), those constituents are understood within quark model. However, no free quarks were ever detected in experiments as one would expect if they are electrically charged. Together with the early jet physics in early 1970s, only high-energy jets of hadronic bound states were found to be aligned with quark direction in electron-positron annihilation process. As an example, typical experimental tests were interested in measuring the cross-section of the inclusive reaction where we may have a single quark as a final state product to be measured:

$$pp \to q(\bar{q})X \tag{1.15}$$

The best cross-section result for such a reaction was given by CMS collaboration with a value of $\sigma < 2.3 \times 10^{-40}\mathrm{cm}^2$ [36]. This value of single quark production cross-section is

[2] Fermion screening from quark loop contributions is strongly compensated by anti-screening from gluon self-interactions

10^{-15} smaller than the total pp cross-section (10^{-15} times per collision), which is extremely hard to observe experimentally.

Result from those experiments is consistent the idea of *confinement* where quarks stay inside colorless bound states of strong interaction called *hadrons*. The hadrons are classified at the first order by the number of their constituent quarks: *baryon* (qqq or $\bar{q}\bar{q}\bar{q}$), *meson* ($q\bar{q}$) and exotic states such as tetraquark ($qq\bar{q}\bar{q}$), pentaquark ($qqqq\bar{q}$), glue-ball (bound state of gluons) and hybrid (quark-antiquark plus gluon excitations).

The color confinement, reflecting the characteristic feature of QCD as a non-Abelian gauge theory, could be partially explained by the running of the strong coupling, which increases rapidly at large distances. As the energy scale decreases, soft processes, namely those with small momentum transfer or low energy properties of hadrons, will start to dominate, they cannot be evaluated using perturbation theory as the coupling constant increases. The underlying mechanism of confinement remains still unsolved. However, many attempts were made to address this problem:

- In lattice gauge theory, Kenneth G. Wilson formulated a gauge-invariant quantity called *Wilson loop* [37] which was used to construct links and plaquettes on lattice. The latter extends to the so-called *Polyakov loop* [38] in the case of finite-temperature. This lattice study leads to the *quark potential model* that will be discussed in the following section concerning quarkonia.
- In the strong-coupling framework, a different approach with string/flux-tube raised from early string-theoretical development was introduced to investigate the hadronic structure.
- Other phenomenological approaches like *Bag model* [39] can also capture the confinement phenomenology and mass spectra. The latter will be discussed in the following section of QCD phase transition and thermodynamics.

Those above mentioned directions are all deserved to be discussed, I shall go through in the next discussions their general idea without getting into the details.

Wilson line and Polyakov loop

Generally in gauge theory, it is hard to compare fields at different space-time points as they transform differently under local gauge transformation. The latter happens especially when one looks for defining a certain derivative of fields such as the directional derivative along a vector n^μ:

$$n^\mu \partial_\mu \psi = \lim_{\epsilon \to 0} \frac{1}{\epsilon} \left[\psi(x + \epsilon n) - \psi(x)\right] \tag{1.16}$$

For the sake of making this comparison physically meaningful in the sense of gauge transformation, the difference in the phase of fields should be compensated by a factor, the

simple way is to introduce a scalar quantity called *comparator* which transforms as [40]:

$$U(y,x) \;\rightarrow\; e^{i\alpha(y)}\, U(y,x)\, e^{-i\alpha(x)}\,. \tag{1.17}$$

and it will reduce to identity if the comparison is made at the same space-time point i.e. $U(x,x) = \mathbb{1}$. In practice, for an infinitesimal displacement, one can explicitly make use of comparator by series expansion around identity. This way we can handle the comparison of fields that are infinitesimally close to each other. However, the same approach does not hold for the case where fields are at far apart space-time points. Kenneth G. Wilson figured out a way by taking analogy from differential geometry, where a gauge theory can be actually defined on a fiber bundle with gauge fields as connections telling us how to parallel-transport from one point to another. The so-called *gauge-invariant Wilson line* is defined as [37]:

$$U_P(z,y) = \exp\left[-ie\int_P dx^\mu\, A_\mu(x)\right] \tag{1.18}$$

where P stands for the path from y to z. This is actually the "integral" of infinitesimal comparators alone the given path. Since the integral is taken on a differentiable manifold, so it is geometrically equivalent to taking infinitesimal parallel-transports by connections alone the path. This quantity, according to Chen-Ning Yang (he called it *non-integrable phase factor*), encodes the most fundamental ingredient for a gauge theory'[14]. If we glue together the starting point and endpoint of the phase factor integral, we arrive at the so-called *Wilson loop* which is locally gauge invariant by construction:

$$U_P(y,y) = \exp\left[-ie\oint_P dx^\mu\, A_\mu(x)\right] \tag{1.19}$$

In this way, all gauge-invariant functions of field A_μ can be actually imagined as the combinations of *Wilson loops* for different choices of the path P. The latter can be understood by rewriting the *Wilson loop* using Stokes's theorem:

$$U_P(y,y) = \exp\left[-\tfrac{ie}{2}\int_\Sigma d\sigma^{\mu\nu}\, F_{\mu\nu}\right] \tag{1.20}$$

where Σ is the surface enclosed by the loop P, $d\sigma^{\mu\nu}$ is the area element and $F_{\mu\nu}$ is the gauge field tensor. In the case of non-Abelian theory, matrices along the path do not commute, hence it is crucial to define a certain ordering when taking integration along the path and take the trace in order to recover the gauge-invariance. The *path-ordered Wilson line* is written as:

$$U_P(z,y) = \mathrm{Tr}\,\mathcal{P}\left\{\exp\left[ig\int_0^1 ds\,\frac{dx^\mu}{ds}\,A^a_\mu(x(s))\,t^a\right]\right\} \tag{1.21}$$

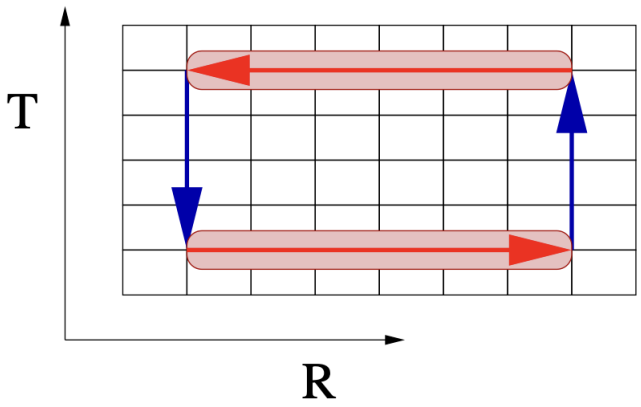

Figure 1.5: The illustration of a lattice rectangle with spatial size R and temporal size T. [41]

Taking the expectation value of the above path-ordered *Wilson loop* over a path defined on a rectangle shown in Fig. 1.5 of lattice with spatial size R and temporal size T, one obtains the relation:

$$\langle U_P(R,T)\rangle \sim e^{-V(R)T} \tag{1.22}$$

where $V(R)$ is the static quark-potential. The large-loop behavior of expectation value of *Wilson loop* points to different phases:

- For confinement phase, the expectation value follows the *area law*:

$$\langle U_P(R,T)\rangle \sim e^{\sigma\Sigma(P)} \tag{1.23}$$

- For deconfined phase, the expectation value follows the *perimeter law*:

$$\langle U_P(R,T)\rangle \sim e^{\sigma\partial\Sigma(P)} \tag{1.24}$$

where σ is the *string tension* which will be emphasized in the next section.

Therefore, the expectation value of *Wilson loop* can be used as an order parameter of the different phases in the case of zero-temperature QCD. However, in the case of thermal quantum field theory, for which the theory is formulated on Euclidean space-time ($\mathbb{R}^3\times S^1$) with a compactified imaginary temporal direction of length β such that the time interval is given by $\tau\in[0,\beta]$ and $\beta=\frac{1}{T}$ where T is the temperature. The formulation of *Wilson loop* on this specific setup leads to topologically non-trivial loops winding around the compact direction, the latter is called *Polyakov loop* [38]:

$$P(\vec{x}) = \frac{1}{N_c}\,\mathrm{Tr}\,\mathcal{P}\left\{\exp\left[\int_0^\beta d\tau\, A_0(\vec{x},\tau)\right]\right\} \tag{1.25}$$

Similarly, taking the expectation value of *Polyakov loop* leads to different phases as $\langle P(\vec{x})\rangle \sim e^{-\beta F}$ where F is the quark free energy.

- If $\langle P \rangle = 0$, one gets an infinite free energy, hence quarks are confined.
- If $\langle P \rangle \neq 0$, one gets a finite free energy, leading to the deconfinement of quarks.

In a sense, *Polyakov loop* is like a *Wilson line* closed by periodic boundary conditions [3].

Flux-tube (string) approach

During the golden age of hadron spectroscopy, a huge number of hadronic resonances were discovered. At that time, there was no unified framework for strong interaction, physicists were more familiar with the so-called *Regge field theory* introduced by Tullio Regge in 1959 [42] together with the S-matrix theory.

In Regge's theory, the orbital angular momentum l which is supposed to take values in 0,1,2,3..., can be analytically continued to the complex plane as the Legendre polynomial in partial waves can be generalized to Legendre function of complex order. Therefore, the original summation of partial waves for a typical $2 \to 2$ scattering can be rewritten in the form of a contour integral of orbital angular momentum as complex variable using Sommerfeld–Watson transform:

$$\sum_{\ell=0}^{\infty}(2\ell+1)\,a_\ell(s)\,P_\ell(\cos\theta) = \frac{1}{2i}\int_C d\nu\,\frac{2\nu+1}{\sin(\pi\nu)}\,a_\nu(s)\,P_\nu(\cos\theta) \tag{1.26}$$

where a_ν is the analytically continued partial wave amplitude, and ν is the complexified orbital angular momentum. As one can read from the denominator of integrand $\sin(\pi\nu)$, poles sit on real-axis of ν at 0,1,2,3...

At high energies, the poles will dominate the integral, so for a given process, the exchange of particles involves the whole family lying on the Regge trajectory. The experimental results of hadronic states actually followed linear Regge trajectories, but Regge's theory was not able to explain the underlying mechanism.

The story was changed by Gabriele Veneziano who proposed in 1968 a first Dual Resonance Model (DRM) for 4-meson scattering [43]:

$$A(s,t) = \frac{\Gamma(-\alpha(s))\,\Gamma(-\alpha(t))}{\Gamma(-\alpha(s)-\alpha(t))} \tag{1.27}$$

By many pioneers of early string theory development from early 1970s, including Miguel Angel Virasoro, Leonard Susskind, Holger Bech Nielsen, Yoichiro Nambu and Ziro Koba, the first DRM was soon generalized and then understood as described by a relativistic vibrating string.

[3] Coming from the trace in partition function, which implies the same initial and final states of the system.

Within this framework, mesons are modeled as open strings (flux tube) with quark and antiquark as endpoints. At low energy, string energy is proportional to its length:

$$V(r) \sim \sigma r \tag{1.28}$$

This linear potential grows up as quarks get pulled apart, leading to the confinement. Once the quark-antiquark pair gets separated far enough, the string or tube will break while creating new quark-antiquark pair at the break-point, resulting in two mesons. An illustration of this process is shown in Fig. 1.6. This linear potential at large distances was supported by lattice QCD simulation [41]

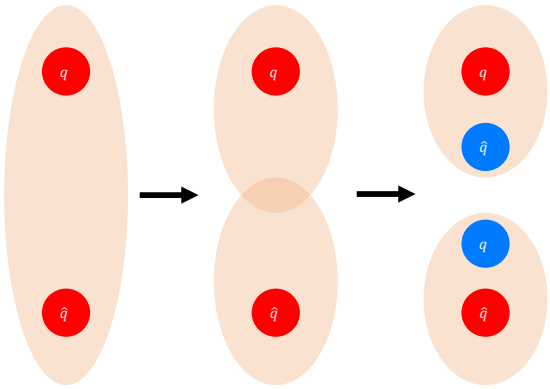

Figure 1.6: The illustration of a breaking tube of quark-antiquark pair, resulting in two new mesons.

1.2.4 . Quark-Gluon Plasma

Following the characteristic feature of QCD as non-Abelian gauge theory of color symmetry $\mathrm{SU}(3)$, we have seen from the previous discussion that the running coupling of strong interaction leads to the so-called asymptotic freedom at very short distances or extremely high energies. A certain phase transition would be therefore expected naturally if one can significantly heat or compress nuclear matters. However, the original asymptotic freedom was formulated in vacuum QCD where no thermal effect would happen, the latter must be generalized to the case of finite-temperature especially in the case of heavy-ion collisions where a thermal medium is supposed to be created.

Deconfinement in hot medium

To answer this question, Eduard Shuryak proposed in 1978 his solution using the one-loop approximation [44]. He managed to calculate the gluon propagator and the thermal

potential between two quarks of temperature T:

$$V(r) = \frac{Q}{4\pi r} e^{-mr}, \tag{1.29a}$$

$$m^2 = \frac{1}{3} g^2 \left(N_c + \tfrac{1}{2} N_f\right) T^2. \tag{1.29b}$$

The form of this potential is similar to the Debye screening potential in a classical plasma, which is the reason this hot dense matter of deconfined quarks and gluons was called Quark-Gluon Plasma (QGP). A simplified illustration of color deconfinement is shown in Fig. 1.7 This new state of matter should be created in heavy-ion collisions where the required extreme conditions can be reached, hence much experimental effort from early 1990s were dedicated to justify and investigate the properties of the QGP, including the Super Proton Synchrotron (SPS), Relativistic Heavy Ion Collider (RHIC), and Large Hadron Collider (LHC).

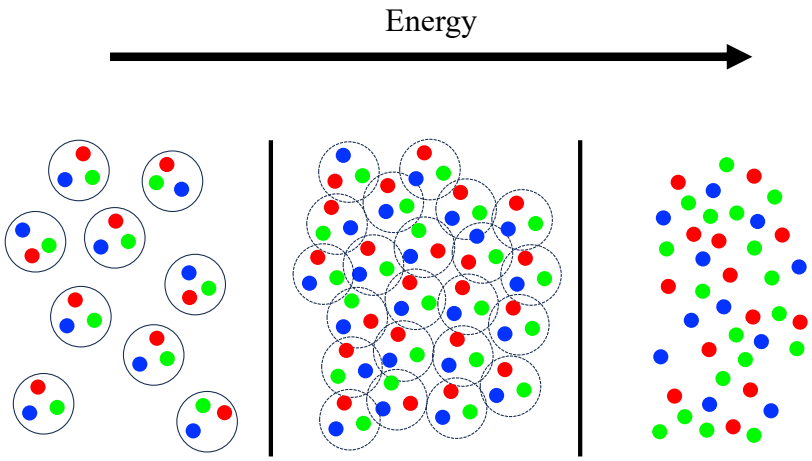

Figure 1.7: The illustration of color deconfinement as energy increases.

Despite the strong theoretical suggestion, the study of the QGP was still non-trivial. Following the description of asymptotic freedom, a weakly interacting gas of quarks and gluons is expected at high temperature and high energy density. This picture was changed after the remarkable discovery at RHIC at 2000, where data showed a strong elliptic flow which is twice larger than result from SPS. This result was in agreement with the simulation of a nearly ideal fluid, leading to the so-called strongly coupled picture. Moreover, since the QGP is considered as a hot medium, all strongly interacting matters traveling through the QGP may "feel" it in the sense that their transport properties and dynamic evolution should be modified by the surrounding medium, this includes the studies of jet quenching, quarkonia production, strangeness enhancement etc. Sitting in the core of

heavy-ion physics, the QGP is at the crucial place to sketch out the whole dynamic evolution of the system starting from the initial conditions, initial stage dynamics, isotropization and thermalization, hydrodynamic evolution of the QGP to the hadronization.

Chiral symmetry and anomaly

As another crucial feature of QCD, here I shall go through the discussion of chiral symmetry in QCD and how it is related to the hot QGP through the chiral phase transition.

For the sake of simplicity, we will consider only light quarks u and d as the following study can be naturally extended to the case where one treats also the s quark as light. Now, let's first recall the fermionic part of the QCD Lagrangian in u, d quarks representation:

$$\mathcal{L} = \bar{u}\, i\not{D} u + \bar{d}\, i\not{D} d - m_u \bar{u} u - m_d \bar{d} d \tag{1.30}$$

If the masses of u and d quarks are very small, then the two mass terms can be dropped. Therefore the resulting massless Lagrangian, despite $\mathrm{SU}(2)$ isospin symmetry between the two light flavors, involves no mixing of left- and right-handed quark fields, and remains invariant under the separate unitary transformations:

$$\begin{pmatrix} u \\ d \end{pmatrix}_L \to U_L \begin{pmatrix} u \\ d \end{pmatrix}_L, \qquad \begin{pmatrix} u \\ d \end{pmatrix}_R \to U_R \begin{pmatrix} u \\ d \end{pmatrix}_R \tag{1.31}$$

If one separates the $\mathrm{U}(1)$ and $\mathrm{SU}(2)$ components of the transformations, the symmetry group of the classical massless Lagrangian reads actually $\mathrm{SU}(2) \times \mathrm{SU}(2) \times \mathrm{U}(1) \times \mathrm{U}(1)$. The chiral components of quark doublet will be then given by:

$$Q_L = \left(\frac{1-\gamma^5}{2}\right)\begin{pmatrix} u \\ d \end{pmatrix}, \qquad Q_R = \left(\frac{1+\gamma^5}{2}\right)\begin{pmatrix} u \\ d \end{pmatrix} \tag{1.32}$$

Similarly to the Bardeen–Cooper–Schrieffer theory (BCS theory) of superconductivity [45], where in the ground state of a metal a condensate of electron pairs – so-called *Cooper pairs*, is formed by small electron-electron attraction. In the case of massless QCD, with the strong attraction between quark-antiquark pairs, the energy needed to create an extra quark-antiquark pair is quite small. This latter consideration points to, in analogy to BCS theory, a condensate of quark-antiquark pairs in QCD vacuum. Under conservation laws, these quark-antiquark pairs should have zero total momentum and angular momentum, therefore one can get a natural order parameter using VEV of the quark pair:

$$\langle \bar{Q} Q \rangle = \langle \bar{Q}_L Q_R + \bar{Q}_R Q_L \rangle \neq 0 \tag{1.33}$$

This mixing of two quarks helicities in vacuum allows light quarks to acquire effective masses in the vacuum. The non-zero VEV implies that the chiral symmetry is already spontaneously broken at zero temperature with the massless quarks approximation which is good enough since the masses of light quarks are much smaller than hadronic mass scale.

In the chiral symmetry breaking picture, pions are actually pseudo-Goldstone's bosons following Gell-Mann–Oakes–Renner relation [46]:

$$m_\pi^2 = (m_u + m_d)\,\frac{M^2}{f_\pi} \tag{1.34}$$

where f_π is *pion decay constant* obtained from π^+ via weak interaction. And the associated currents for the full symmetry group are written as:

$$j_L^\mu = \bar{Q}_L \gamma^\mu Q_L, \qquad j_R^\mu = \bar{Q}_R \gamma^\mu Q_R, \tag{1.35}$$

$$j_L^{\mu a} = \bar{Q}_L \gamma^\mu \tau^a Q_L, \qquad j_R^{\mu a} = \bar{Q}_R \gamma^\mu \tau^a Q_R, \tag{1.36}$$

where $\tau^a = \sigma^a/2$ are the generators of $\mathrm{SU}(2)$ and σ^a are Pauli matrices. Moreover, the sums of left- and right-handed currents give the baryon number and isospin currents:

$$j^\mu = \bar{Q}\gamma^\mu Q, \qquad j^{\mu a} = \bar{Q}\gamma^\mu \tau^a Q, \tag{1.37}$$

while their differences give the corresponding axial vector currents:

$$j^{\mu 5} = \bar{Q}\gamma^\mu \gamma^5 Q, \qquad j^{\mu 5 a} = \bar{Q}\gamma^\mu \gamma^5 \tau^a Q. \tag{1.38}$$

The axial current $j^{\mu 5}$ is associated to the $\mathrm{U}(1)$ symmetry, which corresponds to the transformation: $\psi \to e^{i\alpha\gamma^5}$. The invariance of the classical massless Lagrangian under this transformation leads to the conservation of axial current:

$$\partial_\mu j^{\mu 5 a} = 0. \tag{1.39}$$

This is an exact symmetry at classical level. However, Stephen L. Adler, John S. Bell and Roman W. Jackiw showed that, at quantum level, this current is no longer conserved, leading to the so-called *Adler–Bell–Jackiw anomaly* [47, 48]:

$$\partial_\mu j^{\mu 5 a} = \frac{g^2}{16\pi^2}\, F^a_{\mu\nu}\, \tilde{F}^{a\,\mu\nu}, \tag{1.40}$$

where $F^a_{\mu\nu}$ is the gauge field strength tensor and $\tilde{F}^{a\,\mu\nu} = \frac{1}{2}\epsilon^{\mu\nu\rho\sigma} F^a_{\rho\sigma}$ is the dual field strength. This explains the process of $\pi^0 \to \gamma\gamma$ which is classically forbidden if the axial $\mathrm{U}(1)$ symmetry is exact.

Chiral restoration in the hot QGP

At high enough temperature ($T \sim 150$-$170\ \mathrm{MeV}$ from lattice QCD calculation) or high baryon chemical potential μ_B, the chiral condensate melts as the VEV of quark pair goes to zero. Hence, the chiral symmetry is restored in the QGP phase. This chiral phase transition at finite temperature was expected to be first-order from the calculation of effective models such as linear σ-model.

From an experimental perspective, chiral symmetry restoration in the QGP is not observed through a direct order parameter, but rather inferred from consistent in-medium modifications of hadronic observables. Since the quark condensate is not experimentally accessible, evidence is sought through electromagnetic probes, particularly low-mass dileptons, which escape the medium largely intact and carry information about the in-medium vector spectral function.

Measurements across energies show a strong broadening of the ρ meson spectral shape rather than a simple mass shift, a behavior compatible with the progressive degeneracy of chiral partners expected near the pseudo-critical temperature. Complementary support comes from the success of thermal models in describing hadron yields at temperatures close to those predicted by lattice QCD for chiral crossover, suggesting that hadrons emerge from a medium where chiral symmetry is largely restored. Experimentally, chiral restoration appears not as a sharp signal, but as a coherent pattern of medium effects consistent with a smooth crossover rather than a true phase transition.

Having discussed the elementary of chiral symmetry and the its transition property, in the next section I shall go through the *topological map* of QCD thermodynamics from which the transition of different phases and critical conditions of the hot QCD matter would be classified. Yet, completing this map remains one of the biggest program for heavy-ion physics and thermal QCD.

1.2.5 . QCD thermodynamics and phase diagram

Let's quickly recall the statistical physics ingredients that are essential for the discussion of QCD thermodynamics. Consider a system of particles within a volume V with conserved baryon numbers, surrounded by a thermal bath at temperature T. The statistic ensembles (statistical distribution of possible states) encode all system features at thermal equilibrium. In the case of QCD where particle numbers are not really conserved (some charges are conserved instead), the thermodynamic partition function in the Grand Canonical Ensemble (GCE) (particle numbers and charges may not conserved and fluctuations are allowed, in contrast to Canonical Ensemble (CE) for which the conservation laws are exact and often used in small systems and elementary particle collisions) is written as:

$$\mathcal{Z}(T, V, \mu_B) = \mathrm{Tr}\,\rho = \mathrm{Tr}\,\exp\left[-\frac{H - \mu_B N_B}{T}\right] \tag{1.41}$$

where H is the system Hamiltonian, μ_B is the baryon chemical potential and N_B is the baryon number. Important physical quantities like total energy E, Helmholtz free energy F, entropy S, pressure p and average particle numbers $\bar{N}$ etc as well as their corresponding densities (divided by V) can be fully determined by the thermodynamic partition function.

General concepts in thermal field theory

In thermal quantum field theory, the thermodynamic partition function is equivalent to the Wick-rotated path-integral:

$$\mathcal{Z}(T,V,\mu_B) = \mathrm{Tr}\,\rho = \mathrm{Tr}\,\exp\left[-\frac{H-\mu_i N_i}{T}\right] = \int \mathcal{D}A\,\mathcal{D}\bar{\psi}\,\mathcal{D}\psi\; e^{-S_E[\bar{\psi},\psi,A_\mu]} \tag{1.42}$$

where S_E stands for Euclidean action after applying a Wick rotation for the imaginary time. And the fields satisfy periodic condition as the time direction was compactified, see previous discussion in Sec. 1.2.3. The periodicity condition allows us to expand fields in terms of Fourier series, where the modes are identified as *Matsubara frequencies* from Matsubara Green's function. Then taking the thermodynamic limit ($V \to \infty$, $N \to \infty$ and $\frac{N}{V}$ is constant) where momentum integrals are identified as Matsubara sum plus momentum integral, one should then be able to make the calculations in the framework of perturbation theory. This latter description summarizes the general setup for the computational ground of imaginary-time formalism of thermal QCD called Matsubara formalism in contrast to real-time formalism for the case of non-equilibrium. In particular, the energy and pressure density read:

$$\varepsilon \equiv \frac{E}{V} = \frac{T^2}{V}\left(\frac{\partial \ln \mathcal{Z}}{\partial T}\right)_{V,\mu_q} + \mu_i \frac{N}{V}\,, \qquad p = T\left(\frac{\partial \ln \mathcal{Z}}{\partial V}\right)_{T,\mu_i}\,, \tag{1.43}$$

from which the Equation of State (EoS) can be deduced.

Lattice calculation

Beyond the perturbative regime as one goes to soft scales ($2\pi T \to gT \to g^2 T$), some effective models are developed but have a hard time to capture the details or even fail. Perturbation theory in this sense is very limited even with a very weak coupling, due to the effective scales.

However, lattice calculation provided a genuine framework at relatively low energy scales by discretizing directly the QCD partition function, this formalism can capture the non-perturbative features that are not covered by effective model calculations and plays a particularly important role in studying the phase transition from first principles. Important observables like order parameters and their associated susceptibilities (fluctuation) can be directly evaluated on lattice.

Phenomenological models of phase transition

Apart from first-principle calculations, there were several phenomenological models trying to describe the picture of QCD phase transition including the *MIT Bag model* [39] and NJL model by Yoichiro Nambu and Giovanni Jona-Lasinio [49].

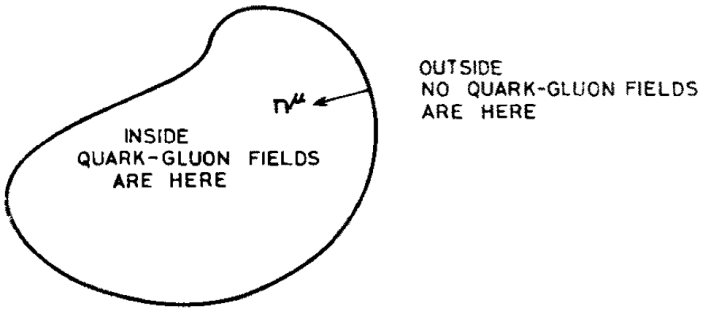

Figure 1.8: An illustration of bag model configuration where n^μ is the inward normal vector on the boundary of the bag. [39]

In the picture of *MIT Bag model*, hadrons are modeled as constrained in a finite region of space containing free quarks and gluons, with a radius $R \sim \Lambda_{\rm QCD}^{-1}$ surrounded by physical vacuum, a simple illustration is shown in Fig. 1.8. The energy density cost to create a bag is called *Bag constant* B. The latter represents the energy difference between the interior and exterior of the bag, providing confinement pressure that keeps quarks inside the bag where quarks follow Dirac equation, while the confinement is ensured and maintained by imposing suitable boundary conditions to prevent leakage of color currents as one can read:

$$T^{\mu\nu}_{\rm Hadron} = \begin{cases} T^{\mu\nu}_D - g^{\mu\nu}B, & \text{inside the bag,} \\ 0, & \text{outside,} \end{cases} \tag{1.44}$$

where $T^{\mu\nu}_{\rm Hadron}$ is the hadron stress tensor and $T^{\mu\nu}_D$ is the Dirac stress tensor. In a realistic scenario, one would consider color coupling as well following a Yang-Mills fashion, so hadrons are actually a mix bag of colored quarks and gluons with modified boundary conditions.

Within the Bag model description, when matter is heated to sufficiently high temperatures, atomic nuclei dissolve into their constituents, nucleons. Meanwhile, light hadrons (predominantly pions) are produced thermally, gradually filling the space between the nucleons. Because hadrons have a finite spatial extent, these thermally produced pions and other hadrons start to overlap with one another and with the quark “bags” of the original nucleons. As the temperature rises, these overlapping regions form an extended network of zones containing quarks, antiquarks, and gluons. At a certain critical temperature $T_{\rm c}$, this network "percolates" throughout the entire system, marking the transition to a new state of matter: the QGP. Similarly, nucleons can overlap at a critical density number $n_{\rm c}$, giving raise to a cold degenerate QGP which is mostly dominated by quark degrees of freedom. In the simplified scenario of a free gas of massless quarks, thermodynamic quantities of the QGP like the pressure as a function of temperature can be evaluated following Gibbs construction of boundary phase:

$$p_{\rm QGP}(T, \mu_i) = \frac{37\pi^2}{90}T^4 + \mu_i^2 T^2 + \frac{\mu_q^4}{2\pi^2} - B \tag{1.45}$$

However, the Bag model was not able to incorporate the chiral symmetry aspect of QCD dynamics, another phenomenological approach implementing chiral symmetry breaking mechanism was also introduced, inspired by the BCS theory of superconductivity, known as the NJL model which was at the first place an effective model for pions. Similar to the previous discussion of the chiral symmetry in Sec. 1.2.4, an approximate Lagrangian is defined where only u, d quarks are considered:

$$\mathcal{L}_{\mathrm{NJL}} = \bar{Q}(i\not{\partial} - m_0)Q + G[(\bar{Q}Q)^2 + (\bar{Q}i\gamma^5\tau^a Q)^2] \tag{1.46}$$

where Q is the u, d quarks doublet, m_0 is the bare mass of light quarks (leading to the explicit chiral symmetry breaking) and G is the coupling constant of the four-fermion interaction. The four-fermion interaction creates quark condensate $\langle\bar{Q}Q\rangle \neq 0$ leading to the spontaneous chiral symmetry breaking where quarks acquire dynamical mass following:

$$M = m_0 - 2G\langle\bar{Q}Q\rangle \tag{1.47}$$

And similarly, the VEV of quark-antiquark pairs can serve as an order parameter signaling chiral phase transition with a critical temperature T_{c}. At $\mu_B = 0$, NJL model predicts a smooth crossover chiral transition similar to lattice results, while at finite μ_B, NJL predicts a first-order chiral transition at low T and large density.

Certainly, there are many other models which are not covered here in the above discussion, such as statistical model based on bootstrap and massive two-flavors effective potential model etc. However, none of these models can give a fully realistic description. The advance of current understanding for the phase diagram needs more effort from both theoretical and experimental sides.

To summarize the discussion, in the Fig. 1.9, a sketch of current theoretical and experimental knowledge on the phase diagram of strongly interacting matter is presented.

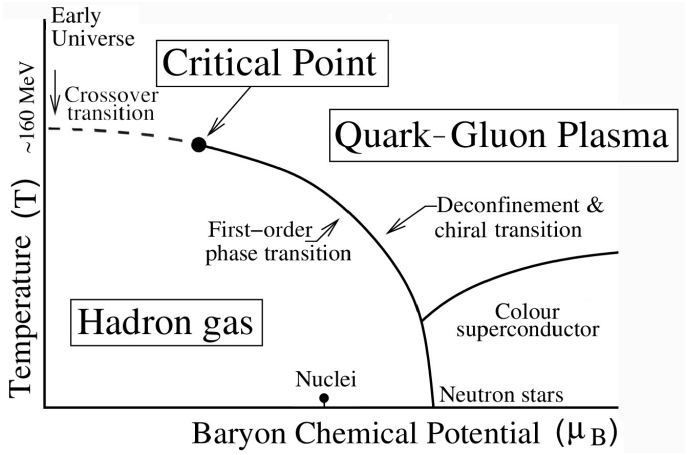

Figure 1.9: An illustration of phase diagram of strongly interacting matter in the plane of temperature and baryon chemical potential.

1.3 Ultrarelativistic heavy-ion collisions

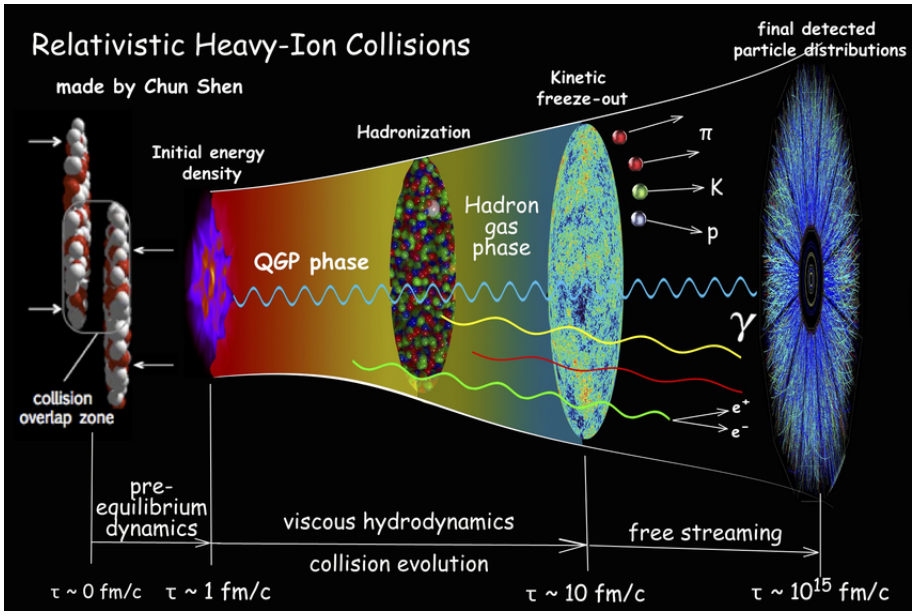

Figure 1.10: A sketched view of the system evolution of relativistic heavy-ion collisions [50].

With the demand of a complete understanding for the strongly interacting nuclear matter from the experimental side, pioneering experiments in heavy-ion collisions (for those having beam energy $E_{\rm lab} > 1\,{\rm GeV}$ per nucleon) started from early 1970s in US and Russia. At the first time, nuclear physicists managed to compress the nuclear matters under fairly extreme conditions to study their thermal properties. A remarkable point was from the NA35 experiment at the highest SPS energy, the latter reached for the first time the theoretical energy density $2\,{\rm GeV/fm^3}$ to create the Quark-Gluon Plasma (QGP) in S–S collisions [51]. The subsequent goal of later Pb–Pb collisions was to look for the onset of QGP formation by decreasing collision energy.

Genuine collider physics with heavy-ions started with RHIC at Brookhaven National Laboratory from 2000, where initial experiments were carried out at a center-of-mass collision energy of $\sqrt{s_{\rm NN}} = 130\,{\rm GeV}$ then $200\,{\rm GeV}$ per nucleon pair. Later, the Beam Energy Scan program was initiated with the motivation of looking for the critical point of the phase diagram. Experimental measurements for the early QGP studies including charge particle multiplicities, hadron spectra, anisotropic flow, heavy flavors and jet quenching were carried by the experimental collaborations BRAHMS [52], PHOBOS [53], PHENIX [54], and STAR [55]. The very first plausible result of elliptic flow measurement was done as well during that time, as a strong experimental support for early hydrodynamic calculations.

The Large Hadron Collider (LHC), which started taking data in 2010, brought the real breakthrough in heavy-ion experiments with the available beam energy an order of magnitude higher than at RHIC. At this energy level, the formation of the QGP in large systems becomes unquestionable. The main program at LHC includes pp, p–Pb as well as Pb–Pb collisions, the latter providing an ideal place to study precisely the hot dense fireball. Similar to RHIC, flow measurements and jet quenching studies are also part of the center of interest for the LHC, while an unexpected surprise was spotted from the flow measurements in smaller systems like p–Pb or high-multiplicity pp collisions, the latter bringing in a challenge to the applicability and deeper understanding of hydrodynamics.

From a sketched view of the general structure, ultrarelativistic heavy-ion experiments span a multi-stage dynamic picture of strongly interacting nuclear matter, as shown in Fig. 1.10, from colliding systems before the collision to the final observables as captured in the detectors. This multi-stage picture includes: pre-collision stage related to the collision kinematics, collision and initial conditions, the initial expansion and pre-equilibrium dynamics, the formation and thermalization of the QGP, hydrodynamic expansion and system cooling, freeze-out and hadronization, and final stage transport.

In the following sections, our discussions shall follow the same order of stages in the system evolution of heavy-ion collisions. The main goal here is rather to resemble a logically consistent picture through the most important ingredients.

1.3.1 . Kinematics and space-time evolution

In this section, some necessary elements for heavy-ion collision kinematics will be reviewed, as well as the early developments in describing space-time evolution of the colliding system.

Kinematic variables in heavy-ion collisions

Before we talk about the early system expansion, it will be useful to introduce a few important kinematic variables in a typical colliding system. In ultrarelativistic heavy-ion collisions, it is often convenient to consider the *light-cone variables* as the system in the center-of-mass frame is highly boosted longitudinally. The light-cone momenta and coordinates are defined respectively following:

$$p^{\pm} = \frac{1}{\sqrt{2}}\left(E \pm p_z\right),\ x^{\pm} = \frac{1}{\sqrt{2}}\left(t \pm z\right) \tag{1.48}$$

where the transverse (perpendicular to the beam axis) part remains unchanged: $x_{\mathrm{T}} = (x, y)$ and $p_{\mathrm{T}} = (p_x, p_y)$. The corresponding four-vectors for space-time and momentum coordinates in the light-cone representation become:

$$x^{\mu} = (x^{+}, x^{-}, x_{\mathrm{T}}),\ p^{\mu} = (p^{+}, p^{-}, p_{\mathrm{T}}) \tag{1.49}$$

with the associated metric reads:

$$p \cdot x = p^+ x^- + p^- x^+ - p_{\mathrm{T}} \cdot x_{\mathrm{T}} \tag{1.50}$$

And the on-shell relation follows:

$$p^2 = 2p^+ p^- - p_{\mathrm{T}}^2 = m^2 \tag{1.51}$$

where m is the invariant mass. The usefulness of using light-cone coordinates can be seen as it can largely simplify the scenario of a high energy colliding system, which is highly longitudinally boosted. Following which, for a left moving particle having $p_z \sim E$, it has $p^+ \sim \sqrt{2}E$ while $p^- \sim 0$; meanwhile for a right moving particle, $p^- \sim \sqrt{2}E$ and $p^+ \sim 0$ instead. A *rapidity* variable can be also defined as:

$$y = \frac{1}{2} \ln \left(\frac{p^+}{p^-} \right) \sim \ln \left(\frac{2E}{m_{\mathrm{T}}} \right) \tag{1.52}$$

where $m_{\mathrm{T}} = m^2 + p_x^2 + p_z^2 = E^2 - p_z^2$. In high energy physics experiments, one usually considers another variable called *pseudo-rapidity*, and as $m \ll |p|$ rapidity and pseudo-rapidity converge:

$$\eta = \frac{1}{2} \ln \left(\frac{|\mathbf{p}| + p_{\mathrm{L}}}{|\mathbf{p}| - p_{\mathrm{L}}} \right) \tag{1.53}$$

Impact parameter and collision geometry

In heavy-ion collisions, the *impact parameter vector* b is extremely important in determining the initial geometry of a given collision, the latter relies on classifying the overlap zones across all collisions. Following this way, the impact parameter is defined naturally as the transverse distance between the centers of two colliding nuclei, shown in Fig. 1.11.

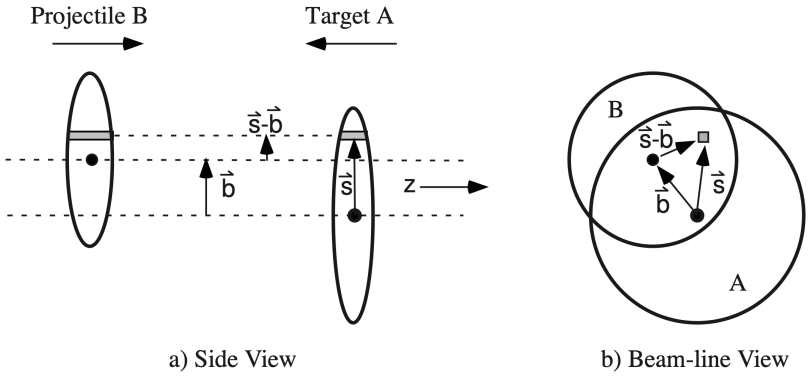

Figure 1.11: An illustration of Optical Glauber model geometry with transverse (a) and longitudinal (b) views. [56]

The impact parameter is by definition a pure geometric variable that cannot be directly accessed from experiments. However, the connection between impact parameter

and some global experimental observables is provided by the *Glauber model* [57] as an effective description of nucleus-nucleus interaction in terms of elementary nucleon-nucleon interactions.

The Glauber model is constructed within the optical-limit approximation, where the total phase shift of the incoming projectile is expressed as the sum of all possible two-nucleon phase shifts. The imaginary part of these phase shifts is directly connected, via the optical theorem, to the nucleon–nucleon scattering cross section. In addition, the model assumes that at high energies nucleons will carry sufficiently high momentum that keeps the nucleon traveling on a straight line path.

Consider, as shown in Fig. 1.11, a target A and a projectile B. Their basic geometry is parametrized by the impact parameter vector b. For the collision, we consider a flux tube located at $\vec{s}$ measured from the center of target A, the probability per unit transverse area of a given nucleon at the location of this flux tube reads:

$$\hat{T}_A(\mathbf{s}) = \int \hat{\rho}_A(\mathbf{s}, z_A)\, dz_A \tag{1.54}$$

where $\hat{\rho}_A(\mathbf{s})$ is the probability per unit of volume normalized to 1, the latter is parametrized by a Fermi distribution (Wood-Saxon) with three parameters:

$$\rho(r) = \rho_0 \cdot \frac{1 + w\left(\frac{r}{R}\right)^2}{1 + \exp\left(\frac{r-R}{a}\right)} \tag{1.55}$$

where ρ_0 corresponds to nucleon density at the center of the nucleus. The key quantity called *thickness function* as a function of impact parameter is obtained by integrating the joint probability in the respective overlapping target and projectile flux tubes:

$$\hat{T}_{AB}(\mathbf{b}) = \int \hat{T}_A(\mathbf{s})\hat{T}_B(\mathbf{s}-\mathbf{b})\, d^2\mathbf{s} \tag{1.56}$$

Together with the total cross-section in case the nuclei are not polarized:

$$\sigma_{\text{inel}}^{A+B} = \int_0^\infty 2\pi b\, db \left\{1 - \left[1 - \hat{T}_{AB}(b)\, \sigma_{\text{inel}}^{\text{NN}}\right]^{AB}\right\} \tag{1.57}$$

where $\sigma_{\text{inel}}^{\text{NN}}$ is the nucleon-nucleon inelastic cross-section.

The total number of nucleon-nucleon collision and the number of participants can be evaluated:

$$N_{\text{coll}}(b) = AB\, \hat{T}_{AB}(b)\, \sigma_{\text{inel}}^{\text{NN}}, \tag{1.58}$$

$$\begin{aligned} N_{\text{part}}(b) = A \int \hat{T}_A(\mathbf{s}) \left\{1 - \left[1 - \hat{T}_B(\mathbf{s}-\mathbf{b})\, \sigma_{\text{inel}}^{\text{NN}}\right]^B\right\} d^2\mathbf{s} \\ + B \int \hat{T}_B(\mathbf{s}-\mathbf{b}) \left\{1 - \left[1 - \hat{T}_A(\mathbf{s})\, \sigma_{\text{inel}}^{\text{NN}}\right]^A\right\} d^2\mathbf{s}. \end{aligned} \tag{1.59}$$

From where we can get $\langle N_{\mathrm{coll}} \rangle$ and $\langle N_{\mathrm{part}} \rangle$ that are accessible via global observables. This "participant-spectator" picture in a nuclei-nuclei collision is illustrated in Fig. 1.12

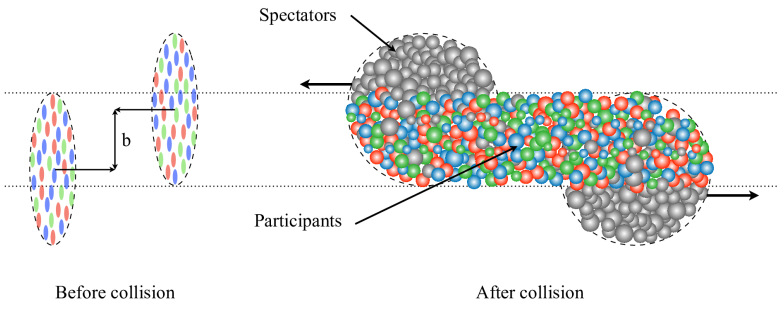

Figure 1.12: A schematic view of impact parameter as well as participants and spectators illustration in heavy-ion collisions. [58]

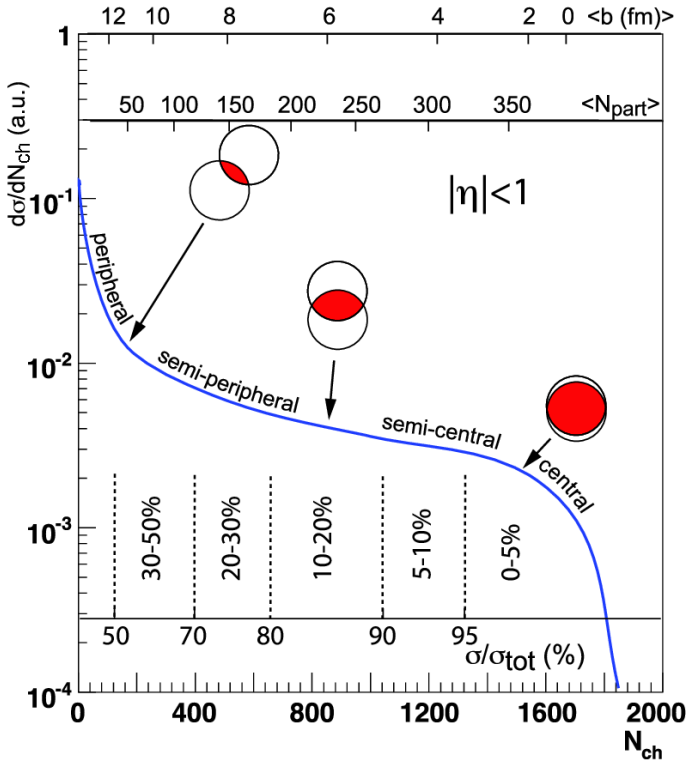

Figure 1.13: An example of correlation between number of charged-particles with Glauber calculations together with different centrality classes.[56]

In practice, $\langle N_{\rm coll} \rangle$ and $\langle N_{\rm part} \rangle$ can be related to final state observables such as charged-particle multiplicity, transverse energy from calorimeter or direct estimation of number of spectators from the energy measured in the Zero-Degree Calorimeter (ZDC). The determination of impact parameter can be done by matching experimental global observables to results from Monte&Carlo Glauber model simulation. From purely experimental consideration, one can classify the collision geometry directly by identifying the regions of measured $\langle N_{\rm part} \rangle$ histogram with different *centrality* classes as shown in Fig. 1.13

Space-time evolution of collision system from Bjorken's model

As an early attempt trying to sketch out the space-time evolution of the collision process, it is worth going through the essential of Bjorken's formalism [59], which provides a rather simplified and yet insightful description of the system evolution in the central rapidity region. The latter was formulated based on Landau's framework of hydrodynamics, but Bjorken considered a different initial boundary condition:

- **Landau's model** [60, 61]: at relatively low energy, full-stopping at collision moment.
- **Bjorken's model**: at high energy, transparency as the colliding nuclei pass through each other. The longitudinal direction is taken as the beam direction, the latter is strongly boosted, which makes colliding nuclei look like thin disks or "pancakes" as illustrated in Fig. 1.14.

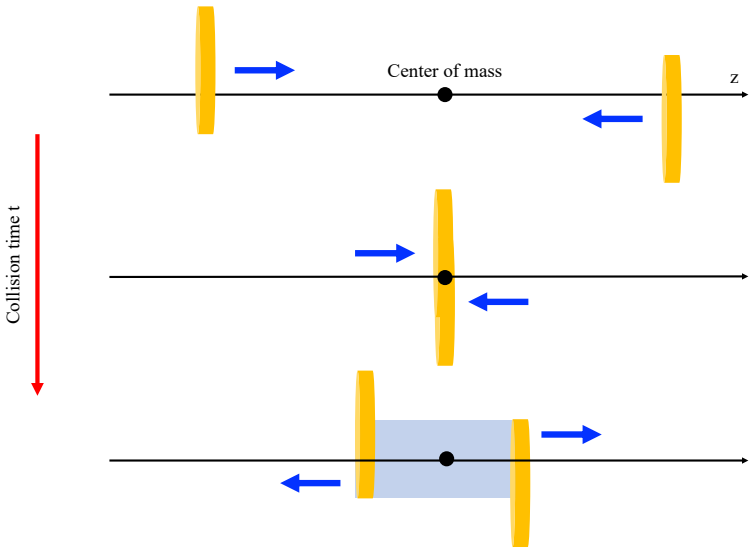

Figure 1.14: A simplified illustration of collision process in the Bjorken's formalism.

Based on what was observed in e^+e^-collisions, Bjorken's model assumed a symmetric "central-plateau" structure of particle production as a function of rapidity at sufficiently

high energy. This assumption states that the full system evolution becomes only a function of the *proper time* τ:

$$\tau = \sqrt{t^2 - z^2} \tag{1.60}$$

After the collision, the receding nuclei leave the overlap region where the fluid undergoes a boost-invariant longitudinal expansion. However, at the boundary between the hot medium and vacuum along the transverse direction, a rarefaction front induced by the difference of pressure will drive the inside hot plasma to expand into the vacuum outside.

The equation of motion for expanding ideal fluid is then given by the conservation of energy-momentum stress tensor:

$$\partial_\mu T^{\mu\nu} = 0 \tag{1.61}$$

where $T^{\mu\nu} = (e + P)u^\mu u^\nu - Pg^{\mu\nu}$ with the fluid four-velocity $u^\mu = (\frac{t}{\tau}, 0, 0, \frac{z}{\tau})$ satisfying $u^\mu u_\mu = 1$, e is the energy density in the fluid's local rest frame and P is the pressure. The fluid equation of motion then reduces to:

$$\frac{\partial e}{\partial \tau} = -\frac{e + P}{\tau} \tag{1.62}$$

The solution gives:

$$e(\tau) = e(\tau_0)\left(\frac{\tau}{\tau_0}\right)^{-4/3} \tag{1.63}$$

where $\tau_0 \sim 1\,\mathrm{fm}/c$ and $e(\tau_0) = e_0 \sim 1 - 10\,\mathrm{GeV}/\mathrm{fm}^3$. This solution leads to Bjorken's picture of a simplified hydrodynamic evolution as illustrated in Fig. 1.15

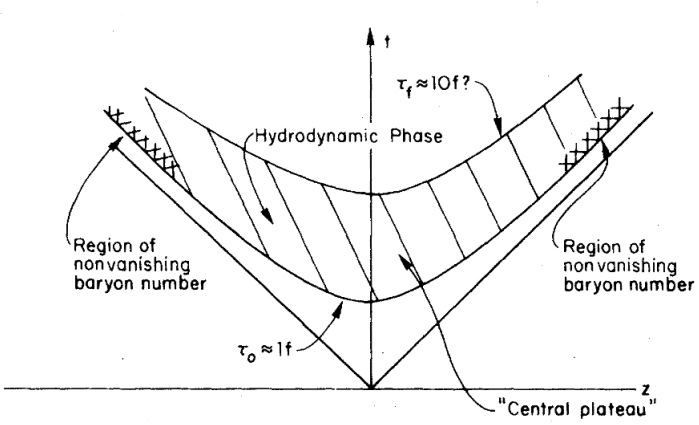

Figure 1.15: The Bjorken's solution of collision system expansion. [59]

Despite many limitations in this primitive model, Bjorken's approach was indeed a insightful starting point, and more importantly, the very first "visualization" of the collision system evolution. In the following discussions, we shall complete this initial attempt with

more details toward the modern understanding of collision kinematics and the underlying dynamic mechanism.

1.3.2 . Initial conditions and early time dynamics

The Bjorken's picture of space-time evolution for the collision system followed a rather simplified physics scenario such as the initial conditions assumed for the calculation and the absence of transverse dynamics or further detailed considerations in hydrodynamics. In this section, I would rather start from the beginning of this time-ordered multi-stage evolution, where we shall discuss the initial conditions of heavy-ion collisions. Then to complete the discussion of the initial stage, I will go through a short discussion of early time dynamics which becomes more and more important nowadays as it encodes the onset and justification for hydrodynamic calculation and the applicability.

Initial conditions

For a general physics scenario at the moment right before nuclei come to collide, the wavefunctions of the pancakes, as they are strongly Lorentz-contracted, consist of the "slow", i.e. small x, degrees of freedom, predominantly gluons at the the central rapidity region in high-energy collisions. At large energies these gluons form a dense system that is characterized by a *saturation scale* $Q_{\rm s}$. The degrees of freedom below the saturation scale are considered as classical Yang-Mills fields taking feed-down from large-x partons. Below, we shall review different aspects of initial conditions including geometry-focused phenomenological Glauber-type models, parametric-phenomenological TRENTo [62], and QCD-based saturation models like Color-Glass Condensate (CGC)/IP-Glasma.

Glauber type models As roughly discussed in the previous section, the Glauber model provides a rather simplified effective picture to describe nucleus-nucleus collision in terms of nucleon-nucleon interactions. In modern approaches, the standard Glauber model can be extended by introducing event-by-event fluctuations in nucleon position and deposited entropy. A more advanced model as *IP-Glauber* implements an Impact-Parameter Saturation Model capturing the small-x behavior in a gluon saturated initial setup. The linear evolution given by DGLAP [63–65] for $\frac{\partial f}{\partial \ln \mathrm{Q}^2}$ and by BFKL [66, 67] for $\frac{\partial f}{\partial \ln(1/x)}$ give a rather too strong growth at low-x leading to an exponential radiation of gluons, which violates the unitarity as well as the Froissart bound at some point. For this reason one must account for the nonlinear contribution in the evolution, leading to the saturation effect.

Transport-Relativistic Events iNiTial cOnditions (TRENTo) framework This effective model was introduced by the Duke team in 2015 [68], the idea is to provide a realistic Monte&Carlo initial entropy profile without assuming specific physical mechanisms for entropy production, pre-equilibrium dynamics, or thermalization. It provides a rather flexible parametric model with the advantage of being fast and tunable to data. Similar to Glauber-type models, the key quantity is the thickness function of the two nuclei. The

deposited entropy can be described by a reduced thickness function following:

$$s(\mathbf{s}) \propto \left(\frac{T_A^p(\mathbf{s}) + T_B^p(\mathbf{s})}{2} \right)^{1/p} \tag{1.64}$$

leaving p as free parameter which has to be tuned to data. The event-by-event fluctuation in deposited entropy can be accounted by assigning a random weight for each participant nucleon. And the $\langle N_{\rm part} \rangle$ can be written as:

$$\langle N_{\rm part} \rangle \propto \int dx\, dy\, T_R \tag{1.65}$$

Color-Glass Condensate (CGC) formalism In the CGC framework, the saturation scale, depending on Bjorken-x and nucleus size, actually separates two regimes in describing the partonic composition of a nucleus at high energies:

- **Dilute regime** ($k_{\rm T} \gg Q_{\rm s}$), where the gluon occupation numbers are small $f(k_{\rm T}) \ll 1$, so perturbative QCD calculation (DGLAP/BFKL) will still hold, scatterings are described using PDFs.
- **Saturation regime** ($k_{\rm T} \leq Q_{\rm s}$), where gluon occupation numbers become large $f(k_{\rm T}) \sim 1/\alpha_{\rm s} \gg 1$, nonlinear effects dominate as gluons overlap, and the smooth connection from pQCD to dense regime is handled by an eikonal resummation that restores the unitarity. The degrees of freedom in this dense regime are transverse color fields called Color-Glass Condensate (CGC).

Following this description, for the case of heavy ions like Pb at the LHC, the incoming nuclei before getting to collide look mostly like two sheets of transverse gluon fields, the initial color density information is encoded in a *weight functional* $W_y[\rho]$ with rapidity y dependency. The early framework for the evolution of weight functional uses McLerran-Venugopalan model [69–71], which gives a Gaussian form with fixed $Q_{\rm s}$. In the current setup, advanced models consider rather Balitsky-Kovechegov (BK) equation [72–74] with running coupling (rcBK) or NLO-BK and JIMWLK equation [75–77]. In the formalism of JIMWLK, the Wilsonian renormalization group equation for probability function $W_y[\rho]$ is determined by the JIMWLK Hamiltonian, leading to an evolution equation which has the form of a functional Fokker-Planck equation:

$$\frac{\partial W_y[\rho]}{\partial y} = H_{\rm JIMWLK}\, W_y[\rho] \tag{1.66}$$

Following this picture, a new state called *glasma* will be formed right after the collision of two CGCs, giving rise to longitudinal chromo-electric and chromo-magnetic fields that form flux-tubes along rapidity. The solution of weight functional from JIMWLK equation allows us to define the source term in the Yang-Mills equations describing the glasma. Solving Yang-Mills equations give input data for further hydrodynamic evolution.

In modern developments, models like b-CGC [78] (BK-based and fitted to dipole magnitude) usually incorporate an impact parameter dependency, as mentioned in the discussion about Glauber-type models, to account for fluctuations and subnucleon structure. Different approach like IP-Sat (DGLAP-based) [79] plus glasma with classic Yang-Mills equations gives rise to the so-called IP-Glasma model [80] that is widely used with the initial setup for hydrodynamics.

Early time dynamics

Despite the success of hydrodynamics as an effective model in describing the expansion of the QGP after the onset of *hydrodynamization*, the standard hydrodynamic description with gradient expansion would not be sufficiently justified as the fields and energy density profiles are extremely anisotropic and vary extremely fast at early times, and yet the standard hydrodynamic simulations require a certain *initialization* time for the onset of hydrodynamics with local equilibrium. The stage before this onset of hydrodynamics is called *pre-equilibrium* or *pre-thermal*, where the system is far-from-equilibrium and highly anisotropic ($P_{\mathrm{L}} \ll P_{\mathrm{T}}$). Moreover, as a minimal requirement for almost all early stage dynamics models, the pre-thermal calculations should smoothly converge to the hydrodynamic regime, therefore, this nonphysical initialization time for standard hydrodynamics is supposed to be promoted to a physical model parameter often called *thermalization time* that should be extracted from data.

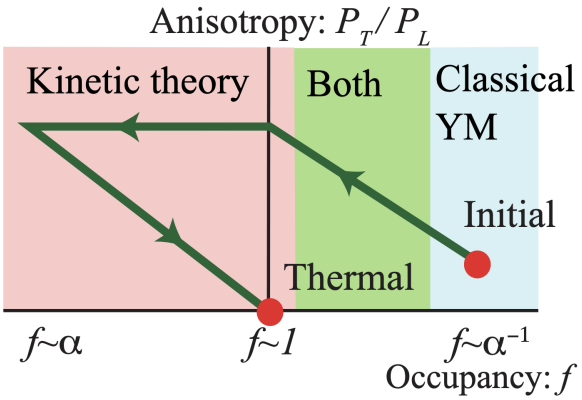

Figure 1.16: An illustration of domain of applicability and the evolution of system anisotropy for different models in terms of occupation number [81].

Two competing strategies are often discussed for the pre-thermal evolution, the latter include the weak- and strong-coupling pictures.

Strong-coupling picture This first strategy follows the AdS/CFT correspondence for certain supersymmetric Yang-Mills theories at the limit of infinite t'Hooft coupling ($g^2 N_c \to \infty$), the latter converts the QFT calculation to the solution of the space-time geometry

within a gravitational model where the thermalization time can be identified as the formation time of black-hole in the gravity dual picture [82]. The emergence of a nearly perfect-fluid like behavior at later time was justified in this framework as the unique non-singular gravity solution [83]. This formalism provided the shear viscosity $\frac{\eta}{s}$ at the strongly coupled limit, as a lower bound. Despite the beautiful connection between QFT and gravitational calculations, the major problem in this approach is the difficulty of formulating an exact correspondence with QCD. Although a strict bottom-up AdS/QCD correspondence does not exist, holography provides a controlled strong–coupling laboratory where qualitative and sometimes semi–quantitative universal features of strongly interacting plasmas can be extracted and compared to QCD phenomenology [84, 85].

Weak-coupling picture Therefore, the most pragmatic considerations would tend to follow the second strategy which is to proceed calculations in the weak-coupling limit ($\sqrt{s} \to \infty$) where Boltzmann-based kinetic theory becomes applicable. In this limit, the initial condition for the pre-thermal evolution is fairly well understood in terms of the physics of saturation and the Color-Glass-Condensate framework [86]. In the picture of saturation physics, the post-collisional glasma (with the occupation number $f \sim 1/\alpha_s \gg 1$) in the midrapidity region will evolve according to classical Yang-Mills equations and eventually turn into a hydrodynamically expanding medium. An illustration of a path from the initial conditions to thermal equilibrium in the weak-coupling picture across different the model effective domains in the phase space of anisotropy P_T/P_L and occupancy f is shown in Fig. 1.16. However, for a system at thermal equilibrium, the phase space occupancies would be close to unity for a given temperature T, this bring the subtlety of how to make the bridge between the over-occupied initial far-from-equilibrium states to a thermal state under the rapidly expanding geometry of the collision system [81].

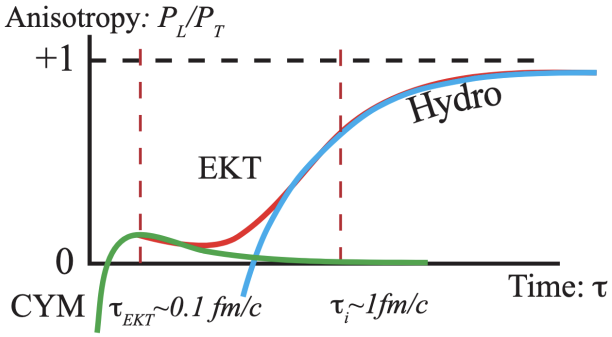

Figure 1.17: An illustration of the connection between different time regions corresponding to different dynamic conditions in the weak coupling picture where the green line shows calculation from classic Yang-Mills evolution, the red line gives the profile from effective kinetic theory calculation and the blue line describes the later hydrodynamic evolution once the system reaches thermal equilibrium [81].

The modern approach considers an Effective Kinetic Theory (EKT) [87] as a bridge between the classic Yang-Mills evolution of gluon fields and the onset of hydrodynamics. The initial conditions for the EKT are parametrized by a classic Yang-Mills evolution [4] at a switching time $\tau_{\rm EKT} = 1/Q_{\rm s}$ [81]. The equivalence between EKT and classical Yang-Mills evolution at over-occupied regime was numerically demonstrated in [88] with an isotropic setup. As the kinetic evolution drags the system close to the thermal equilibrium, there will be eventually a moment of switching on hydrodynamics. The illustration of the switching in the weak coupling limit across different model domains is shown in Fig. 1.17.

Some modern developments implement viscous hydrodynamics that describe surprisingly well the data at a close-to-hydrodynamization time $\tau \sim 0.5\text{-}1\,{\rm fm}/c$. The latter was justified from the kinetic theory viewpoint with the early Boltzmann equation in relaxation-time approximation and the later QCD EKT calculations including $2 \to 2$ scattering and effective $1 \to 2$ collinear splittings, by the fact that pre-thermal calculations from a far-from-equilibrium setup actually display a universal convergence: all non-equilibrium memories are lost and the system is "automatically" dragged to the fixed-point called *hydrodynamic attractor* [89, 90]. Also for hydrodynamics beyond gradient expansion, a proper resummation using *Borel transformation* and subsequent *alien calculus* within the framework of *resurgence theory* has illustrated the emergence of attractor [91]. Following these considerations, hydrodynamics can be actually understood as an effective solution to the far-from-from-equilibrium dynamics, which makes the idea of the ambiguous onset time for hydrodynamics moot. Therefore, hydrodynamics with large viscous corrections can be applied almost immediately after the collision [92].

Another relevant approach is to use the so-called Functional Renormalization Group (FRG) formalism using scale-dependent n-point irreducible effective action (n-PI) Γ (with a suitable truncation) for which the evolution is governed by Wetterich equation [93]. In the case of non-equilibrium, the standard FRG framework can be extended to the real-time case formulated on Keldysh contour where the truncations are more crucial [94]. In contrast to weak-coupling perturbative calculations, even with relatively small truncations, one would be able to capture (part of) nonperturbative effects and subtle effects such as non-thermal fixed-points as quasi-stable local vacua of the non-equilibrium dynamics and attractors.

1.3.3 . Hydrodynamic description

As the most successful working description in heavy-ion collisions, one of the first reasons this picture was introduced was to explain the strong collective flow measured at RHIC and also later at LHC. The surprisingly good predictions from hydrodynamics provided also strong arguments for the fluid-like nature of the QGP. Despite being viewed as a phenomenological modeling at beginning of its application in heavy-ion physics, hydrodynamics becomes now an effective description of long-wavelength QCD modes with the

[4] As long as the system is over-occupied.

recent progress of the hydrodynamic attractor discussed in the previous section.

The standard starting point of hydrodynamics is to assume that the system is close to local thermal equilibrium in addition to two extra assumptions:

- **Isotopization** The system right after the collision will remain in a far-from-equilibrium state and highly anisotropic. Further interactions will drive the longitudinal and transverse pressure to be nearly equal.
- **Thermalization** During the early time dynamics, distribution functions will tend to converge to global thermal distributions.

Those two standard conditions are necessary for a system to be considered sufficiently equilibrated. However, this paradigm was slightly shifted due to the discovery of global fixed-point, hydrodynamic attractor. One would be able to apply the hydrodynamic framework even before the system reaches the thermalization time where local equilibrium is required. The key signature in this case is rather the so-called *hydrodynamization* [89], which is identified as the moment when the system's stress tensor evolution matches the hydrodynamic attractor solution even if the system is still highly anisotropic and microscopic distributions are still far from equilibrium.

However, for the general (macroscopic) continuum fluid dynamic framework with gradient expansion to hold in contrast to the (microscopic) discrete particle-like framework such as the Boltzmann kinetic model, the remaining requirement lies on identification of system's relevant degrees of freedom where the mean free path should be much smaller than the system size, which is equivalent to exhibiting a very small Knudsen number K_n.

For the general setup of standard hydrodynamics with gradient expansion (small K_n), similar to the previous discussion of Bjorken's model 1.3.1, we start from the elementary equations of hydrodynamics, which consist of the conservation of the stress tensor and the charges, plus some eventual constitutive relations between physical quantities:

$$\partial_\mu T^{\mu\nu} = 0 \tag{1.67}$$

$$\partial_\mu j^\mu = 0 \tag{1.68}$$

where $T^{\mu\nu}$ is the usual stress tensor of the fluid field, and j^μ is the four-current of conserved charges which is defined as $j^\mu = nu^\mu$ with n the particle density. The main configuration of hydrodynamics addresses the following aspects:

- **The dimensionality**: such as (2+1)D or (3+1)D in case the transverse dynamics are included
- **The Equation of State (EoS)**: $p = p(e, n)$, connecting pressure to energy density and conserved charge density, encodes all features of the fluid
- **The input data (fluidization) and event-by-event fluctuations**

- **Viscous corrections**

- **The freeze-out conditions and Cooper-Frye formula (particlization)**

One of the most important advantages of hydrodynamics is that it can capture the details of EoS evolution, therefore one can study explicitly the implications of the QGP to hadron gas phase transition on experimental observables.

As input data, hydrodynamics usually require the energy density e and baryon density n_b at a given proper time. Those quantities can be provided by initial condition models as discussed in Sec. 1.3.2. Modern implementations include CGC/IP-Glasma, CGC-inspired Kharzeev-Levin-Nardi (MC-KLN) [95–97] or the Monte&Carlo Glauber model. To account for initial state fluctuations from collision to collision, one should also perform the explicit event-by-event calculations by taking many simulations with different setup of initial conditions then averaging the final results. This latter consideration is crucial in reproducing higher order harmonics in flow analyses.

The simple ideal hydrodynamic equations follow a similar form as we saw in Bjorken's model 1.3.1, where the fluid field stress tensor takes the form $T^{\mu\nu} = \mathrm{Diag}(e, p, p, p)$, with the additional four-current term. The usual ideal hydrodynamics would require strict local equilibrium and the dissipative effects to be neglected. The systematic study of a perturbation beyond local equilibrium requires higher order terms in gradient (derived from constitutive relations):

$$T^{\mu\nu} = T^{\mu\nu}_{(0)} (\equiv T^{\mu\nu}_{\mathrm{ideal}}) + T^{\mu\nu}_{(1)} + T^{\mu\nu}_{(2)} + \ ... \tag{1.69}$$

The small perturbation from equilibrium can be handled by viscous hydrodynamics. The first relativistic generalizations of Navier-Stokes theory were initiated by Carl Eckart, Lev Landau and Evgeny Lifshitz. These were considered first-order theories as only first-order gradient terms were considered. The so-called gradient expansion requires as for any other perturbation theory a certain perturbative scale, in the case of hydrodynamics, one considers the Knudsen number K_n to be small enough. This expansion in higher order stress tensors needs however a certain microscopic description: a standard approach is to consider a Boltzmann equation and expand the density distribution functions around the local equilibrium; insert the series into the equation; then solve it order by order. The corresponding macroscopic inputs needed for hydrodynamics can be obtained using corresponding moments and taking their integration (fluidization/coarse-graining). The general classification follows:

- The 0th-order: ideal hydrodynamics with no gradient corrections.

- The 1st-order: incorporates shear η, bulk ζ viscosity and shear tensor $\sigma^{\mu\nu}$ such as Navier-Stokes (nonrelativistic) / Landau-Lifshitz (relativistic), but leading to non-causal propagation and instabilities.

- The 2nd-order: promotes bulk viscosity and shear tensor as dynamic degrees of freedom that evolve with relaxation time, and involves quadratic gradient corrections, to restore the stability and causality. There are two major frameworks: BRSSS based on effective field theory [98] and conformal plasma, and DNMR based on kinetic theory [99].

In the modern developments, some models based on a certain resummation technique for large gradients are introduced as well [100], these include anisotropic hydrodynamics (aHydro) for the largest shear anisotropy, and moment resummation based models [101]. Other advanced techniques like resurgence theory using transseries and Borel transformation were also introduced, the latter can significantly capture the non-perturbative modes (non-hydrodynamic modes), and provide an intrinsic explanation for hydrodynamic attractor as the consequence of re-summed nonperturbative contributions.

At the final stage of hydrodynamic evolution, one would expect a phase transition between fluid (field) degrees of freedom to particle degrees of freedom at the freeze-out where we distinguish between:

- **Chemical freeze-out** where the inelastic number-changing hadronic reactions stop and hadron multiplicities are fixed.
- **Kinetic freeze-out** where the hadronic elastic collisions stop and momentum distributions are fixed.

The chemical freeze-out happens at a sharp instant usually around 155-$165\,\mathrm{MeV}$, while the kinetic freeze-out occurs later at lower temperature [102, 103]. The initial idea of *Cooper-Frye* was formulated as interface of particlization at the kinetic freeze-out after which all interactions stop and particles free-stream [104]. The standard Cooper-Frye formula takes place at a fixed hypersurface (infinitesimally thick surface element $d\Sigma$) in space-time [104]:

$$p^0 \frac{d^3N}{d^3p} = p^\mu d\sigma_\mu f(p) \tag{1.70}$$

where $d\sigma_\mu$ is a normal four-vector of the hypersurface with length equal to the area of the infinitesimal surface element, and $f(p)$ is the density distribution function assumed to be a boosted thermal distribution for an ideal fluid or perturbed (dissipative corrections) distribution for a viscous fluid. Since the choice of this space-time hypersurface is rather free (orientation and proper-time location), one would imagine a conceptual issue where the hypersurface turns out to be space-like, the latter will generate a negative contribution. In this case, this actually means that there will be particles that scatter back toward the surface and get into the fluid phase, which is physically unacceptable [105]. In practice, we usually apply a certain cut-off function to fix the negative flux problem [106]. In the hybrid model where the hydrodynamics is coupled to transport models such as VISHNU (viscous hydrodynamics + a hadronic microscopic transport afterburner (UrQMD [107, 108])) [109], the Cooper-Frye formula is rather applied at the onset of hadron cascade, which is close

to the chemical freeze-out temperature. Though being conceptually necessary, the limitations for the standard framework make it hard to be implemented. There are actually many approaches trying to bypass the Cooper-Frye prescription, we shall see in the next section.

1.3.4 . Hadronization and final stage dynamics

Hadronization

Hadronization is the last stage before the hadronic transport in this multi-stage system evolution picture. As the system cools during the expansion, it will eventually particlize at a certain space-time hypersurface with the Cooper-Frye formula and finally hadronize into final stage hadronic observables. This process is intrinsically nonperturbative, which makes the problem extremely hard to deal with. In this section, we shall review the current understanding of this process based on different approaches.

The intuitive idea is based on the so-called parton-hadron duality [110, 111], which can be used to build a phenomenological description of hadronization process. In this picture, the inclusive observables are approximately the same at parton and hadron level since the hadronization is a long-distance process involving only small momentum transfers. Hence, one can rely on perturbative theory assuming that the strong coupling α_{s} can be defined for all Q. Despite giving a rather good description for inclusive observables, it does not explain the underlying mechanism and usually fails in regions dominated by resonance structure or strong hadronization effects. However, some modern frameworks implement this dual picture such as the Statistical Hadronization Model (SHM) and coalescence/recombination model. After the hadronization, there will be a phase of hadron gas where the dynamics can be fairly captured by transport models.

String fragmentation model [112–115] The Lund string model as standard implementation in PYTHIA [116, 117] and JETSET [118], is based on the dynamics of relativistic strings describing the color flux tube spanned between the initial $q\bar{q}$. As discussed in the previous section 1.2.3, the dynamics of flux tubes give rise to a linear potential as a function of the distance between the quark pair. The probability amplitude of a specific hadronization process will be proportional to the exponential of the negative area swept by the string in space–time:

$$|\mathcal{M}(q\bar{q} \to \mathrm{hadrons})|^2 \propto e^{-bA} \tag{1.71}$$

where b is a fragmentation slope parameter related to string tension and A is the space–time area spanned by the string world-sheet during hadronization [112, 115]. At high energy, strings will break sequentially into a chain of hadrons via $q\bar{q}$ productions in the vacuum. The string model requires more parameters than cluster model, providing a more detailed description. But this phenomenological model still has limitations in describing baryon productions.

Cluster model [119–123] Implemented in HERWIG, this alternative approach to the string model considers as a starting point the gluon splitting ($g \to q\bar{q}$) after the parton shower, and the so-called *clusters* are formed by color-singlet combinations of $q\bar{q}$ having lower masses and a universal spectrum due to the pre-confinement in parton shower. The clusters will decay isotropically into pairs of hadrons according to the density of states with appropriate quantum numbers. The model is characterized by a small number of parameters and incorporates a natural mechanism for transverse momentum generation and for the suppression of heavy-particle production in hadronization. Nevertheless, it encounters challenges in treating the decays of highly massive clusters and in reproducing the observed suppression of baryon and heavy-quark yields.

Statistical Hadronization Model (SHM) [124–126] In contrast to the previous microscopic models, the SHM follows a thermodynamic description assuming that hadron production at chemical freeze-out follows a thermal-like behavior. A genuine thermalization picture is mostly supported in heavy-ion collisions as the system undergoes rapid rescattering in the hot and dense QGP phase and the hadron yields at freeze-out fit well a true statistical ensemble with a physical temperature. On the computational ground, the SHM usually takes a Grand Canonical Ensemble (GCE) at chemical freeze-out, then the total yield of a given hadron species can be calculated by integrating the phase-space with a thermal distribution:

$$N_i = V \, \frac{g_i}{2\pi^2} \int_0^\infty \frac{p^2 \, dp}{\exp[(E_i - \mu_i)/T_{\rm ch}] \pm 1} \tag{1.72}$$

where g_i is the degeneracy factor, V is the fireball volume, $T_{\rm ch}$ is the temperature at chemical freeze-out and the μ_i are the chemical potentials for baryon number, strangeness, and charge. Moreover, the final result usually has to account for feed-down corrections as:

$$N_i^{(\rm final)} = N_i^{(\rm primary)} + \sum_j {\rm Br}(j \to i) \, N_j^{(\rm primary)} \tag{1.73}$$

The successful description of the hadron abundances by the SHM with a universal temperature parameter in heavy-ion collisions [127] but also in elementary collisions [128] (pp, e^+e^-collisions), where a genuine thermal equilibration is not expected in such small systems (although the applicability of SHM might be attributed to the nature of the hadronization process), led to the genuine question about the underlying nature of thermalization [127]. The general discussion give rise to two pictures:

- A true thermal process (genuine thermalization) where the strong interaction in the QGP phase drive the system to local thermal equilibrium before the onset of hadronization.

- A phase-space dominance where the hadron states saturate available phase-space during the hadronization process, without true thermal equilibrium.

Modern hydrodynamics calculation generally support a local equilibrium, but the SHM, being a macroscopic description, is not able to provide a full explanation.

Recombination/Coalescence models [129–131] Unlike the SHM model, the recombination picture aims rather for a microscopic hadronization mechanism. In the intermediate p_{T} region, the simple fragmentation picture cannot capture all features of the data, such as the enhancement of baryon-to-meson ratio and the hadronic elliptic flow with a Number of Constituent Quarks (NCQ) scaling. The latter led to the following considerations: instead of fragmenting into hadrons, quarks that are close in phase-space will tend to combine into hadrons directly. Therefore, this picture is purely statistical and local, it happens in the overlap of the quark phase-space distributions with the internal hadron wavefunctions, and the hadron yields are given by a phase-space integral. Here an example for meson is given as:

$$E\frac{dN}{d^3P} = g\int d^3r_1\, d^3r_2\, d^3p_1\, d^3p_2\, f_q(\mathbf{r}_1,\mathbf{p}_1)\, f_{\bar{q}}(\mathbf{r}_2,\mathbf{p}_2)\, W(\mathbf{r}_1-\mathbf{r}_2,\mathbf{p}_1-\mathbf{p}_2), \tag{1.74}$$

where f_q and $f_{\bar{q}}$ are quark, antiquark phase-space distributions, W is the *Wigner function* of wavefunction of a given hadron species, and g is the degeneracy factor.

This phenomenological model is widely used for its simplicity as one can bypass the QCD first principle details, especially in explaining the hadronic elliptic flow. It can be extended for heavy-quarks for which we allow the combination of heavy-quarks with light quarks. However, a major limitation of coalescence/recombination models is the absence of a rigorous microscopic derivation from QCD; hadron formation probabilities rely on model assumptions for the parton Wigner functions and hadron wave functions, leading to ambiguities in matching between partonic and hadronic degrees of freedom. The latter was improved in the transport model leading to so-called Resonance Recombination Model (RRM) particularly relevant for heavy-flavor transport, treating hadronization as scattering through broad resonances, ensuring local four-momentum conservation and heavy-flavor detailed balance [132, 133]. Other attempt like the hybrid coalescence plus fragmentation model blend recombination at intermediate p_{T} with fragmentation at high p_{T} , using probabilistic switching consistent with kinematics [134].

Final stage dynamics

As the hadronization provides only a transition mechanism which can be viewed as a sort of mapping between microscopic degrees of freedom to hadronic degrees of freedom, the full dynamic description requires a certain context. For the case of the string model, it is often embedded into the parton kinematics from the event generator. The cluster model, instead, requires the parton shower. In the Cooper-Frye prescription, a hydrodynamic evolution is needed as input data for pre-hadronization, then a sampling from SHM or SHM description for hadronization can be passed to a hadronic transport model for the final dynamic evolution, like UrQMD [107, 108], SMASH [135, 136] etc. For the

coalescence model, it is usually coupled to hydrodynamics or a parton transport model like AMPT [137–139], followed by a hadronic transport or direct hadron spectra. For the final stage dynamics related to heavy-flavors, a dedicated discussion will be given in the following sections.

1.4 Anisotropic flow

As one of the most important and insightful probes in heavy-ion physics, the anisotropic flow stands in the heart of our investigation in this strongly interacting complex dynamical system. It encodes the most profound signature of collective behavior in heavy-ion collisions and led to many revolutionary discoveries in the field among those we had the first experimental evidence for the success of hydrodynamics at RHIC with the observed significant elliptic flow signal.

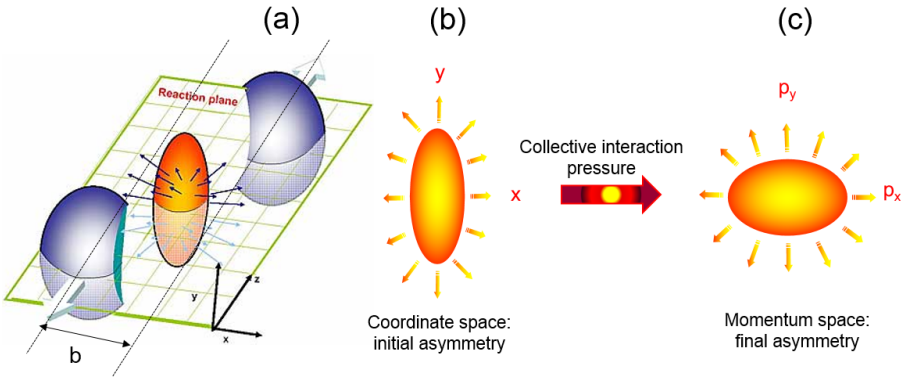

Figure 1.18: A sketched view of the generation of anisotropy in a typical non-central collision: (a) presents schematically the initial overlap region between two incoming nuclei, (b) illustrates initial geometric anisotropy in the collision zone, and (c) shows the final state momentum anisotropy by the pressure gradients. [140].

In heavy ion collisions, depending on the initial collision geometry as discussed in Sec. 1.3.1 and illustrated in Fig. 1.18, one would get a non-spherical overlap region for non-central collisions, the latter translates into spatial eccentricities (elliptic, triangular etc.) of initial density $e(x, y)$ in the transverse plane. This initial spatial asymmetry then leads to momentum space anisotropy by pressure gradients [141]. This anisotropy can be measured from final state particle yields as one can expand the particle azimuthal distribution in terms of a Fourier series:

$$E\frac{d^3N}{d\mathbf{p}_\mathrm{T}} = \frac{1}{2\pi}\frac{d^2N}{p_\mathrm{T}dp_\mathrm{T}dy}\left\{1+\sum_{n=1}^{\infty} v_n \cos[n(\varphi-\Psi_n)]\right\} \tag{1.75}$$

where φ is the particle azimuthal angle, Ψ_n is the n-th order event plane angle, and v_n is the Fourier harmonic coefficient for different modes namely *the flow coefficient*.

As one may realize here, the flow coefficient was a pure mathematical construction or data analysis tool by definition to study the symmetry, the usage of the Fourier expansion is not constrained by any underlying physical processes. Its physical relevance becomes clear only when one makes use of system collective expansion to connect the final stage observable with the initial geometry and fluctuations.

1.4.1 . From initial geometry to final state anisotropy

The initial eccentricities which characterize the initial transverse spatial geometry of the collision zone are defined as:

$$\varepsilon_n e^{in\Phi_n} = -\frac{\int r^n e^{in\phi} e(r,\phi)\, r\, dr\, d\phi}{\int r^n e(r,\phi)\, r\, dr\, d\phi} \tag{1.76}$$

where ε_n is the eccentricity coefficient of order n, $e(r,\phi)$ is the initial energy density in the transverse plane, and Φ_n is the participant plane angle. For collisions between nuclei of the same species, e is averaged over many events and the angle ϕ is measured relative to the impact parameter vector.

The connection between initial eccentricity and final state flow coefficient follows at first order the linear hydrodynamic response:

$$v_n e^{in\Psi_n} = \kappa_n \varepsilon_n e^{in\Phi_n} \tag{1.77}$$

where κ_n is the response coefficient measuring the efficiency of geometry-to-flow conversion, it depends on the shear and bulk viscosity, system size, lifetime, and freeze-out conditions. For $n = 2, 3$, this linear relation fits well the QGP-dominated regime, while higher orders require nonlinear responses involving mode couplings (mixing) [142, 143]. Moreover, the response coefficient provides a practical way to extract the QGP shear viscosity knowing:

$$\kappa_n \sim \exp\left[-n^2 \frac{\eta/s}{(RT)}\right] \tag{1.78}$$

where R is the system size and T is the average temperature of the medium. Hence one can compare order-by-order the measurement of flow coefficients with initial state models like TRENTo to constraint the QGP transport properties.

Viscous effects in flow development

The ability for a system to reach local thermal equilibrium from a highly non-equilibrium induced by pressure gradients is characterized by the viscosity. Small viscosity is often interpreted as strong interaction among microscopic constituents, giving rise to a short relaxation time. *Bulk viscosity* induces locally isotropic deviations of the fluid field stress tensor in the local rest frame from the equilibrium, by isotropic we mean that it contributes only in diagonal components with a bulk viscous pressure $\Pi\delta^{ij}$. In an isotropically expanding fireball, bulk viscosity reduces the radial acceleration and therefore inhibits the onset of radial flow. In contrast to bulk viscosity, *shear viscosity* causes anisotropic local deviation from equilibrium with an anisotropic contribution to the fluid stress tensor [144]. As a counteraction against flow anisotropies, shear viscosity will try to balance the transverse flow which develops later in response to transverse pressure gradients in the initial state, by building a shear viscous pressure π^{ij} in the local rest frame, which tends to reduce longitudinal pressure and enhance transverse pressure. Therefore, shear viscosity is a feature that limits the system ability of converting initial state transverse pressure

anisotropies into flow anisotropies. Anisotropic transverse flow modifies the shape of the transverse momentum spectra of the emitted particles through a direction-dependent blue-shift effect [145]. Bulk viscosity, by reducing the overall radial flow component, tends to steepen the p_{T} spectra, while shear viscosity, by enhancing the effective radial expansion, leads to a flatter spectral shape.

1.4.2 . Flow observables

In practice, flow coefficients of different harmonics encode different physical information and sensitivity: (an illustration of flow patterns for $n = 2, 3$ is shown in Fig. 1.19)

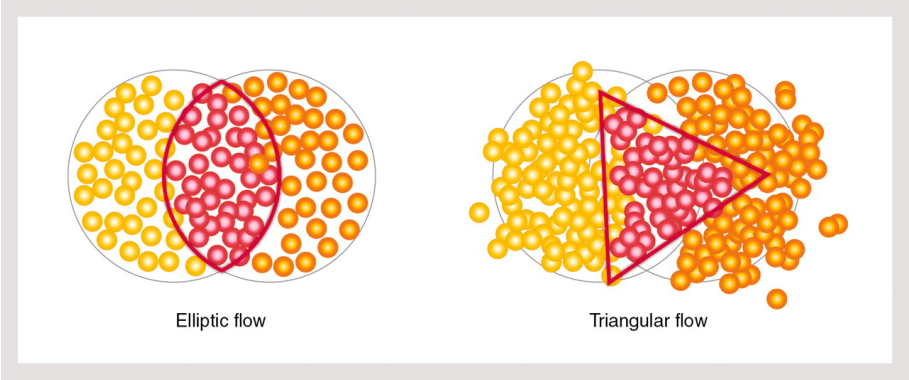

Figure 1.19: Elliptic and triangular flow patterns arise from the locations of individual nucleons at the instant when two nuclei interpenetrate. [146].

- **Radial flow** ($n = 0$) gives the average expansion of the hot medium without any azimuthal modulation, roughly like a "blast wave" pushing particles radially in the transverse plane. This gives rise to the mass ordering of elliptic flow as a function of p_{T} in the low p_{T} region.
- **Directed flow** ($n = 1$) describes a collective sideward motion of the medium, which is sensitive to early time pressure gradients and baryon stopping. It has two components: rapidity-odd and rapidity-even. The first one is the main component signaling the tilt of fireball and sensitive to the early time pressure buildup and the evidence of a first order phase transition. The second reflects the initial state fluctuations.
- **Elliptic flow** ($n = 2$) represents the dominant flow observable as it probes directly the almond-shaped overlap region having a difference of pressure gradients along the in- and out-of-plane axis. It has been considered as the most relevant signature for a collective expansion and is fairly easy to measure experimentally.
- **Triangular flow** ($n = 3$) measures purely the initial state event-by-event fluctuations in the energy-density distribution of the fireball, which may occur even in the central collisions due to random fluctuations in the positions of nucleons or color fields. It is sensitive to different setups of initial condition models.

1.4.3 . Methods of flow measurement

In this section, we shall review the major advancement in the development of flow measurement methods in heavy-ion physics, our discussion here will rather focus on the historical follow-up together with a clarification of how the methods have emerged in the logical order.

The general idea of flow measurement started with the intuitive method aiming to reconstruct directly the event-plane and perform the particle angular correlation with the reconstructed event-plane as a "rough" estimation of the genuine reaction plane. The reconstruction of event-plane can be done using the so-called event Q-vector:

$$Q_n = \sum_i^M e^{in\phi_i} \tag{1.79}$$

where n is the order of harmonic, ϕ is the particle azimuthal angle and M is the multiplicity of particles within a single event. The Q-vector plays a particularly crucial role in flow analysis as it encodes actually all the particle azimuthal degrees of freedom into an ensemble from which the event-plane angle can be easily evaluated as the ratio between imaginary and real part of complex Q-vector. This idea led to the so-called Event-Plane (EP) method [147] following the definition:

$$v_n = \langle \frac{\cos(n(\phi - \Psi_n))}{R_n} \rangle \tag{1.80}$$

where R_n is the event-plane resolution. This primitive and yet direct approach was soon understood to be strongly biased by auto-correlation, inexact resolution factor and non-flow contamination [148]. Then new techniques were introduced including the standard Scalar Product (SP) method using directly Q-vector to perform the correlation with three-subevent method providing a better estimation of resolution factor

$$v_n = \langle \frac{u \cdot Q^*}{R_n} \rangle \tag{1.81}$$

where the resolution factor R_n is evaluated with three-subevents taking from three independent detector systems. However, these two methods were understood later as special cases of genuine 2-particle correlation methods, the latter was formulated with pair correlations without direct access to event-plane or any reaction-plane estimation:

$$(v_n\{2\})^2 = \langle\langle e^{in(\phi_i - \phi_j)} \rangle\rangle \tag{1.82}$$

where the average $\langle\langle \dots \rangle\rangle$ is taken firstly within a single event then over all events. For the same reason from SP and Event-Plane (EP) methods, 2-particle correlation suffers also from nonflow contribution. A major conceptual leap then came up with the development of multi-particle correlation (cumulant) method [149] as a natural extension of the 2-particle correlation method, this new method is interested in higher-order correlations

such as $v_n\{4\}$, $v_n\{6\}$ and $v_n\{8\}$, with the advantage of being able to suppress significantly nonflow contribution which scales as $1/M^{k-1}$ for k-particle correlation. On the other side, a method first introduced in the context of phase transition in thermodynamic limit of statistical system using the idea of generating function for partition function [150], was later shown to be relevant for flow analysis, from which cumulant and multiparticle correlator can be identified with the coefficient from the expansion of a generating function through *moment-correlation relation* and the flow coefficient can be extracted from the zero of the real part of this generating function:

$$G(ir) = \left\langle \prod_{j=1}^{M} (1 + ir\, w_j \cos(n\varphi_j)) \right\rangle \tag{1.83}$$

The heavy-ion field later entered a new phase with the realization that flow fluctuates event-by-event due to initial geometry fluctuations. The shift from simply measuring the $\langle v_n \rangle$ to reconstructing full flow distributions marked another conceptual turning point. ATLAS demonstrated direct unfolding of event-by-event v_n distribution [151], showing that fluctuations encode rich information about the initial state and medium response.

More recently, with the emergence of collectivity studies in high-multiplicity pp and p–A collisions, the dominant experimental difficulty became suppression of short-range nonflow correlations (jets, di-jets, mini-jets), especially in small systems. This motivated the development of subevent cumulant methods [152, 153], where the event is partitioned into separated pseudorapidity regions to ensure long-range collectivity dominance. Subevent cumulants represent the most robust modern implementation of multi-particle cumulants, especially crucial when dealing with small collision systems or wide kinematic acceptance.

1.5 Heavy-quark dynamics in heavy-ion collisions

Heavy-quarks, particularly charm c and bottom b quarks, provide a theoretically well-controlled probe of the QGP created in ultrarelativistic heavy-ion collisions. Their large masses, $m_Q \gg \Lambda_{\rm QCD}, T_{\rm QGP}$, ensure that they are produced predominantly during the earliest stage of the collision, in the initial hard partonic scatterings, calculable within the framework of perturbative QCD [154, 155]. Subsequent to their production, heavy-quarks propagate through the evolving hot medium and interact with its constituents via both collisional (elastic) and radiative (inelastic) processes, where the gluon bremsstrahlung of heavy-quarks suffers from the *dead cone effect* [156], which suppresses the gluon emission at small angles. Heavy-quark propagation hence encodes information about the medium microscopic and transport properties. Given the insufficient thermal energy of the QGP medium, heavy-quarks can be hardly produced or annihilated in the medium, leading to an approximate conservation of their numbers throughout the system's evolution. Therefore, their production mechanism and the induced medium effects can be well separated.

The dynamics of heavy-quarks in the QGP are commonly described within the framework of stochastic transport theory, where their momentum evolution is governed by Langevin or Boltzmann kinetic equations. These approaches encapsulate the interplay between drag, diffusion, and radiative energy-loss, characterized by transport coefficients such as the spatial diffusion constant $D_{\rm s}$ and the momentum broadening parameter $\hat{q}$. The temperature dependence of these coefficients, constrained by lattice QCD and phenomenological models, provides critical insight into the coupling strength between heavy-quarks and the strongly interacting medium.

Moreover, the transition from the partonic to the hadronic phase involves nonperturbative processes of hadronization, including fragmentation and recombination with thermal light quarks. The relative contributions of these mechanisms significantly affect the observed spectra and flow patterns of heavy-flavor hadrons. Consequently, a unified theoretical description of heavy-quark production, in-medium transport, and hadronization offers a powerful means to connect first-principles QCD calculations with experimental observables, pushing forward our understanding of strongly coupled QCD matter.

1.5.1 . Initial production of heavy-quarks

The production of heavy-quarks in high-energy nuclear collisions originates predominantly from hard partonic scatterings that occur within the first fraction of $1\,{\rm fm}/c$ after the collision, well before the formation and thermalization of the QGP. The production can be described by perturbative Quantum Chromodynamics within the *collinear factorization* description [157]:

$$\frac{d\sigma_{Q\bar{Q}}}{dp_T\,dy} = \sum_{i,j}\int dx_1\,dx_2\,f_i(x_1,\mu_F^2)\,f_j(x_2,\mu_F^2)\,\frac{d\hat{\sigma}_{ij\to Q\bar{Q}}(\hat{s},\mu_R^2,\mu_F^2)}{dp_T\,dy} \tag{1.84}$$

where $f_i(x, \mu_F^2)$ are the PDF for parton species i with a momentum fraction x from the parent nucleon evaluated at the *factorization scale* μ_F. The partonic cross-section $\hat{\sigma}_{ij\to Q\bar{Q}}$ can be handled by perturbative QCD with a renormalization scale μ_R.

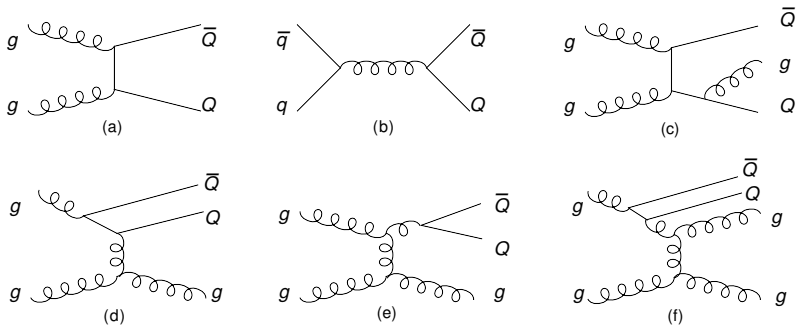

Figure 1.20: Heavy-quark production diagrams up to NLO. LO diagrams: (a) gluon fusion, (b) quark-antiquark annihilation. NLO diagrams: (c) pair creation with gluon emission, (d) flavor excitation, (e) gluon splitting, (f)together gluon splitting and flavor excitation. [158]

At Leading-Order (LO), the dominant mechanisms are gluon–gluon fusion ($gg \to Q\bar{Q}$) and quark–antiquark annihilation ($q\bar{q} \to Q\bar{Q}$). While at next-to-leading order or through resummation schemes as Fixed-Order plus Next-to-Leading Logarithms (FONLL) [159] , corrections from gluon splitting ($g \to Q\bar{Q}$) and flavor excitation ($gQ \to gQ$) are incorporated.

In the case of nucleus-nucleus (A–A) collisions, the following Cold Nuclear Matter (CNM) effects [160] will also contribute to the observed production spectra:

- **Shadowing**: the nuclear PDFs differ from those of free nucleons, in particular gluons are suppressed at low x.
- **Antishadowing**: enhancement of parton densities at intermediate-x (~ 0.1) compared to free partons, hence compensating the suppression at small-x and ensuring the overall momentum conservation.
- **EMC effect** [161]: suppression of parton distributions at relatively large x ($0.3 - 0.7$).
- **Fermi motion**: broadening of parton distributions by Fermi motion of nucleons inside the nucleus, giving raise to a tail from high momentum partons.
- **Cronin effect** [162]: enhancement of intermediate p_{T} hadron yields in proton-nuclear collisions by multiple soft partonic scatterings before the hard interactions.
- **Nuclear absorption** suppression of quarkonium spectra by pre-resonant $Q\bar{Q}$ pairs which can break up in the cold nucleus.

The resulting initial heavy-quark yield scales approximately with the number of binary nucleon–nucleon collisions, reflecting the hard nature of the production process. Since

subsequent thermal production or annihilation of heavy-quarks in the QGP is negligible at current collider energies, their number remains approximately conserved throughout the system's evolution. This property makes the heavy-quark population a well-defined and calculable input for subsequent transport modeling, providing a clean baseline from which to study medium-induced modifications.

1.5.2 . Transport models for heavy-quarks

The dynamical evolution of heavy quarks inside the medium can be formulated in terms of transport theory, where the microscopic interactions are coarse–grained into effective transport coefficients. In this framework, heavy–quark diffusion, drag, and energy-loss can be described using Boltzmann equations, Fokker–Planck evolution, or stochastic Langevin dynamics, depending on the assumed coupling regime and approximations. In this section, some major approaches for heavy-quark transport will be discussed.

Kinetic (Boltzmann) approach

In the modern consideration, where a heavy-quark thermalization picture is favored, the production of quarkonium may happen throughout the QGP phase following a time-dependent balance between dissociation and formation processes [163]. This time-dependent evolution requires the transport calculation with loss and gain terms:

$$p^{\mu}\partial_{\mu}f_H = -\alpha E f_H + \beta E, \tag{1.85}$$

where the left-hand side is the diffusion operator of Boltzmann equation and the right-hand side is separated into a gain and a loss term with loss and gain factors α and β. Integrating out over the whole phase space and assuming spatial independence for α and β, one arrives at the *Rate equation* [164]:

$$\frac{dN_H(t)}{dt} = -\Gamma_H(t)\left[N_H(t) - N_H^{\mathrm{eq}}(t)\right], \tag{1.86}$$

where $\Gamma_H(t)$ is the time-dependent dissociation rate, which incorporates both suppression and regeneration mechanisms.

Comover (Rate-type) approach [165–171]

The Comover Interaction Model (CIM) is a phenomenological approach without the assumption of a thermal equilibrium, in which quarkonium suppression is attributed to final–state interactions with the medium of comoving particles produced in the collision, rather than (or in addition to) pure color-screening and deconfinement. The physical picture of quarkonium suppression in this framework is formulated based on two major contributions: nuclear absorption of the pre-resonant heavy-quark pairs with nucleons of the colliding nuclei; comover dissociation, where the heavy-quark pair may be absorbed by the medium made of hadron and parton degrees of freedom that "comove" approximately with it in rapidity. The dissociation happens when the density of surrounding local

comovers is large and quarkonium states in this case are subject to inelastic scattering with the comovers. The general evolution equation of quarkonium density N_ψ follows a Rate-equation:

$$\tau \frac{dN_\psi}{d\tau} = -\sigma_{\rm co}\, n_{\rm co}(\tau)\, N_\psi(\tau), \tag{1.87}$$

where $n_{\rm co}(\tau)$ is the transverse density of comoving medium and $\sigma_{\rm co}$ is the cross-section of quarkonium dissociation due to interaction with comovers. At high-energy scales like RHIC and LHC, the model includes also regeneration from recombination as a gain term in the Rate-equation. This model prior to the general consensus of the QGP in heavy-ion community managed to reproduce well the observed J/ψ suppression at SPS, and is still relevant nowadays for p–A collisions where a genuine formation of the QGP is still under strong discussion.

Diffusion (Langevin/Fokker-Planck) approach [172, 173]

Originated from the kinetic approach, the diffusion approach is an approximation of Boltzmann equation where we assume the heavy-quark mass is well separated from the thermal scale and each scattering takes only a small momentum transfer. The collision kernel (right hand side of Boltzmann equation) can then be expanded using Kramers-Moyal formula, this will convert the Boltzmann equation into Fokker-Planck or equivalently Langevin equation (assuming the heavy quark undergoes many such soft scatterings over short time intervals so the accumulated effect becomes diffusive, then Langevin becomes a stochastic representation of Fokker-Planck with Gaussian white noise):

$$\frac{dp_i}{dt} = -\eta_D p_i + \xi_i(t), \tag{1.88}$$

where η_D is the drag coefficient and $\xi_i(t)$ with $\langle \xi_i(t)\xi_j(t')\rangle = \kappa\, \delta_{ij}\, \delta(t-t')$ being the stochastic noise term in the Ito sense and κ is the momentum diffusion coefficient. Physically speaking, the diffusion model is taken as the soft limit (applicable at low to intermediate $p_{\rm T}$ region) of a microscopic description, where the degrees of freedom in the theory are assumed to follow the Brownian motion. In a full $p_{\rm T}$ -range calculation of heavy-quark transport covering low- to high-$p_{\rm T}$ regions, the low-$p_{\rm T}$ ($p_{\rm T} \leq 4-5$ GeV/c) part is usually well handled by Langevin calculation then using Boltzmann kernel for high-$p_{\rm T}$ region ($p_{\rm T} \geq 6$ GeV/c), the smooth interpolation between the two domains requires usually the drag and diffusion coefficients are consistent in both calculations.

1.5.3 . Heavy-quark thermalization

For a complete picture of heavy-quark evolution in the hot medium, a thermalization description is usually applied in different transport calculations. The typical kinetic thermalization scales of heavy-quarks can be estimated by [172]:

$$\tau_{\rm thermalization} \simeq \frac{m_Q}{T} D_s \tag{1.89}$$

where D_s is the spatial diffusion coefficient that follows $D_s = \frac{2T^2}{\kappa}$.

In the diffusion models, the thermal convergence of quark distribution functions is ensured by the *fluctuation-dissipation relation* $\eta_D = \frac{\kappa}{2m_Q T}$, hence if the medium temperature stays as a constant, then the distribution functions evolve automatically toward Maxwell's distribution. In kinetic models, the thermalization is incorporated in the *detailed balance* where the thermal limit is controlled by the in-medium binding energy and medium temperature [163]. Following which, the degree of thermalization is a function of the time scale of the QGP expansion $\tau_{\rm QGP}$ and the dissociation rate Γ_H^{-1} from Eq. 1.5.2: if the rate is much smaller than the expansion time scale, the heavy-quarks will undergo the interactions driving the system into thermal equilibrium; however, if the rate is much bigger than the expansion time scale, the system will not be able to complete the thermalization process. When coupling to the hydrodynamic medium, each space-time cell will provide the fluid temperature and velocity and heavy-quarks may interact with local fluid cells via diffusion coefficients depending on the cell temperature. The medium will change with the expansion, hence local thermal exchange encoded in transport equation will be updated as the system cools down.

Experimental measurements of open heavy-flavor suppression and anisotropic flow at RHIC and the LHC indicate that charm quarks couple strongly to the QGP and develop substantial collective flow at low to intermediate transverse momentum, consistent with diffusion coefficients $2\pi T D_s \sim 2-7$ [174, 175]. Bottom quarks also exhibit non-zero flow but remain further away from kinetic equilibration. Enhanced heavy-flavor baryon/meson and strange-to-non-strange charm ratios support hadronization via coalescence with a flowing medium, which further amplifies heavy-flavor flow [176]. Together, these observations point to partial kinetic thermalization of charm within the QGP lifetime and limited thermalization of bottom, while leaving open quantitative questions on the temperature dependence of transport coefficients and the interplay of collisional and radiative processes – particularly at high $p_{\rm T}$ and in small systems.

1.5.4 . Quarkonium production and in-medium properties

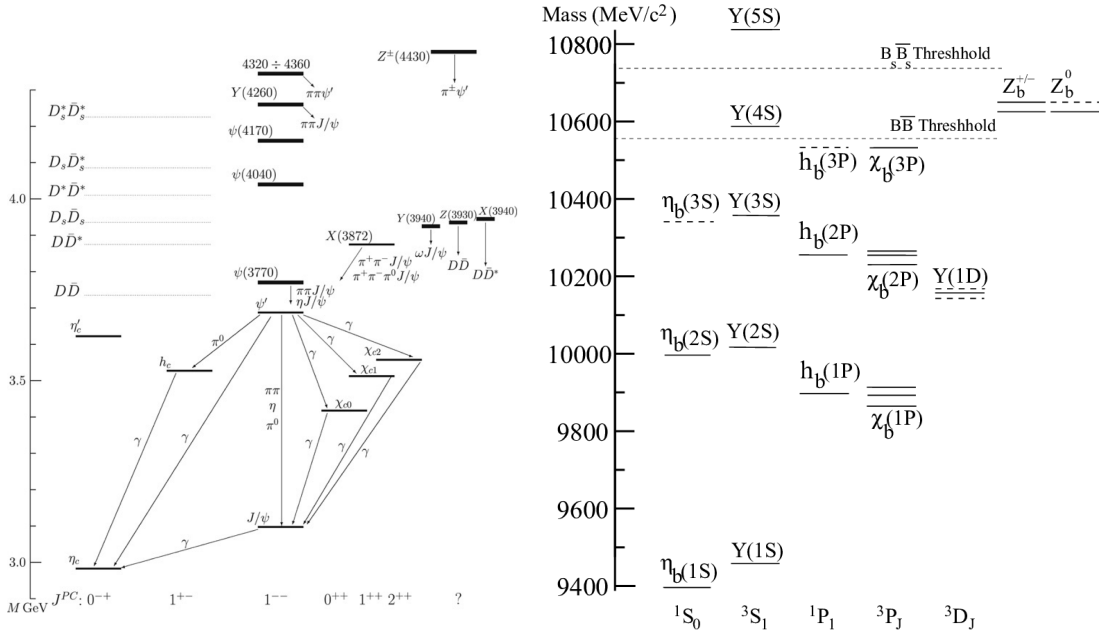

(a) Charmonium family (b) Bottomonium family

Figure 1.21: An illustration of charmonium [177] and bottomonium [178] family in terms of spin-parity and their effective masses.

Quarkonia are bound states of heavy-quark-antiquark pairs. Their production reflects the genuine interplay between perturbative and nonperturbative QCD and the subsequent propagation of quarkonia is strongly affected by the surrounding hot dense medium, making them good probes to study the medium properties and understanding the QGP in particular. There are two families of quarkonia:

- **Charmonia** bound-states of $c\bar{c}$: generally with binding energies close to the QGP temperature and extremely weak for excited states. The fundamental family members are: J/ψ (most studied ground-state), $\psi(2S)$ (weakly bound and can be easily suppressed), χ_c (feed-down to J/ψ) and η_c (singlet counterpart of J/ψ).

- **Bottomonia** bound-states of $b\bar{b}$: have large binding energies compared to charmonia and the regeneration contribution is significantly reduced at LHC energies, providing a cleaner pattern for in-medium suppression (sequential melting) with well-established and hierarchical feed-down structure. The fundamental family members are: $\Upsilon(\mathrm{n}S)$, χ_b (feed-down) and η_b (singlet counterpart of $\Upsilon(1S)$).

An illustration of charmonium and bottomonium family with their decay pattern is illustrated in Fig. 1.21.

Quarkonium production

The theoretical understanding of quarkonia as bound states of heavy-quark-antiquark pairs ($c\bar{c}$ and $b\bar{b}$) requires both aspects from perturbative and nonperturbative treatments. Although the heavy-quark production can be well controlled by perturbative calculations, the subsequent evolution of quark-antiquark pairs into bound states remains nonperturbative. The general paradigm of quarkonium study in A-A collisions requires a baseline knowledge from pp collisions where no nuclear effects and medium modifications are involved. In this section, we shall take a look at some nonperturbative models.

Color-Evaporation Model (CEM) [179, 180] The model takes the approximation of color blindness in which the color and spin quantum numbers of the produced heavy-quark pairs are not specified at the perturbative level. The pair can be in any color and spin state, however the onset of subsequent hadronization into a quarkonium state is controlled by a threshold for open heavy-flavor production. And the probability that a subthreshold $Q\bar{Q}$ becomes a specific quarkonium state is a universal constant.

Color-Singlet Model (CSM) [181–183] In this picture, quarkonia are assumed to be produced with a highly peaked wavefunction in the momentum space. The latter leads to an expression of quarkonium production cross-section as if heavy-quark pairs have almost zero relative velocity.

Color-Octet Model (COM) [184, 185] In this description, the $Q\bar{Q}$ before hadronization is not restricted to a color-singlet state but can instead be created in a color-octet configuration. In the framework of Non-Relativistic Quantum chromodynamics (NRQCD), since the heavy-quark relative momentum in the quarkonium rest frame is much smaller than their rest mass $v \equiv \frac{|p_Q|}{m_Q} \ll 1$ [5] and because the scale hierarchy $m_Q \gg m_Q v \gg m_Q v^2 \sim \Lambda_{\rm QCD}$ allows a systematic expansion in powers of v, then the quarkonium production cross-section can be factorized into a short-distance part Short-Distance Coefficients (SDCs) representing the hard heavy-quark production, and a long-distance part (Long-Distance Matrix Elements (LDMEs)) encoding the probability that the pair evolves into a given quarkonium state as shown below:

$$d\sigma(H) = \sum_n d\hat{\sigma}(Q\bar{Q}[n]) \, \langle \mathcal{O}_n^H \rangle, \tag{1.90}$$

where $d\hat{\sigma}(Q\bar{Q}[n])$ is the short distance cross-section and $\mathcal{O}_n^H$ are the LDMEs and are considered to be universal and fixed from fits to data.

Heavy-flavor properties in the vacuum

The behavior of produced heavy flavors in the vacuum is often described within the framework of potential models which turn a quantum field theoretical problem into a

[5] $v^2 \sim 0.3$ for charmonium and 0.1 for bottomonium

quantum mechanical problem by solving the Schrodinger equation (nonrelativistic) or Dirac equation (relativistic) with a proper quark potential

$$\left[-\frac{\nabla^2}{m_Q}+V(r)\right]\psi(\mathbf{r})=E\psi(\mathbf{r}). \tag{1.91}$$

Here E is the binding energy eigenvalue, and $V(r)$ is an effective modeling of the quark potential, called *Cornell potential* [186], having Coulomb and linear parts:

$$V(r)=-\frac{4\alpha_s}{3r}+\sigma r. \tag{1.92}$$

The first term is a Coulomb potential with the strong coupling α_s and the second is a linear confinement potential with σ the string tension obtained from lattice simulations. This effective model captures smoothly the connection between asymptotic freedom and confinement in the vacuum. In this picture, the quarkonium system can be treated as a two-body bound state in the Schrodinger or Dirac sense using the effective potential.

In-medium color screening

The vacuum potential model can be extended to the case where the system is surrounded by a hot bath. The latter will consider a *Debye mass* which accounts for the *color screening* and *quarkonium dissociation* at high temperatures [187]:

$$V(r,T)=-\frac{4}{3}\frac{\alpha_s e^{-m_D r}}{r}+\frac{\sigma}{m_D}\left(1-e^{-m_D r}\right), \tag{1.93}$$

where m_D is the Debye mass, which can be evaluated as

$$m_D=\begin{cases}\sqrt{\dfrac{6}{g_q e_q^2}}\,\dfrac{1}{T}, & \text{Abelian approximation,}\\[2ex] \dfrac{1}{\sqrt{\left(\dfrac{N_c}{3}+\dfrac{N_f}{6}\right)g^2}}\,\dfrac{1}{T}, & \text{pQCD.}\end{cases} \tag{1.94}$$

This Debye screening picture gives rise to the suppression mechanism of quarkonia in the static limit of the heavy-quark potential, where the dissociation temperature T_d of quarkonia can be estimated within the framework of finite-temperature potential models. In such models, the effective potential between the heavy-quark and antiquark depends on how the pair interacts thermally with the surrounding medium during the dissociation process. For a rapid dissociation, where there is no significant heat exchange between the heavy-quarks and the medium, the appropriate potential is the internal energy U. In contrast, for a slow dissociation process, where the system has sufficient time to exchange heat and reach thermal equilibrium with the medium, the relevant potential is the free energy F. In the picture of *sequential suppression*, with continuously increasing temperature of the fireball, quarkonia will melt into the medium according to their mass scales.

However, not all in-medium effects are incorporated in the screened potential. There are actually subtleties pointed by effective field theory approaches when one wants to extend the calculations at finite temperature, the additional thermal scale mentioned before in Section 1.2.5 makes the situation more complicated [34]. In the weak coupling regime, the quark potential at finite temperature from the leading thermal effects becomes complex. The imaginary part comes from two main mechanisms: the first one is the imaginary part of gluon self-energy from Landau damping effect in the plasma and the second one is the transition of quark pairs from color-singlet to color-octet. At a very high-temperature, the Landau damping dominates and the potential is constrained by Hard-Thermal Loop (HTL) re-summed perturbation theory.

Collisional dissociation and quarkonium regeneration

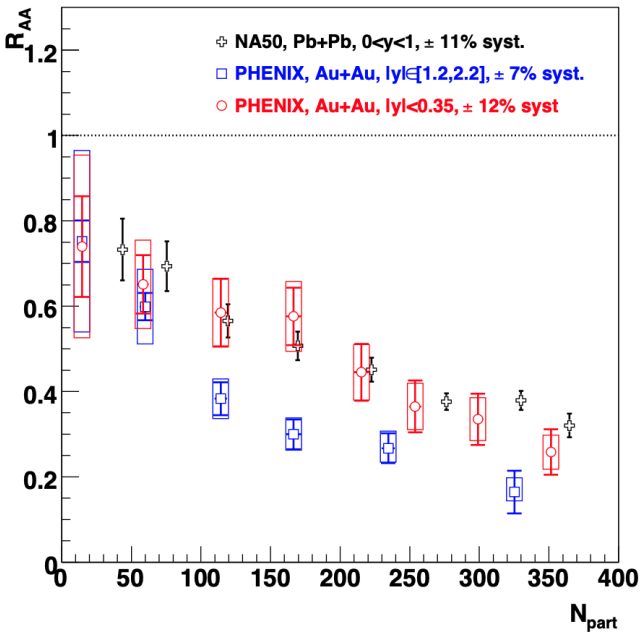

Figure 1.22: J/ψ modification factor as a function of number of participants from SPS (Pb–Pb collisions) and RHIC (Au–Au collisions). [188]

In contrast to the static Debye screening picture, produced quarkonium states can propagate in the medium and have the chance to interact with the in-medium degrees of freedom. In particular, charmonia can be destroyed below the dissociation temperature and survive above it. Two collision processes are usually considered when the quarkonium state travels through the medium:

- **Gluon dissociation**: $Hg \to Q\bar{Q}$.

- **Inelastic scattering** (quasi-free dissociation): $Hp \rightarrow Q\bar{Q}p$ (where p is the in-medium gluons, or (anti)quarks)

On the other side, people found hard to explain the early experimental data if one considers only the screening effect, the measurement of J/ψ nuclear modification factor, shown in Fig. 1.22, across different energy scales showed a counterbalance enhancement which was considered as the first confirmation of regeneration with respect to the pure screening picture [6], together with a rapidity dependent suppression, where the suppression at forward rapidity is stronger than at midrapidity. The latter pointed to the **regeneration mechanism**, which accounts for the recombination of uncorrelated in-medium charm quarks. The underlying process was understood as the inverse processes of collisional dissociation, in the kinetic models where this evolution happens in a continuous and time-dependent way. In contrast to the SHM picture, these inverse processes are encoded in the formation rate term in the transport model with a *detailed balance* between dissociation and formation rates.

Collisional and radiative energy-loss

When a heavy-quark traverses the QGP medium, it continuously exchanges energy and momentum with the medium, resulting in a net degradation of its momentum relative to the vacuum baseline. This *energy-loss* phenomenon arises from two qualitatively distinct microscopic mechanisms.

- **Collisional (elastic) energy-loss** [189]: attributed to multiple soft-scatterings ($Q + q/g \rightarrow Q + q/g$) between the heavy-quark and thermal quarks/gluons, which lead to drag and momentum diffusion and manifests mostly in the low-p_{T} region.

- **Radiative (inelastic) energy-loss** [190]: dominant at high p_{T} , coming from gluon bremsstrahlung ($Q \rightarrow Q+g$) induced by multiple interactions with the medium, and strongly constrained by quantum interference effects, most importantly *Landau-Pomeranchuk-Migdal interference*. For heavy-quarks, the radiation is suppressed by the *dead-cone effect* at small angle [191].

For heavy quarks, the relative importance of these two channels depends sensibly on the quark mass and momentum: at low and intermediate p_{T} the dynamics are dominated by multiple soft elastic momentum transfers, whereas at high p_{T} medium-induced gluon radiation becomes increasingly relevant. The observed suppression of high-p_{T} heavy-flavor yields and the development of anisotropic flow, therefore encode the interplay between collisional and radiative processes, offering a direct probe of transport properties of the QGP.

[6] Although, depending on the different considerations in the modeling, the observed discrepancy may be solely explained by in-medium suppression and CNM effects [170].

Summary of heavy-flavor in-medium transport models

Below is a summary of current models for heavy-quark transport:

- **Open-heavy flavors**:
  - **Duke/Linear Boltzmann Transport (LBT) [192–194]**: Matrix-element based elastic + medium-induced radiation (with LMP) in a hydrodynamic background; widely used, and high-p_{T} capable.
  - **Lido (Linearized Boltzmann–Langevin hybrid) [195–197]**: Hybrid model with hard scatterings from pQCD Boltzmann and soft sector via Langevin diffusion; used also in Bayesian extractions.
  - **TAMU model (open heavy-flavor branch) [176, 198–201]**: heavy-quark diffusion which accouts for Space-Momentum Correlations (SMCs), and Rate equation with a dynamical decoupling between charm diffusion and regeneration (with RRM).
  - **Catania model** [202, 203]: coalescence and transport with the Wigner formalism for recombination at hadronization. Works at low-to-mid p_{T} for R_{AA} and v_2.
  - **POWLANG (INFN Torino) [204, 205]**: POWHEG initial production and relativistic Langevin in the QGP, with in-medium hadronization.
- **Quarkonia**:
  - **TAMU model (quarkonium rate and transport) [206–209]**: kinetic rate (or Boltzmann) equations with in-medium spectral properties constrained by lattice; includes regeneration and CNM effects.
  - **Tsinghua model** [210, 211]: Boltzmann transport model including spatial diffusion and transverse momentum dependent regeneration, enabling simultaneous description of R_{AA} and v_2.
  - **Comover model [212, 213]**: Comover interaction models describe quarkonium suppression via inelastic scatterings with the dense medium of produced comoving particles. For charmonium, both dissociation and regeneration are considered due to large charm yield at RHIC/LHC. For bottomonium, regeneration is negligible, suppression mostly driven by comover dissociation.
  - **EPOS4-HQ [214–218]**: event generator EPOS4 (Gribov-Regge formalism) with simultaneous multiple scattering and core-corona separation allowing detailed treatment for the QGP formation, upgraded by heavy-quark calculations using Wigner formalism based coalescence model.

1.5.5 . Quarkonium collectivity in heavy-ion collisions

The leading motivation in measuring J/ψ v_2 was to confirm the regeneration mechanism, the very first measurement shown in Fig. 1.23 was done by the STAR collaboration. Back then, people were expecting a positive flow signal in the low-p_{T} region that could be attributed to in-medium regenerated J/ψ and that a pure suppression scenario could not explain. This first result, despite the large uncertainties, was compared to coalescence models including J/ψ regeneration. A clear discrimination was not possible as the results gave values compatible to zero, however the motivation was not reduced as an eventual evidence from J/ψ v_2 would be definitely an important signature for the charm thermalization.

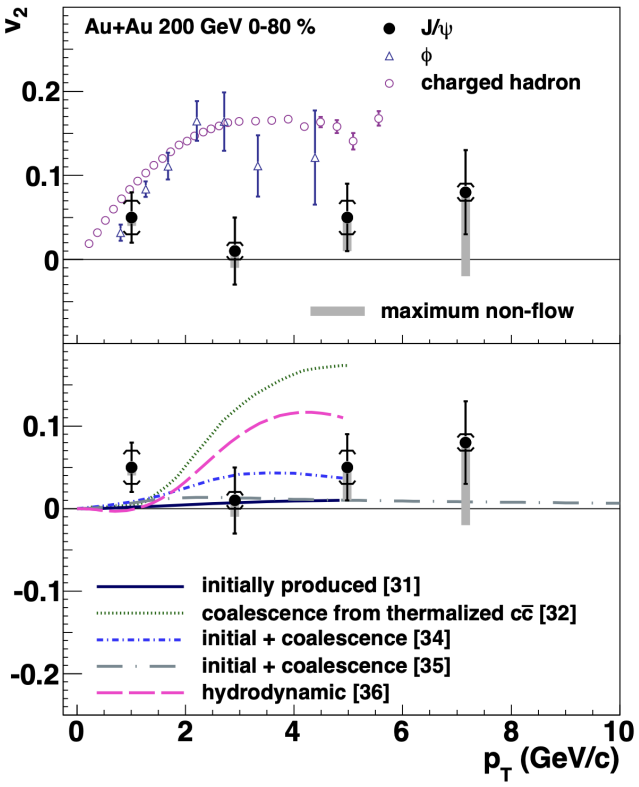

Figure 1.23: The first J/ψ v_2 measurement in Au–Au Collisions at $200\ \mathrm{GeV}$ by STAR collaboration, the results are compared to prediction from coalescence model and hydrodynamic calculation [219].

For this reason, the heavy-ion program at LHC mostly driven by the ALICE collaboration, was pushing this direction forward with higher collision energy. The first result came out from ALICE at $\sqrt{s_{\mathrm{NN}}} = 2.76\ \mathrm{TeV}$ in Pb–Pb collisions, a landmark result presented in Fig. 1.24, where for the first time a clean and significantly positive J/ψ v_2 was seen at low to intermediate p_{T} with a maximal value of ~ 0.1 at around $3\ \mathrm{GeV}/c$ [220]. The latter provided a strong evidence of the regeneration description by comparing to transport model

calculations that implement charm thermalization.

From that moment on, experiments involved in heavy-ion program were focused on more precise and differential measurements of the quarkonium flow, the latter include a first evidence of a centrality dependency of J/ψ v_2 at 5.02 TeV from ALICE [221], then a first prompt/non-prompt J/ψ v_2 measurement in Pb–Pb collisions at $\sqrt{s_{\mathrm{NN}}} = 2.76$ by CMS collaboration [222] – giving access to the B decay contribution for beauty thermalization study. Also at the same time, some advanced techniques like Event-Shape Engineering (ESE) [223] were developed to selectively probe the correlation between the initial geometry/fluctuations and final state observables by binning events not only by centrality, but also by the magnitude of an event–by–event flow vector. Some recent J/ψ flow results from ALICE Run 2 will be discussed in comparison with the analysis conducted in this thesis. In addition, the v_2 of Υ was also measured by CMS [224] and ALICE [225] as a first attempt to probe the beauty thermalization through the direct measurement of bottomonium flow. No significant positive signal was ever confirmed so far. These experimental efforts pushed the theoretical understanding to converge to a nowadays standard charm thermalization picture that was quite well confirmed by low-p_{T} v_2 measurement so charm must have already developed collective flow before the hadronization.

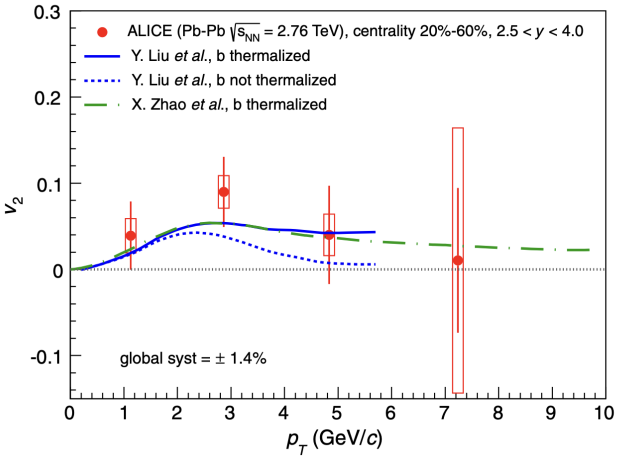

Figure 1.24: J/ψ v_2 in Pb–Pb collisions at $\sqrt{s_{\mathrm{NN}}} = 2.76$ TeV from ALICE collaboration [220].

Despite huge achievements from the past measurement of quarkonium flow, future flow measurement with higher precision and larger dataset will still be motivated with improved differential constraints on v_2 for both p_{T} - and centrality-dependence. Also higher-order correlation of quarkonium flow will also shed light on charm medium coupling and reflect the initial geometry.

1.6 Main focus in this thesis

In the previous sections, the main topics and general interest in heavy-ion physics are reviewed, despite some missing technical details for deeper discussion. As the field itself is as complex as the heavy-ion collision, my intention in this thesis is rather to restrict the broad discussion of various topics to the small but very crucial and profound corner which consists of the study of quarkonia and their collectivity as important probes for the properties of the QGP. In the following chapters, I shall first go through a discussion of experimental setup as the very context for later physics analysis, then to complete the technical aspect I would give a rough discussion on detector alignment applied to the ALICE Muon Spectrometer as part of the Run 3 commissioning, and a complete presentation of the physics analysis conducted during thesis followed by a general conclusion.

Chapter 2

Experimental setup

Contents

2.1 The Large Hadron Collider at CERN

The Standard Model (SM) describes the fundamental interactions among elementary particles. These interactions, depending on their strength, may manifest at extremely small length scales, like the strong and weak interaction being effective only at very short range. To uncover the "unobservable" secrets of nature, we must break matter down into progressively smaller components: from atoms to nuclei, and further into quarks and gluons. Following this demand, at an intergovernmental meeting of UNESCO held in Paris in December 1951, the creation of a European Council for Nuclear Research (in French, Conseil Européen pour la Recherche Nucléaire) was initiated. This direction was soon proven to be plausible, with the weak neutral current predicted by Sheldon Glashow, Abdus Salam and Steven Weinberg in their electro-weak theory being awaiting from 1968, and finally discovered at CERN's Proton Synchrotron accelerator. With this pioneering discovery, further discoveries came out with new accelerator facilities constructed at CERN (Fig. 2.1), the latter included the discovery of W bosons [1] and Z boson [2] – a beautiful cross-check between theory and experiment.

Together with other remarkable discoveries from late 1960s to 1990s, a bigger accelerator providing much higher beam energy was believed to be necessary and approved in December 1994 to be built on the Franco-Swiss border near Geneva, this is known

[1] Decay into electron and neutrino.

[2] Through dielectron or dimuon decay channels despite $\sim$10 times less frequent than the W events

as the Large Hadron Collider (LHC). With maximum beam energy of $6.84\ \mathrm{TeV}$ of Run 3 recommissioning resulting in $39.7\ \mathrm{fb}^{-1}$ integrated luminosity for the beginning of Run 3 started in 2022 and reaching already $100\ \mathrm{fb}^{-1}$ for 2025 (targeting $120\ \mathrm{fb}^{-1}$) on the 6th October [226, 227], LHC already made its landmark discovery of Higgs boson in 2012 from both ATLAS [228] and CMS [229]; provided us unique possibilities for subsequent studies of Higgs mechanism, theoretical predictions for Beyond Standard Model (BSM) particles and of course heavy-ion physics with the growing interest in investigating the new nuclear matter QGP.

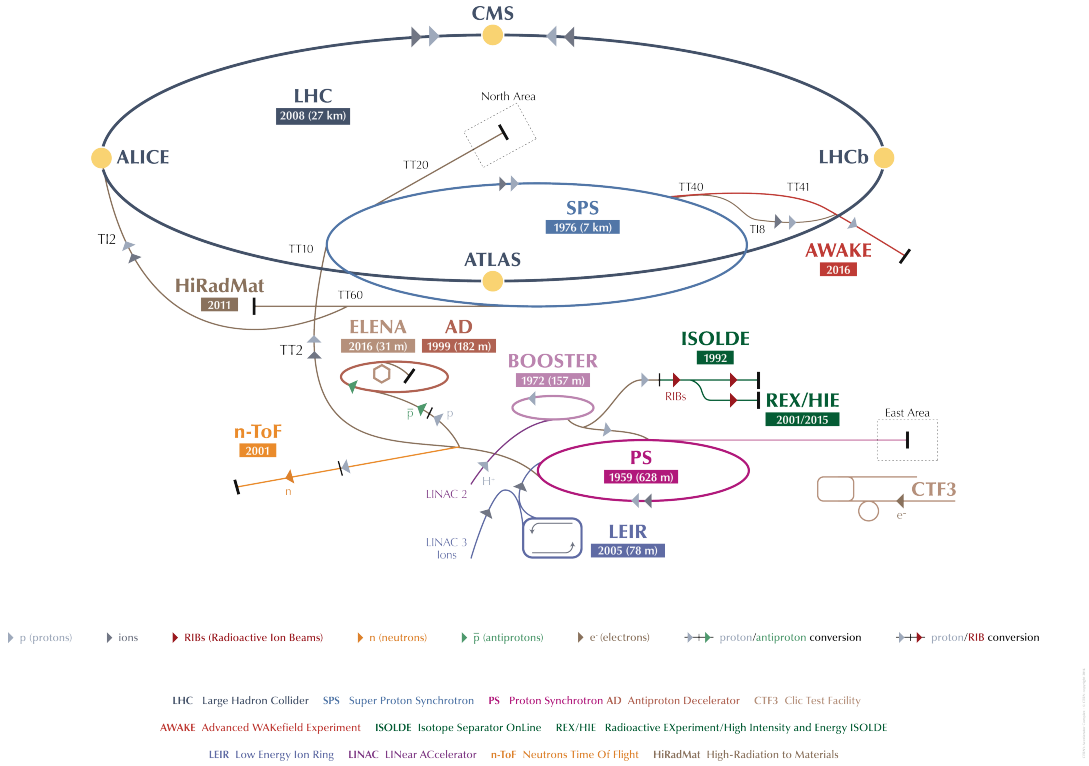

Figure 2.1: Illustration of accelerator facilities at CERN [230].

LHC – the last in the series of hadron colliders after the Intersecting Storage Ring (ISR), Super Proton Synchrotron (SPS), Tevatron, Hadron Elektron Ring Anlage (HERA) and Relativistic Heavy Ion Collider (RHIC) – is situated within a circular underground tunnel measuring 26.7 kilometers in circumference, at depths ranging from 50 to 175 meters beneath the surface. The collider consists of two high energy particle beams traveling in opposite direction within two separate beam pipes kept at ultrahigh vacuum. Particle beams are accelerated at close to speed of light and guided around the accelerator ring by a strong magnetic field maintained by superconducting electromagnets. Much of the accelerator is connected to a distribution system of liquid helium, which cools the magnets, in order to keep coils of special electric cable operating in a superconducting state.

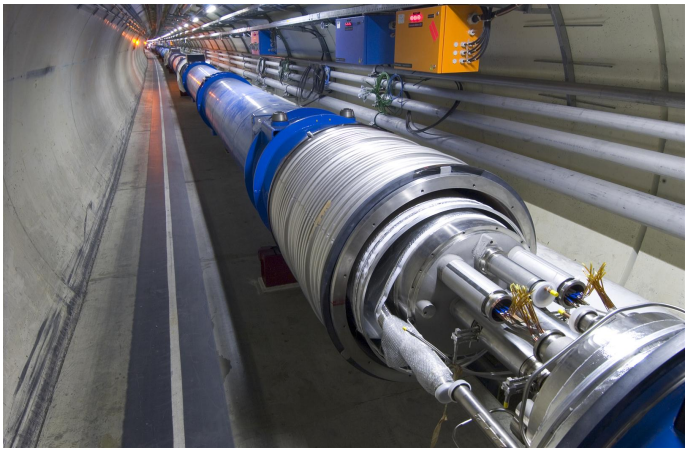

Figure 2.2: View of the beam pipe in tunnel [231].

The collider has eight Interaction Point (IP) where the accelerated particles can collide, and four detectors on the ring, each designed to detect different phenomena, positioned around the crossing-points (Fig. 2.3). Two beam sources circulate in the ring, as shown in Fig. 2.3. Beam 1 is injected close to IP2 and circulate clockwise while Beam 2 is injected close to IP8 and circulate counter-clockwise. The two beams exchange their position between outside and inside of the ring at interaction points where experiments are installed to ensure the same path length for both beams and there are two beam dumps located around IP6. The LHC primarily collides proton beams, but it can also accelerate beams of heavy ions, such as to also provide lead–lead and proton–lead collisions. The ring consists of eight arcs and of eight Long straight sections (LSSs), four large particle physics experiments are installed on the ring at four interaction points (Fig. 2.3), namely:

- **A Toroidal LHC Apparatus (ATLAS)**: located at IP1, is the largest multi-purpose particle detector experiment. It is a many-layered instrument centered around the beam with a cylindrically symmetric form covering an acceptance range of $|\eta| < 2.5$ in pseudorapidity. ATLAS has the privilege to perform precision measurements for Higgs boson and Beyond Standard Model related studies, while it contributes also to heavy-ions physics by taking lead-lead data. ATLAS has recorded integrated luminosity of $\sim 117.9\,\mathrm{fb}^{-1}$ during proton-proton fills of 2025 data-taking period [232].

- **Compact Muon Solenoid (CMS)**: located at IP5, it is also a general purpose detector but with different technical solutions and a different magnetic-system design compared to ATLAS detector. It covers almost the same physics cases as ATLAS as well as a strong contribution to heavy-ion physics. The CMS detector is constructed around a huge solenoid magnet, with the same acceptance range as ATLAS. It takes the form of a cylindrical coil of superconducting cable that generates a field of $4\mathrm{T}$. CMS has received integrated luminosity of $\sim 112.05\,\mathrm{fb}^{-1}$ during 2025 proton-proton data-taking period [233].

- **Large Hadron Collider beauty (LHCb)**: located at IP8, is a forward spectrometer in contrast to ATLAS and CMS, uniquely designed to study, CP violation, beauty physics as well as charm physics. Its initial objective was to explore the asymmetry of matter-antimatter of the Universe but it is also strongly involved in heavy flavor related measurements. LHCb operates at the precision frontier, focusing on subtle effects in heavy-flavor physics. Its asymmetric, single-arm geometry covering pseudorapidity range $2 < \eta < 5$, is optimized for detecting B mesons produced at small angles. LHCb deliberately runs at lower luminosity compared to ATLAS and CMS, with a recorded integrated luminosity of $12\,\mathrm{fb}^{-1}$ in pp runs of 2025 data-taking [234, 235], to ensure only less than two proton-proton interactions per bunch crossing for precise B-meson reconstruction.
- **A Large Ion Collider Experiment (ALICE)**: located at IP2, is uniquely designed to study heavy-ion physics especially the Quark-Gluon Plasma (QGP), in contrast to ATLAS and CMS as pp collisions focused experiments. Its design combines a central barrel covering the midrapidity range $|\eta| < 0.9$ and a forward Muon Spectrometer covering the forward rapidity region $-4 < \eta < -2.5$. The detector and data-taking system is optimized for huge event multiplicities in Pb–Pb collisions over a wide momentum range and a privilege of particle reconstruction down to zero p_{T} in both forward and midrapidity with the Run 3 upgrades. In 2025 data-taking, ALICE recorded already $50\,\mathrm{nb}^{-1}$ for proton-proton runs and aims a target integrated luminosity of $2.4\,\mathrm{nb}^{-1}$ for the lead-lead runs [234, 235]. A more detailed presentation of the ALICE detector will be given in the following sections.

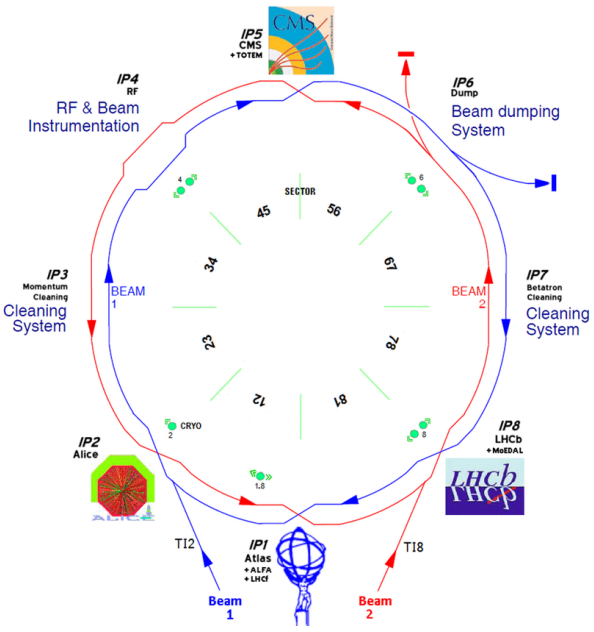

Figure 2.3: Layout of the collider ring with illustration of interaction points and four particle physics experiments.[236]

2.1.1 . Central performance metrics for particle collider

In this section, we shall quickly review some of the key metrics characterizing performance of detector in the context of collider physics.

Global metrics In the context of collider physics, the two most important global metrics are center-of-mass energy $\sqrt{s}$ and luminosity (instantaneous and integrated). The center-of-mass energy is used for the sake of commodity as the collision system consists of two heads-on incoming ion or proton beam. In Run 3, LHC delivers proton beam of $6.8\ \mathrm{TeV}$ for pp collisions at $\sqrt{s} = 13.6\,\mathrm{TeV}$ and lead beam of $2.68\ \mathrm{TeV}$ per nucleon [3] for Pb–Pb collisions at $\sqrt{s_{\mathrm{NN}}} = 5.36\,\mathrm{TeV}$.

The other quantity, *luminosity*, is frequently used as the unique and fundamental metric in characterizing the performance of a collider to produce interactions and determining the total visibility of events with the cross-section. In analogy to the light, luminosity tells you how bright the source you have in the collisions, where the basic instantaneous luminosity reads:

$$L = \frac{N_1 N_2 f}{A} \tag{2.1}$$

where N_1, N_2 are numbers of particles per bunch in the beam, f is the bunch-crossing frequency and A is the effective transverse overlap of the two beams. Accordingly, the integrated luminosity is the integral of the instantaneous luminosity accumulated within a given time window and it is more convenient to use than the instantaneous one as an average metric describing the average performance during a certain data-taking period:

$$\mathcal{L}_{\mathrm{int}} = \int L\,dt = \int \frac{1}{\sigma}\frac{dN}{dt}\,dt. \tag{2.2}$$

where $\frac{dN}{dt}$ is the event rate which is constrained by the trigger and readout system, and σ is the total cross-section for the interaction.

Beam parameters and pile-up As the underlying metrics in defining the luminosity and the overall performance of data-taking, the beam parameters include the number of particles per bunch, the number of bunches in each beam, and the bunch spacing, these three parameters define the overall interaction rate and the two last parameters are configured by the so-called *filling scheme* taking care of distribution of bunches on the beam. Additional parameters are β^* for the degree of beam focusing at the interaction point, the transverse emittance ϵ describing the phase-space closeness of beams, and a geometric correction factor F for the crossing angle. In the LHC running operation, these parameters must be tuned and stabilized to optimize the beam performance and the running conditions.

[3] $E_N = (Z/A)E_p$ where E_N is beam energy per nucleon, E_p is the proton beam energy, Z the atomic number and A mass number of nucleus.

At the same time, the high instantaneous luminosity introduces *pile-up*, i.e. multiple interactions in the same bunch crossing. The latter can badly affect reconstruction performance, which is crucial for some of the experiments like LHCb (usually need to suppress the pile-up to 1-2 in Run 1 and 2 for a clean vertex reconstruction). It can be controlled by adjusting the beam parameters, a higher-granularity design for detectors, a pile-up subtraction algorithm, or a better trigger system.

2.1.2 . LHC long-term schedule

The Long-Term Schedule of the LHC, shown in Fig. 2.4, outlines its operation and upgrade road-map through the 2030s and beyond. Currently, the accelerator is in Run 3 (2022–2026), during which all four major experiments: ATLAS, CMS, ALICE, and LHCb are collecting data at increased luminosities following major upgrades for ALICE and LHCb.

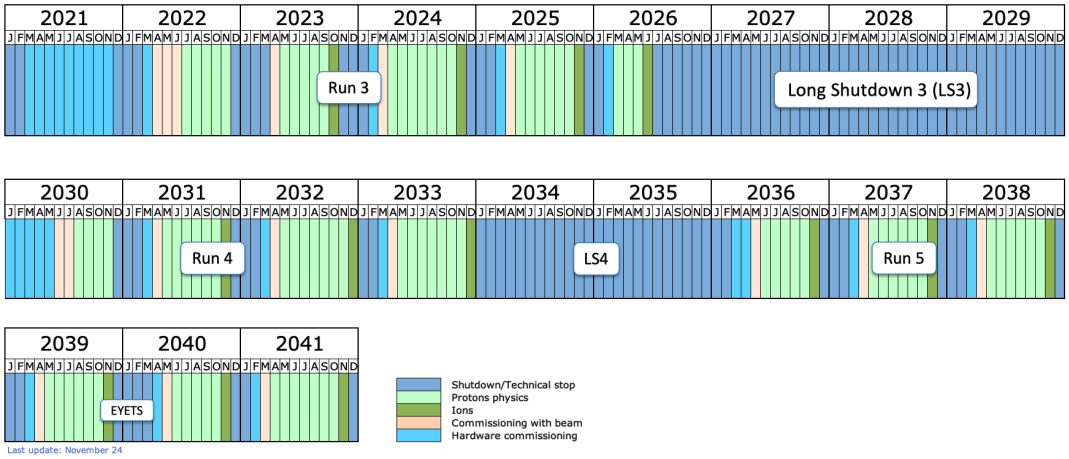

Figure 2.4: The LHC long-term schedule from 2021 to 2041.

After Run 3, the LHC will enter a major Long-Shutdown (LS) from 2026 to 2030 (LS3), dedicated to installing the High-Luminosity LHC (HL-LHC) upgrades. These improvements will significantly boost the collider's luminosity, allowing much higher data collection rates and unprecedented precision in measurements while ATLAS and CMS will undergo significant upgrades for Run 4 and 5. The HL-LHC phase (Run 4) is expected to begin around 2030 and continue into the late 2030s, aiming for an integrated luminosity of several thousand fb^{-1}. Then there will be major upgrades foreseen for ALICE and LHCb during LS4. Further runs (Run 5) are planned after LS4 up to 2041 after which the LHC will shutdown, subsequent preparations will start to build the new Future Circular Collider (FCC) program. This long-term plan ensures that the LHC remains the world's leading facility for exploring fundamental physics for at least the next two decades.

2.2 A Large Ion Collider Experiment

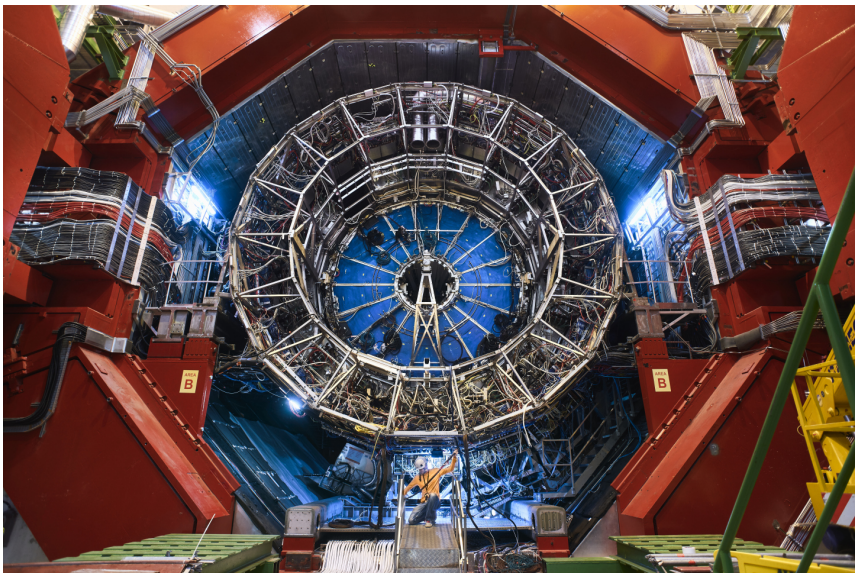

Figure 2.5: A photo of ALICE experiment during LS2 [237].

The A Large Ion Collider Experiment (ALICE) detector was conceived in the early 1990s as part of CERN's plan to explore heavy-ion collisions at unprecedented energies using the LHC. A photo from inside is shown in Fig. 2.5. Its primary goal was to study the QGP as a new state of matter believed to have existed a few microseconds after the Big Bang, when quarks and gluons were not yet confined inside hadrons. The ALICE Collaboration was formally approved in 1997, and construction began soon after, adapting one of the former Large Electron–Positron Collider (LEP) experimental caverns at Point 2 of the LHC ring. The detector's design, centered on high-precision tracking and comprehensive particle identification, was specifically optimized for the extremely high particle densities expected in lead–lead collisions. ALICE recorded its first collisions in 2009, and quickly produced landmark results confirming the creation of a strongly interacting QGP behaving like an almost perfect fluid. Over the following decade, it underwent significant upgrades to enhance readout speed, resolution, and data processings for Run 3 (from 2022). In particular, the special runs for oxygen-oxygen and proton-oxygen collisions were recorded during the end of Run 3, this opened a unique chance to explore the collective behavior with small system and reveal the deeper connection between the QGP which should be expected only within large enough system and emergent collective phenomena from complex system behavior. In the following sections, we shall take a look at the ALICE apparatus and review the major upgrades from Run 2 to Run 3.

2.2.1 . ALICE apparatus in Run 3

In LHC Run 3, the objective of ALICE (with the corresponding Run 3 detector layout presented in Fig. 2.6) is extended to focus more on heavy-flavor production, quarkonium production and related measurement, low-mass dileptons, jet related measurements and heavy nuclear states. These rare processes require larger datasets and higher precision, and involve complex probes at low p_{T} in the most of cases, where triggering methods in Run 2 become inefficient and even non applicable [238].

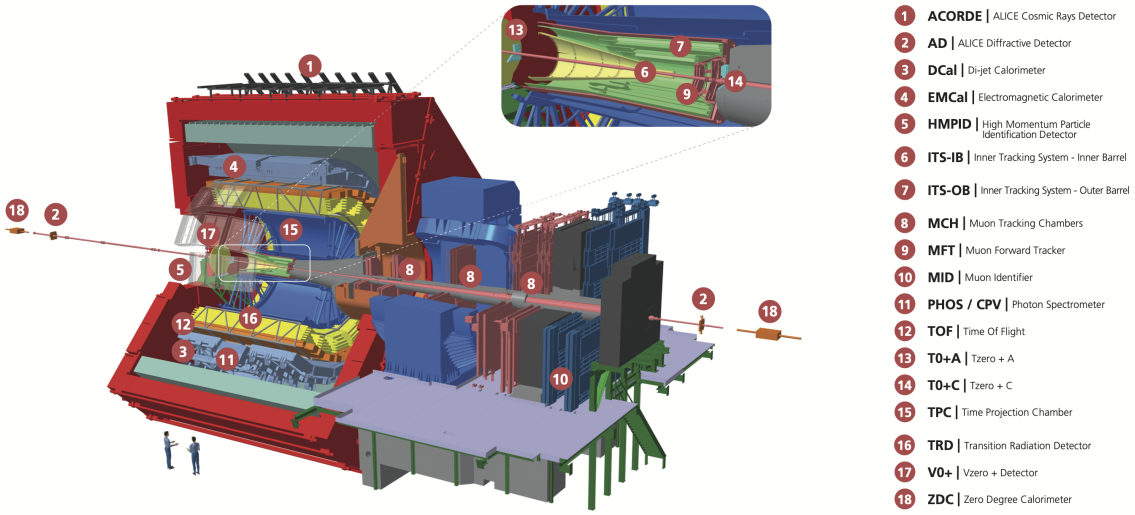

Figure 2.6: The ALICE detector layout in Run 3 [239].

For this reason, the ALICE collaboration has upgraded the detector during the LS2 by improving its low-momentum vertexing and tracking capability, and allowing data-taking at substantially higher rates. The upgrade (installation of new detectors shown in Fig. 2.7) includes a beam pipe with reduced outer radius, moved from $28\,\mathrm{mm}$ to $18\,\mathrm{mm}$, a new Inner Tracking System (ITS2), a new Muon Forward Tracker (MFT), a new GEM-based Time Projection Chamber (TPC) readout, and a new Fast Interaction Trigger (FIT) detector. Moreover, the readout and trigger system have been extensively upgraded to record Pb—Pb collisions at up to $50\,\mathrm{kHz}$ in continuous mode, ensuring sensitivity to signals having no triggerable signature. In the upgraded version, the ALICE detector will take all Pb–Pb interactions. High statistics Pb–Pb measurements will be accompanied by precision measurements with pp and p–Pb collisions as well as the new oxygen beam program for the study of small systems, providing a quantitative base for comparison with results from Pb–Pb collisions.

The ALICE detector has two separate components:

- The **Central Barrel** enclosed in a large solenoid magnet with $B = 0.5\,\mathrm{T}$ covering the pseudorapidity range of $|\eta| < 0.9$ dedicated to quarkonium via dielectron (e^+e^-) channel and charged hadron measurements

- The **Muon Spectrometer** at forward region covering the pseudorapidity range of $-4.5 < \eta < -2.5$ for quarkonium via dimuon ($\mu^+\mu^-$) channel and charged hadron measurements.

Some of the detectors including Fast Interaction Trigger (FIT)s and Zero-Degree Calorimeter (ZDC) located at forward and backward rapidity are not included in these two components, they are mainly used as complementary facilities for global event characterization and interaction triggering. A quick journey through the major detectors and upgrades will be presented in the following discussion.

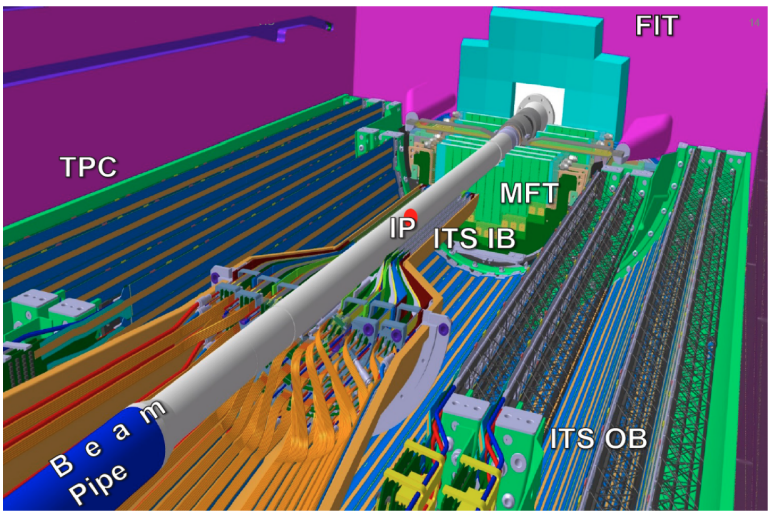

Figure 2.7: The installation of new detectors in Run 3 [240].

Central barrel detectors

Inner Tracking System (ITS) The new Inner Tracking System (ITS2) detector (with a layout shown in Fig. 2.8) consists of seven cylindrical silicon pixel layers, made of ALICE Pixel Detector (ALPIDE) chips arranged in longitudinal staves. The innermost three layers form the Inner Barrel (IB), the layers are installed at radii between 22 mm to 40 mm, while the outermost layer of the Outer Barrel (OB) is located at a radius of 40 cm. The ALPIDE chips plus an ultra-light mechanical support result in a material budget of $0.36\%\ X_0$ [4] per layer for the IB and $1.1\%\ X_0$ per layer for the OB [241].

[4]The interaction length characterizing the energy-loss of particles by electromagnetic interaction with detector material

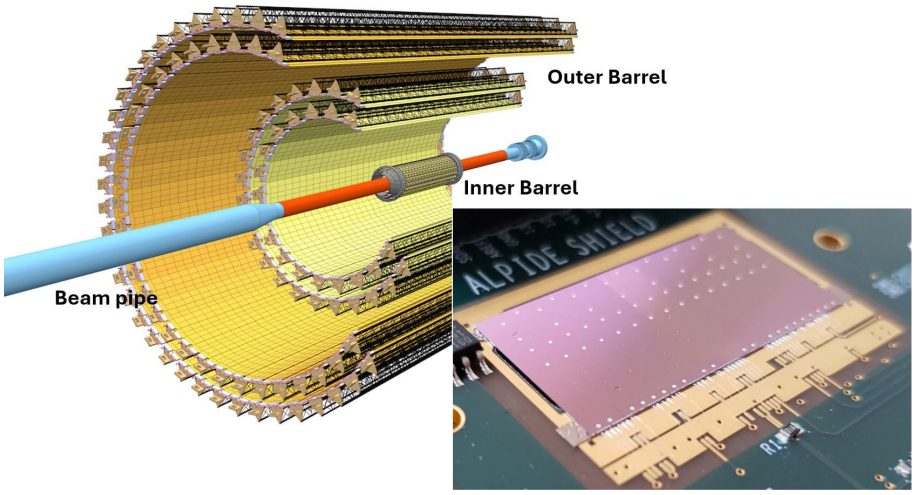

Figure 2.8: The ITS2 detector layout and a photo of ALPIDE chip [241].

Time Projection Chamber (TPC) The Time Projection Chamber (TPC) (a sketch shown in Fig. 2.9) is the main central tracking and particle identification detector of ALICE experiment. It is the largest gaseous tracking detector ever built and one of the most important components for studying the high-multiplicity environments produced in heavy-ion collisions. The detector field cage is cylindrical in shape with an active volume of about $90\ \mathrm{m}^3$. In Run 3, TPC uses Ne-CO_2-N_2 (90-10-5) with additional $5\%\ \mathrm{N}_2$ compared to Run 2 gas. The field cage and most of the services in Run 2 remain the same, while the Multi Wire Proportional Chamber (MWPC)-based readout chambers are replaced by Gas Electron Multipliers (GEM) in quadruple stacks as well as new front-end and readout electronics [242].

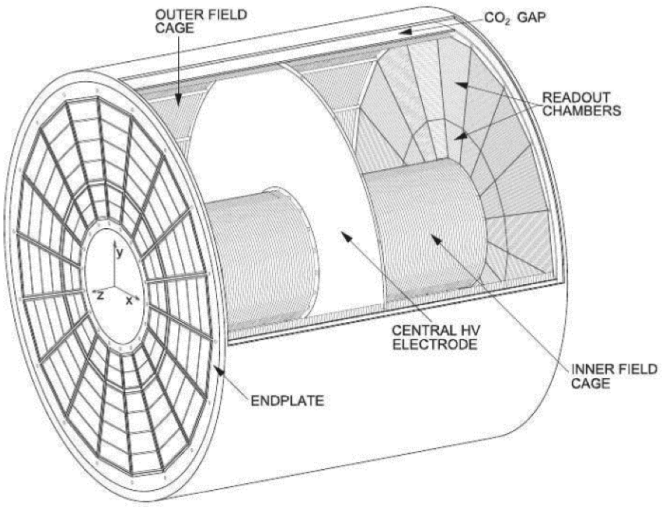

Figure 2.9: A sketch of ALICE Time Projection Chamber (TPC) detector [242].

Forward detectors

Muon Forward Tracker (MFT) The Muon Forward Tracker (MFT) (with a photo of half cone shown in Fig. 2.10) is a new silicon pixel detector in Run 3, designed to extend the physics reach of the Muon Spectrometer by providing precise vertexing and impact parameter measurements at forward rapidity covering $-3.6 < \eta < -2.3$. The detector consists of five disks, each composed of two detection planes built from ultra-thin Monolithic Active Pixel Sensors (MAPS) based on the ALPIDE chip technology, identical to that used in the upgraded ITS2. With a pixel size of $29 \times 27\ \mu\mathrm{m}^2$, material budget of only $0.3\%\ X_0$ per layer, and spatial resolution below $5\ \mu\mathrm{m}$, the detector offers high granularity and minimal multiple scattering – crucial for precise track reconstruction before the hadron absorber. The MFT is fully integrated into new continuous readout system, achieving timing precision of about $10\ \mu\mathrm{s}$ and seamless synchronization with the new real-time data processing framework. It enables the possibility of prompt and nom-prompt separation in quarkonium production.

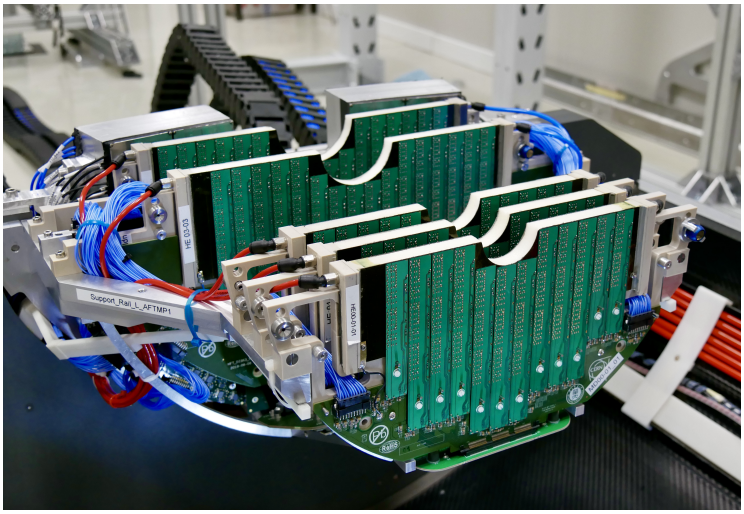

Figure 2.10: A photo of half cone of MFT detector [243].

Muon Chambers (MCH) The Muon Chambers (MCH) ($-4.5 < \eta < -2.5$) of ALICE constitutes the tracking system of the Muon Spectrometer, designed to precisely reconstruct muon trajectories after they pass through the hadron absorber. The detector consists of 10 detection planes arranged in five tracking stations within a dipole magnetic field (with a field integral along the beam axis $\int |B|\, dz \sim 3\ \mathrm{Tm}$) for the bending momentum ($|p_{zy}|$) determination, covering a total active area of about 100 m^2. Figure 2.11 shows a photo of the tracking chambers from within the dipole. Each plane is a Cathode Pad Chamber (CPC) ($< 0.3\%\ X_0$), which is a MWPC using an Ar–$\mathrm{CO_2}$–$\mathrm{CF_4}$ gas mixture for fast signal collection and stability under high particle rates. The readout pads, varying from a few millimeters to several centimeters in size, provide a spatial resolution of 100-$400\ \mu\mathrm{m}$, enabling precise momentum reconstruction of muons up to $100\ \mathrm{GeV}/c$. The Run 3 upgrade

introduced new Scalable Amplifier and ADC (SAMPA)-based front-end electronics and continuous readout capability via the Common Readout Unit (CRU), fully integrated into the new real-time data processing framework.

Figure 2.11: A view of MCH from the dipole [244].

Muon Identifier (MID) In Run 3, the old muon trigger system was renamed as Muon Identifier (MID) consisting of 72 Resistive Plate Chambers (RPC)s arranged in two stations, each containing two planes [245]. The RPCs of MID are $2\ \mathrm{mm}$ single gap detectors with electrodes made of $2\ \mathrm{mm}$ thick high-pressure laminate. As the detector started to operate in continuous readout mode, an upgrade of readout electronics was implemented with new front-end electronics and a change of operation mode for RPCs from maxi-avalanche to avalanche mode.

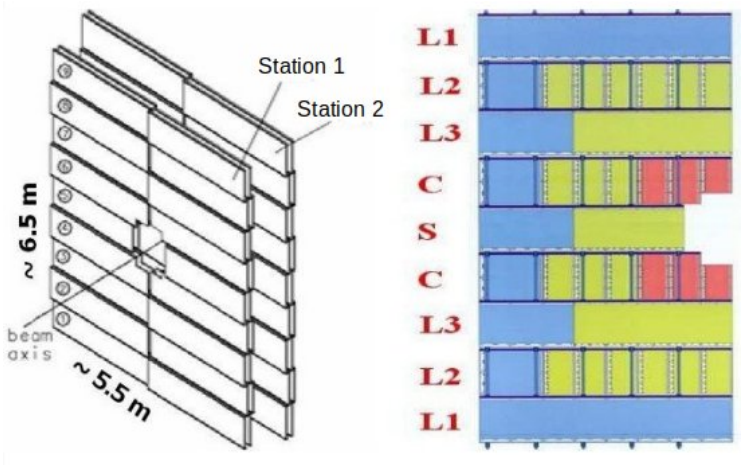

Figure 2.12: A schematic view of the MID detector and the detector composition of an half plane [246].

Global events and interaction triggering

Fast Interaction Trigger (FIT) As a new detector of Run 3 replacing T0 and V0 detectors, the Fast Interaction Trigger (FIT) detector, shown in Fig. 2.13, consists of five arrays of sensors grouped into three subdetectors (Forward Diffractive Detector (FDD), Fast Timing and Trigger (FT0), Fast V0 (FV0)), surrounding the beam pipe on both sides of the interaction point in the forward regions of ALICE. The FT0 is based on Cherenkov radiators coupled to Micro-Channel Plate Photomultiplier (MCP-PMT)s, and the FV0 is a segmented plastic scintillator disk read out by Silicon Photomultiplier (SiPM)s. Together, they cover the pseudorapidity range $-3.4 < \eta < -2.9$ (FT0-C) and $2.0 < \eta < 5.0$ (FV0, FT0-A), providing interaction time measurements with ~ 20 ps precision, minimum-bias and centrality triggers, and luminosity monitoring.

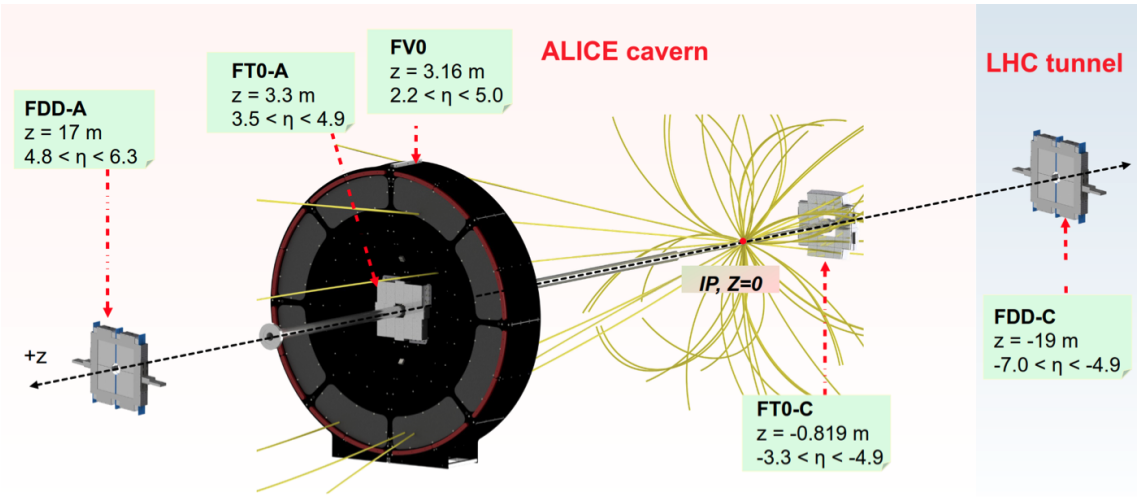

Figure 2.13: A schematic view of the FIT detector with the positioning of all five subdetectors [247].

Zero-Degree Calorimeter (ZDC) The Zero-Degree Calorimeter (ZDC) of ALICE is a forward detector system designed to measure neutral particles (mainly neutrons and photons) emitted close to zero degrees relative to the beam axis, providing crucial information on collision centrality, event characterization, and luminosity monitoring. During Run 3, the ZDC underwent significant electronics and readout upgrades to operate within the continuous data acquisition framework. The system consists of two neutron calorimeters (ZN-A, ZN-C) and two proton calorimeters (ZP-A, ZP-C) placed approximately 112.5 m from the interaction point on both sides of ALICE, beyond the absorbers. Each calorimeter is a sampling hadronic calorimeter made of tungsten absorber plates interleaved with quartz fibers, detecting Cherenkov light produced by shower particles. The ZDC provides precise measurements of forward energy flow, enabling determination of spectator nucleons in Pb–Pb collisions and serving as a minimum-bias trigger in conjunction with the FIT detector.

Real-time data processing: Online-Offline (O2) framework

As ALICE is supposed to take all Pb–Pb interactions in Run3 and operate in the continuous mode for Pb–Pb collisions at $50\ \mathrm{kHz}$ interaction rate without trigger, a new computing system (Online-Offline (O2)) was introduced to overcome this challenge in Run 3. The new system performs a partial calibration and reconstruction online and replace the original raw data with compressed data. The online detector calibration and data reconstruction will therefore be instrumental for keeping the total data flow within an envelope compatible with the available computing resources, and an asynchronous data processing with full functionalities, such as refined calibration, full reconstruction and online quality control, using compressed raw data can be performed offline to optimize the computing resource usage [248].

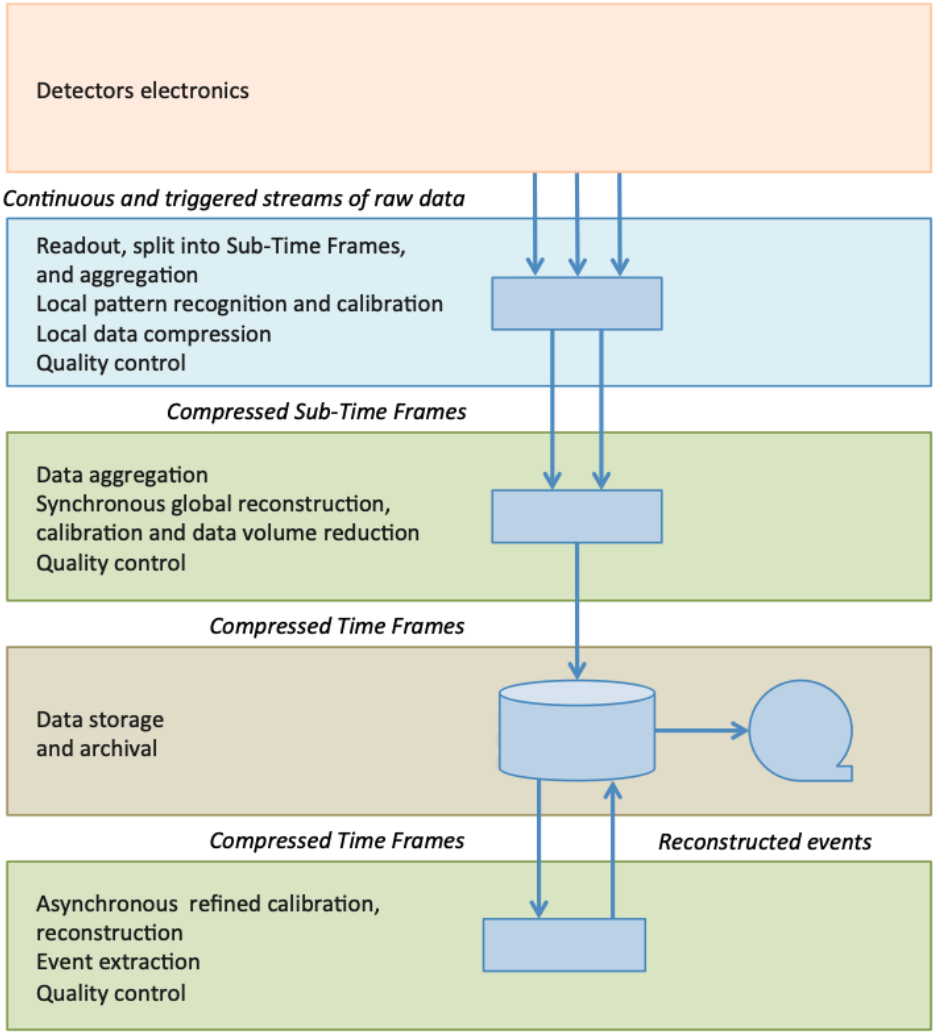

Figure 2.14: The functional flow of the Online-Offline (O2) computing framework [248].

The functional flow and compression levels are illustrated in Fig. 2.14. The continuous streams of data samples are sliced into Data Frame (DF)s, synchronized by HeartBeat (HB) triggers embedded in the raw data streams. The frames will have a time-window of 128 HeartBeat (HB) frames (one HB frame is set to have the same length as an LHC orbit $\sim 88.92\ \mu$s, which is approximately the time required to fully read out the hits from TPC). Raw data are compressed following different levels from Time-Frame (TF)s to Compressed Time-Frame (CTF)s in order to optimize the data storage and computing resources supported by O2 facility and The Worldwide LHC Computing Grid (WLCG).

2.3 Muon reconstruction

As the data analysis conducted in this thesis relies on quarkonia reconstructed in the dimuon decay channel at forward rapidity, it is worth going through some of the major steps in muon reconstruction with the ALICE Muon Spectrometer.

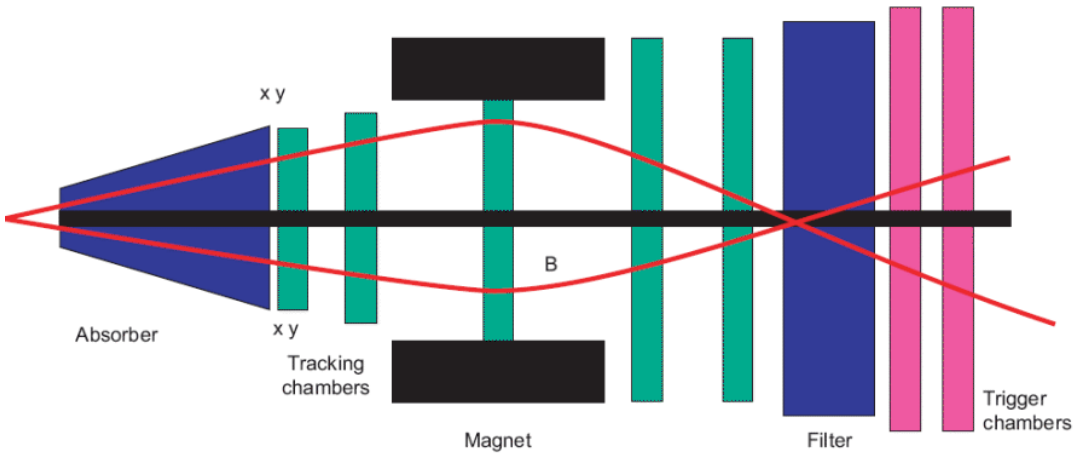

Figure 2.15: A sketched view of the ALICE Muon Spectrometer.

Following the simplified schematic of the Muon Spectrometer shown in Fig. 2.15, tracks originated from the primary vertex (initial collision point) are first filtered by an absorber (blue) made of a thick (~ 10 interaction length) assembly of carbon, concrete, and steel, the latter will stop most hadrons and photons produced in collisions and allowing mainly muon to pass through. The MCH (green) is presented with its five tracking stations containing each of them two chambers (two half-chambers per chamber) resulting in 10 detection planes in total. The hits of a muon passing through CPCs will be recorded by inducing signals on cathode pads where the local coordinates of hits can be extracted from pad charge distribution, then the magnet dipole will curve the muon track to enable the bending momentum determination. An additional filter after the MCH will filter out residual hadrons and low energy background noises. The timing of detected muons will be ensured by the MID with a time resolution of $1\text{-}2$ ns.

2.3.1 . Clustering

The data and functional flow of the whole muon reconstruction factory is presented in Fig. 2.16. The recorded raw signal from the charge released by a charged track that passes trough a chamber will be first converted to MCH digits and filtered using Condition and Calibration Data Base (CCDB) calibration files, for example the bad channels, then it will be followed by a *time-clustering*, which consists of time grouping of digits taking into account the MCH time resolution with respect to the true ReadOut Frame (ROF). Then,

in the framework of a traditional *cluster finding* method, the pad charge distribution will be approximated by a 2D-integral of the *Mathieson function* [249], and the single track local coordinates can be extracted using a Mathieson-based expression. In case there are several tracks close to each other, the number of fit parameters has to be adjusted accordingly, and the number of tracks is estimated by the local maxima in the charge distribution.

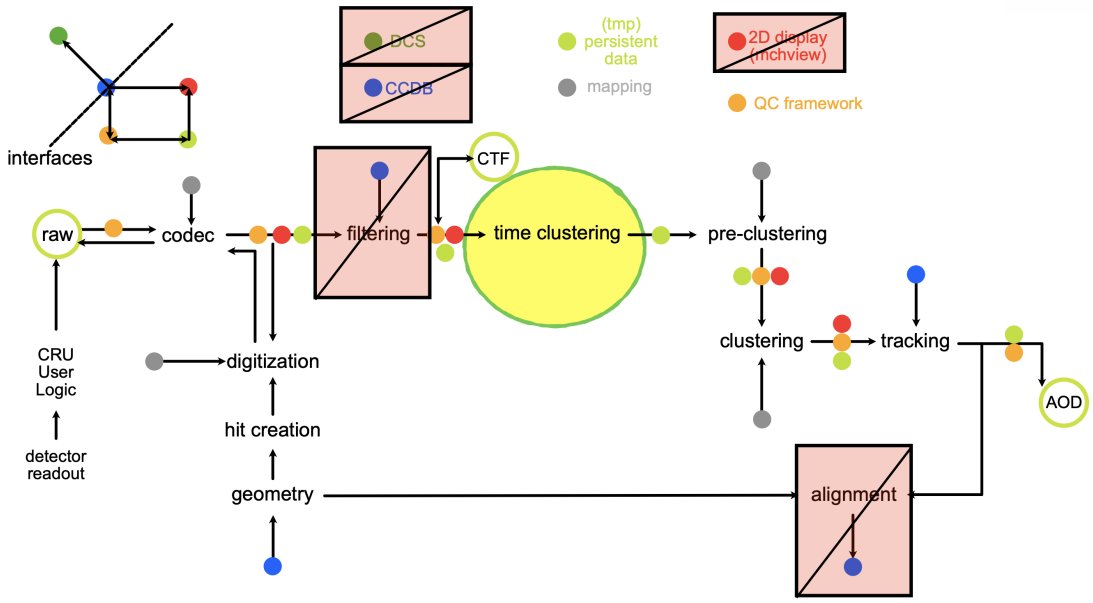

Figure 2.16: The data and functional flow of muon reconstruction.

This traditional cluster finding method was improved by a cluster finding algorithm [250] based on a Maximum-Likelihood-Expectation Maximization (MLEM) method consisting of solving the inversion problem of a signal deconvolution iteratively. This algorithm first tries grouping adjacent pads on one cathode and overlapping with them pads on the other cathode, which makes a so-called *pre-cluster*. Then, for each pre-cluster a corresponding pixel array will be made in the anode plane with the size defined by the overlap of pads on both cathodes. And a iterative procedure for pixel intensity is given by:

$$q_j^{k+1} = \frac{q_j^k}{\sum_{i=1}^{N_{pads}} c_{ij}} \sum_{i=1}^{N_{pads}} c_{ij} \frac{Q_i}{f_i^k} \quad \text{with} \quad f_i^k = \sum_{j=1}^{N_{pix}} c_{ij} q_j^k \tag{2.3}$$

where q_j^k is the intensity for pixel j at k-th iteration, Q_i is the measured signal on pad i, f_i its expected signal, c_{ij} is the pixel-to-pad coupling given by the Mathieson integral, and N_{pix} is the number of pixels in the array. The iteration stops when the pixel size is getting sufficiently small close to 1 mm, and resulting pixel clusters will be used for the subsequent fitting procedure.

2.3.2 . Tracking

After we successfully gathered clusters from the previous step, the following tracking will be performed based on the *Kalman Filter* method [251, 252]. The whole tracking task consists of *track finding* and then *track fitting*. The advantage of the Kalman Filter is that it provides a unified framework for both track finding and track fitting. Mathematically, Kalman Filter is basically a sequential-least square minimization with covariance propagation, it consists of updating the track parameters step-by-step instead of a global fit.

$$\begin{aligned} x_k &= f_{k-1}(x_{k-1}) + \eta_{k-1} \\ y_k &= h_k(x_k) + \epsilon_k \end{aligned} \tag{2.4}$$

where: in the first equation: x_k is the track state vector at the state k, f_{k-1} is the track state propagation model from state $k-1$ to k, and η_{k-1} encodes the noise when propagating from $k-1$ to k; in the second equation: y_k represents the measurement vector at state k, h_{k-1} is the measurement projection model from track state to measurement, and ϵ_k is the measurement noise vector at state k. In the *linearized Kalman Filter*, the propagation and projection operators can be approximated by their 1st-order Taylor expansion.

The state-to-state propagation is done by transport calculation with the Jacobian given specific kinematics involving process noises such as energy-loss and Multiple Coulomb Scattering (MCS) effects. In the actual implementation, this propagation will be performed for a first time in the backward direction (from station 4,5) until chamber 1 [250]. Since the magnetic field delivered by the dipole is generally non-uniform, then the propagation is performed with Runge-Kutta algorithm. In the application to the Muon Spectrometer, the tracks are parametrized by $(x, y, t_x, t_y, q/p)$ where t_x, t_y are track slope respectively in the non-bending and bending plane, and q/p is the charge-to-momentum ratio. A first group of candidates will be created in station 4 and 5, then a candidate seed will be propagated down to chamber 1, and all collected tracks will be checked by the quality using χ^2. The found tracks will be refitted again will Kalman Filter for finalization, while a smoothing procedure may be applied for the evaluation of track parameters at any point along the track after its reconstruction [253].

Chapter 3

Alignment of the Muon Spectrometer

Contents

In this chapter, the alignment of Muon Spectrometer will be discussed as a crucial step in detector software calibration without which one would not expect a reliable quarkonium reconstruction, therefore necessary for all subsequent data analyses. Also for the data analysis conducted in this thesis, the alignment of the Muon Spectrometer and the corresponding commissioning in Run 3 are important premises; in the following discussion, we shall first clarify the physics motivation and the necessity of software detector alignment approach, especially in large physics experiments like ALICE. Then a section introduces the modern detector alignment framework `MillePedeII` including the principal ideas and subsequently how the latter was applied to the ALICE Muon Spectrometer regarding its specifics and subtle details. Finally, the commissioning of software detector alignment with ALICE Muon Spectrometer conducted during the thesis work will be presented, where the basic strategy and some technical points will be highlighted as well. To some extent, the main goal of this chapter is dedicated to summarize a rather structured and concise instructional journey through the topic of detector software alignment applied to the case of the ALICE Muon Spectrometer.

3.1 Why detector alignment matters ?

In the modern grand physics experiments including RHIC, LHC etc, many important and interesting physics processes require high-performance tracking (momentum, spatial and angular resolutions), which is important, e.g. for quarkonium reconstruction and correlation studies, primary and secondary vertexing being crucial for the prompt/non-prompt separation etc. Those physics processes rely on a good enough reconstruction of particle trajectories (defined by some track parameters) using hits from detector elements in the tracking system. In the case of LHC, the tracking systems in general are designed to handle a high-multiplicity environment at high signal frequency. For the case of ALICE TPC tracking system, the total number of readout channels $\sim 550,000$ with the front-end electronics operating at 5-$10\ \mathrm{MHz}$; for ALICE ITS tracking system, 7 cylindrical layers comprises 3 inner barrel layers with 48 staves $\times\ 1,200$ chips and 4 outer barrel layers with 96 staves $\times 6,400$ chips.

In the case of ALICE Muon Spectrometer, though the expected particle multiplicity is much lower (with front absorber where most hadrons, electrons and photons are stopped) than midrapidity region, it contains still a total number of 156 detection elements (5 stations and 10 chambers). In addition to the huge number of detection elements in the tracking system, which appeared to be necessary in achieving an efficient and robust tracking performance to reach physics requirements, each detection element in the tracking system has an intrinsic spatial resolution which reflects directly on the resolution of momentum reconstruction. The latter constrains directly the quarkonium reconstruction resolution where for the case of ALICE Muon Spectrometer a spatial resolution of order of 100μm is necessary to reconstruct the J/ψ invariant mass with a width of $70\ \mathrm{MeV}$. Moreover, this requirement of momentum resolution becomes much more strict for the Υ reconstruction.

Although a detector element may have an excellent intrinsic spatial resolution with a nominal alignment technical design and initial optical survey, this would only guarantee an estimation of corresponding momentum resolution in the optimal situation where detection elements remain mechanically fixed during installation in their initial global positions. However, in practice, the mechanical precision of detection element's position is relatively low compared to the intrinsic resolution. In addition, the global position of the detection elements could actually change due to thermal effect from variation of temperature, the magnetic field (for example the positions of detection elements of MFT can significantly vary with the magnetic field turned on), possible mechanical deformation with ageing, and eventual technical intervention (for example in the case of MCH, where the chambers have to be opened and closed during technical intervention). Therefore, the resulting resolution of each detection element can be badly smeared out due to the mechanical resolution for their global positions.

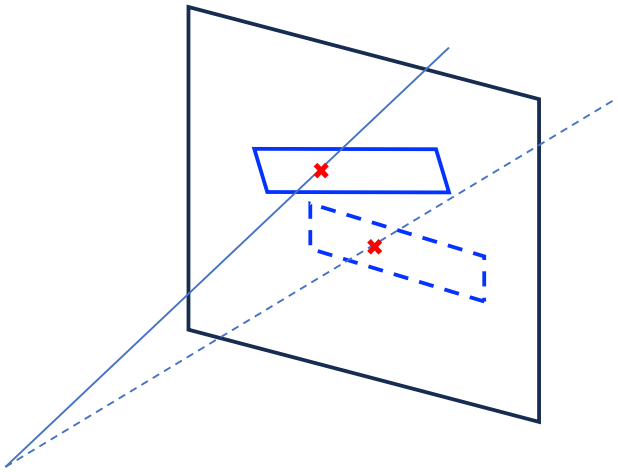

Figure 3.1: An illustration of effect of detection element positioning on tracking performance.

An example illustrating how the change in global position of detection element will affect the tracking is shown in Fig. 3.1, where the detection elements in the frame of half-chamber (black rectangle) before (dashed blue rectangle) and after (solid blue rectangle) the change of global position are illustrated, hence the tracking is directly modified (the difference between dashed line and solid line that will pass through different hits) as a result of the change of corresponding global position of the hit (the coordinates in detection element local frame will remain unchanged) with the detection element.

For these reasons, the detector alignment is indeed necessary, which consists of adjusting the global position of detector elements. Two major approaches were proposed in general:

- **Hardware-based approach**: Hardware-based alignment systems require usually a certain optical system which can monitor the position of detection element with time. For example, in ALICE Run 2, the relative displacement of a half-chamber with respect to a reference chamber was periodically monitored by a Geometrical Monitoring System (GMS) with a spatial resolution about $20\ \mu\mathrm{m}$, and the position of reference chamber is monitored with a resolution of $\sim 500\mu\mathrm{m}$. Also in the central barrel, there is a dedicated optical system ITS Alignment Monitoring System (ITSAMS) to monitor the global relative alignment between Inner Tracking System (ITS) and TPC that are both used and critical for central barrel tracking. Although laser or other optical monitoring systems are commonly deployed for detector alignment, most of them are used as either stability survey for detection element position or a rather global monitoring (no dedicated monitoring for each individual detection element).
- **Software (track) -based approach**: Due to the crucial limitation in hardware-based

alignment approach, which becomes powerless in monitoring the variation of global position down to a detection element level (which may be nearly impossible for some of the detector systems regarding the number of detection elements and the resulting number of degrees of freedom), and moreover, even though hardware-based monitoring system may provide enough information for each detection element, one would still not be able to "mechanically" move the detection elements into their ideal positions, therefore the software-based or track-based approach becomes much more convenient and even the unique and realistic way of doing detector alignment. This approach consists of performing a minimization for a certain objective function (usually χ^2) using particle tracks from reconstruction, which accounts for the discrepancy between track propagation and hit position from detector clusters [254]. The minimization algorithm may be constrained using global monitoring information from hardware-based alignment system.

In the following discussions, we shall essentially focus on the software (track) -based detector alignment approach and see how it is applied and implemented in the concrete scenario of ALICE Muon Spectrometer. In the next section, the core methodology and framework of track-based alignment using `MillePedeII` [254, 255] will be introduced at the first place and followed by the implementation in Muon Spectrometer.

3.2 Track-based alignment with `MillePedeII`

As partially discussed in the previous section, the principal idea of an alignment algorithm relies on data survey which in the current context consists of reconstructed tracks using the being-aligned detector system. The reconstructed tracks are defined at each detection element by their *track parameters* containing the complete local kinematic information for a trajectory, which, depending on the trajectory parametrization (usually in accordance with the detector geometry) in the tracking algorithm, may have different representation and number of degrees of freedom (for example, in ALICE, the tracking of MFT uses a helix-parametrization, while a parabolic-parametrization is used for MCH).

3.2.1 . General setup and geometry

The survey data is defined in this context as the difference between the reconstructed trajectory of a track and the hit (cluster) from detector signal at the position of a given detection element. In the tracking algorithm of MCH, the track parameters characterizing the reconstructed track trajectory are always associated to a reconstructed cluster, this paired information allows us to easily evaluate a crucial quantity called *residual* defined formally by:

$$\mathrm{Residual}_{x/y} = \mathrm{TrackParameter}_{x/y} - \mathrm{Cluster}_{x/y} \tag{3.1}$$

where only x, y directions are considered since the z position used for the track propagation in tracking algorithm is taken from the cluster. The residual measures the discrepancy between reconstructed track parameters and hits from detection element, therefore characterizes how good was the tracking. In case where the detection elements are not in their ideal position, the effect of misalignment will reflect on the distribution of residual with larger width and eventually shifts of mean value away from zero. The distribution of residual encodes many aspects related to the observed resolution, which reads:

$$\Delta(\mathrm{Residual}) = \Delta(\mathrm{Tracking}) \oplus \Delta(\mathrm{Cluster\,intrinsic\,resolution}) \oplus \Delta(\mathrm{Misalignment}) \tag{3.2}$$

The tracking and cluster intrinsic parts are beyond the scope of the detector alignment topic, they require separate investigation in parallel to alignment study. Even if the detection elements are perfectly aligned, the tracking may still smear the residual distribution as the latter introduces indeed energy-loss effect and Multiple Coulomb Scattering (MCS), which generate random fluctuations in the momentum and thus enlarge the momentum resolution ($\Delta p/p$). Therefore, the goal of alignment regarding the residual distribution is rather to reduce the misalignment contribution in the observed resolution as much as possible. The used approach is to minimize the normalized $\chi 2$ distribution with respect to alignment parameters and track parameters:

$$\begin{aligned}\chi^2 &= \sum_{\text{events}} \sum_{\text{tracks}} \sum_i \left(\frac{\overbrace{f^{\mathrm{loc}}(p_i, q_i) - m_i^{\mathrm{loc}}}^{\text{Local residual } r}}{\sigma_i}\right)^2 \\ &= r^{\intercal} \cdot V^{-1} r\end{aligned} \tag{3.3}$$

where p_i represent the global (alignment) parameters of the detection element where the track in question left a hit, q_i represent the local (track) parameter depending on the track parameterization, which may differ from one system to another in terms of the geometry of tracking, $f^{\mathrm{loc}}(p_i, q_i)$ is the local hit position predicted by a parametric trajectory, m_i^{loc} is the local position of the cluster measured by the detection element (given as input data), and σ_i is the resolution of cluster (which can be packed into the measurement covariance matrix V). The sum is running first over all track intercepts of a given track with a detection element, then over all tracks and all events involved in the alignment study. The global parameter tells us how the detection element is positioned with respect to a certain module which can be, in the context of MCH, half-chamber, chamber or the global ALICE frame. It is just a matrix transformation sending the local measure of cluster to another (global) frame or vice versa, an illustration of a simplified 2D case is shown below in Fig. 3.2. However, one should be careful when generalizing to 3D, as the local representation will still remain 2D (detection element measures only the 2D-coordinates), therefore a more rigorous formulation in 3D is to use $q_{\mathrm{loc}} = \begin{pmatrix} q_{\mathrm{loc}}^x \\ q_{\mathrm{loc}}^y \\ 0 \end{pmatrix}$ where the z-coordinate is automatically omitted in the local frame.

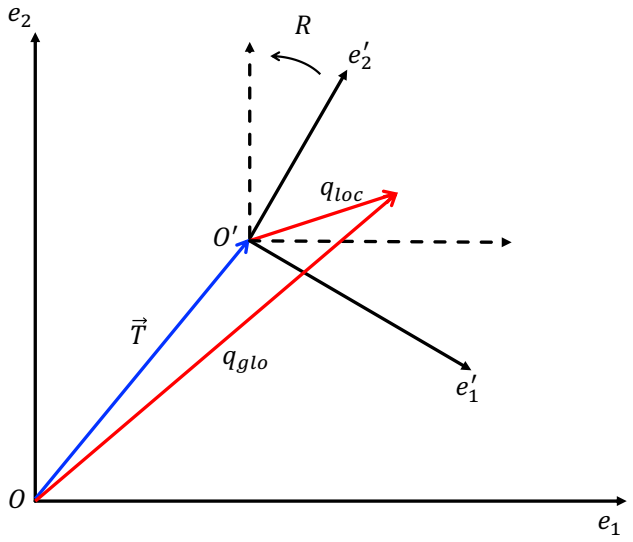

Figure 3.2: An illustration for the geometry of local frame and misaligned local frame for detection element with respect to a global frame.

The transformation p [1] from a local frame O' with basis ($\mathbf{e}_1'$, $\mathbf{e}_2'$) to a global frame O with basis ($\mathbf{e}_1$, $\mathbf{e}_2$) can be understood as taking following successive actions: first taking the vector sum of $\vec{q}_{\mathrm{loc}}$ and the translation $\vec{T}$ ($\overrightarrow{OO'}$) vector between the global and local

[1]Which is a passive transformation, i.e. one moves the frame instead of moving the vector.

frames:

$$\begin{aligned}\vec{q}_{\mathrm{glo}} &= \vec{q}_{\mathrm{loc}} + \vec{T} \\ \vec{q}_{\mathrm{glo}} &= \begin{pmatrix}\mathbf{e}_1^{'} & \mathbf{e}_2^{'}\end{pmatrix} \begin{pmatrix} q^x_{\mathrm{loc}} \\ q^y_{\mathrm{loc}} \end{pmatrix} + \begin{pmatrix}\mathbf{e}_1 & \mathbf{e}_2\end{pmatrix} \begin{pmatrix} T^x \\ T^y \end{pmatrix}\end{aligned} \tag{3.4}$$

where $q_{\mathrm{loc}} = \begin{pmatrix} q^x_{\mathrm{loc}} \\ q^y_{\mathrm{loc}} \end{pmatrix}$ is the invariant local coordinates [2] of the hit (the hit position within the frame of a detection element will remain unchanged with respect to rigid transformation of the detection element). However, the above vector sum is irreducible as the two vectors being summed live in different basis. The latter introduces naturally the transformation between ($\mathbf{e}_1^{'}$, $\mathbf{e}_2^{'}$) and ($\mathbf{e}_1$, $\mathbf{e}_2$), which is simply a rotation R as the geometry of basis is affine where one can imagine as shown in Fig. 3.2 that we parallel transport the basis vector of global frame at O to the origin $O^{'}$ of local frame then we rotate the local frame for the basis vectors can coincide with global ones keeping the correct permutation. In a concrete implementation, one should be careful with the convention of the order of non-commutative 3D-rotation with respect to the three rotation axes. Moreover, the affine transformation is transitive such that $R_{OO''} = R_{OO'}R_{O'O''}$. The rotation from O to $O^{'}$ follows:

$$\begin{pmatrix}\mathbf{e}_1^{'} & \mathbf{e}_2^{'}\end{pmatrix} = \begin{pmatrix}\mathbf{e}_1 & \mathbf{e}_2\end{pmatrix} R \tag{3.5}$$

inserting the above transformation into Eq. 3.2.1 gives:

$$\begin{aligned}\vec{q}_{\mathrm{glo}} &= \begin{pmatrix}\mathbf{e}_1 & \mathbf{e}_2\end{pmatrix} R \begin{pmatrix} q^x_{\mathrm{loc}} \\ q^y_{\mathrm{loc}} \end{pmatrix} + \begin{pmatrix}\mathbf{e}_1 & \mathbf{e}_2\end{pmatrix} \begin{pmatrix} T^x \\ T^y \end{pmatrix} \\ \vec{q}_{\mathrm{glo}} &= \begin{pmatrix}\mathbf{e}_1 & \mathbf{e}_2\end{pmatrix} \left[R \begin{pmatrix} q^x_{\mathrm{loc}} \\ q^y_{\mathrm{loc}} \end{pmatrix} + \begin{pmatrix} T^x \\ T^y \end{pmatrix} \right]\end{aligned} \tag{3.6}$$

From where one can define the whole transformation acting on coordinates $p : O^{'} \to O$ and its inverse transformation (from global to local frame) $p^{-1} : O \to O^{'}$ in a compact way as:

$$\begin{aligned} p(q_{\mathrm{loc}}) = q_{\mathrm{glo}} &= R \cdot q_{\mathrm{loc}} + T = \begin{pmatrix} R & T \\ 0 & 1 \end{pmatrix} \begin{pmatrix} q_{\mathrm{loc}} \\ 1 \end{pmatrix} \\ p^{-1}(q_{\mathrm{glo}}) = q_{\mathrm{loc}} &= R^{-1} \cdot (q_{\mathrm{glo}} - T) = \begin{pmatrix} -R & R \cdot (-T) \\ 0 & 1 \end{pmatrix} \begin{pmatrix} q_{\mathrm{glo}} \\ 1 \end{pmatrix} \end{aligned} \tag{3.7}$$

Now, we can then consider the case where there might be a misalignment with respect to the frame $O^{'}$, leading to a new local frame of detection element $O^{''}$ with basis ($\mathbf{e}_1^{''}$, $\mathbf{e}_2^{''}$). And we introduce in the *natural approach* the so-called alignment parameter as the delta-transformation between frame $O^{'}$ and $O^{''}$ with a delta-rotation ΔR ($\Delta R_x \cdot \Delta R_y \cdot \Delta R_z$ in the general 3D setup) from $O^{'}$ to $O^{''}$ and a global delta-translation $\Delta\vec{T}$ defined in the global frame O. An illustration of degrees of freedom for misalignment with respect to the local frame $O^{'}$ of the detection element is shown below in Fig. 3.3

[2] One needs to be careful with the vector $\vec{v}$ and its coordinates v

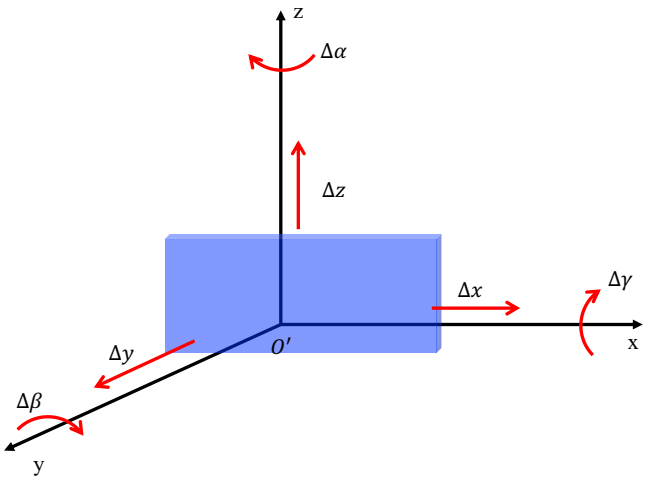

Figure 3.3: The degrees of freedom for misalignment in the local frame of a detection element.

In the *natural (local) picture*, for which the starting point relies on the invariance of local coordinates, the delta-transformation represents exactly a local transformation between original detection element local frame and misaligned frame. The new global coordinates $\vec{q}_{\text{glo}}$ now reads:

$$\begin{aligned}
\vec{q}_{\text{glo}} &= \vec{q}_{\text{loc}} + \vec{T} + \Delta\vec{T} \\
&= \begin{pmatrix} \mathbf{e}_1'' & \mathbf{e}_2'' \end{pmatrix} \begin{pmatrix} q^x_{\text{loc}} \\ q^y_{\text{loc}} \end{pmatrix} + \begin{pmatrix} \mathbf{e}_1 & \mathbf{e}_2 \end{pmatrix} \begin{pmatrix} T^x \\ T^y \end{pmatrix} + \begin{pmatrix} \mathbf{e}_1' & \mathbf{e}_2' \end{pmatrix} \begin{pmatrix} \Delta T^x \\ \Delta T^y \end{pmatrix} \\
&= \begin{pmatrix} \mathbf{e}_1' & \mathbf{e}_2' \end{pmatrix} \Delta R \begin{pmatrix} q^x_{\text{loc}} \\ q^y_{\text{loc}} \end{pmatrix} + \begin{pmatrix} \mathbf{e}_1 & \mathbf{e}_2 \end{pmatrix} \begin{pmatrix} T^x \\ T^y \end{pmatrix} + \begin{pmatrix} \mathbf{e}_1 & \mathbf{e}_2 \end{pmatrix} R \begin{pmatrix} \Delta T^x \\ \Delta T^y \end{pmatrix} \\
&= \begin{pmatrix} \mathbf{e}_1 & \mathbf{e}_2 \end{pmatrix} R\Delta R \begin{pmatrix} q^x_{\text{loc}} \\ q^y_{\text{loc}} \end{pmatrix} + \begin{pmatrix} \mathbf{e}_1 & \mathbf{e}_2 \end{pmatrix} \begin{pmatrix} T^x \\ T^y \end{pmatrix} + \begin{pmatrix} \mathbf{e}_1 & \mathbf{e}_2 \end{pmatrix} R \begin{pmatrix} \Delta T^x \\ \Delta T^y \end{pmatrix} \\
&= \begin{pmatrix} \mathbf{e}_1 & \mathbf{e}_2 \end{pmatrix} \left[R(\Delta R \cdot q_{\text{loc}} + \Delta T) + T \right]
\end{aligned} \tag{3.8}$$

Using the definition of transformation representation p, the above result can be rewritten as:

$$\begin{aligned}
R(\Delta R \cdot q_{\text{loc}} + \Delta T) + T &= \underbrace{\begin{pmatrix} R & T \\ 0 & 1 \end{pmatrix}}_{p} \underbrace{\begin{pmatrix} \Delta R & \Delta T \\ 0 & 1 \end{pmatrix}}_{\Delta p} \begin{pmatrix} q_{\text{loc}} \\ 1 \end{pmatrix} \\
&= p \cdot \Delta p \cdot \begin{pmatrix} q_{\text{loc}} \\ 1 \end{pmatrix}
\end{aligned} \tag{3.9}$$

where Δp is called *misalignment parameter* consisting of ($\Delta\gamma$(x-rotation),$\Delta\beta$(y-rotation),$\Delta\alpha$(z-rotation), Δx, Δy, Δz). And the representation of delta-transformation following this way

will be called *local picture*, and we shall see later in the implementation for ALICE Muon Spectrometer, where the ALICE convention introduces a *global picture* which is equivalent to the local one up to a similarity transformation. Now, the local residual can be then expressed as:

$$r(p+\Delta p, q+\Delta q) = \underbrace{\Delta R^{-1} \cdot R^{-1} \cdot \left[q_{\mathrm{glo}}(q+\Delta q) - T - \Delta T\right]}_{f^{\mathrm{loc}}(p+\Delta p, q+\Delta q)} - m_{loc} \tag{3.10}$$

The linearization of residual around the nominal value is given by:

$$r(p+\Delta p, q+\Delta q) = r_0 + A_{ij}\Delta p_j + B_{ij}\Delta q_j \ldots \tag{3.11}$$

where A_{ij} and B_{ij} are partial derivatives with respect to global and local parameters. In the context of track-based alignment, A_{ij} is called *global derivatives* associated to global parameters and B_{ij} is called *local derivatives* associated to local parameters, they need to be calculated and given as input to the alignment algorithm. In the next section, the explicit form of local and global derivatives with respect to specifics of ALICE Muon Spectrometer will be given. Inserting the linearized residual into χ^2 expression, the first order approximation leads to the linearized least-squares problem, which then consists of solving the linear matrix system below:

$$\begin{bmatrix} B^{\intercal}V^{-1}B & A^{\intercal}V^{-1}B \\ B^{\intercal}V^{-1}A & A^{\intercal}V^{-1}A \end{bmatrix} \begin{pmatrix} \Delta q \\ \Delta p \end{pmatrix} = \begin{pmatrix} A^{\intercal}V^{-1}r_0 \\ B^{\intercal}V^{-1}r_0 \end{pmatrix} \tag{3.12}$$

Therefore, the initial mathematical problem of χ^2 minimization is now converted into a problem of solving the linear system of block matrices with respect to local and global parameters given as input global and local derivatives as well as the survey data defining the nominal residual r_0. The solution of the above type of linear equation is usually done with iterative approach, meaning that at the first iteration one needs to solve the $\Delta p,\ \Delta q$ from the linear system with given input measure and insert resulting delta-parameter to the initial values, then repeat this procedure by adding the previous correction to the new step and solve again for new corrections till the process gets (approximately/numerically) converged at some point. Once we manage to solve the linear system, the resulting set of global parameters Δp for each detection element will be applied as final corrections for misalignment to the reference geometry which is, in the context of above formulation, the geometry of $O^{'}$. The latter consists of putting the obtained (ΔR, ΔT) into the form of Δp in Eq. 3.2.1.

A simplified schematic illustrating the idea of track-based alignment process in 2D scenario is shown in Fig. 3.4: before alignment, an initial pattern of residuals within each detection element is visible, then the minimization process with respect to χ^2 will calculate the optimal global parameters for each detection element and the latter will be applied to the geometry of detection element as alignment parameters. In the simple example above, the detection elements are moved accordingly, resulting in a corrected residual pattern across all detection elements with respect to a given track.

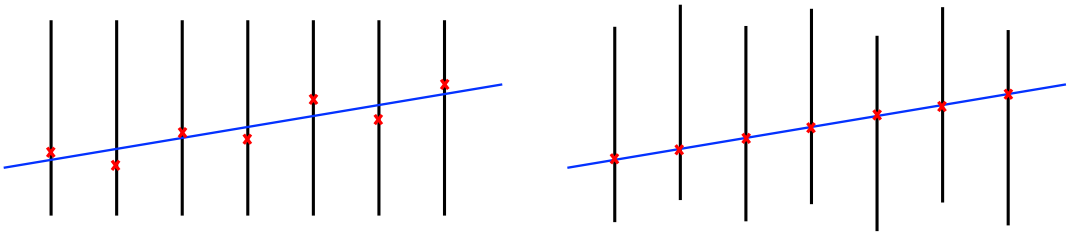

(a) Before alignment (b) After applying alignment parameters

Figure 3.4: An illustration of the result of track-based detector alignment for a simplified 2D (locally 1D) scenario.

So far, everything we discussed in this section is about general formalism and geometrical consideration. Now, we are ready to discuss in the next section, how `MillePedeII` comes into the game to solve the above stated mathematical problem.

3.2.2 . Essentials of `MillePedeII`

In the previous section, we went through the general formulation of a χ^2-minimization problem in the context of track-based detector alignment and how it was converted finally into a mathematical problem of solving a block matrix with respect to global and local parameters. When we think of the solution of the problem, the most intuitive way is to apply an inversion or direct matrix methods.

However, in practice, the problem is much complicated due to the huge number of total degrees of freedom: $\#\text{track} \otimes \#\text{events} \otimes \#\text{local parameters}$ for local parameters and $\#\text{detection elements} \otimes \#\text{global parameters}$ for global parameters. In large high-energy physics experiments like CMS, ATLAS and ALICE, the typical number of tracks used for alignment is around millions leading to number of equations of order ~ 10 times number of tracks depending on the number of hits per track for a given tracking system. This renders the problem extremely hard to solve with trivial methods.

`MillePede` as a solver for linear system

As a mathematical optimization problem, what usually happens in the real situation is that the objective function (χ^2 in the case of track-based detector alignment) is often non-linear, which means that the problem to solve might not be convex at all, leading to non-trivial structure of minima (highly sensitive to initial conditions).

In the previous section, the purely geometrical component of the objective function, giving rise to global parameters, encodes already non-linearity in the rotation matrix. Moreover the global coordinates of track parameter are also by definition highly non-linear, as the latter is obtained from the whole tracking procedure (usually Kalman Filter with backward refinement). So to say, the linearization process of global parameter and conjectured track model replacing "black-boxed" global coordinates of track parameter is actually a strong approximation or at least locally correct. Solving linear system in this case is like going through a path following local small steps given a certain initial conditions, but the path might be strongly dependent on the initial values and may lead to bifurcation due to global non-linearity even your initial conditions are seemly close enough. The dedicated discussion in how to better treat nonlinear objective function beyond linearization deserves its own particular attention. In the context of `MillePede` [254, 255], we shall focus on how a solver of linear system can be optimized to the scenario of large physics experiments facing the challenges.

Mathematical foundation of `MillePede`

The very foundation of `MillePede` lies on a cleaver mathematical trick called *Schur complement* which amounts to reduce the size of the system to solve. As we discussed in the previous section, the linear system consists of solving simultaneously global and local parameters, and a huge contribution to the system size comes from the local equations (every-time you add a hit). However, the presence of local parameters is only an internal fit with respect to the track model, and we are only interested at the end in the global parameters that give us the final corrections for misalignment. Therefore, the trick of Schur complement was introduced to analytically remove the local equations by substitution. In the idea of `MillePede`, the internal fit will be performed before we proceed with global parameter solutions using Schur complement, this step is called *local fit* consisting of a minimization for track local parameters. Then, the general idea of Schur complement can be illustrated in the following steps: consider first a generic block matrix equation preserving the same structure of our matrix system from Eq. 3.2.1:

$$\begin{bmatrix} C & D \\ D^{\intercal} & E \end{bmatrix} \begin{pmatrix} x \\ y \end{pmatrix} = \begin{pmatrix} f \\ g \end{pmatrix} \tag{3.13}$$

where the block matrices and other elements can be identified with Eq. 3.2.1, the diagonal blocks are identified with pure global or local contribution while off-diagonal terms encode global-local coupling. Then, the idea follows the same way as we eliminate one variable for 2D system to solve another one, therefore one may proceed to express the first variable x in terms of y using the first row of blocks:

$$C \cdot x + D \cdot y = f \Longrightarrow x = C^{-1}(f - D \cdot y). \tag{3.14}$$

Then substituting the expression of x for the second block row equation leads to:

$$(E - D^{\intercal}C^{-1}D)y = g - D^{\intercal}C^{-1}f \Longrightarrow S \cdot \Delta p = b, \tag{3.15}$$

where $S = E - D^\intercal C^{-1} D$ corresponds to the Schur complement of block matrix C, and $b = g - D^\intercal C^{-1} f$ which is the measure updated from local fit. The original system hence reduces to a single linear equation of matrices. Solving this final linear equation is called *global fit* in the context of `MillePede` as it amounts to solve directly the final global parameters. Following these ideas, the main structure of `MillePede` algorithm based on the method of Schur complement can be viewed as a two-step solver for linear system, including a first step of local fit for local parameters followed by a second step of global fit for final global parameters.

From `MillePede` to `MillePedeII`

Although the initial construction of `MillePede` was designed to be able to handle a large size matrix by reducing the system with Schur complement, solving directly the remaining global fit of the linear system with respect to the global parameters using matrix inversion can still be tedious and require large computational resources due to the huge total number of degrees of freedom (global parameters). For instance, there are $240,000$ global parameters for ATLAS's silicon tracker and $90,000$ for the tracker of CMS. Therefore, a new version `MillePedeII` was introduced mainly to optimize the whole calculation workflow and advanced treatment in solving the global linear problem using different and iterative methods. A summary of the available features in `MillePedeII` is presented below:

- **Linear constraints** (inherited): the framework allows externally defined constraints to weakly or undefined degrees of freedom using *linear equality constraint* equations of type:

$$a^\intercal \Delta p = c, \tag{3.16}$$

  where the equation introduces an hypersurface to the space of the matrix, reducing the phase space of solutions. For example, a constraint of "zero-average displacement" looks like $\sum_i \Delta x_i = 0$. A commonly used method to account for constraints is the *Lagrange multiplier* in which one adds a corresponding term $\lambda(a^\intercal \Delta p - c)$ in the linearized residual. Gathering all constraints together gives a linear system:

$$A \Delta p = c \tag{3.17}$$

  then the global linear system can be extended to:

$$\begin{bmatrix} S & A \\ A^\intercal & 0 \end{bmatrix} \Delta p = \begin{pmatrix} b \\ c \end{pmatrix} \tag{3.18}$$

- **Outlier rejection** (inherited): data cut in iterative solution with standard deviation and χ^2 of local track fit is implemented to reduce the impact of outliers to the alignment result.

- **Iterative method with sparse matrix storage** (new): using an iterative method based on Generalized Minimal Residual Method (GMRES), for which one assumes the large matrices in question are sparse meaning that most of the non-zero values are distributed along the diagonal, gives access to solve the system with sparse structure. At the same time, giving the sparse structure, a dedicated compression was also applied.

- **Variable-band matrix method** (new): with the sparse matrix assumption, the global linear system is actually a band-matrix with a certain semi-bandwidth (a limit beyond which no coupling between modules is considerable). The latter can be reduced using *Cholesky decomposition*. Adding constraints to the global linear system will surely break up the band matrix structure, however, for matrices with a variable-bandwidth, the decomposition of sparse matrix with *Gaussian elimination* without interchanges preserves the band structure as well.

- **Limited-memory BFGS method** (new): based on the quasi-Newton iterative approach in which the global parameters are solved iteratively using gradient of χ^2 function:

$$\Delta p = B_k \nabla \chi^2, \tag{3.19}$$

  where B_k is the inverse Hessian matrix to be updated iteratively. The limited-memory BFGS method consists of updating B_k using only recent iterations without explicitly building it.

Features such as outlier rejection and constraints inherited from `MillePede` are used directly for detector alignment in the ALICE collaboration. For solving local or global systems, matrix methods are preferred at the first place as they are computationally faster. Iterative approaches, which may capture subtle convergence behavior, are reserved for cases in which the matrix methods do not yield satisfactory results.

3.3 Commissioning with ALICE Muon Spectrometer

In this section, we shall apply the aforementioned track-based detector alignment approach in the case of the ALICE Muon Spectrometer. A review of the explicit implementation will be presented first, followed by the practical alignment strategy and commissioning in ALICE Run 3.

3.3.1 . General setup and implementation

As discussed in Sec. 3.2.1, the very first step for track-based alignment is to derive from the geometrical setup an explicit expression of the local residual. For this reason, it is worth going through the detailed geometrical configuration in the scenario of the ALICE Muon Spectrometer.

Let's first recall the geometry of the Muon Spectrometer, illustrated below in Fig. 3.5 showing the simplified schematic in the bending plane (yOz) where the z direction points to the interaction point (backward) and y is the bending axis. The stations (green) of the tracking system MCH of the Muon Spectrometer are located in between a front absorber (blue) and a filter (blue)) before MID. There are 5 stations ($\mathrm{St1}$, $\mathrm{St2}$, $\mathrm{St3}$, $\mathrm{St4}$, $\mathrm{St5}$ from absorber to filter), where the $\mathrm{St3}$ is inside the dipole magnet region. Each station has two chambers, and each chamber comprises two half-chambers (left-right).

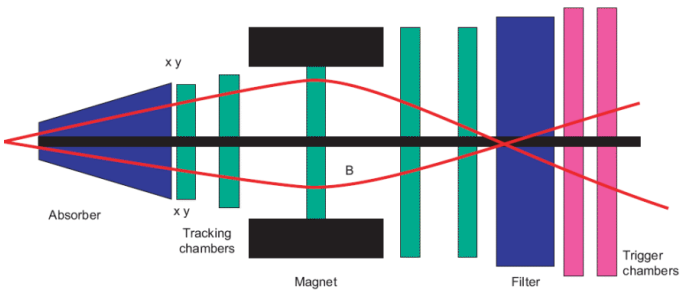

Figure 3.5: A sketched view of the ALICE Muon Spectrometer.

Specific details for the chambers in the different stations can be found below:

- **Chambers in station 1 and 2** Stations 1 and 2 are located in the region between the front absorber and the dipole magnet. Each chamber within these stations comprises four independent quadrants as shown in Fig. 3.6. The four quadrants of a given chamber are mounted on two separate aluminium support structures, thereby forming two mechanically independent half-chambers positioned symmetrically on either side of the beam axis along the non-bending (x) direction. In total, the quadrants of stations 1 and 2 constitute 16 independent detection elements:

$$4\,\mathrm{quadrants/chamber} \otimes 2\,\mathrm{chambers/station} \otimes 2\,\mathrm{stations} \tag{3.20}$$

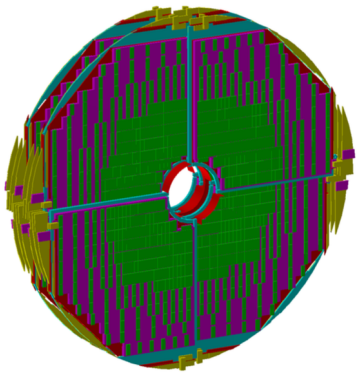

Figure 3.6: A view of chamber in station 1 and 2, where detection elements consist of quadrants.

- **Chambers in station 3** Station 3 is located within the dipole magnet and plays a crucial role in bending-momentum determination. Owing to the large active area covered by this station, a modular design based on a slat geometry was adopted, presented in Fig. 3.7. Each chamber consists of 18 independent slats, which are mounted on two separate support structures made of carbon/epoxy composite panels. In total, Station 3 comprises 36 independent detection elements:

$$18\,\text{slats/chamber} \otimes 2\,\text{chambers/station} \otimes 1\,\text{stations} \tag{3.21}$$

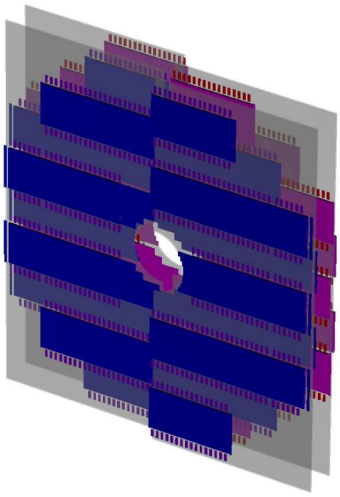

Figure 3.7: A view of chamber in station 3, where detection elements consists of slats.

- **Chamber in station 4 and 5** Stations 4 and 5 are positioned between the dipole magnet and the muon filter wall. A slat geometry, similar to that employed in Station

3, is also used for these stations. Each chamber comprises 26 independent slats mounted on two half-chambers. In total, Stations 4 and 5 together consist of 104 independent detection elements:

$$26\,\mathrm{slats/chamber} \otimes 2\,\mathrm{chambers/station} \otimes 2\,\mathrm{stations} \tag{3.22}$$

Therefore, the tracking system consists of 10 detection planes meaning 10 nominal hits in total (for tracks finishing the whole journey in MCH and possibly reaching MID, without crossing overlapping detection elements.) The total number of detection elements in the whole tracking system is $104 \oplus 36 \oplus 16 = 156$, hence the number of total global degrees of freedom (3 rotations plus 3 translations) reads $156 \otimes 6 = 936$. The intrinsic resolution for each detection element in Run 3 is at $< 100\,\mu$m for bending coordinate and $1\ \mathrm{mm}$ for non-bending coordinate.

Residual within ALICE convention (global picture)

In the geometry framework of ALICE, the geometry classes are defined as physical *volume* inside a geometry tree, and the latter possesses a well-defined hierarchy of geometrical modules in the detection system. In such a way that, from the top to the bottom, the whole detection system lives at the first place in the unique global frame called the ALICE frame, then the latter is followed by the station volumes containing chambers, and so on until one gets to the relevant level for detection alignment, which is the detection element. For the alignment parameter to be universal meaning that it has to be represented in the global frame, the following definition of global delta-transformation is defined as:

$$q_{\mathrm{glo}} = \Delta p\, p \cdot q_{\mathrm{loc}} \tag{3.23}$$

where $p = \left(\begin{smallmatrix} R & T \\ 0 & 1 \end{smallmatrix}\right)$ and $\Delta p = \left(\begin{smallmatrix} \Delta R & \Delta T \\ 0 & 1 \end{smallmatrix}\right)$. In this case the definition of p is not altered from what was discussed in the previous section, however, the meaning of Δp is indeed changed and it represents no longer a local delta-transformation but rather the delta-transformation in the global frame (for an equivalent derivation from the local picture, see Appendix. A). Following this new convention the local coordinates then read:

$$q_{\mathrm{glo}} = \Delta R(R \cdot q_{\mathrm{loc}} + T) + \Delta T \Longrightarrow q_{\mathrm{loc}} = R \cdot (\Delta R^{-1}(q_{\mathrm{glo}} - \Delta T) - T) \tag{3.24}$$

From which the local residual follows:

$$\begin{aligned} r(p + \Delta p, q) &= R^{-1} \cdot (\Delta R^{-1}(q_{\mathrm{glo}} - \Delta T) - T) - m_{\mathrm{loc}} \\ &= R^{-1} \cdot (\Delta R^{-1}(q_{\mathrm{glo}} - \Delta T) - T) - R^{-1} \cdot (m_{\mathrm{glo}} - T) \end{aligned} \tag{3.25}$$

where in the second line, the local coordinates of the cluster measure are represented using global coordinates with transformation p. In the ALICE convention, the global rotation matrix R and the delta-rotation ΔR are defined with the ordering: $z(\mathrm{yaw}) \rightarrow y(\mathrm{pitch}) \rightarrow$

$x(\mathrm{roll})$ as:

$$
\begin{aligned}
R &= \overbrace{\begin{pmatrix} 1 & 0 & 0 \\ 0 & \cos\psi & -\sin\psi \\ 0 & \sin\psi & \cos\psi \end{pmatrix}}^{roll}
\overbrace{\begin{pmatrix} \cos\theta & 0 & \sin\theta \\ 0 & 1 & 0 \\ -\sin\theta & 0 & \cos\theta \end{pmatrix}}^{pitch}
\overbrace{\begin{pmatrix} \cos\phi & -\sin\phi & 0 \\ \sin\phi & \cos\phi & 0 \\ 0 & 0 & 1 \end{pmatrix}}^{yaw} \\
&= \begin{pmatrix} \cos\theta\cos\phi & -\cos\theta\sin\phi & \sin\theta \\ \sin\psi\sin\theta\cos\phi + \cos\psi\sin\phi & -\sin\psi\sin\theta\sin\phi + \cos\psi\cos\phi & -\cos\theta\sin\psi \\ -\cos\psi\sin\theta\cos\phi + \sin\psi\sin\phi & \cos\psi\sin\theta\sin\phi + \sin\psi\cos\phi & \cos\theta\cos\psi \end{pmatrix}
\end{aligned}
\tag{3.26}
$$

$$
\begin{aligned}
\Delta R &= \overbrace{\begin{pmatrix} 1 & 0 & 0 \\ 0 & 1 & -\Delta\psi \\ 0 & \Delta\psi & 1 \end{pmatrix}}^{roll}
\overbrace{\begin{pmatrix} 1 & 0 & \Delta\theta \\ 0 & 1 & 0 \\ -\Delta\theta & 0 & 1 \end{pmatrix}}^{pitch}
\overbrace{\begin{pmatrix} 1 & -\Delta\phi & 0 \\ \Delta\phi & 1 & 0 \\ 0 & 0 & 1 \end{pmatrix}}^{yaw} \\
&= \begin{pmatrix} 1 & -\Delta\phi & \Delta\theta \\ \Delta\phi & 1 & -\Delta\psi \\ -\Delta\theta & \Delta\psi & 1 \end{pmatrix} = \mathbb{1} + \begin{pmatrix} 0 & -\Delta\phi & \Delta\theta \\ \Delta\phi & 0 & -\Delta\psi \\ -\Delta\theta & \Delta\psi & 0 \end{pmatrix} \\
&= \mathbb{1} + \Delta
\end{aligned}
\tag{3.27}
$$

Taking into account as well the infinitesimal variation of local parameters around the nominal values, we are now ready to get the linearized local residual:

$$
\begin{aligned}
r(p+\Delta p, q+\Delta q) &= R^{-1}\cdot(\Delta R^{-1}(q_{\mathrm{glo}}(q+\Delta q) - \Delta T) - T) - m_{\mathrm{loc}} \\
&= R^{-1}\cdot((\mathbb{1}+\Delta^{-1})(q_{\mathrm{glo}} + \Delta q_{\mathrm{glo}} - \Delta T) - T) - R^{-1}\cdot(m_{\mathrm{glo}} - T) \\
&= R^{-1}\cdot((\mathbb{1}-\Delta)(q_{\mathrm{glo}} + \Delta q_{\mathrm{glo}} - \Delta T) - T) - R^{-1}\cdot(m_{\mathrm{glo}} - T) \\
&= \underbrace{R^{-1}(q_{\mathrm{glo}} - m_{\mathrm{glo}})}_{r_0} - \underbrace{R^{-1}(\Delta\cdot q_{\mathrm{glo}} + \Delta T)}_{global\ equations} + \underbrace{R^{-1}\Delta q_{\mathrm{glo}}}_{local\ equations}
\end{aligned}
\tag{3.28}
$$

In the χ^2 minimization, the derivatives $\frac{\partial\chi^2}{\partial(p,q)}$ up to the first order leads to the linear equation:

$$
\underbrace{R^{-1}(\Delta\cdot q_{\mathrm{glo}} + \Delta T)}_{global\ equations} - \underbrace{R^{-1}\Delta q_{\mathrm{glo}}}_{local\ equations} = \underbrace{R^{-1}(q_{\mathrm{glo}} - m_{\mathrm{glo}})}_{r_0}
\tag{3.29}
$$

And the track parametric model uses a local linear model:

$$
q_{\mathrm{glo}} = \begin{cases} x_0 + t_x(z - z_0) \\ y_0 + t_y(z - z_0) \end{cases}
\tag{3.30}
$$

where the reference point (x_0,y_0,z_0) is chosen to be the track parameter at the first plane of MCH, the slopes (t_x, t_y) will be taken at the reference plane for the case of no magnetic field *B-off* and from the local track parameter at z for the case where magnetic field is turned on *B-on*. The reason one has to chose a certain track model is mostly due to the non-trivial tracking process which is supposed to be the "function" that gives the corresponding track global coordinates, which does not always have an analytic form. For

this reason, the track model has to be as close as possible to the realistic situation. The corresponding expansion of local parameters with respect to nominal values follows:

$$\begin{aligned} q_{\mathrm{glo}}(q+\Delta q) &= q_{\mathrm{glo}} + \Delta q_{\mathrm{glo}} \\ &= \begin{pmatrix} x_0 + t_x(z-z_0) \\ y_0 + t_y(z-z_0) \\ z \end{pmatrix} + \begin{pmatrix} \Delta x_0 + \Delta t_x(z-z_0) \\ \Delta y_0 + \Delta t_y(z-z_0) \\ 0 \end{pmatrix} \end{aligned} \tag{3.31}$$

Here, instead of taking directly the z position of the cluster for the corresponding detection element, the z position in the track model has to be calculated as the intersection of the track propagation and the misaligned detection element. This amounts to solve the plane equation of the misaligned detector element and track parametric model with the origin and normal vector of the plane of the misaligned detection element given by:

$$\begin{aligned} O^{''} &= \Delta R \cdot T + \Delta T \\ \vec{n}_{O^{''}} &= (\Delta R \cdot R)_{\cdot,3} \end{aligned} \tag{3.32}$$

And the equation to solve follows:

$$(\vec{q}_{\mathrm{glo}} - O^{''}) \cdot \vec{n}_{O^{''}} = 0 \tag{3.33}$$

The solution of the above equation up to first order approximation ($\Delta^2 = 0$) gives the new z position:

$$z^* = \frac{a}{b} + \frac{a \cdot \Delta b - b \cdot \Delta a}{b^2} \tag{3.34}$$

where,

$$\begin{aligned} a &= R_{(0,2)}T^x + R_{(1,2)}T^y + R_{(2,2)}T^z - R_{(0,2)}x_0 - R_{(1,2)}y_0 + R_{(0,2)}t_x z_0 + R_{(1,2)}t_y z_0 \\ b &= R_{(2,2)} + R_{(0,2)}t_x + R_{(1,2)}t_y \\ \Delta a &= \Delta T^x R_{(0,2)} - \Delta x_0 R_{(0,2)} + \Delta T^y R_{(1,2)} - \Delta y_0 R_{(1,2)} + \Delta T^z R_{(2,2)} + \Delta\phi R_{(1,2)}x_0 \\ &\quad - \Delta\theta R_{(2,2)}x_0 - \Delta\phi R_{(0,2)}y_0 + \Delta\psi R_{(2,2)}y_0 + \Delta t_x R_{(0,2)}z_0 + \Delta t_y R_{(1,2)}z_0 \\ &\quad - \Delta\phi R_{(1,2)}t_x z_0 + \Delta\theta R_{(2,2)}t_x z_0 + \Delta\phi R_{(0,2)}t_y z_0 - \Delta\psi R_{(2,2)}t_y z_0 \\ \Delta b &= \Delta t_x R_{(0,2)} - \Delta\theta R_{(0,2)} + \Delta t_y R_{(1,2)} + \Delta\psi R_{(1,2)} - \Delta\phi R_{(1,2)}t_x \\ &\quad + \Delta\theta R_{(2,2)}t_x + \Delta\phi R_{(0,2)}t_y - \Delta\psi R_{(2,2)}t_y \end{aligned} \tag{3.35}$$

Inserting the new z in the local residual expression and keeping only first-order terms yield the corresponding local (global) derivatives (in the most general situation with all 6 global degrees of freedom) with respect to local (global) parameters summarized below:

- Global parameters Δp: $(\Delta\phi, \Delta\theta, \Delta\psi, \Delta x, \Delta y, \Delta z)$
- Local (track) parameters Δq: $(\Delta x_0, \Delta t_x, \Delta y_0, \Delta t_y)$

And the corresponding derivatives for local and global parameters are given as well:

- **Global derivatives**:
  - $\frac{\partial r}{\partial \phi} = \begin{cases} \frac{\partial r^x}{\partial \phi} & = -R_{(0,0)} q^y_{\text{glo}} + R_{(1,0)} q^x_{\text{glo}} \\ & -(R_{(0,0)} t_x + R_{(1,0)} t_y + R_{(2,0)}) \frac{b(R_{(0,2)}(t_y z_0 - y_0) + R_{(1,2)}(x_0 - t_x z_0)) - a(t_y R_{(0,2)} - t_x R_{(1,2)})}{b^2} \\ \frac{\partial r^y}{\partial \phi} & = -R_{(0,1)} q^y_{\text{glo}} + R_{(1,1)} q^x_{\text{glo}} \\ & -(R_{(0,1)} t_x + R_{(1,1)} t_y + R_{(2,1)}) \frac{b(R_{(0,2)}(t_y z_0 - y_0) + R_{(1,2)}(x_0 - t_x z_0)) - a(t_y R_{(0,2)} - t_x R_{(1,2)})}{b^2} \end{cases}$
  - $\frac{\partial r}{\partial \theta} = \begin{cases} \frac{\partial r^x}{\partial \theta} & = R_{(0,0)} \frac{a}{b} - R_{(2,0)} q^x_{\text{glo}} \\ & -(R_{(0,0)} t_x + R_{(1,0)} t_y + R_{(2,0)}) \frac{bR_{(2,2)}(t_x z_0 - x_0) - a(R_{(2,2)} t_x - R_{(0,2)})}{b^2} \\ \frac{\partial r^y}{\partial \theta} & = +R_{(0,1)} \frac{a}{b} - R_{(2,1)} q^x_{\text{glo}} \\ & -(R_{(0,1)} t_x + R_{(1,1)} t_y + R_{(2,1)}) \frac{bR_{(2,2)}(t_x z_0 - x_0) - a(R_{(2,2)} t_x - R_{(0,2)})}{b^2} \end{cases}$
  - $\frac{\partial r}{\partial \psi} = \begin{cases} \frac{\partial r^x}{\partial \psi} & = -R_{(1,0)} \frac{a}{b} + R_{(2,0)} q^y_{\text{glo}} \\ & -(R_{(0,0)} t_x + R_{(1,0)} t_y + R_{(2,0)}) \frac{bR_{(2,2)}(y_0 - t_y z_0) - a(R_{(1,2)} - R_{(2,2)} t_y)}{b^2} \\ \frac{\partial r^y}{\partial \psi} & = -R_{(1,1)} \frac{a}{b} + R_{(2,1)} q^y_{\text{glo}} \\ & -(R_{(0,1)} t_x + R_{(1,1)} t_y + R_{(2,1)}) \frac{bR_{(2,2)}(y_0 - t_y z_0) - a(R_{(1,2)} - R_{(2,2)} t_y)}{b^2} \end{cases}$
  - $\frac{\partial r}{\partial x} = \begin{cases} \frac{\partial r^x}{\partial x} = R_{(0,0)} - \frac{(R_{(0,0)} t_x + R_{(1,0)} t_y + R_{(2,0)}) R_{(0,2)}}{b} \\ \frac{\partial r^y}{\partial x} = R_{(0,1)} - \frac{(R_{(0,1)} t_x + R_{(1,1)} t_y + R_{(2,1)}) R_{(0,2)}}{b} \end{cases}$
  - $\frac{\partial r}{\partial y} = \begin{cases} \frac{\partial r^x}{\partial y} = R_{(1,0)} - \frac{(R_{(0,0)} t_x + R_{(1,0)} t_y + R_{(2,0)}) R_{(1,2)}}{b} \\ \frac{\partial r^y}{\partial y} = R_{(1,1)} - \frac{(R_{(0,1)} t_x + R_{(1,1)} t_y + R_{(2,1)}) R_{(1,2)}}{b} \end{cases}$
  - $\frac{\partial r}{\partial z} = \begin{cases} \frac{\partial r^x}{\partial z} = R_{(2,0)} - \frac{(R_{(0,0)} t_x + R_{(1,0)} t_y + R_{(2,0)}) R_{(2,2)}}{b} \\ \frac{\partial r^y}{\partial z} = R_{(2,1)} - \frac{(R_{(0,1)} t_x + R_{(1,1)} t_y + R_{(2,1)}) R_{(2,2)}}{b} \end{cases}$
- **Local derivatives**:
  - $\frac{\partial r}{\partial x_0} = \begin{cases} \frac{\partial r^x}{\partial x_0} = -R_{(0,0)} + \frac{(R_{(0,0)} t_x + R_{(1,0)} t_y + R_{(2,0)}) R_{(0,2)}}{b} \\ \frac{\partial r^y}{\partial x_0} = -R_{(0,1)} + \frac{(R_{(0,1)} t_x + R_{(1,1)} t_y + R_{(2,1)}) R_{(0,2)}}{b} \end{cases}$
  - $\frac{\partial r}{\partial t_x} = \begin{cases} \frac{\partial r^x}{\partial x_0} & = \frac{-R_{(0,0)}(R_{(0,2)}(T^x - x_0) + R_{(1,2)}(T^y - y_0) + R_{(2,2)}(T^z - z_0))}{b} \\ & + (R_{(0,0)} t_x + R_{(1,0)} t_y + R_{(2,0)})(bR_{(0,2)} z_0 - aR_{(0,2)}) \\ \frac{\partial r^y}{\partial x_0} & = \frac{-R_{(0,1)}(R_{(0,2)}(T^x - x_0) + R_{(1,2)}(T^y - y_0) + R_{(2,2)}(T^z - z_0))}{b} \\ & + (R_{(0,1)} t_x + R_{(1,1)} t_y + R_{(2,1)})(bR_{(0,2)} z_0 - aR_{(0,2)}) \end{cases}$
  - $\frac{\partial r}{\partial y_0} = \begin{cases} \frac{\partial r^x}{\partial x_0} = -R_{(1,0)} + \frac{(R_{(0,0)} t_x + R_{(1,0)} t_y + R_{(2,0)}) R_{(1,2)}}{b} \\ \frac{\partial r^y}{\partial x_0} = -R_{(1,1)} + \frac{(R_{(0,1)} t_x + R_{(1,1)} t_y + R_{(2,1)}) R_{(1,2)}}{b} \end{cases}$
  - $\frac{\partial r}{\partial t_y} = \begin{cases} \frac{\partial r^x}{\partial x_0} & = \frac{-R_{(1,0)}(R_{(0,2)}(T^x - x_0) + R_{(1,2)}(T^y - y_0) + R_{(2,2)}(T^z - z_0))}{b} \\ & + (R_{(0,0)} t_x + R_{(1,0)} t_y + R_{(2,0)})(bR_{(1,2)} z_0 - aR_{(1,2)}) \\ \frac{\partial r^y}{\partial x_0} & = \frac{-R_{(1,1)}(R_{(0,2)}(T^x - x_0) + R_{(1,2)}(T^y - y_0) + R_{(2,2)}(T^z - z_0))}{b} \\ & + (R_{(0,1)} t_x + R_{(1,1)} t_y + R_{(2,1)})(bR_{(1,2)} z_0 - aR_{(1,2)}) \end{cases}$

where (x, y, z) are the coordinates of q_{glo} obtained from the tracking parameters and the matrix elements of the rotation matrix can be read for a given detection element from the geometry interface in the ALICE framework using the unique ID (DEID).

These derivatives then have to be implemented in the framework as input data for the linear system. The global parameters need to be setup with certain *allowed variation range* usually based on the chamber resolution and mechanical precision. This setup might have to be tuned in certain circumstances as an indirect way to constrain the behavior of global parameters and the solution space. A standard configuration for the allowed variation range uses (assuming only ϕ-rotation): $1.5\ \mathrm{cm}\ (\Delta x)$, $0.3\ \mathrm{cm}\ (\Delta y)$, $2\ \mathrm{cm}\ (\Delta z)$, $0.002\ \mathrm{rad}\ (\Delta\phi)$. Although the covariance matrix of the chamber resolution does not enter explicitly in the global and local derivatives, they are used to weight the local residual measures ($1/\sigma^2_{x,y}$).

Local fit for track parameters

As discussed in the previous section, the idea of `MillePedeII` consists of a two-step fit for the χ^2 minimization. Let's first recall the matrix representation of the linearized χ^2 function:

$$\begin{aligned}\chi^2 &= r_L^{\intercal} \cdot V^{-1} \cdot r_L \\ &= (r_0 + A \cdot \Delta p + B \cdot \Delta q)^{\intercal} \cdot V^{-1} \cdot (r_0 + A \cdot \Delta p + B \cdot \Delta q).\end{aligned} \tag{3.36}$$

In the local fit, the contribution from global parameters will be first fixed using initial values and pre-defined variation ranges, which leads to the local system:

$$B^{\intercal} V^{-1} B \cdot \Delta q = B^{\intercal} V^{-1} \cdot r_0, \tag{3.37}$$

where in the algorithm a first attempt of using Cholesky decomposition will be made at the first place. In the case the latter decomposition is not successful, then Gaussian elimination will be applied. During the local fit, a corresponding χ^2/ndf for each track will be estimated and a cut-off based on χ^2/ndf threshold is implemented to reject outliers which may contaminate the global fit performance.

Global fit for alignment parameters

Once the local fit is done with success, the next step is to solve the reduced global linear system (see Eq. 3.2.2) with Schur complement by removing local parameter degrees of freedom and the per track fitted information will be transferred into the reduced system. In solving the global system, the algorithm will first proceed with matrix approach (Cholesky, then Gaussian elimination for sparse matrix) which is supposed to be faster than iterative method, then in case the first attempt is not plausible the algorithm will try to use the subroutine Minimal Residual Method (MINRES), then Flexible Generalized Minimal Residual Method (FGMRES) if the previous ones does not work well.

The resulting Δp as alignment parameters will be first checked, whether there are any huge detection element shifts. Then the alignment parameters will be applied to the reference geometry following $p^{'} = \Delta p \cdot p$, and $p^{'}$ will be exported as new (aligned) geometry file that has to be uploaded to the CCDB for the next round of reconstruction.

Constraints

In the application to ALICE Muon Spectrometer, linear constraints were shown to be not efficient during Run 2, probably due to incomplete global degrees of freedom. In Run 3, the main way to constraint the linear system is to fix some of the global degrees of freedom, for instance one may fix some of the individual detection elements (removing their degrees of freedom) or fix a full chamber or half-chamber. In practice, fixing chambers is mostly used providing a rather good convergence performance, where chamber one is preferably fixed as it is rarely opened hence unlikely to be significantly moved.

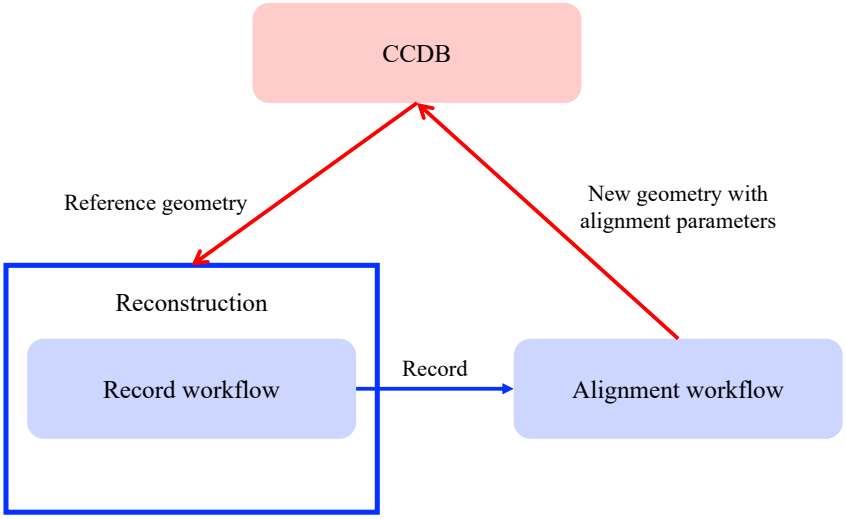

Figure 3.8: The functional workflow of the alignment process.

Alignment workflow

In Run 3, the dedicated alignment workflow is developed as part of the thesis work. The alignment routine has to be performed in an asynchronous way with respect to the reconstruction as some details and subtleties might still need to be checked for the alignment. However, the alignment process is optimized in such a way that the input data providing measures and derivatives for later alignment workflow can be generated with a dedicated record workflow during the reconstruction, hence one only needs to take the

record file and run alignment process. The advantage being that the record workflow can be parallelized. A schematic functional illustration of alignment routine is presented in Fig. 3.8: with a reconstruction based on a certain reference geometry fetched from CCDB, the record file for alignment can be generated on-the-flight. This record file then is taken by alignment workflow, which will then provide a new geometry with alignment correction found out by `MillePedeII`.

3.3.2 . Alignment strategy in Run 3

In Run 3, since the optical monitoring system is no longer available, one has to rely on the strategy with different data-taking options. These consist actually in two types of data-taking:

- **B-off data**: for which the data-taking was operated with the dipole magnet turned off, therefore the tracks should be not curved. Usually, only a few runs before the physics data-taking are taken with this configuration and they are dedicated to alignment related studies.

- **B-on data**: this corresponds to the normal data-taking for physics purpose, where the magnetic field is on and charged tracks are curved. There are at the beginning of the physics data-taking some calibration runs dedicated to technical commissioning, software checks and detector calibrations.

As mentioned in the previous section, the track model for global track coordinates is implemented differently in B-off and B-on cases. And one should be conscious that the tracking in the case of B-off is supposed to be more trivial since the tracks are subject to straight line trajectory for which the linear track model is considered to be a good approximation for the real situation up to the MCS and energy-loss correction. The misalignment pattern from residuals is often easier to be captured in this case. For this reason, the basic strategy in Run 3 consists of for each alignment period a first step of *B-off alignment* where the reference geometry is either picked from the latest one in CCDB or the ideal geometry, the final decision is usually done based one test trials with the two options. Then for B-on physics data-taking, the aligned geometry provided by the previous step will be used as reference and the calibration runs will be used to run alignment workflow in order to prepare optimized geometry for the subsequent physics runs.

For a whole data-taking period, there are usually two alignment processes to be done, meaning two aligned geometry files to be submitted to CCDB.

3.3.3 . Commissioning with data-taking periods

In this section, I will review the major moves of alignment during 2022-2023 data-taking periods. Some technical details might be incorporated in the discussion. In the alignment process, all tracks before getting into the algorithm have to go through a refit process, where the setup for tracking parameters are listed below:

- For pp runs ("pp set"):
  - Chamber resolution $0.4\ \mathrm{cm}$ for both x and y direction
  - $\sigma_{\mathrm{tracking}}$ cut for tracking is set to 7
  - σ_{χ^2} cut for track improvement is set to 6
- For Pb–Pb runs ("Pb–Pb set"):
  - Chamber resolution $0.2\ \mathrm{cm}$ for both x and y direction
  - $\sigma_{\mathrm{tracking}}$ cut for tracking is set to 5
  - σ_{χ^2} cut for track improvement is set to 4

About 20% of the tracks are removed with the "pp set" and 40% with the "Pb–Pb set". The tracks used for the alignment process are required to be MCH-MID matched muon tracks. For the following results from the alignment process, the two rotation degrees of freedom pitch and roll are assumed to be small regarding the geometry and mechanical constraints. Therefore, their global parameters are not taken into account in the global equations.

B-off alignment The B-off alignment as the first step for alignment of 2022-2023 data-taking period was done using runs 520495 and 520496 from period LHC22h with $2.7\mathrm{M}$ MCH-MID matched tracks. At the same time, the alignment algorithm was completed with track refit. The residuals for all detection elements extracted from run 520495 and 520496 of LHC22h before alignment are presented below in Fig. 3.9 (red), where one may observe that the initial residual distributions along x and y directions were all quite distorted mostly due to technical intervention and hardware commissioning during the previous TS.

Given the above initial residuals as input measure, the result of the alignment process with chamber 1 and 10 fixed is illustrated in Fig. 3.10 (each blue point corresponds to a detection element, and the plot is sectored into chambers 1 to 10 from left to right), where the algorithm found significant corrections for all global degrees of freedom especially regular shifts in x direction signaling that the chambers were not well closed. However, there were a few outlier displacements of detection elements in chamber 5 and 6 along the z direction. The latter (concerning DE500, DE509, DE600, DE609) had to be accounted carefully with appropriate initial values to avoid overlaps: $-2.0\ \mathrm{cm}$ (DE500), $-2.0\ \mathrm{cm}$ (DE509), $-4.0\ \mathrm{cm}$ (DE600) and $-2.5\ \mathrm{cm}$ (DE609). The corresponding residuals after alignment (blue) are also illustrated in Fig. 3.9 from which one may directly observe the improvement compared to the starting point.

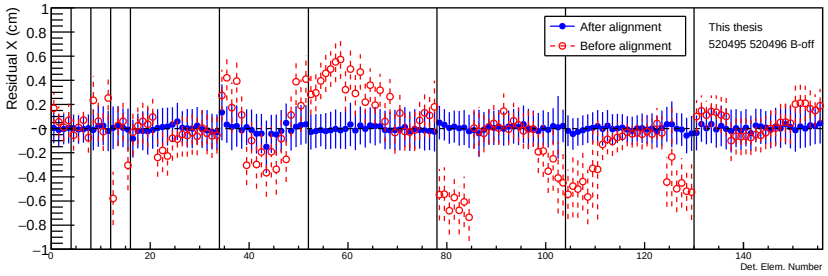

(a) Residual in x (cm)

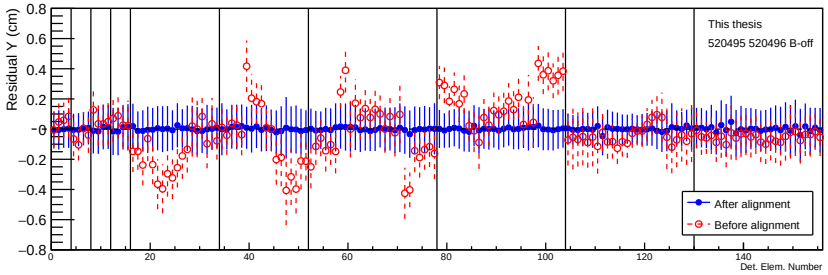

(b) Residual in y (cm)

Figure 3.9: Residuals along x and y for all detection elements with run 520495 and 520496 of LHC22h.

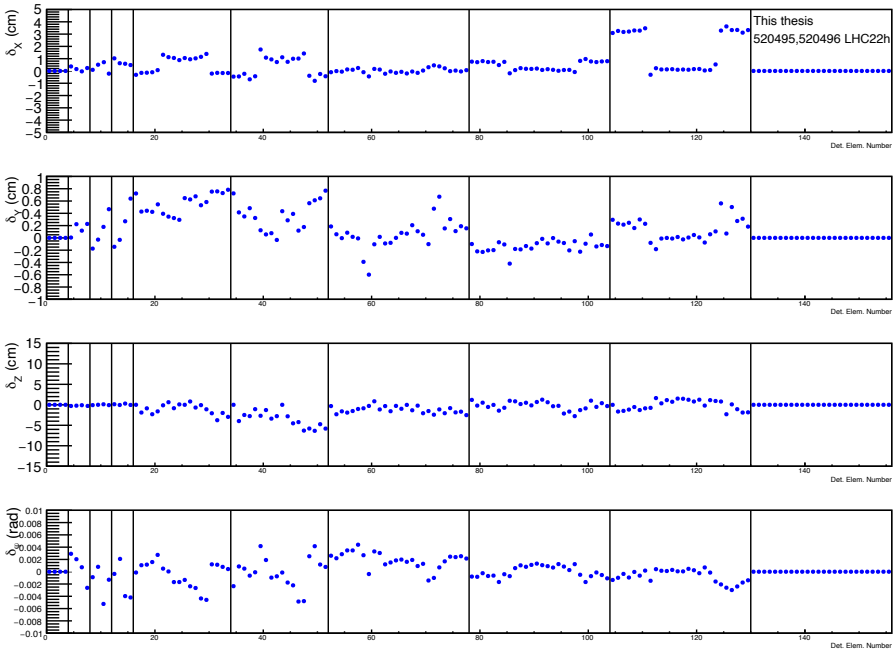

Figure 3.10: The alignment parameters (δ_x, δ_y, δ_z in cm and δ_ϕ in radian) as a function of detection element number for run 520495 and 520496 of LHC22h.

B-on alignment Three dataset periods from pp runs (LHC22m, LHC22o and LHC22t) were tested each one with one run. A quick summary of the dataset information is given below. During the data-taking there was a Technical Stop (TS) (from the 12th to 16th September 2022) where the detector experts had to access the stations of the Muon Spectrometer, thus the datasets will be labeled as pre- or post-TS; the corresponding polarity of the dipole and solenoid fields will be indicated as well:

- Pre-TS: LHC22m(--), runs: 523183(0800), 523792(1830), 5238978(0730)
- Post-TS:
  - LHC22o(++), runs: 528094(2110), 528105(2240)
  - LHC22t(++), runs: 529691(0230,0250)

Below I will highlight in details the alignment with LHC22t post-TS period, while quickly going through the pre-TS alignment. The alignment of pre-TS period was done using the aligned geometry from B-off data, the new aligned geometry was checked with pass 2 data, where the new geometry was used in the reconstruction. Displacements were expected due to the expert intervention during the TS but also because of the transition from B-off to B-on, the latter especially for station 3 (chamber 5 and 6), which is inside the dipole magnet region. For post-TS period, a first attempt was made by fixing chamber 1 and 10, the corresponding alignment parameters are shown in Fig. 3.11

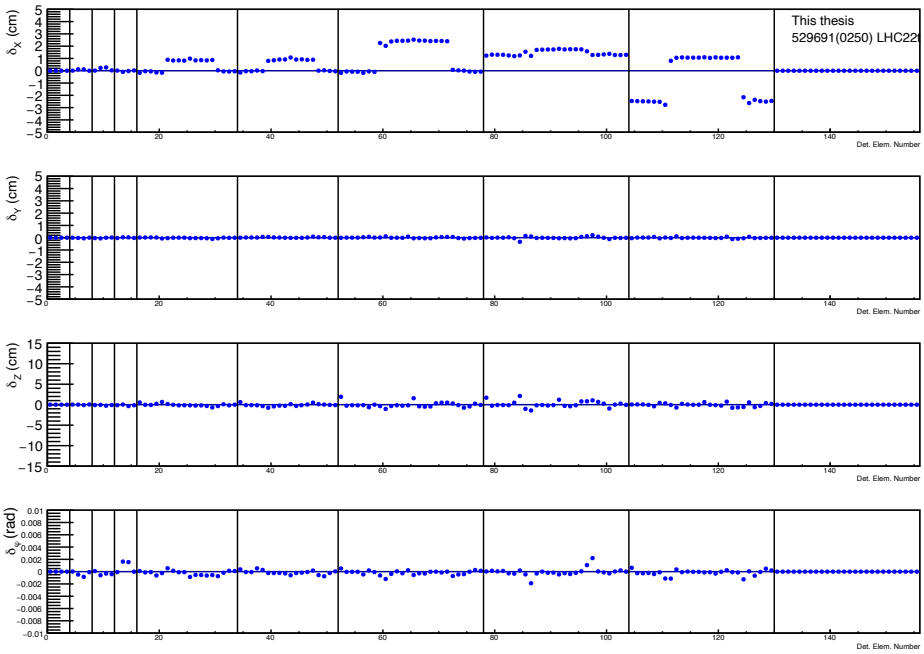

Figure 3.11: The alignment parameters (δ_x, δ_y, δ_z in cm and δ_ϕ in radian) as a function of detection element number with chamber 1 and 10 fixed for run 529691 of LHC22t.

The degrees of freedom other than the displacement in the x direction seem to be under control, while the x direction exhibits significant and regular displacements in chambers from 5 to 9. The displacements could be understood as due to the TS knowing that the these chambers have to be closed horizontally, hence the observed shifts are from the fact that those chambers were not well closed. However, the fact that the chamber 10 (the closest one to MID) did alter the MCH-MID matching performance as illustrated in Fig. 3.12, since the chamber 10 was actually not well closed either. From the Distance of the Closest Approach (DCA) plots one can observe a significant shift between MCH and MID in the x direction, leading to a moderate χ^2 performance for the matching.

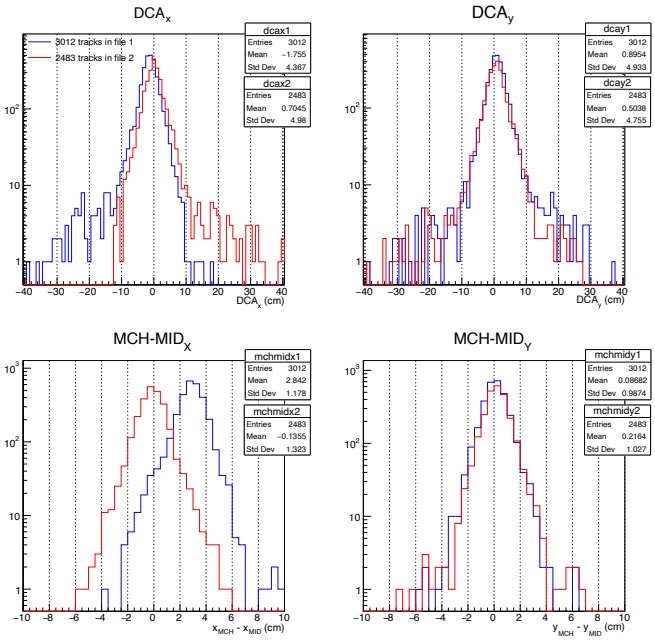

(a) Distance of the Closest Approach (DCA) checks

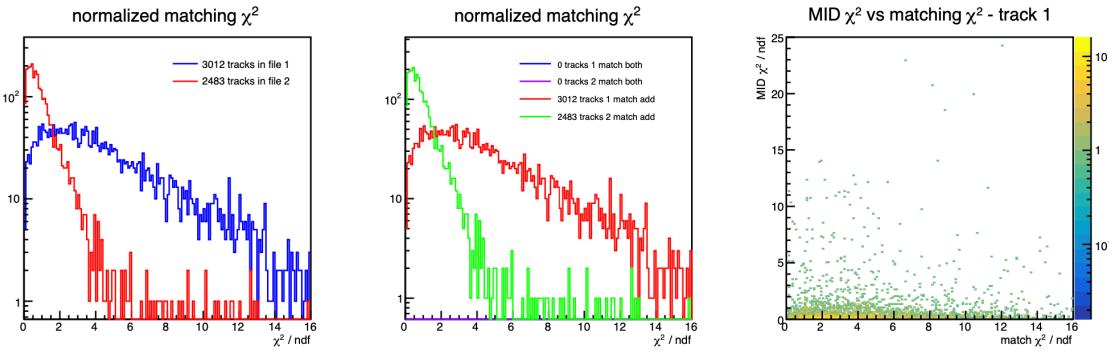

(b) Matching χ^2 checks

Figure 3.12: The quality checks for MCH-MID matching.

For this reason, the alignment was repeated, this time with chambers 1 and 6 fixed

instead of chamber 10. The resulting alignment parameters are presented in Fig. 3.13, where significant and regular displacements in chamber 10 were spotted and corrections in other chambers are rearranged accordingly since they were previously trying to compensate the misalignment in chamber 10.

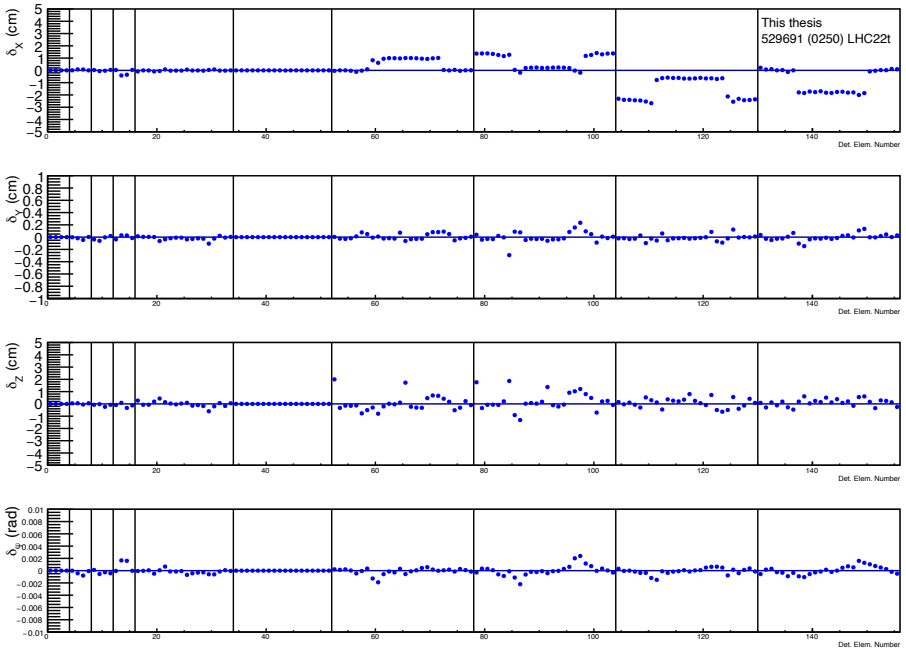

Figure 3.13: The alignment parameters (δ_x, δ_y, δ_z in cm and δ_ϕ in radian) as a function of detection element number with chamber 1 and 6 fixed for run 529691 of LHC22t.

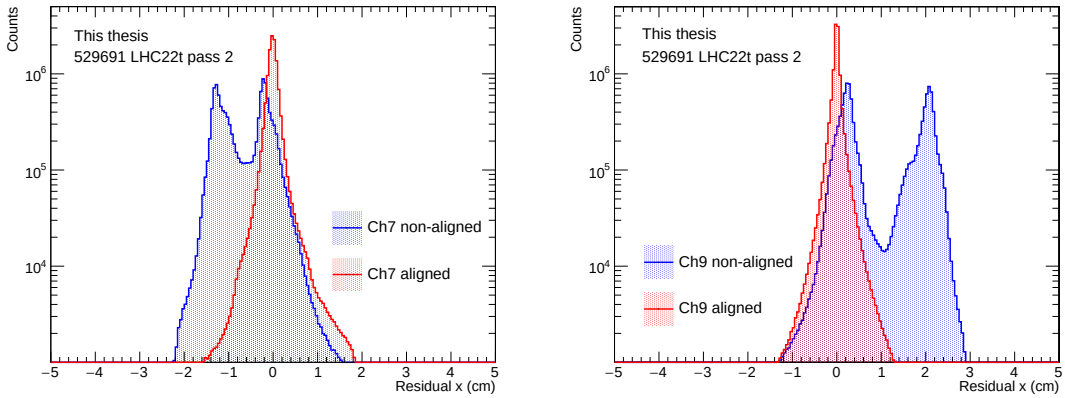

(a) Chamber 7 (b) Chamber 9

Figure 3.14: Comparison of residuals in chamber 7 and 9 along x direction before and after alignment.

The corresponding comparisons of residual before and after alignment along the x direction for chambers which are supposed to undergo significant displacement, are illustrated in Fig. 3.14 for chambers 7 and 9 as examples. The observed two-peak behavior for the residuals before alignment is subject to the problem of not well closed chambers where the two peaks correspond actually to two half-chambers. The symmetry of residual with corrections of geometry from alignment parameters is restored, and the distribution is now centered at zero.

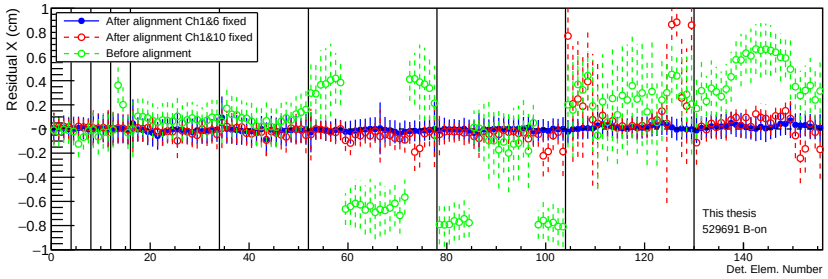

(a) Residual in x (cm)

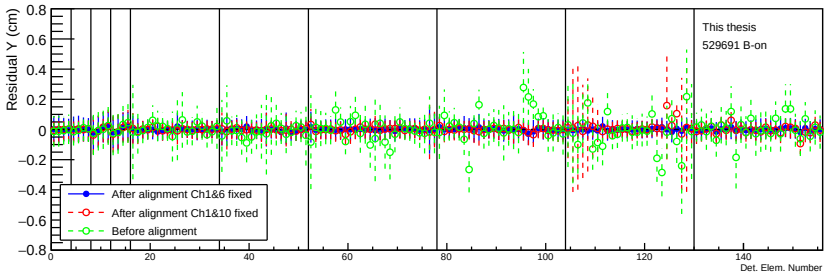

(b) Residual in y (cm)

Figure 3.15: Residuals along x and y for all detection elements with run 529691 of LHC22t for initial values (green), alignment with chamber 1,10 fixed (red) and alignment with chamber 1,6 fixed (blue).

A general comparison between the initial residual (green) and the residuals after alignment with different configurations: chamber 1,10 fixed (red) and chamber 1,6 fixed (blue), is also presented in Fig. 3.15. From where, one can clearly, at the first place in x direction, the new alignment setup with chamber 1,6 fixed managed to recover the misalignment (especially in chamber 9) induced by displacement in chamber 10 that was previously fixed in the alignment; also, in y direction, the fluctuations of residual with chamber 1, 10 fixed are restored by new setup as well as the corresponding resolution of residual.

The J/ψ peak and width were checked using MCH-MID tracks from LHC22o which underwent the same issue as LHC22t, to confirm the improved performance with aligned geometry as illustrated in Fig. 3.16. The Signal-to-Noise Ratio (SNR) of J/ψ peak is significantly improved with the new geometry and in particular the J/ψ width was narrowed

from 190 MeV to 96 MeV.

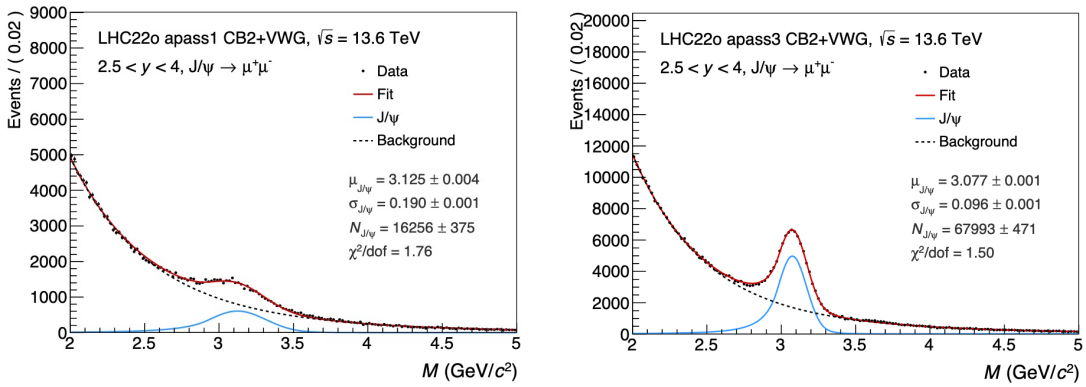

(a) Before alignment (b) After alignment

Figure 3.16: Physics performance check with J/ψ invariant mass fit before and after alignment using LHC22o.

Re-alignment at analysis level In the traditional routine, to see the effect of a new geometry, one needs to either wait for the next construction or require a special reconstruction, then run analysis code in the framework to get physically relevant quantities such as dimuon spectra.

In Run 3, this old paradigm was changed with another huge software improvement which makes the MCH clusters available at analysis level. The latter allows easier physics performance check for alignment tests and switching between different geometries. This is the so-called *re-alignment* process, which is based on the fact that for reconstructions with the same dataset the local coordinates of clusters remain invariant no matter which global geometry was used for local-to-global transformation:

$$\begin{aligned} q_{\mathrm{glo}} &= p \cdot q_{\mathrm{loc}} \\ q^{'}_{\mathrm{glo}} &= p^{'} \cdot q_{\mathrm{loc}} \\ q^{'}_{\mathrm{glo}} &= p^{'} \cdot p^{-1} q_{\mathrm{glo}} \end{aligned} \tag{3.38}$$

where p and $p^{'}$ correspond to global transformations from different geometries, and q_{glo}, $q^{'}_{\mathrm{glo}}$ are the corresponding global coordinates in the representation of the corresponding geometries. The latter operation can be easily done within the analysis framework. Therefore, to check the physics performance related to a new aligned geometry, one only needs to perform the above matrix transformation with MCH clusters.

An example of study of the J/ψ width and peak with different alignment test trials is shown in Fig. 3.17.

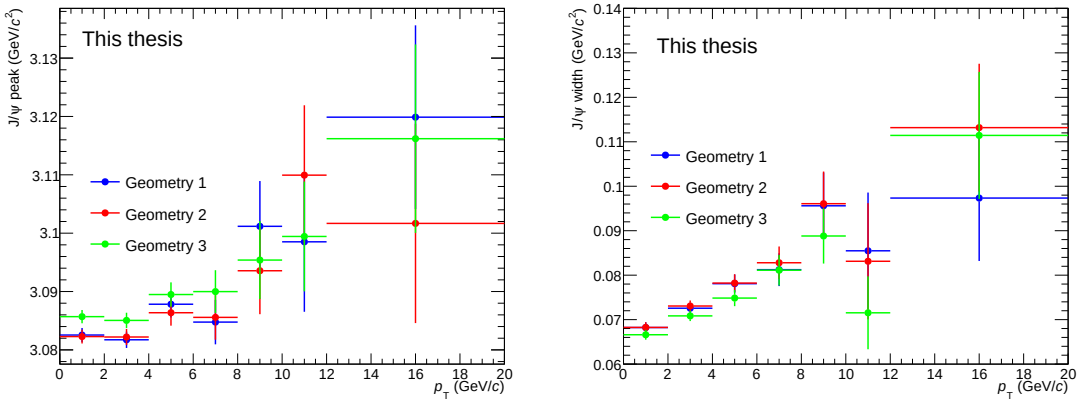

(a) J/ψ peak as a function of p_{T}

(b) J/ψ width as a function of p_{T}

Figure 3.17: Physics performance check using re-alignment at analysis level with three different geometries from alignment test trials.

3.3.4 . Outlook and discussion

To conclude this discussion of detector alignment with ALICE Muon Spectrometer, we have seen in this section through the general idea of track-based detector alignment, the `MillePedeII` algorithm, which was largely optimized compared to the previous version and dedicated to large size systems, then a concrete implementation for the case of ALICE Muon Spectrometer with a detailed discussion about geometry and derivation for local and global derivatives as input for the global linear system after linearization, and finally the commissioning with real data-taking periods and the highlights of big moves for muon alignment in Run 3. Although most of the crucial points have been incorporated in the previous discussions, there is still room for improvement with respect to the current implementation:

- **Global degrees of freedom**: although in the derivation of linearized system for the general situation all possible global degrees of freedom were included, the first attempt of alignment in the commissioning neglected two rotation degrees of freedom, namely yaw and roll. However, we have seen already in the recent regular checks of the residuals that those two rotations may actually contribute to the misalignment, in the current setup, part of their contribution could be compensated by the three active global parameters but in a very limited way. Therefore, in the future, these two rotations have to be implemented as well in the algorithm, and consequently, adding more degrees of freedom means larger phase space, so one might need to consider suitable constraints to control the behavior of global convergence.

- **Track parametrization**: as slightly discussed before in the general setup part, the choice of track parametrization leads directly to different local parameters and derivatives, and in principle, one would expect the track parametric model as close

as possible to the tracking which does not have an analytical closed-form expression and the tracking is highly black-boxed from the viewpoint of `MillePedeII`. The current parametrization, especially in the B-on case, involves a pseudo-local linear approximation, while the choice of the reference point may still be questionable.

- **Physics-tagged alignment**: the alignment performance might be tuned with a specific physics process. In the case of the Muon Spectrometer, the most interesting physics observable involve, to the first order, the J/ψ decay vertex. The latter can be used to tune the alignment using the mass of dimuon as constraints. This technique helps us as well to constrain the eventual weak modes (undefined or weakly defined) such as the Δz, which can only weakly contribute to the transverse local coordinates through its coupling to rotations.

- **Global misalignment and mutual alignment**: in the previous section, a special case where fixing the chamber 10 induced the matching problem between MCH and MID, was discussed. The latter concerns actually the topic of mutual or relative alignment between different detector systems. This requires different treatment, since the aforementioned alignment process applies to a specific detector system and is thus a standalone alignment. Combining different detection system is more complicated because they may use a different tracking algorithm and track representation, have different geometry, could also be separated by some filter like the front absorber between MFT and MCH or the iron filter between MCH and MID. These facts renders nearly impossible to incorporate multiple detector systems into a same compact alignment process or a sort of global minimization problem. Also, the standalone alignment is by definition blind to the global misalignment of the whole detector system (imagine the system as a big rigid box) with respect to interaction point and beam axis, which may significantly affect the performance of quarkonium reconstruction especially in the case of Υ, which are more sensitive to tracking performance. Therefore, the detection of global and mutual misalignment often needs different treatment such as the DCA mentioned in the previous discussion or eventually the method of propagation of tracks from one detector system to another and vice versa. In addition, the track matching (for example, tracks from MFT and MCH) plays a crucial role in prompt- and non-prompt separation of quarkonium production, and the latter usually requires a good relative alignment between the detector systems in question as a premise, especially in Pb–Pb collisions where the much higher number of matching candidates will break the traditional χ^2 matching method.

Chapter 4

Forward J/ψ flow measurement in Pb–Pb collisions at $\sqrt{s_{\mathrm{NN}}} = 5.36\,\mathrm{TeV}$

Contents

In this chapter, the data analysis conducted in this thesis for the inclusive J/ψ flow measurement in the dimuon decay channel at $\sqrt{s_{\mathrm{NN}}} = 5.36\,\mathrm{TeV}$ will be presented, this analysis was done using ALICE Run 3 data collected in 2023. It incorporates three flow analysis methods including the Event-Plane (EP), Scalar Product (SP) and cumulants. It was the first Run 3 quarkonium flow analysis at forward rapidity, with the brand-new software framework. Though the analysis was brought to a preliminary level, it built up a solid flow analysis framework with the full implementation in ALICE Online-Offline (O2), the latter will facilitate all subsequent forward quarkonium flow analyses in the future once the whole Run 3 data-taking is concluded.

4.1 Physics motivation

As probably the most fundamental bound state of charm quarks, J/ψ ($c\bar{c}$) has the privilege of being a suitable hard probe for the QGP medium at LHC energies due to the abundance of charm quark pairs produced from hard partonic scatterings. It has two significant branching ratios into dimuon ($\sim 5.96\%$) and dielectron ($\sim 5.97\%$) decay channels with a lifetime of about $7.2\times10^{-21}\,\mathrm{s}$, which is beyond the time scale of the QGP phase, with a fairly clean signal, even if with large combinatorial backgrounds. This makes J/ψ one of the most convenient hard probes in investigating the QGP properties through its production and in-medium modifications. Especially, its collective behavior in the hot medium, quantitatively characterized by anisotropic flow, encodes the heavy-quark thermalization mechanism. The (partially) thermalized charm quarks can effectively contribute to observed elliptic flow, and the underlying transport properties in the QGP, therefore providing the key ingredients for the dynamic picture of charmonium production in the QGP.

4.2 Methods of flow analysis

Three methods are actually implemented in this analysis including the Event-Plane (EP) method as the easiest baseline, the standard but yet very robust Scalar Product (SP) method, and also the multi-particle correlation based cumulants method. The basic ideas and principles of these methods were loosely discussed in Sec. 1.4.3, here we shall review more in depth some of their defining ingredients for flow observable with some detailed subtleties of their usages in practice.

At the very first place, no matter what kind of method one is addressing, the crucial and even the most important quantity in flow analysis is the so-called *event Q-vector*:

$$Q_n \equiv \sum_{i=1}^{M} w_i(\phi, p_{\mathrm{T}}) \cdot e^{in\phi_i} \tag{4.1}$$

where n is the order of Fourier harmonic and ϕ_i is the particle azimuthal angle. This above definition is a generalized one with associated particle weight w_i which will account for the systematic bias from detector Non-Uniform Acceptance (NUA) and Non-Uniform Efficiency (NUE). The sum is taken within a single event where M stands for the particle multiplicity in this event. As the Q-vector is by definition a complex number, it will also be convenient later to consider its complex components:

$$Q_n = Q_n^x + iQ_n^y \tag{4.2}$$

All flow observables consist of evaluating a certain correlation between an ensemble of reference particles and the target particle or Particle of Interest (POI). In our case, the reference part will be measured in the central barrel region ($|\eta| < 0.8$) using all charged-particles, and the Particle of Interest (POI) will be inclusive J/ψ reconstructed in the Muon

Spectrometer at forward rapidity ($-4.5 < \eta < -2.5$) in the dimuon channel. Following this setup, the nonflow effect arising from the *near-side edge* (small $\Delta\eta$ short range correlations) will be strongly suppressed by this natural gap between the central barrel and muon spectrometer.

All flow analysis methods are to reproduce experimentally the fundamental defining formula for flow coefficient as the angular correlation between the azimuthal angle of particles and the reaction plane:

$$v_2 = \langle \cos(n(\phi - \Psi_n^{\mathrm{RP}})) \rangle \tag{4.3}$$

where Ψ_n^{RP} is the conceptual reaction plane angle that is not directly accessible through experiment, therefore in a sense, all experimentally relevant flow analysis methods are trying to provide a rather proper estimation of the symmetry plane explicitly (EP method) or implicitly (SP and cumulants methods).

4.2.1 . Event-Plane (EP) method

In the approach of Event-Plane (EP) method, the aim is to provide an explicit estimation of the reaction plane using the event-plane from a finite sample of final state particles. The event-plane can be measured using the Q-vector calculated within a specific detector:

$$\Psi_n^{\mathrm{EP}} = \frac{1}{n} \arctan\left(\frac{Q_n^y}{Q_n^x}\right) \tag{4.4}$$

from which the flow coefficient can be evaluated as:

$$v_n^{\mathrm{EP}} = \langle \frac{\cos(n(\phi - \Psi_n^{\mathrm{EP}}))}{R_n^{\mathrm{EP}}} \rangle_{\mu^+\mu^-} \tag{4.5}$$

where ϕ is the azimuthal angle of the POI, in our case muon pairs, Ψ_n^{EP} is the event-plane, R_n^{EP} is the event-plane resolution factor which is usually computed using three-subevent method, and the average is taken over all muon pairs within a given centrality and p_{T} bin. In the initial two-subevent method, the detector is divided into two azimuthally symmetric parts A, B and each of them gives an event-plane estimation. One can follow the calculation below by assuming they both estimate the same true symmetry plane and have equal resolution:

$$\begin{aligned} \mathrm{Re}\{\langle e^{in(\Psi_n^A - \Psi_n^B)} \rangle\} &= \mathrm{Re}\{\langle e^{in(\Psi_n^A - \Psi_n^{\mathrm{RP}})} e^{-in(\Psi_n^B - \Psi_n^{\mathrm{RP}})} \rangle\} \\ &= \langle \cos[n(\Psi_n^A - \Psi_n^B)] \rangle = (R_n^{\mathrm{EP}})^2 \end{aligned} \tag{4.6}$$

In this approach, it is often hard to avoid short-range correlations (without sufficient gap in phase space) that will bias the estimation and the two subevents within a same detector may not have equal resolution. To overcome these limitations, a more robust method using three independent subevents is usually favored in two-particle correlation

based method including Event-Plane (EP) and Scalar Product (SP) methods. Using three subevents, we can calculate the mixed products of resolution in different events following:

$$\begin{aligned}\langle\cos[n(\Psi_n^A-\Psi_n^B)]\rangle &= R_n^A\,R_n^B,\\ \langle\cos[n(\Psi_n^B-\Psi_n^C)]\rangle &= R_n^B\,R_n^C,\\ \langle\cos[n(\Psi_n^C-\Psi_n^A)]\rangle &= R_n^C\,R_n^A.\end{aligned} \tag{4.7}$$

from where one can solve for each subevent resolution, in particular:

$$R_n^A=\sqrt{\frac{\langle\cos[n(\Psi_n^A-\Psi_n^B)]\rangle\langle\cos[n(\Psi_n^A-\Psi_n^C)]\rangle}{\langle\cos[n(\Psi_n^B-\Psi_n^C)]\rangle}} \tag{4.8}$$

Following this approach, the independence of subevents can be ensured using different detectors, like in the case of our analysis where the tracks from ITS+TPC, and the particle multiplicities measured in FT0A and FT0C (A and C side of Fast Interaction Trigger (FIT), see Sec.2.2.1) are used as independent subdetector systems.

In the following discussion, we shall follow the convention for the definition of three subevents: A: ITS+TPC matched tracks, B: multiplicities from FT0A, C: multiplicities from FT0C.

4.2.2 . Scalar Product (SP) method

Since one of the original reasons to use Event-Plane (EP) method was to access the event-plane estimation as an important quantity to study the initial geometry, a mathematically equivalent alternative called Scalar Product (SP) method using directly Q-vectors without going through the event-plane reconstruction was introduced as well in our analysis:

$$v_n^{\rm SP}=\langle\frac{u_nQ_n^{A*}}{R_n^{\rm SP}}\rangle_{\mu^+\mu^-}, \tag{4.9}$$

where u_n is the unit vector of POI in the transverse plane, and $R_n^{\rm SP}$ is the resolution factor, which follows using *three-subevent method*:

$$R_n^{\rm SP}=\sqrt{\frac{\langle Q_n^BQ_n^{A*}\rangle\langle Q_n^AQ_n^{C*}\rangle}{\langle Q_n^BQ_n^{C*}\rangle}}. \tag{4.10}$$

The consistency of this expression can be easyly checked by considering the simple case of constant Q-vectors, say $Q_n^A=a$, $Q_n^B=b$ and $Q_n^C=c$, hence the flow coefficient reads:

$$v_2=\langle\frac{u_na^*}{R_n}\rangle=\langle\frac{u_na^*}{\sqrt{\frac{ba^*\,ac^*}{bc^*}}}\rangle=\langle\frac{u_na^*}{|a|}\rangle. \tag{4.11}$$

Taking the real part results in the same correlation formula than in the initial definition, therefore, up to the normalization of Q-vectors, EP and SP methods are mathematically equivalent if the subevents are defined in the same way and resolution is evaluated with

the same centrality binning.

Finally, the remaining question is when to take the real part in SP method, as the above formulae are using complex numbers, while flow coefficients have to be taken as real numbers at the end. In this analysis, the following convention is applied:

$$v_n^{\mathrm{SP}} = \langle \frac{\mathrm{Re}\{u_n Q_n^{A*}\}}{R_n^{\mathrm{SP}}} \rangle_{\mu^+\mu^-} \tag{4.12}$$

, and the resolution factor will read:

$$R_n^{\mathrm{SP}} = \sqrt{\frac{\mathrm{Re}\{\langle Q_n^B Q_n^{A*}\rangle\}\mathrm{Re}\{\langle Q_n^A Q_n^{C*}\rangle\}}{\mathrm{Re}\{\langle Q_n^B Q_n^{C*}\rangle\}}}. \tag{4.13}$$

Though it might be better to take the real part after the square root to avoid a global internal rotation effect, which can be compensated as a global factor in complex calculations.

4.2.3 . Cumulants method

Similar to the SP method, the cumulant method does not rely on an explicit derivation of an estimation for the reaction plane but rather implicitly from multi-particle correlations. The general idea was developed based on the cumulant expansion of Moment Generating Function (MGF) where the connection to Lee-Yang Zero (LYZ) method was mentioned in Sec. 1.4.3. In this section, we shall go through the essentials of the foundation of cumulant method through a slightly different formalism of MGF

Cumulants from Moment Generating Function (MGF)

Consider the *two-component* (symmetrized) complex Moment Generating Function (MGF):

$$G_n(z) = \left\langle \prod_{j=1}^{M} \left(1 + \frac{z}{M} e^{in\phi_j}\right)\left(1 + \frac{z^*}{M} e^{-in\phi_j}\right) \right\rangle \tag{4.14}$$

where z is a complex variable, $z*$ its complex conjugate and $\langle\cdot\rangle$ denotes the average over all events, which implies an integral over all reaction plane angles uniformly distributed on $(0, 2\pi]$ [1]. Taking the expansion of the MGF results in:

$$G_n(z) = \sum_{i=1}^{\infty} (\frac{z}{M})^i (\frac{z^*}{M})^i \mu_{2i} \tag{4.15}$$

where $\mu_{2i} = \frac{\partial^{2i} G_n(z,z^*)}{\partial z^i \partial z^{*i}}|_{z=0} = \langle\langle 2i\rangle\rangle$, and this coefficient can be used to connect the raw correlation functions: for example in the case of 2-particle correlation

$$\sum_{i\neq j}^{M} e^{in(\phi_i - \phi_j)} = |Q_n|^2 - M = M(M-1)\langle \sum_{i\neq j}^{M} e^{in(\phi_i-\phi_j)}\rangle = M(M-1)\langle 2\rangle. \tag{4.16}$$

[1] There should be no privileged azimuthal direction in the detector

The advantages of using a two-component complex form rather than one-component form are:

- Making the generating function real $G(z) = G^*(z)$
- Preserving the rotational invariance with respect to the reaction plane since angular correlation accounts only for the relative pattern instead of their absolute angular magnitudes. This can be understood from: $u_{l+k} = \frac{\partial^{l+k} G_n(z,z^*)}{\partial z^l \partial z^{*k}}|_{z=0} = \langle (Q_n)^l (Q_n^*)^k \rangle$. The average converts into integral over all possible global rotations from 0 to 2π, therefore $\langle (Q_n)^l (Q_n^*)^k \rangle \propto \int_0^{2\pi} e^{in(l-k)\alpha} d\alpha = 2\pi\delta_{l,k}$.

In analogy to the partition function in statistical mechanics, one can take the logarithm for the MGF and once again expand around o. The latter is the so-called *cumulant expansion* of Moment Generating Function (MGF):

$$\ln(G_n(z)) = \sum_{k=1}^{\infty} \frac{1}{k!} c_n\{k\} z^k \tag{4.17}$$

and similarly $c_{2k} = \frac{\partial^{2k}}{\partial z^k \partial z^{*k}} \ln G_n(z)|_{z=0}$, these coefficients are called *cumulants*. The moment-cumulant relations read:

$$\begin{aligned} c_n\{2\} &= \langle\langle 2 \rangle\rangle, \\ c_n\{4\} &= \langle\langle 4 \rangle\rangle - 2\langle\langle 2 \rangle\rangle^2, \\ &\cdots \end{aligned} \tag{4.18}$$

Taking the large-M and no-fluctuation limit for the two-component generating function yields the flow-cumulant relations:

$$\begin{aligned} v_n\{2\}^2 &= c_n\{2\}, \\ v_n\{4\}^4 &= -c_n\{4\}. \end{aligned} \tag{4.19}$$

As an important property of cumulants, a cumulant coefficient at a given order can be explicitly represented only by lower moments [256], this is known as the *Kubo-Meeron closed-form* for cumulants. From the latter, one can actually turn the tedious cumulant calculations into recurrent relations that can be fairly easy to implement as an iterative algorithm [257].

Event-by-event flow fluctuations

However, in practice, the event-by-event flow fluctuations may be present from initial geometry fluctuations, finite particle sampling, etc. This can be accounted by expanding the flow magnitude with mean and small variance $\sigma_n^2 = \langle v_n^2 \rangle - \bar{v}_n^2, \sigma_n \ll \bar{v}_n$. Since each moment can read for large-M limit: $u_{2n} = \langle v_{2n}^2 \rangle$, therefore one can use flow-cumulant relations from Eq. 4.19:

$$\begin{aligned} v_n\{2\}^2 &\approx \bar{v}_n^2 + \sigma_n^2, \\ v_n\{4\}^2 &\approx \bar{v}_n^2 - \sigma_n^2. \end{aligned} \tag{4.20}$$

From which the fluctuation ratio can be defined as:

$$\frac{\sigma}{\langle v \rangle} = \sqrt{\frac{v_n\{2\}^2 - v_n\{4\}^2}{v_n\{2\}^2 + v_n\{4\}^2}}. \tag{4.21}$$

Flow of Particle of Interest (POI)

For the case of flow analyses for a specific particle species, we usually divide the calculation in two components: the flow of Reference Particle (RFP) and the flow of Particle of Interest (POI). In this analysis, the RFPs are taken as charged-particles from central barrel detectors, and the POIs will be inclusive J/ψ at forward rapidity. This setup makes no overlap between RFP and POI, making the implementation much easier. The full calculation of the correlators and cumulants with weighted Q-vectors are shown in Appendix. B.

In this case, the correlation functions for POI are defined by:

$$\begin{aligned} \langle 2^{'} \rangle &= \langle e^{in(\psi_i - \phi_j)} \rangle, \\ \langle 4^{'} \rangle &= \langle e^{in(\psi_i + \phi_j - \phi_k - \phi_l)} \rangle. \end{aligned} \tag{4.22}$$

For RFP, the so-called reference flow can be evaluated following the flow-cumulant relations:

$$\begin{aligned} v_n\{2\} &= \sqrt{c_n\{2\}}, \\ v_n\{4\} &= \sqrt[4]{-c_n\{4\}}. \end{aligned} \tag{4.23}$$

For POI, their 2nd- and 4th-order cumulants read:

$$\begin{aligned} d_n\{2\} &= \langle\langle 2^{'} \rangle\rangle, \\ d_n\{4\} &= \langle\langle 4^{'} \rangle\rangle - 2\langle\langle 2^{'} \rangle\rangle\langle\langle 2 \rangle\rangle. \end{aligned} \tag{4.24}$$

From which, the corresponding flow coefficients can be evaluated as:

$$\begin{aligned} v_n^{'}\{2\} &= \frac{d_n\{2\}}{\sqrt{c_n\{2\}}}, \\ v_n^{'}\{4\} &= \frac{d_n\{4\}}{(-c_n\{4\})^{3/4}}. \end{aligned} \tag{4.25}$$

From average over events to average over dimuons

In the actual reconstruction chain of the ALICE computing framework, charged-particle (RFP) and dimuon (POI) information are actually available at different levels of the data processing. Since the memory consumption of barrel tracks is huge, a multi-level skimming process is hence strategically necessary. More importantly, performing a first average within a single event followed by a second one over all events seems technically not doable in the current analysis framework. The limitations come from the aforementioned memory consumption, the architecture of the framework, and also from the flow

analysis strategy which relies on the flow of dimuons as a function of their invariant mass. This means, in turn, that the J/ψ mesons are not one-by-one identified as POI in the formulae but rather extracted statistically from dimuon spectra (see Sec. 4.5.1). From these considerations, it is much more convenient to follow a different strategy of average over dimuons instead of events. The symbols used in the following derivation follow the same as in Appendix. B.

For flow of POI The weighted average 2-particle correlations for POI become:

$$\begin{aligned}
\langle\langle 2' \rangle\rangle &= \frac{\sum_{i=1}^{N} (\mathcal{M}'_{01})_i \langle 2' \rangle_i^{evt}}{\sum_{i=1}^{N} (\mathcal{M}'_{01})_i} \\
&= \frac{\sum_{i=1}^{N} p_{n,0}^i (Q_{n,1}^*)_i}{\sum_{i=1}^{N} m_p^i (S_{1,1})_i}, \\
&= \frac{\sum_{i=1}^{N} \sum_{j=1}^{m_p^i} e^{jn\psi_j} (Q_{n,1}^*)_i}{\sum_{i=1}^{N} \sum_{j=1}^{m_p^i} (S_{1,1})_i}, \\
&= \frac{\sum_{i=1}^{Dimuons} e^{in\psi_i} (Q_{n,1}^*)_i}{\sum_{i=1}^{Dimuons} (S_{1,1})_i}, \\
&= \frac{\sum_{i=1}^{Dimuons} (\frac{\mathcal{M}'_{01}}{m_p})_i \{\langle 2' \rangle^{dimuon} \cdot m_p\}_i}{\sum_{i=1}^{Dimuons} (\frac{\mathcal{M}'_{01}}{m_p})_i}.
\end{aligned} \tag{4.26}$$

Following this, one can actually convert a weighted average over events on a weighted average over dimuons, with $(S_{1,1})_i$ being the new weight for each dimuon and $\{e^{in\psi_i}(\frac{Q_{n,1}^*}{S_{1,1}})_i\}$ the exact quantity being summed. This allows us to use directly `ROOT TProfile` for error propagation during post-processing.

Similarly, the weighted average 4-particle correlations for POI become:

$$\begin{aligned}
\langle\langle 4' \rangle\rangle &= \frac{\sum_{i=1}^{N} (\mathcal{M}'_{0111})_i \langle 4' \rangle_i^{evt}}{\sum_{i=1}^{N} (\mathcal{M}'_{0111})_i} \\
&= \frac{\sum_{i=1}^{N} \{p_{n,0}^i \left[Q_{n,1} Q_{n,1}^* Q_{n,1}^* - Q_{n,1} Q_{2n,21}^* - 2 \cdot S_{1,2} Q_{n,1}^* + 2 \cdot Q_{n,3}^*\right]_i\}}{\sum_{i=1}^{N} m_p^i \left[S_{3,1} - 3 \cdot S_{1,1} S_{1,2} + 2 \cdot S_{1,3}\right]_i}, \\
&= \frac{\sum_{i=1}^{N} \sum_{j=1}^{m_p^i} e^{jn\psi_j} \left[Q_{n,1} Q_{n,1}^* Q_{n,1}^* - Q_{n,1} Q_{2n,21}^* - 2 \cdot S_{1,2} Q_{n,1}^* + 2 \cdot Q_{n,3}^*\right]_i}{\sum_{i=1}^{N} \sum_{j=1}^{m_p^i} \left[S_{3,1} - 3 \cdot S_{1,1} S_{1,2} + 2 \cdot S_{1,3}\right]_i}, \\
&= \frac{\sum_{i=1}^{Dimuons} (\frac{\mathcal{M}'_{0111}}{m_p})_i \{\langle 4' \rangle^{dimuon} \cdot m_p\}_i}{\sum_{i=1}^{Dimuons} (\frac{\mathcal{M}'_{0111}}{m_p})_i}.
\end{aligned} \tag{4.27}$$

For reference flow Following the same approach, correlations and weights for reference flow should be also gathered per dimuon.

The weighted average 2-particle correlations for RFP become:

$$\begin{aligned}\langle\langle 2\rangle\rangle &= \frac{\sum_{i=1}^{N}(\mathcal{M}_{11})_i\langle 2\rangle_i}{\sum_{i=1}^{N}(\mathcal{M}_{11})_i}, \\ &= \frac{\sum_{i=1}^{N}\sum_{j=1}^{m_p^i}\frac{1}{m_p^i}(\mathcal{M}_{11})_i\langle 2\rangle_i}{\sum_{i=1}^{N}\sum_{j=1}^{m_p^i}\frac{1}{m_p^i}(\mathcal{M}_{11})_i}, \\ &= \frac{\sum_{i=1}^{Dimuons}\frac{1}{m_p^i}(\mathcal{M}_{11})_i\langle 2\rangle_i}{\sum_{i=1}^{Dimuons}\frac{1}{m_p^i}(\mathcal{M}_{11})_i}.\end{aligned} \tag{4.28}$$

Similarly, the weighted average 4-particle correlations for RFP become:

$$\begin{aligned}\langle\langle 4\rangle\rangle &= \frac{\sum_{i=1}^{N}(\mathcal{M}_{1111})_i\langle 4\rangle_i}{\sum_{i=1}^{N}(\mathcal{M}_{1111})_i}, \\ &= \frac{\sum_{i=1}^{N}\sum_{j=1}^{m_p^i}\frac{1}{m_p^i}(\mathcal{M}_{1111})_i\langle 4\rangle_i}{\sum_{i=1}^{N}\sum_{j=1}^{m_p^i}\frac{1}{m_p^i}(\mathcal{M}_{1111})_i}, \\ &= \frac{\sum_{i=1}^{Dimuons}\frac{1}{m_p^i}(\mathcal{M}_{1111})_i\langle 4\rangle_i}{\sum_{i=1}^{Dimuons}\frac{1}{m_p^i}(\mathcal{M}_{1111})_i}.\end{aligned} \tag{4.29}$$

4.3 Event, track and muon selections

In this section, we shall review the general setup of data preparation for the analysis. The following discussion includes a review of data sample used in this analysis, then the criteria for event, track, muon and dimuon selections.

4.3.1 . Data sample

The Pb–Pb data sample used in this analysis was collected in 2023 at $\sqrt{s_{\rm NN}} = 5.36\,\text{TeV}$ including 9 periods (continuous block of stable LHC running with basically the same accelerator configuration, detector configuration, and similar conditions) with 90 good runs (individual continuous data-taking block inside a period) in total. The corresponding performance check of recorded integrated luminosity for 2023 and 2024 Pb–Pb data-taking is illustrated in Fig. 4.1.

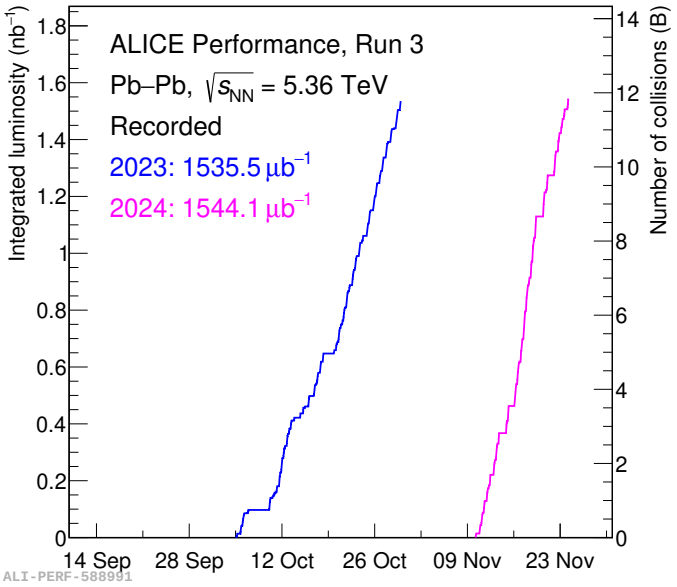

Figure 4.1: The ALICE performance check for integrated luminosity recorded for 2023 and 2024 Pb–Pb data-taking.

The list of good runs (see Appendix. C) was provided by central Quality Control (QC) with `CBT_muon` criteria including the standard muon (MCH,MID) checks plus crucial component checks in central barrel (ITS, TPC and FITs). The latest reconstruction of pass 4 was adopted, which includes as well the latest version of Q-vector correction, NUA weights for cumulants and improved centrality determination using FT0C. In Run 3, the data flow follows a skimming process in order to reduce the largely increased data storage demands in the new continuous data-taking mode. The data went first through a central skimming process based on loose and basic event selections to remove the most obvious unnecessary data, then a subsequent streaming procedure at analysis level, based on detailed event and track selection criteria that might be highly analysis-specific, was performed as

well. The resulting skimmed data reduces to $7.1\ \mathrm{TB}$ from the original size of $2.3\ \mathrm{PB}$ (a reduction factor ~ 324).

4.3.2 . Event selections

Events are selected based on the flag `eventStandardSel8PbPbQuality` consisting of the following cuts:

- `kIsSel8`: enabling event selection decision based on FIT vertex.
- `kVtxZ`: selecting events with vertex position $|\mathrm{Vtx}_z| < 10\,\mathrm{cm}$ with respect to the nominal vertex position as shown in Fig. 4.2.
- `kIsTriggerTVX`: detecting whether the event has FIT triggered vertex.
- `kIsNoTFBorder`: checking whether the BC is far from the TF border.
- `kIsNoITSROFBorder`: checking whether the the BC is far from the start and end of the ITS ROF border.
- `kIsNoSameBunch`: ensuring one single collision within the same BC
- `kIsGoodZvtxFT0vsPV`: filtering out the event with $\left|\mathrm{Vtx}_z^{\mathrm{PV}} - \mathrm{Vtx}_z^{\mathrm{FT0}}\right| > 1\,\mathrm{cm}$

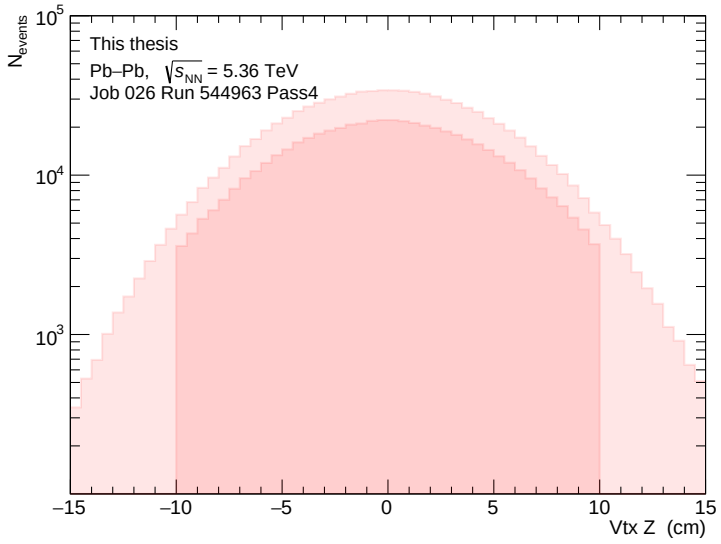

Figure 4.2: The vertex ($\mathrm{Vtx_z}$) distribution before and after cut with run 544963(026) from pass 4.

Centrality determination

In order to study Pb–Pb collisions, where the initial collision geometry is extremely important, it is necessary to classify the collisions in terms of the overlap region between the two colliding nuclei. The latter is characterized geometrically by the impact-parameter, however as we have already discussed in Sec. 1.3.1, this quantity is not experimentally accessible. In ALICE, the centrality is estimated as percentages of the total hadronic cross-section using charged-particle multiplicity measured in a forward or backward pseudorapidity region that is fairly far from midrapidity detector systems to avoid autocorrelations.

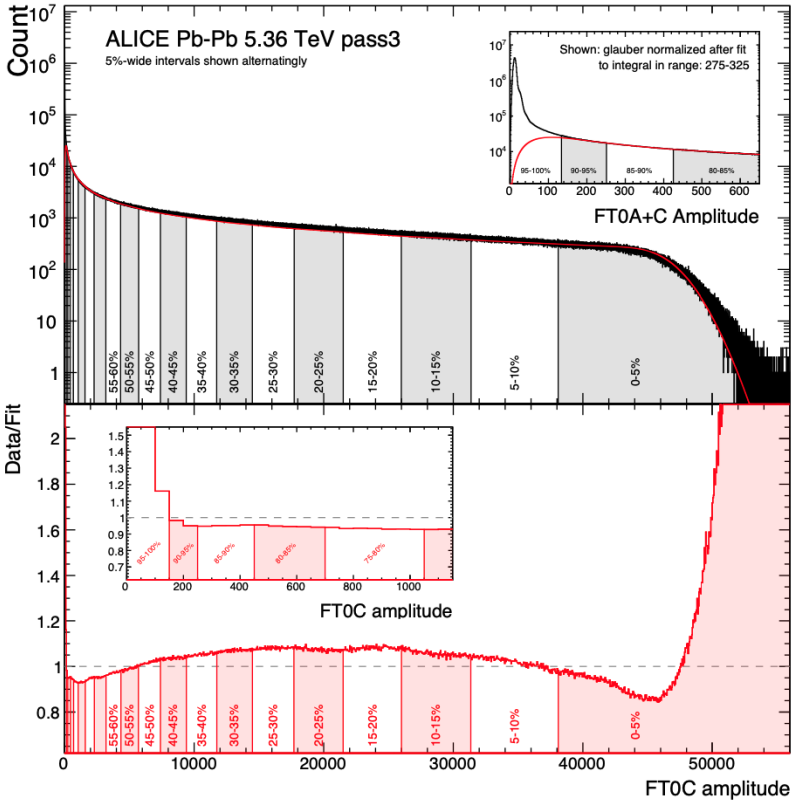

Figure 4.3: "Glauber+NBD" fit to the FT0C amplitude distribution using run 544122 of pass 3 calculated with the BC table approach together with the fit to data ratio showing on the bottom.

At low multiplicity, the electromagnetic processes have strong contributions, while the high multiplicity part will be dominated by hadronic events. In the old approach, the low multiplicity electromagnetic contribution could not be captured, leading to a limited centrality range from 0 to 80%. In Run 3, from pass 3 onward, a new approach was deployed using "Glauber+Negative Binominal Distribution (NBD)" fit, which is able to handle the low multiplicity electromagnetic effect, hence the centrality estimation can be in principle extended to 100 %. An example of new fit approach using data from run 544122 of pass 3

is shown in Fig. 4.3, as well as an example of centrality distribution before and after event cuts with FT0C using run 544963 of pass 4 in Fig. 4.4.

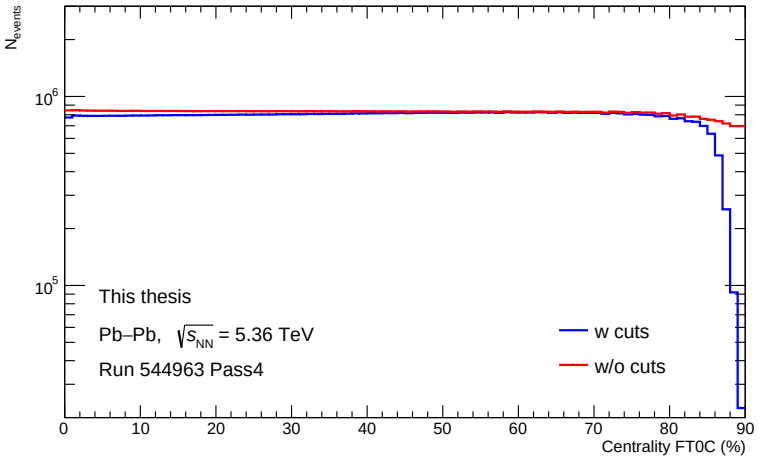

Figure 4.4: The distribution of centrality before and after event cuts using FT0C with run 544963 of pass 4.

4.3.3 . Track selections

The charged-particle tracks from the central barrel for Q-vector construction are selected based on the following criteria:

- Pseudorapidity selection: $|\eta| < 0.8$
- Global track: ITS+TPC matched
- $0.15 < p_{\mathrm{T}} < 3\,\mathrm{GeV}/c$
- Global track standard quality checks:
  - `passedITSNCls` (check for number of ITS clusters)
  - `passedITSHits` (check for required number of hits in ITS layers)
  - `passedITSChi2NDF` (check for χ^2/ndf of ITS track)
  - `passedTPCChi2NDF` (check for χ^2/ndf of TPC track)
  - `passedTPCCrossedRowsOverNCls` (for for minimum number of crossed rows over findable TPC clusters)
  - `passedDCAxy` and `passedDCAz` (check for track DCA)

4.3.4 . Muon and dimuon selections

To ensure good muon track quality for both flow correlation and J/ψ reconstruction, several cuts are applied to single muon and dimuon with the resulting comparison before and after cuts shown in Fig. 4.5:

- Single muon selections:
  - MCH-MID matched tracks
  - Pseudorapidity range $-4 < \eta < -2.5$
  - The transverse radius of the muon track at the end of the front absorber $17.6 < R_{\mathrm{abs}} < 89.5\,\mathrm{cm}$ ($2^{\circ} < \theta_{\mathrm{abs}} < 10^{\circ}$) in order to remove the muons crossing the high-z material part of the absorber, where multiple Coulomb scattering occurs.
  - $p\mathrm{DCA} < 6\sigma$, where $p\mathrm{DCA}$ defined by $|p|$ times Distance of the Closest Approach (DCA), to avoid background contribution from beam-gas interactions.
  - Single muon p_{T} , which is crucially important to remove combinatorial background from low-momentum muons in the dimuon spectrum. In Run 2 the muon system had a non-sharp p_{T} triggering around $0.5\,\mathrm{GeV}/c$, while in Run 3 there is no trigger system, the choice of low-p_{T} cut left as a "free" parameter to be tuned regarding dimuon spectrum and event-mixing. In this analysis, a low-p_{T} cut of $0.7\,\mathrm{GeV}/c$ is applied as an optimal value, important arguments related to signal extraction and event-mixing will be discussed in the following section.
- Dimuon selections for quarkonium reconstruction:
  - Opposite signs of charge are required.
  - The reconstructed dimuon should be also in the rapidity range $2.5 < y < 4$.

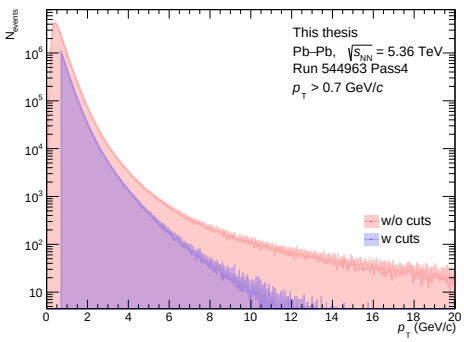

(a) Single muon p_{T}

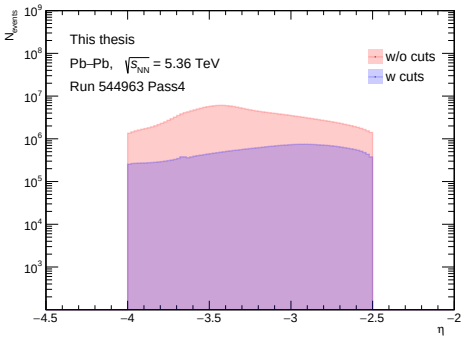

(b) η

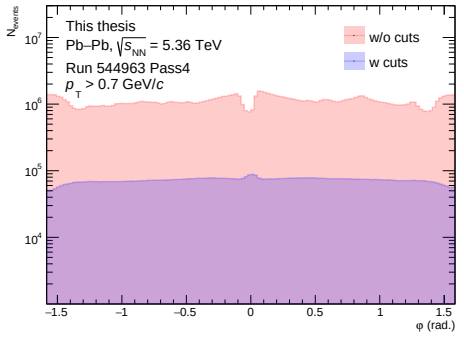

(c) ϕ

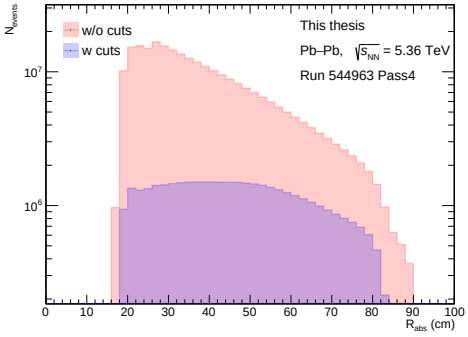

(d) R_{abs}

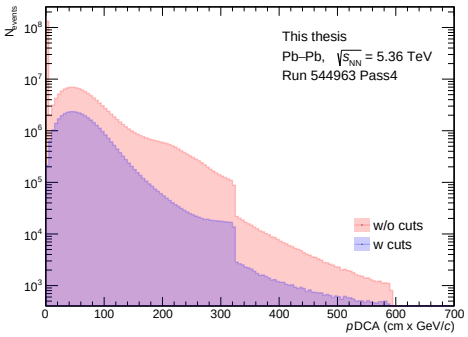

(e) $p\mathrm{DCA}$

Figure 4.5: Comparison of muon kinematic information before and after cuts using run 544963 of pass 4.

4.4 Calibration for flow analysis

In this section, we shall review the major calibration steps one must take in order to perform the flow analysis under suitable conditions. For EP and SP method, they follow the same calibration procedures regarding the systematic checks for symmetry (event) planes, Q-vector calibrations and also resolution embedded in the average with fine centrality bins to account for its variation as a function of centrality gathering different event classes. For cumulants, as it does not require by construction an explicit calibration for symmetry planes and Q-vectors, one only needs to take care of the Q-vector weights encoding the Non-Uniform Acceptance (NUA) and Non-Uniform Efficiency (NUE) corrections.

4.4.1 . Q-vector calibration and symmetry planes

Since the reaction plane distribution over collision events is expected to be azimuthally isotropic in the absence of polarization, then no special direction in the plane of impact parameter should be privileged a priori. However, in practice, the performance of the detector suffers from inefficiencies, thus triggering non-uniformity and modulation in the event-plane distribution. The latter will strongly bias the correlation measurement with unexpected contribution from detector defects. The event-plane determination relies directly on Q-vectors, and the detector defects reflect directly on the form of Q-vector distribution in their (x,y) components. Therefore, Q-vector calibration for detector non-uniformity is considered as a crucial step for flow analyses using SP and EP methods. Moreover, since the resolution for both cases will be evaluated using three-subevents including TPC, FT0A and FT0C, then the calibration process should be done for all three detectors.

In ALICE Run 3, the Q-vector calibration is centralized by the Analysis Objects and Tools (AOT) team from ALICE Data Preparation Group (DPG). In the following discussion, we shall review the main steps for Q-vector calibration introduced in [258] together with some practical details in AOT's implementation.

In the setup of centralized Q-vector calibration framework, events are selected using `Sel8` + `kIsGoodZvtxFT0vsPV` + `kNoSameBunchPileup` criteria:

- `Sel8` (`kNoTimeFrameBorder` + `kIsTriggerTVX` + `kNoITSROFrameBorder`): event selection based on the FT0 vertex and whether the Bunch Crossing (BC) is far away from the ReadOut Frame (ROF) border of the ITS and from the Time-Frame (TF) border.
- `kIsGoodZvtxFT0vsPV` selects events with the distance between FT0 vertex and primary vertex smaller than 1 cm:

$$|\mathrm{VtxZ(FT0)} - \mathrm{VtxZ(PV)}| < 1\,\mathrm{cm} \tag{4.30}$$

- `kNoSameBunchPileup` picks events with at most one collision per BC.

The TPC tracks are selected following the ALICE Run 3 standard cuts detailed in the previous section.

Gain equalization

In the conventional calibration procedure, the gain equalization is usually the first step. The idea is to account for the variation of gain across different detector channels because the detector amplitude is used as weight for measuring the number of particles passing through a given detector channel, the latter could therefore be biased due to the variation of gain in different channels. To fix this bias, one needs to reweight the amplitude of each channel by an average amplitude over all channels, the corrected amplitude reads:

$$M^{\text{corrected}} = M_i \times \left(\frac{\langle M \rangle}{\langle M_i \rangle} \right) \tag{4.31}$$

where M_i is the amplitude for a given channel, $\langle M_i \rangle$ is the average of the amplitude of this given channel over selected events in each run, $\langle M \rangle$ is the same average but for all channels. The result of gain equalization for FT0 using data of run 544510 from pass 2 is shown below in Fig. 4.6.

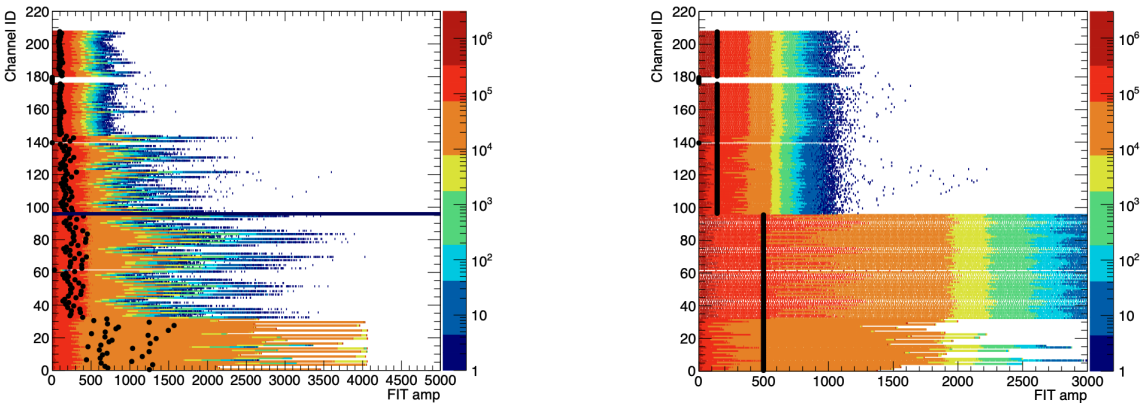

(a) Before gain equalization

(b) After gain equalization

Figure 4.6: Calibration for the gain of FT0 using run 544510 of pass 2.

Q-vector corrections

Recentering The first correction to be done for the shape of Q-vector in the 2D plane is recentering because the event flow vectors should not favor a special direction, which would lead to bias (shift) in calculating the correlation with the POI unitary vector. In the recentering procedure, this shift of origin in event Q-vector distribution can be corrected using its average position along x and y axis respectively:

$$Q'_{n,x} = Q_{n,x} - \langle Q_{n,x} \rangle \tag{4.32}$$

$$Q'_{n,y} = Q_{n,y} - \langle Q_{n,y} \rangle \tag{4.33}$$

Twisting and rescaling To correct the shape of Q-vector distorted by the presence of detector non-uniformity, the procedure of twisting and rescaling is introduced as a conformal transformation by applying to the Q-vector statistical distribution a 2D rotation and a change of scale, parametrized by:

$$b = \rho\,\delta Q_{n,x}\delta Q_{n,y}\sqrt{\frac{2(\delta Q_{n,x}^2 + \delta Q_{n,y}^2 - 2\delta Q_{n,x}\delta Q_{n,y}\sqrt{1-\rho^2})}{((\delta Q_{n,x}^2 - \delta Q_{n,y}^2)^2 + 4(\delta Q_{n,x}\delta Q_{n,y}\rho)^2)}} \tag{4.34}$$

where $\rho = \frac{\mathrm{Cov}(Q_{n,x},Q_{n,y})}{\delta Q_{n,x}\cdot\delta Q_{n,y}}$ and $\delta Q_{n,x}, \delta Q_{n,y}$ are the standard deviations of $Q_{n,x}$ and $Q_{n,y}$, respectively.

The twisting of Q-vectors result in the residual rotation by the reaction plane angle in the 2D Q-vector plane, the latter can be fixed by a diagonalization process:

$$Q''_{n,x} = \frac{(Q'_{n,x} - c_4 Q'_{n,y})}{(1 - c_3 c_4)} \tag{4.35}$$

$$Q''_{n,y} = \frac{(Q'_{n,y} - c_3 Q'_{n,x})}{(1 - c_3 c_4)} \tag{4.36}$$

where c_3, c_4 read:

$$c_{(3,4)} = \frac{b}{\sqrt{2(\delta Q_{n,(x,y)}^2 - b^2)}}. \tag{4.37}$$

Then the rescaling can be done using extra scaling factors,

$$Q'''_{n,x} = \frac{Q''_{n,x}}{c_5} \tag{4.38}$$

$$Q'''_{n,y} = \frac{Q''_{n,y}}{c_6} \tag{4.39}$$

where c_5, c_6 are defined by:

$$c_{(5,6)} = \sqrt{2(\delta Q_{n,(x,y)}^2 - b^2)}. \tag{4.40}$$

The correction steps are separately conducted for eight different centrality classes from 0 to 80%, the whole correction procedure including all steps is performed iteratively and independently for each detector system. The resulting Q-vector ($n = 2$) with TPC tracks in different centrality classes after corrections are presented below in Fig. 4.7.

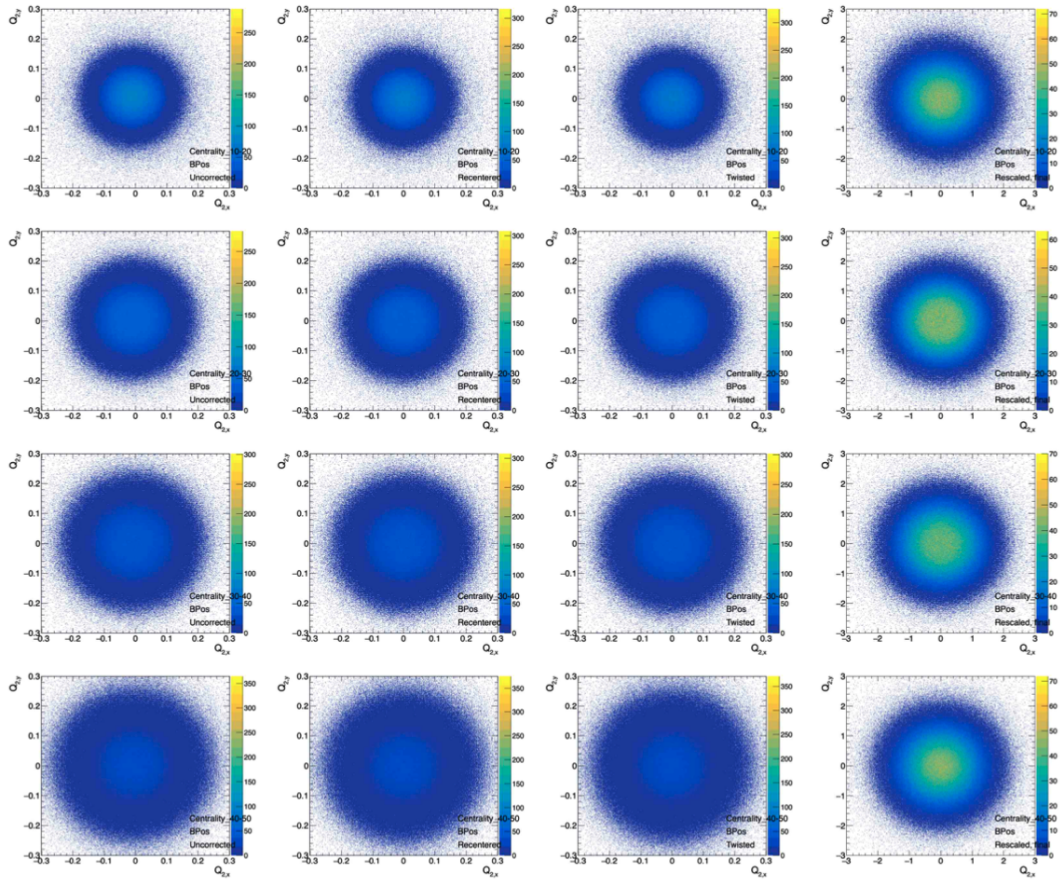

Figure 4.7: Illustration of corrected Q-vectors ($n = 2$) within different centrality classes from forward TPC tracks.

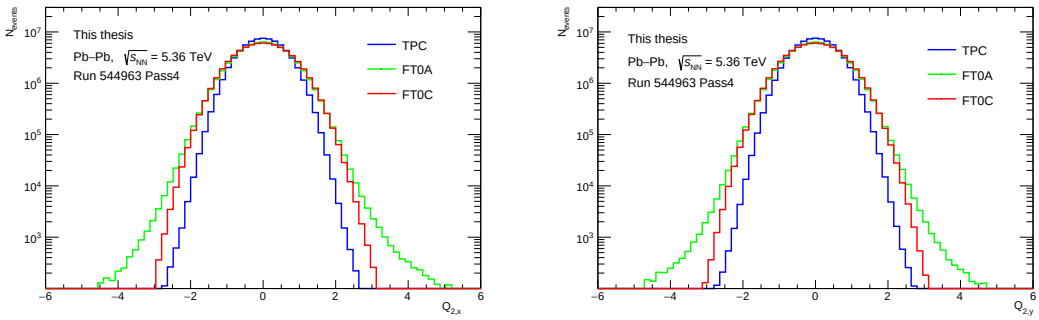

(a) $Q_{2,x}$ (b) $Q_{2,y}$

Figure 4.8: Comparison of centrality-integrated Q-vectors ($n = 2$) from three detectors using run 544963 of pass 4.

The corresponding checks of x,y components for corrected Q-vectors ($n = 2$) from

TPC, FT0A and FT0C as a function of centrality estimated using FT0C are presented below in Fig. 4.9. The distributions of Q-vectors in different detector systems are centered at zero and fairly uniform across the centrality range. The centrality-integrated Q-vector in x,y components for all three detectors are also shown in Fig. 4.8.

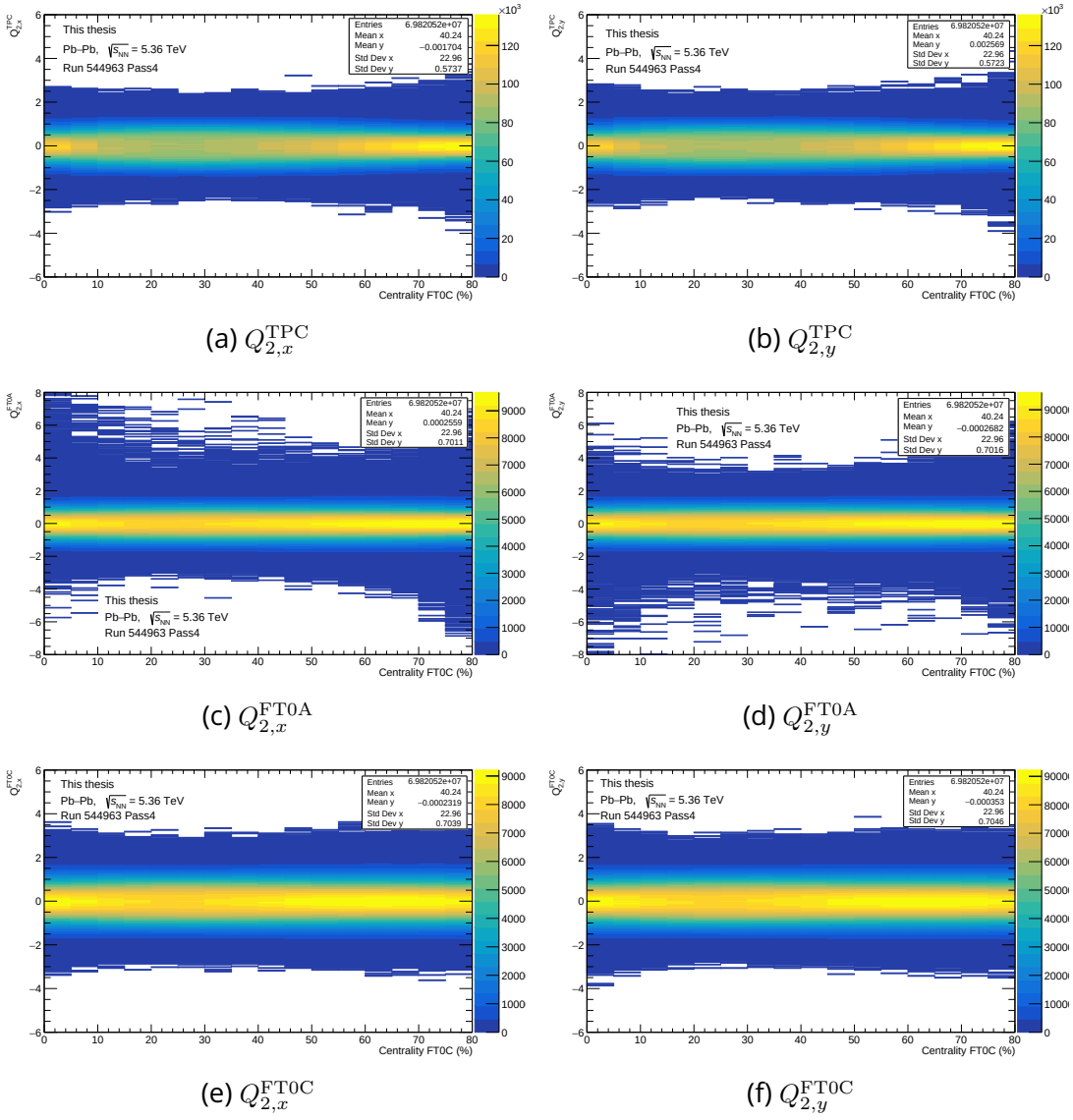

(a) $Q_{2,x}^{\mathrm{TPC}}$ (b) $Q_{2,y}^{\mathrm{TPC}}$

(c) $Q_{2,x}^{\mathrm{FT0A}}$ (d) $Q_{2,y}^{\mathrm{FT0A}}$

(e) $Q_{2,x}^{\mathrm{FT0C}}$ (f) $Q_{2,y}^{\mathrm{FT0C}}$

Figure 4.9: Corrected Q-vectors ($n = 2$) of three detectors as a function of centrality using run 544963 of pass 4.

Event-plane and resolution factors

In addition to reduce the bias in the correlation between POI unitary vector and Q-vector, the detector non-uniformity reflecting in Q-vector distortion can be also seen in

the event-plane reconstruction and the contribution of the imaginary part in the resolution factor. For this reason, a necessary assessment for Q-vector calibration is to check the event-plane distribution and resolution factor.

Event-plane reconstruction Within a given centrality class, the magnitude of the impact-parameter is rather fixed, but its orientation as mentioned before is random event-by-event. For central collisions, the magnitude of the impact-parameter is small or even vanishing leading to a nearly symmetric geometry of the overlap region, hence the measured event-plane of 2nd harmonic is rather dominated by participant fluctuations with random orientations and the latter implies a more natural global flatness in the case of central collisions. For peripheral collisions, the geometric anisotropy is pronounced and the local correlation between event-plane and impact-parameter is strong, however a global flatness is also expected due to the random orientation of the impact parameter event-by-event. Following these considerations, one would expect a fairly flat event-plane distribution after Q-vector calibration. The result of reconstructed event-plane ($n = 2$) using TPC tracks within different centrality classes from 0 to 90% is presented in Fig. 4.10 where a rather good flatness is reached across different centrality classes.

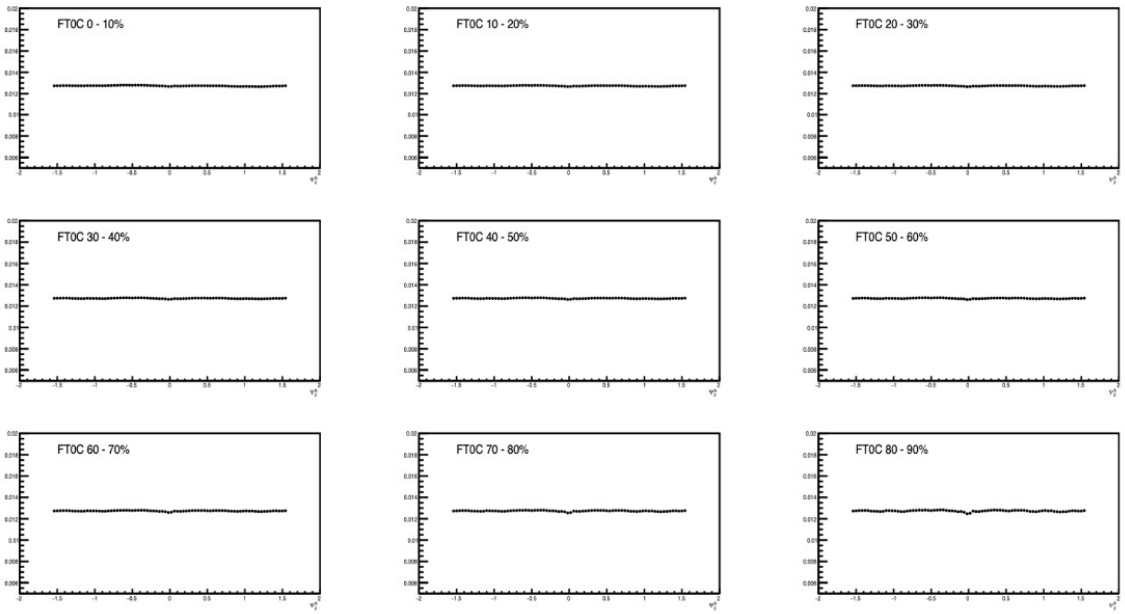

Figure 4.10: Event-plane ($n = 2$) reconstruction using run 545296 of pass 4 with TPC tracks within different centrality classes from 0 to 90%.

Resolution factor As we have discussed before, the event-plane is used as an experimental estimator for the reaction plane, which is a pure geometric and experimentally inaccessible quantity. In the flow analysis with EP method, this biased experimental estimation can be refined a posteriori using resolution factor. In the case of SP method, the resolution factor is also introduced as a measure of reference flow to the POI-to-RFP

correlation on the numerator. Even with slightly different interpretations, the resolution factor used in both EP and SP method follow the same principle of calculation up to the normalization of Q-vectors. Here we shall restrict to the result with SP resolution and the related discussion for residual effect after Q-vector corrections.

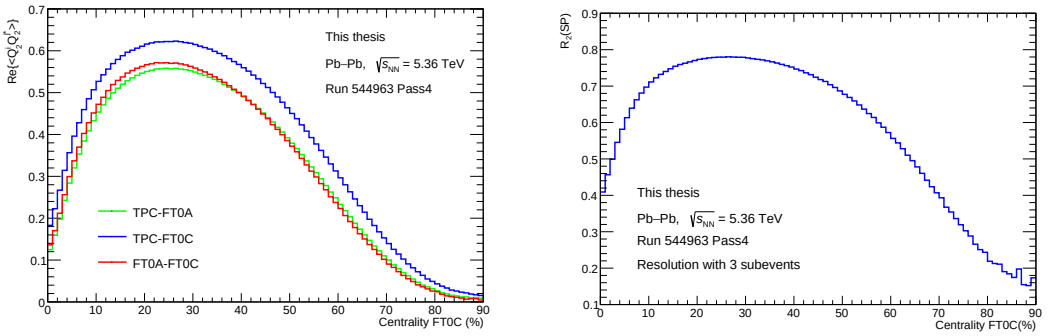

(a) $\mathrm{Re}\langle Q_2^i Q_2^{j*}\rangle$ with 3 detectors (b) $R_2(\mathrm{SP})$ with three-subevent method

Figure 4.11: Real part of Q-vector ($n = 2$) correlations between three detectors and the final resolution using three subevents using run 544963 of pass 4.

As shown in Fig. 4.11, the result of Q-vector correlation between three detectors and the final resolution factor with three subevents is presented. The correlations with different detectors show an increasing trend from the most central to semi-central collisions as the geometric anisotropy starts to dominate with increasing impact-parameter magnitude, and then go down toward peripheral collisions as the overlap region gets smaller. The final result with three-subevent method follows the same trend.

4.4.2 . Resolution with fine centrality binning

Since the final resolution is not uniform across the whole centrality range, the traditional approach taking the weighted average of resolution factor within different centrality bins is not able to capture the subtle variation of resolution estimation as a function of centrality, the latter might have a chance to handle the semi-central region within 15-35 % for the centrality-integrated p_{T} -differential study but clearly not optimal for centrality-differential flow measurement. Moreover, as shown in Fig. 4.12, where the value of each point is taken as the average over all runs in the same centrality classes (per 1 %) and the error represents the standard deviation inside a centrality class, the resolution fluctuates inside a centrality class, and the effect is quite pronounced within semi-central region (10-40 %) where one would expect the highest value of elliptic flow.

From the above considerations, one would rather incorporate the resolution correction to the observed flow in a run-by-run and centrality-dependent way thanks to the large dataset allowing enough precision for run-by-run and centrality-differential calibration, as illustrated in Eq. 4.2.2. This is implemented by pre-loading the run-by-run resolutions with

a fine enough centrality binning (1%) as calibration files saved in ALICE CCDB, so the latter can be accessed on-the-flight during the analysis.

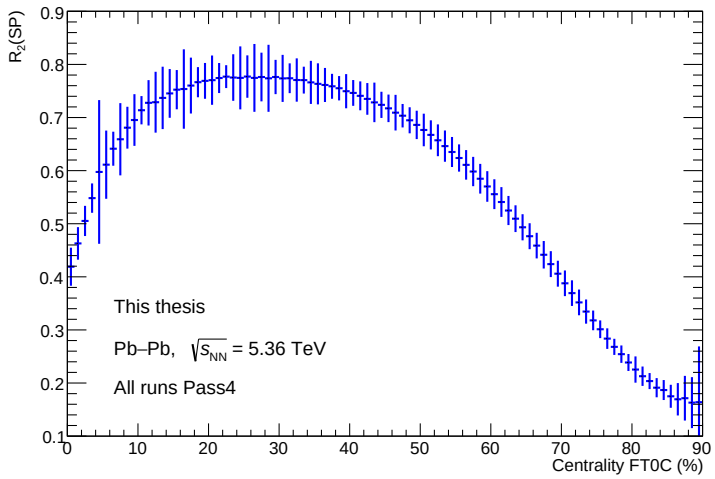

Figure 4.12: Illustration of corrected Q-vectors ($n = 2$) within different centrality classes from forward TPC tracks.

4.4.3 . Non-Uniform Acceptance weights for cumulants

In the approach of multi-particle correlation method, the calibration does not require a strict Q-vector correction procedure. However, the detector imperfections should be incorporated in the weights of Q-vector (concerns only TPC) which would be accounted directly in the calculation of correlators.

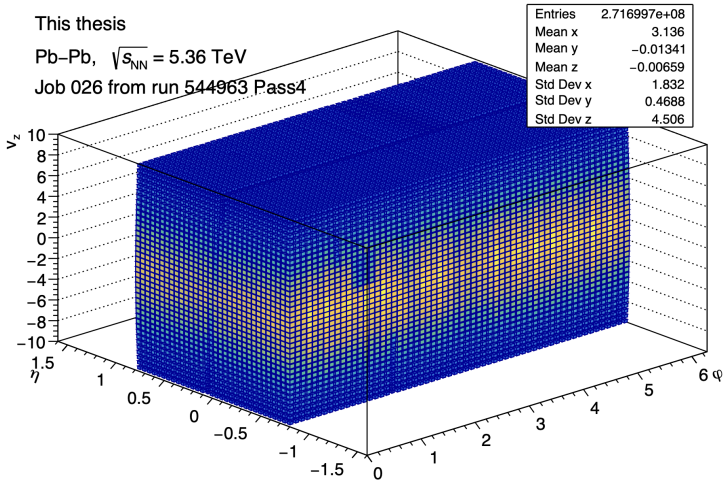

Figure 4.13: An example of Q-vectors weights for Non-Uniform Acceptance (NUA) correction from job 026 of run 544963 of pass 4.

In Run 3, this procedure is handled by a centralized framework, the idea is to fill up the 3D-histogram of tracks in terms of track azimuthal angle ϕ, pseudorapidity η and the z position of PV from the detector with which one would use to build Q-vectors, and the weight will be taken as the inverse of a bin content according to a given kinematic configuration ($\phi, \eta, \mathrm{Vtx}_z$).

As the detector performance may change from run to run as the run conditions might not be identical, a convenient way to prepare Q-vector weights is indeed to record the histogram in a run-by-run way, these histograms shall be later uploaded in ALICE CCDB as calibration files. An example of the 3D-histogram from one job of run 544963 in pass 4 uploaded in CCDB is shown below in Fig. 4.13.

4.4.4 . Reference flow cross-check for cumulants

Playing a similar role as the Q-vector used to calculate the correlation with the POI unitary vector in the SP method, the reference flow ($v_2^{\mathrm{REF}}\{2\}$ and $v_2^{\mathrm{REF}}\{4\}$) for cumulants are measured independently (involving only barrel tracks) from the correlation between POI and RFP for differential flow analysis.

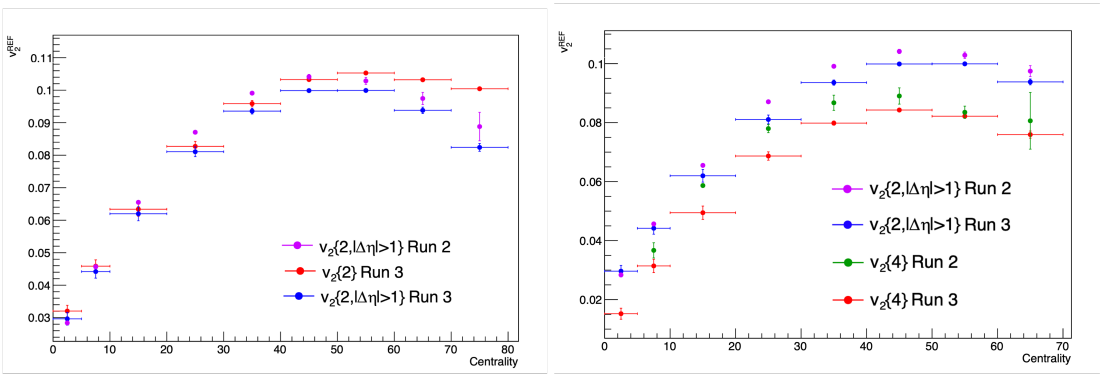

Figure 4.14: Final result of reference flow compared to Run 2: Left, comparison of $v_2\{2\}$ with and without η gap as well as Run 2 data. Right, full comparison of $v_2\{2\}$ and $v_2\{4\}$ with Run 2 and Run 3.

The measurement of reference flow turned out to be very sensitive to the quality of barrel tracks, in particular with respect to the detector performance and tracking condition of TPC and ITS. A few additional selections were applied, especially regarding the TPC occupancy and the time range of no collision. The reference flow fluctuates as well in terms of run conditions as shown in Fig. 4.15. Furthermore, an η-gap ($|\Delta\eta| > 1$) appeared to be necessary in reproducing the correct shape compared to Run 2 results [259] for peripheral collisions as the event-average correlation becomes strongly dependent on the charged-particle multiplicity. The latter being smaller in peripheral than in central collisions, the suppression of non-flow contribution, which scales as $\frac{1}{M^{n-1}}$, is stronger in peripheral than in central collisions, especially in the 2-particle correlation case. Hence

this extra η-gap was applied for $v_2\{2\}$ to remove pronounced non-flow contribution at low multiplicity regions. As we can see in Fig. 4.14, the correct track quality control plus the extra η-gap for 2-particle correlation can reproduce Run 2 shape.

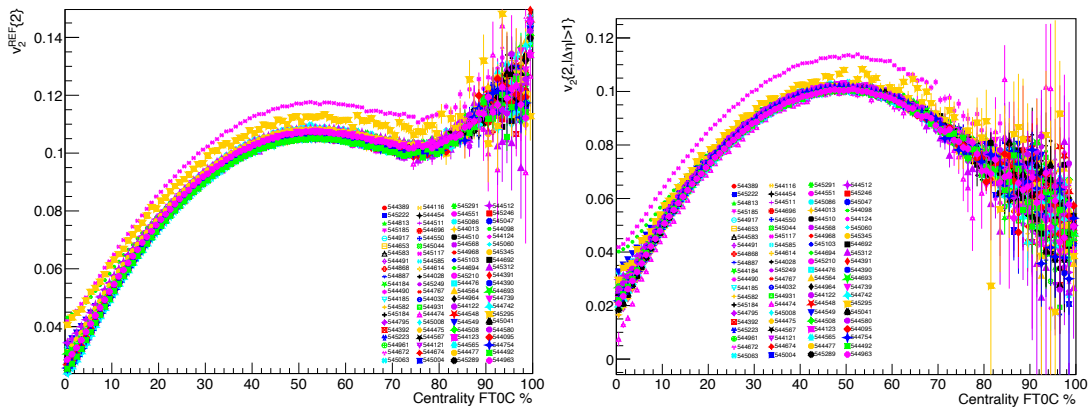

(a) $v_2^{\mathrm{REF}}\{2\}$ (b) $v_2^{\mathrm{REF}}\{2\}$ with η gap

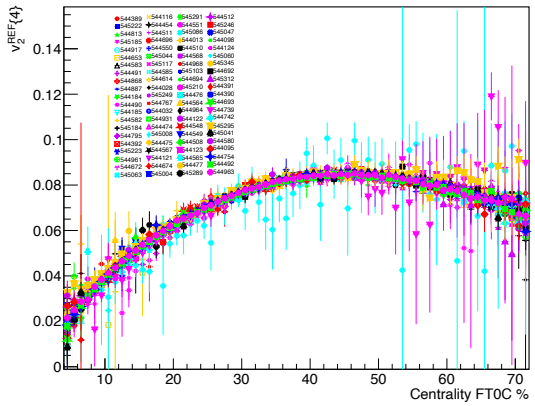

(c) $v_2^{\mathrm{REF}}\{4\}$

Figure 4.15: Result of reference flow $v_2^{\mathrm{REF}}\{2\}$ and $v_2^{\mathrm{REF}}\{4\}$ with all runs of pass 4.

4.5 Data analysis

Having reviewed data preparations, necessary calibrations, and checks for flow analysis described in the previous section, we are now ready to dive into the flow analysis of J/ψ mesons at forward rapidity from their $\mu^+\mu^-$ decay channel using the Muon Spectrometer. The analysis strategy will be reviewed at the first place. The general idea consists of a two-step fit, with a first step for the J/ψ raw yield extraction from the dimuon invariant mass distribution, followed by a second step of v_2 extraction using the J/ψ signal extracted from the previous step. At the same time, associated discussion of event-mixing techniques used in J/ψ signal extraction and flow extraction will be presented as well with some subtleties regarding the difference of implementation in different methods. Finally, different sources of systematic uncertainties in the data analysis shall be discussed and quantified.

4.5.1 . J/ψ raw yield at forward rapidity

The J/ψ signal extraction consists of identifying the resonance ($\mathrm{J}/\psi \to \mu^+\mu^-$) of correlated muon pairs from same-event in the dimuon spectrum within a reasonable mass range. The muon tracks are first reconstructed in the Muon Spectrometer using MCH for the tracking and MID for the timing information, each reconstructed muon track consists of a four-momentum, which will be propagated to the PV. The dimuon invariant mass spectrum is built up combining opposite-sign muon pairs $\mu^+\mu^-$ by summing their four-momentum vectors. The resulting raw dimuon invariant mass spectrum will be fitted into two components: a signal component S of J/ψ mesons and a component of combinatorial background B:

$$N_{\mathrm{tot}}(m_{\mu^+\mu^-}) = N_{\mathrm{J}/\psi} \cdot S(m_{\mu^+\mu^-}) + N_B \cdot B(m_{\mu^+\mu^-}) \tag{4.41}$$

where $N_{\mathrm{J}/\psi}$ and N_B are the corresponding populations for signal and background components. In the fitting procedure, the signal part is parametrized by a Double-Sided Crystal Ball (CB2) function with 6 free parameters including a Gaussian core with mean and width plus 4 tail parameters (details in Appendix. D). In the configuration of the signal function, the peak position and the width of the J/ψ signal are left as free parameters for the Gaussian core with a dedicated mass window centered around the Particle Data Group (PDG) [260] value, which is also used as the initial condition. The tail parameters, instead, where fixed in the fitting procedure. Two sets of tails were used: first, a set extracted from invariant mass fits to high purity and precise data from pp collisions at $\sqrt{s} = 13\ \mathrm{TeV}$ from Run 2 [261]; second from embedded Monte&Carlo simulated J/ψ into real Pb–Pb collisions at $\sqrt{s_{\mathrm{NN}}} = 5.02$ TeV, also from Run 2. Table 4.5.1 summarizes the used tail parameters. The $\psi(2\mathrm{S})$ yield is also accounted in the signal component with the mass peak position relative to the J/ψ one fixed to the mass difference between J/ψ and $\psi(2\mathrm{S})$ from the PDG and the width fixed to the J/ψ width with the ratio from Run 2 [261]. The tail parameters for $\psi(2\mathrm{S})$ signal function are fixed to the same of J/ψ configuration.

Tail parameters	Data $13\,\mathrm{TeV}$ pp	MC $13\,\mathrm{TeV}$ pp
α_L	0.883	0.993
n_L	9.940	2.9075
α_R	1.832	2.182
n_R	15.323	3.122

Table 4.1: Tail parameters for CB2 function extracted from pp collisions at $\sqrt{s} = 13\,\mathrm{TeV}$ from Run 2 [261].

Uncorrelated muon pairs originating from different resonance decay vertices (random coincidence of unrelated muon tracks) constitute a much more smeared distribution shape in contrast to the sharp peak of J/ψ resonance decays in the dimuon spectrum, the contribution of uncorrelated muons to the dimuon spectrum is called the combinatorial background, which need to be properly estimated for a complete description of total distribution in Eq. 4.5.1. As the combinatorial background shape at forward rapidity with a suitable single muon p_T cut is fairly regular, some well-behaved empirical functions can be used to approximate the background shape such as Chebyshev polynomials, Variable-Width Gaussian (VWG) or double-exponential function. Though some of them like Chebyshev polynomials may be able to handle fairly sophisticated shapes with a reasonable order, those empirical functions are purely mathematical, i.e. without constraints from physics information, hence becoming not efficient enough for the case where the Signal-to-Noise Ratio (SNR) is relatively small. A better option in reconstructing the combinatorial background for Pb–Pb collisions is to use the so-called *event-mixing technique*.

Background subtraction with event-mixing

The idea is to consider different sign-combinations ($+-$,$++$,$--$) of muon pairs from both same- and mixed-events in the same centrality classes defined by the mixing pool and vertex position criteria. The event-mixing setup applied in this analysis follows:

- Mixing-pool `CentralityFT0C5`: $[0, 5, 10, 20, 30, 40, 50, 60, 70, 80, 90]\%$
- Mixing-depth: 5 tracks stored
- Vertex criteria: $\mathrm{Vtx}_z \in [-10, 10]/\{0\}\,\mathrm{cm}$

Since opposite-sign muon pairs from different events within the same centrality class should be purely combinatorial, they could be used, up to a proper normalization, to match the combinatorial background of the same-event opposite-sign dimuon spectrum. The normalization factor F within a given centrality and p_T range is defined by:

$$F = \frac{\int 2R\sqrt{N^{++}_{\mathrm{same}} N^{--}_{\mathrm{same}}}\,\mathrm{d}M_{\mu\mu}}{\int N^{+-}_{\mathrm{mix}}\,\mathrm{d}M_{\mu\mu}} \tag{4.42}$$

where $N^{\pm\pm}_{\mathrm{same/mix}}$ denotes the multiplicity of muon pairs with different sign-combinations in same- and mixed-events and $R = N^{+-}_{\mathrm{mix}}/2\sqrt{N^{++}_{\mathrm{mix}}N^{--}_{\mathrm{mix}}}$ is a factor that accounts for the different acceptance of μ^+ and μ^-. In Run 3, because no single-μ low-p_{T} selection was applied online, special care should be taken in the calculation of the R factor. In particular, clear variations are seen for different single muon p_{T} cuts as shown in Fig. 4.16. On the left panel, the R factor measured in different centrality classes is presented, with fluctuations being mostly statistical. On the right panel, the p_{T} -integrated R factor within 0-5% centrality is shown with two different single muon p_{T} cuts. A peak-like behavior is observed due to low-momentum muon kinematics, and the peak moves toward the mass window of J/ψ resonance peak position with single muon p_{T} cuts from $0.7\,\mathrm{GeV}/c$ to $1\,\mathrm{GeV}/c$. As the typical lower bound for J/ψ mass window is around $2\,\mathrm{GeV}/c^2$, for the case of $1\,\mathrm{GeV}/c$ p_{T} cut the peak will strongly contribute to mixed-event subtracted background shape. The intuitive option to reduce the peak contribution in background shape is to move the peak toward low-mass region leading to the choice of $0.7\,\mathrm{GeV}/c$. On the other side, due to the presence of the peak, the R factor within J/ψ mass window is slightly below 1, and the latter can be compensated by choosing a large integration range $[1\text{-}5]\,\mathrm{GeV}/c^2$.

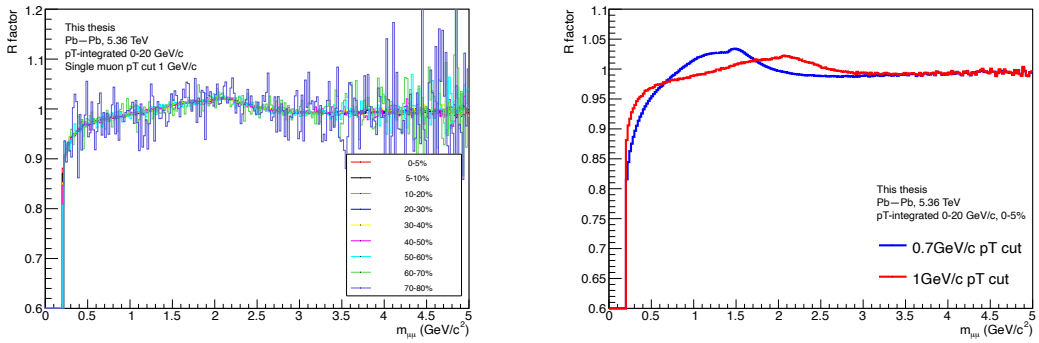

Figure 4.16: Example of R factor calculation: Left: in different centrality classes within 0-$20\,\mathrm{GeV}/c$ using $1\,\mathrm{GeV}/c$ single muon p_{T} cut. Right: with different single muon p_{T} cuts within 0-$20\,\mathrm{GeV}/c$ and 0-5% centrality.

To take into account the fluctuation within different centrality and p_{T} configurations, the final normalization factor F was calculated in different p_{T} bins and re-weighted for each centrality classes using the same binning as the mixing pool. The resulting re-weighted F factor within different p_{T} bins is illustrated below in Tab. 4.2. An example of comparison between dimuon distributions of same- and mixed-event after proper normalization procedure is shown in Fig. 4.17, where the background shape is well reproduced with a proper normalization procedure applied.

Normalization factors in different p_{T} GeV/c (column) and centrality % (row)										
	0-1	1-2	2-3	3-4	4-5	5-6	6-8	8-10	10-12	12-15
0-10	0.102	0.102	0.101	0.101	0.102	0.102	0.102	0.102	0.100	0.101
10-30	0.104	0.103	0.102	0.102	0.103	0.104	0.104	0.104	0.106	0.101
30-50	0.108	0.105	0.103	0.104	0.105	0.107	0.107	0.110	0.108	0.090
20-40	0.106	0.103	0.102	0.102	0.104	0.105	0.104	0.107	0.107	0.099
10-50	0.105	0.103	0.102	0.102	0.103	0.104	0.105	0.105	0.107	0.103

Table 4.2: F factor in different p_{T} (GeV/c) and centrality (%) configurations used in this analysis.

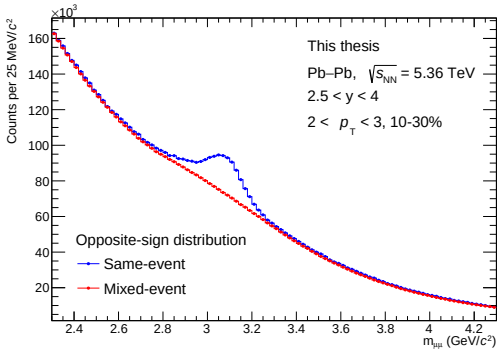

(a) Opposite-sign (+-) distributions

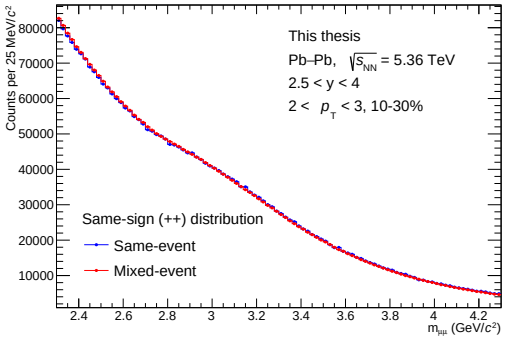

(b) Same-sign (++) distributions

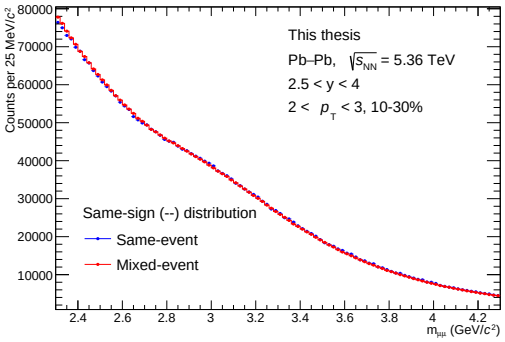

(c) Same-sign (--) distributions

Figure 4.17: Comparison between same- and mixed-event distributions of opposite- and same-sign dimuons after proper normalization for $2 < p_{\mathrm{T}} < 3\,\mathrm{GeV}/c$ and 10-30% centrality.

Although the event-mixing technique can significantly remove combinatorial background from uncorrelated muon pairs with detector acceptance correction, there is still a residual correlated non-signal background arising mostly from semileptonic decays of

open heavy-flavors, and possibly additional thermal radiation from the QGP and hadronic matter. For this reason, an extra parametric background shape should be added to the fit of mixed-event subtracted dimuon spectrum, this extra background is usually modeled by a single exponential function or some power-law polynomials. However, due to the presence of the peak-like behavior from the low-momentum kinematic effect, in the low-p_{T} regions the mixed-event subtracted residual background does not have a trivial form, the best result was obtained using a Landau distribution as shown in Fig. 4.18 (a). Finally, an illustration of J/ψ invariant mass fits within different p_{T} bins is presented as well in Fig. 4.18. The minimizer was set to `Minuit2` and the fit validation was controlled first by the fit status flag which checks typically the general convergence and status of covariance matrix, then a rather good $\chi^2/\mathrm{ndf} < 1.8$ was also required to ensure the fit quality. The significance ($(S/\sqrt{S+B})_{3\sigma}$) and SNR ($(S/B)_{3\sigma}$) within 3σ are also shown in the fit parameter panel, while a fit-to-data pull histogram is also presented on the lower pads.

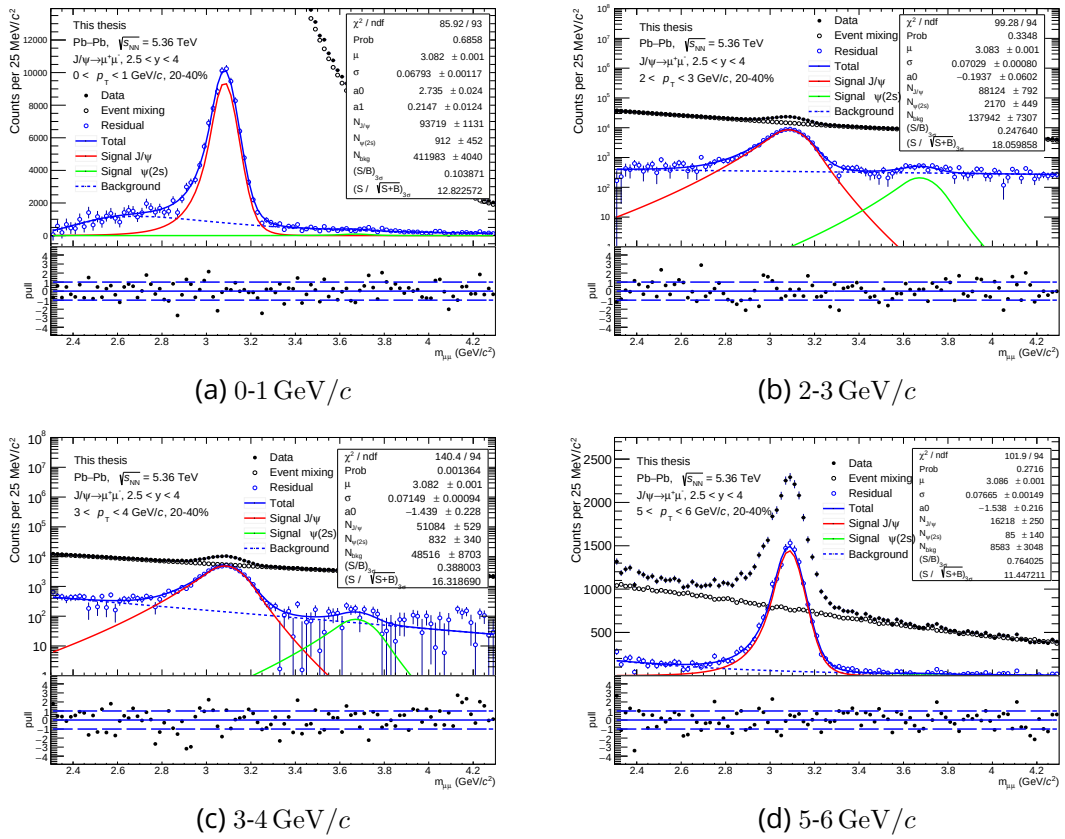

(a) 0-$1\,\mathrm{GeV}/c$ (b) 2-$3\,\mathrm{GeV}/c$

(c) 3-$4\,\mathrm{GeV}/c$ (d) 5-$6\,\mathrm{GeV}/c$

Figure 4.18: Illustration of J/ψ invariant mass fit within 20-40% for different p_{T} bins.

4.5.2 . v_2 extraction

In the quarkonium flow analysis, the dimuon flow observable is first evaluated using opposite-sign dimuons as POI in the correlation functions. The example of raw v_2 as a function of dimuon invariant mass is presented in Fig. 4.19, where for the dimuon v_2 measured in 2-3 GeV/c one can already spot a resonance peak around J/ψ invariant mass region. The intuitive understanding is to consider the dimuon v_2 spectrum as a sum of two components, where one corresponds to the J/ψ flow signal and the other one represents the background. The dimuon flow can be formalized no matter what kind of flow measurement method one will be using as:

$$v_2^{\mathrm{tot}}(m_{\mu\mu}) = \alpha(m_{\mu\mu}) \cdot v_2^{\mathrm{J}/\psi} + (1 - \alpha(m_{\mu\mu})) \cdot v_2^{\mathrm{bkg}} \tag{4.43}$$

s2where $\alpha(m_{\mu^+\mu^-}) = S(m_{\mu^+\mu^-})/(S(m_{\mu^+\mu^-}) + B(m_{\mu^+\mu^-}))$ is the signal fraction as a function dimuon invariant mass from the J/ψ invariant mass fit in the previous step, $v_2^{\mathrm{J}/\psi}$ will be the scalar value of J/ψ v_2 to be fitted, and v_2^{bkg} will be the background modeled by ad-hoc functions or extracted using event-mixing technique. And the total v_2 signal function as a function of dimuon invariant mass is already averaged value in a given centrality and p_{T} configuration.

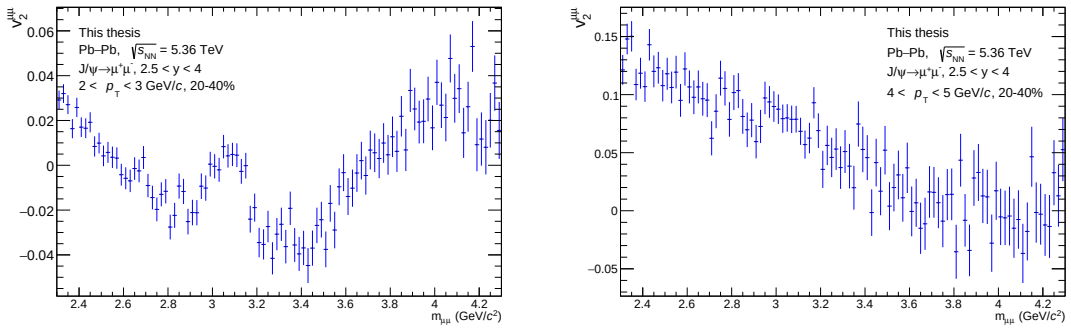

(a) 2-3 GeV/c (b) 4-5 GeV/c

Figure 4.19: Example of dimuon v_2 as a function of dimuon invariant mass within 20-40 % for two different p_{T} bins.

Background subtraction with event-mixing

Often, the background shape in the dimuon v_2 spectrum is not trivial and therefore difficult to reproduce with ad-hoc functions. Generic orthogonal polynomials like Chebyshev can, in principle, reproduce those shapes but probably requiring high-order corrections. In addition, as already mentioned for the J/ψ yield extraction, empirical functions will always find difficulties to capture real physics information. Therefore, a dedicated event-mixing technique for the combinatorial background in v_2 distribution was already developed [262]: the idea is based on the fact that the two-point particle density function of uncorrelated muons can be factorized into the product of two one-point particle

density functions of single muons where each can decompose into Fourier series hence acquire corresponding flow coefficients, namely:

$$\frac{\mathrm{d}N^{\mathrm{bkg}}}{\mathrm{d}\varphi_{\mu\mu}} \propto \left(1 + 2\sum_{n=1}^{\infty} v_n^{(1)}(p_{\mathrm{T}}^{(1)})\cos\big[n(\varphi_1 - \Psi_n)\big]\right)\left(1 + 2\sum_{m=1}^{\infty} v_m^{(2)}(p_{\mathrm{T}}^{(2)})\cos\big[m(\varphi_2 - \Psi_m)\big]\right) \tag{4.44}$$

where $v_{m(n)}^{1(2)}(p_{\mathrm{T}}^{(1(2))})$ are single-muon flow coefficients evaluated as the correlation between single-muon unitary vector and the event Q-vector in the case of SP method or from single-muon correlator in the case of cumulants method, $\varphi_{1(2)}$ are the corresponding azimuthal coordinates of single-muons, and $\Psi_{n(m)}$ are event-plane angles from events of each single-muon. From which the expression of background v_2 distribution, averaged over all muon pairs belonging to a given dimuon mass bin within the same centrality and p_{T} configuration, is given by:

$$v_n^{\mathrm{bkg}}(m_{\mu\mu}) = \frac{\left\langle v_n^{(1)}\cos\big[n(\varphi_1 - \varphi_{12})\big] + v_n^{(2)}\cos\big[n(\varphi_2 - \varphi_{12})\big]\right\rangle_{\mu\mu}}{\left\langle 1 + 2\sum_{m=1}^{\infty} v_m^{(1)} v_m^{(2)}\cos\big[m(\varphi_1 - \varphi_2)\big]\right\rangle_{\mu\mu}} \tag{4.45}$$

where φ_{12} is the azimuthal angle of the dimuon vector made of the two single-muons. The denominator in Eq. 4.5.2 corresponds to a scaling factor to the mixed-event dimuon v_2 distribution regarding the single-muon flow signal contribution, which is determined assuming no correlated background contribution (this assumption will be released in the study of systematic uncertainties and modeled by a free parameter) by the ratio between the opposite-sign same-event background population to the mixed-event opposite-sign population $N_{+-}^{\mathrm{bkg}}/N_{+-}^{\mathrm{mix}}$ where N_{+-}^{mix} is normalized using the procedure detailed in the yield extraction. The numerator consists of calculating mixed-event v_2 of uncorrelated muon pairs from their single-muon v_2 signal, the concrete implementation differs in different methods. In the following discussion, we shall explicit bit more how the numerator is evaluated in SP (idem for EP) and cumulant method.

Single-muon v_2 for SP method This consists simply of evaluating the correlation between the single-muon unitary vector and the event Q-vector corrected by the corresponding resolution, leading to the numerator where the average is taken over all mixed-event muon pairs in the same event class and p_{T} range for a given invariant mass bin:

$$\left\langle \frac{u_2^{(1)}Q_2^{(1)\mathrm{TPC}*}}{R_2^{(1)}}\cdot\cos[n(\varphi_1 - \varphi_{12}] + \frac{u_2^{(2)}Q_2^{(2)\mathrm{TPC}*}}{R_2^{(2)}}\cdot\cos[n(\varphi_2 - \varphi_{12}]\right\rangle_{\mu\mu} \tag{4.46}$$

Single-muon correlators for cumulants method In order to evaluate the single-muon flow coefficient for cumulants method, one will need to provide all correlator calculations taking POI as single-muon instead of dimuon, leading to $\langle\langle 2_\mu^{'}\rangle\rangle$ and $\langle\langle 4_\mu^{'}\rangle\rangle$ as a function of p_{T} and centrality (with fine binning). The four single-muon correlators will be pre-calculated before the event-mixing analysis and uploaded to CCDB in a run-by-run way. During the event-mixing analysis, the single-muon correlators for a given run will be

fetched from CCDB and used to calculate $c_2^{\mu}\{2,4\}$ and $d_2^{\mu}\{2,4\}$, then the latter will allow us to get the corresponding single-muon flow coefficients following:

$$v_2^{\mu}\{2\} = -\frac{d_2^{\mu}\{2\}}{\sqrt{c_2\{2\}}}, \tag{4.47}$$

$$v_2^{\mu}\{4\} = -\frac{d_2^{\mu}\{4\}}{\big(-c_2\{4\}\big)^{3/4}}. \tag{4.48}$$

An example of single-muon v_2 as a function of p_{T} within $10\text{-}30\%$ centrality is shown below in Fig. 4.20.

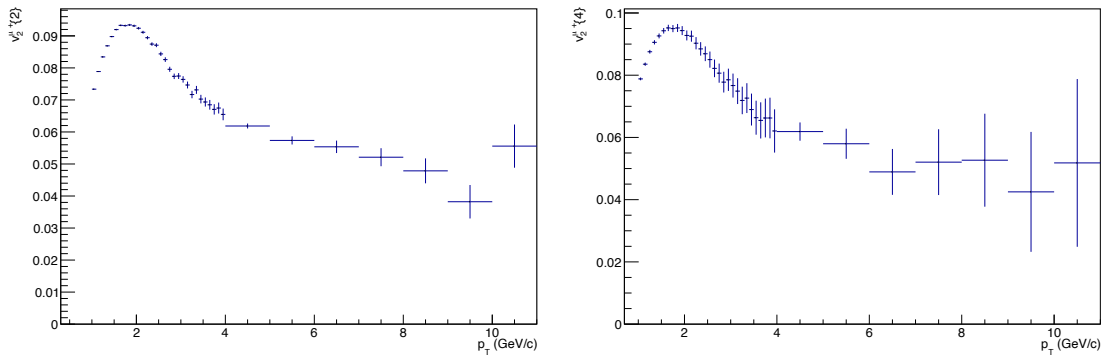

(a) $v_2^{\mu}\{2\}$ (b) $v_2^{\mu}\{4\}$

Figure 4.20: Single-muon v_2 as a function of p_{T} within $10\text{-}30\%$ centrality.

4.5.3 . Systematic uncertainties

In this section, available sources of systematic uncertainties will be discussed including those from yield and v_2 extraction, as well as the imperfect Q-vector calibration leading to systematic bias in correlation and residual nonflow contribution. In this sense, the following discussion regarding the current results conducted in the thesis would be considered as preliminary.

J/ψ yield and v_2 extraction

The systematic uncertainties arising from J/ψ yield and v_2 extraction will be investigated by varying the fitting configuration, which consists of signal shapes including the choice of fitting function and/or tail parameters from either data or Monte&Carlo, mass window for J/ψ yield extraction, and event-mixing. From the two-step viewpoint of the fit procedure, the systematic uncertainties in the final v_2 extraction arise from the determination of $\alpha(m_{\mu\mu})$ originating from the J/ψ yield extraction step, and configuration of event-mixing in describing the background in the dimuon v_2 spectrum.

Systematic uncertainties from $\alpha(m_{\mu\mu})$ The options for different fit configurations for the J/ψ yield extraction are then summarized below:

- **Signal shapes**: CB2 function (tail parameters from data or Monte&Carlo from Run 2 [261]), NA60 function (tail parameters fixed from Run 2 Monte&Carlo [261])
- **Background shapes**: Chebyshev polynomials, event-mixing with correlated residual contribution parametrized by Landau function at low p_{T} and single exponential for intermediate- to high-p_{T} regions
- **Mass window**: $[2.2\text{-}4.2]$, $[2.3\text{-}4.3]$, $[2.4\text{-}4.4]$ GeV/c^2

To investigate the fit stability with different options, the fit process has to be repeated with all possible combinations of the options, resulting in a total number of trials of 18 (3 signal shapes $\otimes$ 2 background shapes $\otimes$ 3 mass windows). An example of fit stability investigation is shown below in Fig. 4.21.

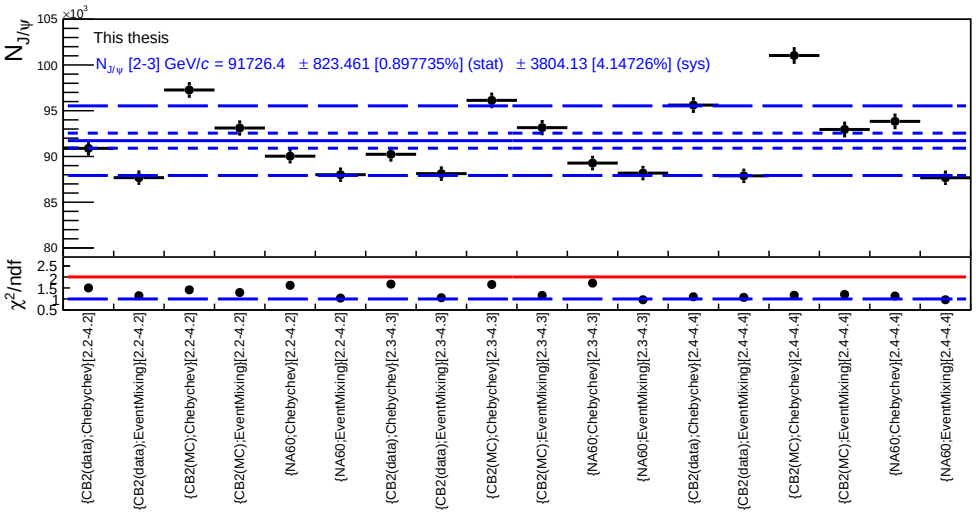

Figure 4.21: An example of 18 trials with different fit setups for J/ψ yield extraction within $2\text{-}3\,\mathrm{GeV}/c$ and $20\text{-}40\%$ centrality.

On the upper panel, the J/ψ yield value and uncertainties from each fit setup are presented together with a solid line representing the mean value of J/ψ yield over all trials, two short-dashed lines representing the mean uncertainty over all trials with respect to solid line of mean value, and two long-dashed lines showing the Root Mean Square (RMS) of all trials with respect to the solid line of the mean value; on the lower panel, the corresponding χ^2/ndf for each fit setup are also presented. For the final evaluation, all points above $1.5\times$RMS will be dropped. The final J/ψ yield for the corresponding p_{T} bin will be given by the mean value over all yield values of accepted trials, with the mean value of all uncertainties of accepted trials as statistical uncertainty and RMS over all yield values of accepted trials as the systematic uncertainty. The final result of J/ψ yield as a function of p_{T} within $20\text{-}40\%$ centrality is shown below in Fig. 4.22 and the numerical values are summarized in Tab. 4.3. There was a small subtle point when Chebyshev polynomials were used as an alternative option in the trials: despite considered as being able to

handle most signal shapes, it had to go up to a certain high order to be able to cover the unusual shape in the low-mass region for low-p_{T} bins due to the modulation induced by low-momentum muon kinematics. For this reason configurations, as can be seen in Fig. 4.21, exhibit an unstable behavior compared to other setups, thought the fit quality and χ^2/ndf were totally fine. This can be explained by the powerfulness of Chebyshev polynomials which have the ability to make the fit converge, even if not really physically meaningful.

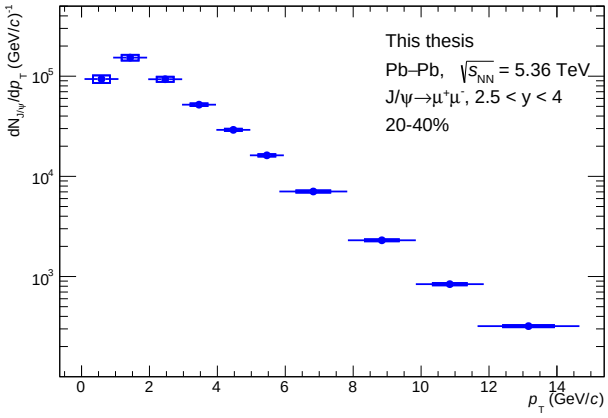

Figure 4.22: The final result of J/ψ yield with systematic uncertainties extracted from trials as a function of p_{T} within 20-40% centrality.

p_{T} (GeV/c)	$N_{\mathrm{J}/\psi}$ [20-40%]
0-1	93679 ± 1668 [stat.] $(1.3\%) \pm 8156$ [sys.] (6.4%)
1-2	153314 ± 1904 [stat.] $(0.9\%) \pm 10183$ [sys.] (7.7%)
2-3	93260 ± 1189 [stat.] $(0.9\%) \pm 5511$ [sys.] (4.2%)
3-4	51956 ± 635 [stat.] $(1.0\%) \pm 1572$ [sys.] (3.5%)
4-5	29118 ± 383 [stat.] $(1.3\%) \pm 767$ [sys.] (2.8%)
5-6	16217 ± 248 [stat.] $(1.5\%) \pm 448$ [sys.] (3.1%)
6-8	14124 ± 205 [stat.] $(1.5\%) \pm 362$ [sys.] (3.0%)
8-10	4600 ± 106 [stat.] $(2.5\%) \pm 106$ [sys.] (2.4%)
10-12	1678 ± 62 [stat.] $(4.0\%) \pm 45$ [sys.] (3.0%)
12-15	959 ± 46 [stat.] $(4.8\%) \pm 23$ [sys.] (2.5%)

Table 4.3: An example of J/ψ raw yield for all p_{T} bins within 20-40% centrality. The first error corresponds to statistical uncertainty and the second is the systematic uncertainty.

Systematic uncertainties from event-mixing in v_2 extraction Having investigated the source of systematic uncertainties coming from the $\alpha(m_{\mu\mu})$ determination in the J/ψ

yield extraction, the remaining source of systematic uncertainty in the v_2 extraction procedure lies on the hypothesis we have made to determine the denominator in Eq. 4.5.2, where in the previous discussion the only contribution from uncorrelated muon pairs was assumed. Because, as already discussed for the yield extraction, a correlated residual background may still contribute to the observed background shape, then the ratio $N_{+-}^{\mathrm{bkg}}/N_{+-}^{\mathrm{mix}}$ should be replaced by $N_{+-}^{\mathrm{bkg}}/(N_{+-}^{\mathrm{mix}} + \beta(N_{+-}^{\mathrm{bkg}} - N_{+-}^{\mathrm{mix}}))$ where β varying from 0 to 1 parametrizes the contribution of the correlated background. In the study of systematic uncertainties from v_2 extraction, two extra options are added to account for the background shape with event-mixing:

- $\beta = 0$, which corresponds to the hypothesis of no correlated background contribution.
- β free, where the previous hypothesis is released and β will be left as a free parameter with a range of $[0\text{-}1]$ in the fit procedure.

Taking into account the above two extra options in v_2 extraction fit setup, we now have a total number of 36 trials (18 from α determination $\otimes$ 2 β configurations) combining those from the previous investigation for J/ψ yield extraction. An example of systematic uncertainty investigation for v_2 extraction within $2\text{-}3\ \mathrm{GeV}/c$ and $20\text{-}40\%$ is presented below in Fig. 4.23. Similar to the systematic uncertainty for the J/ψ yield extraction, the upper panel shows the fit result of each trial, and the lower panel provides the systematic checks for fit quality with χ^2/ndf. As one may observe, the major discrepancy between the trials is attributed to the parametric background shape with Chebyshev especially in the low-p_{T} region where the low-mass background shape is much less trivial.

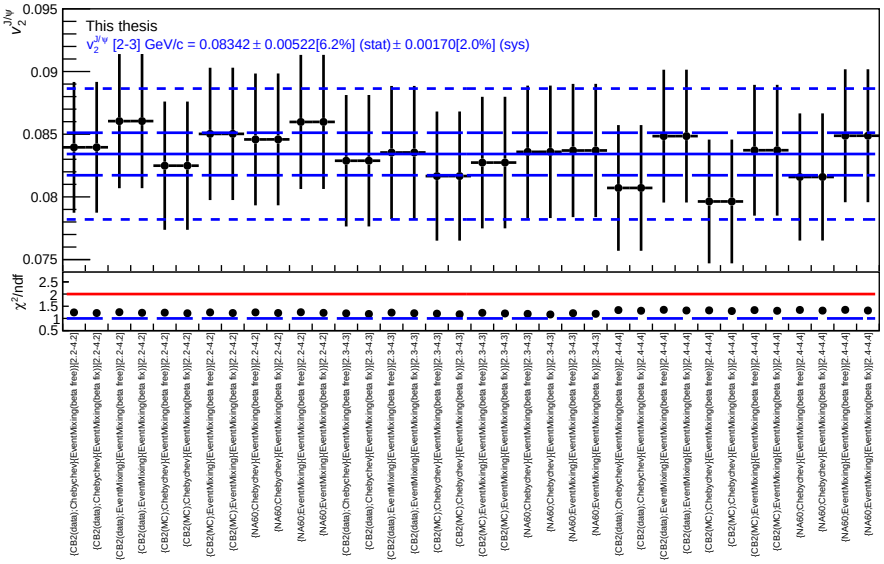

Figure 4.23: An example of 36 trials with different fit setups for J/ψ v_2 extraction within $2\text{-}3\ \mathrm{GeV}/c$ and $20\text{-}40\%$ centrality.

Resolution factor with imperfect calibration

As the quality of final results from SP method depends strongly on the Q-vector calibration, there is another important check to be done as discussed before in Sec. 4.2.2 regarding the bias in resolution factor from imperfect calibration. In our setup of scalar product evaluation, the pairwise detector correlations with Q-vectors take only the real part assuming a perfect calibration, which is supposed to leave no residual imaginary part coming from the cross-product terms in the scalar product calculation since the detectors should be independent in principle. However, the Q-vector calibration in practice will never be perfect; for this reason, the residual imaginary part in the Q-vector correlations could bias the resolution, which could then result in a bias of the final flow coefficient leading to a source of systematic uncertainties.

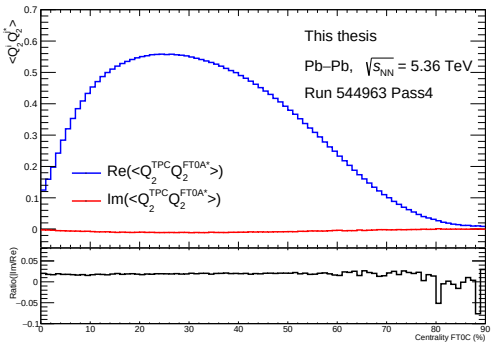

(a) TPC-FToA

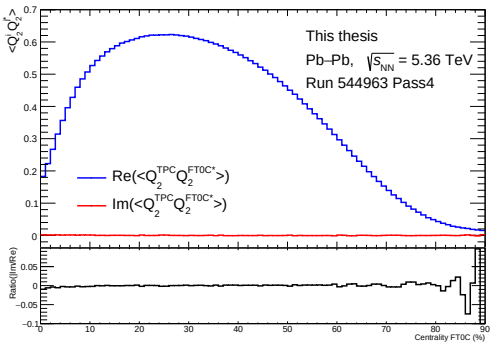

(b) TPC-FToC

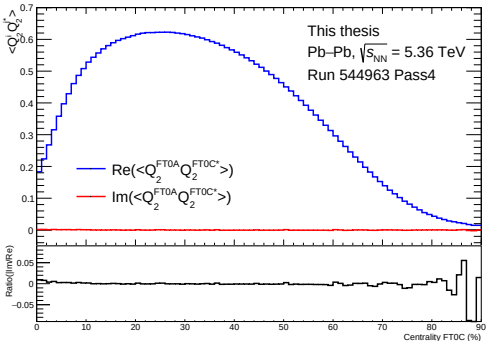

(c) FToA-FToC

Figure 4.24: Q-vector ($n = 2$) correlations between three detectors using run 544963 from pass 4, comparison between real and imaginary parts.

Figure 4.24 presents the comparison between real and imaginary parts of Q-vector correlations between three detectors. The observed imaginary part are nearly negligible compared to the real part; and the ratio Im/Re is independent of centrality, reflecting a rather uniform calibration across the whole centrality range, except a bit more fluctua-

tions from 60% toward the most peripheral collisions. As the resolution factor depends only on centrality event-by-event, meaning that it can be factorized regardless of the p_{T} -dependency encoded in the POI unitary vector. An overall contribution (relative uncertainty) from the imaginary part can be evaluated, with an upper bound of about 2% for all Q-vector correlations across the whole centrality range up to 80% where the fluctuation is getting stronger due to lower multiplicity. This upper bound value results in a systematic bias for the final three-subevent resolution about $\sim 1.73\%$. Furthermore, the residual effect (residual nonflow contribution despite η-gap and imperfect Q-vector calibration) from the cross-product in the POI and Q-vector correlation was found to be independent of p_{T} and centrality, with a value that remains smaller than the contribution from the resolution factor. The ratio of imaginary part to real part in Q-vector scalar product for all runs is shown below in Fig. 4.25: for the cases of TPC-FToA and TPC-FToC, the ratios are stable across the whole range of centrality with upper bounds 3% for TPC-FToA and 1% for TPC-FToC; for the case of FToA-FToC, a small variation with centrality is present for the most central collisions (0-10%), however the overall ratio across the whole range is bounded by 2%.

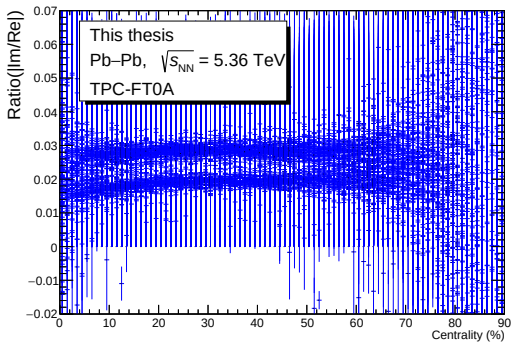

(a) TPC-FToA

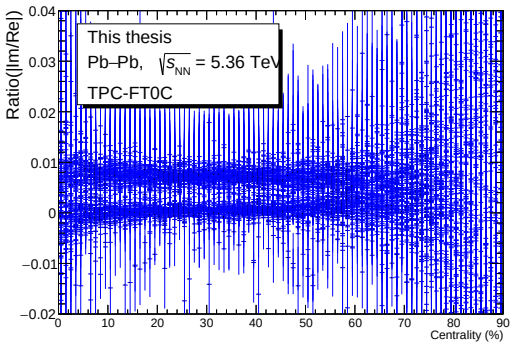

(b) TPC-FToC

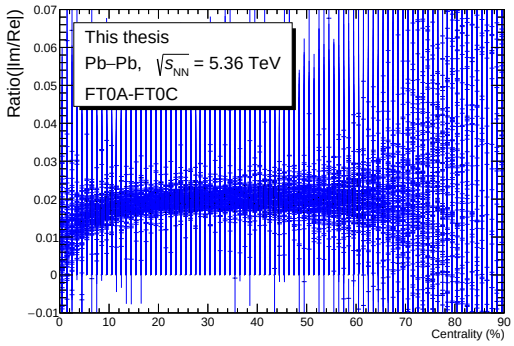

(c) FToA-FToC

Figure 4.25: The ratio of imaginary part to real part in Q-vector scalar product with all runs in this analysis.

Summary of systematic uncertainties

The final result of J/ψ v_2 will account for all absolute values of above mentioned sources of systematic uncertainties. The available sources of systematic uncertainties in this analysis are summarized below in Tab. 4.4 for both p_{T} - and centrality-differential v_2 with SP and cumulants methods.

Sources	$v_2(p_{\mathrm{T}})$	$v_2\{2,4\}(p_{\mathrm{T}})$	$v_2(\mathrm{centrality})$	$v_2\{2,4\}(\mathrm{centrality})$
Signal extraction	0.001-0.013	0.001-0.02	0.0001-0.0022	0.001-0.024
Q-vector calibration	$< 1.73\%$	negl.	$< 1.73\%$	negl.

Table 4.4: Summary of absolute and/or relative systematic uncertainties for the J/ψ v_2 analysis at forward rapidity.

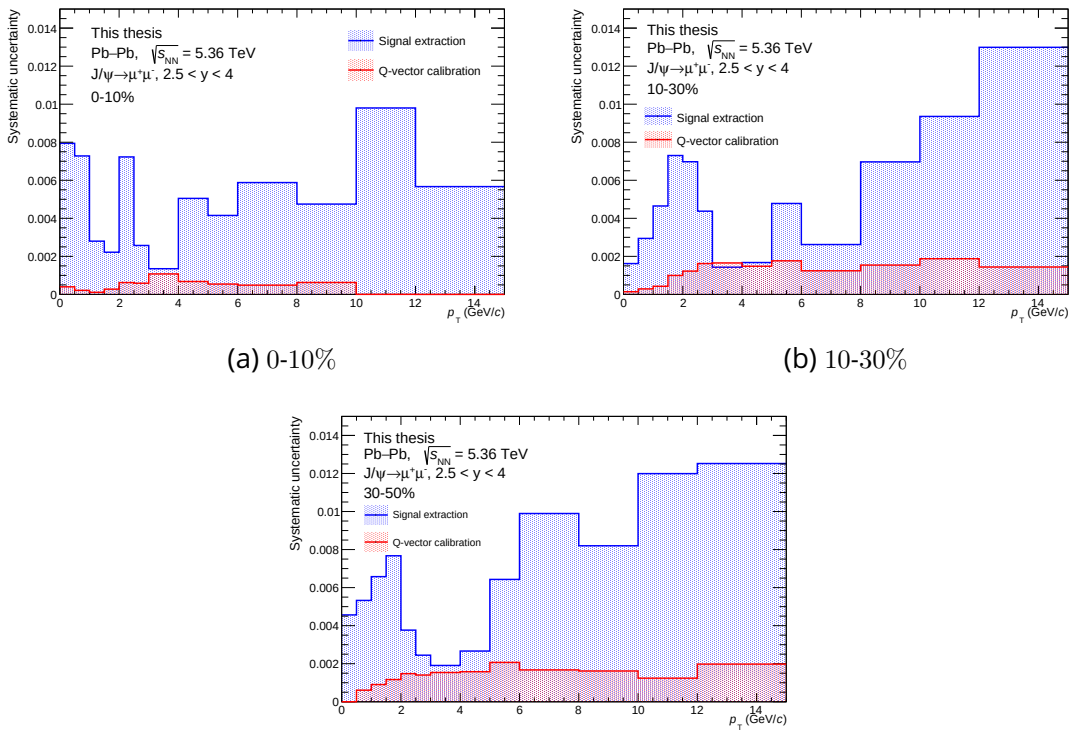

(a) 0-10%

(b) 10-30%

(c) 30-50%

Figure 4.26: Systematic uncertainties as a function of p_{T} for three different centrality classes: 0-10%, 10-30% and 30-50%.

The corresponding systematic uncertainties as a function of p_{T} are reported in Fig. 4.26. The contribution from signal extraction is quite large at low p_{T} ($< 4\mathrm{GeV}/c$) for all three centrality classes, due to low-mass modulation from low-momentum muon kinematics,

which complicates the convergence toward an appropriate background shape for the fit option with Chebyshev polynomials. Toward high p_{T} , the correlated residual background in the event-mixing for v_2 starts to dominate, especially for semi-central collisions, while it does not contaminate the low-p_{T} region where the major contribution is from hydrodynamic expansion of the QGP.

The systematic uncertainties as a function of centrality are also presented below in Fig. 4.27. The contamination from imperfect Q-vector calibration is relatively large at high-p_{T} region ($5 < p_{\mathrm{T}} < 20\,\mathrm{GeV}/c$) compared to low-$p_{\mathrm{T}}$ region ($p_{\mathrm{T}} < 5\,\mathrm{GeV}c$), while for central collisions the Q-vector calibration contributes at the same level compared to signal extraction for both high- and low-p_{T} region. toward peripheral collisions, the signal extraction becomes dominant as the multiplicity of muon pairs decreases.

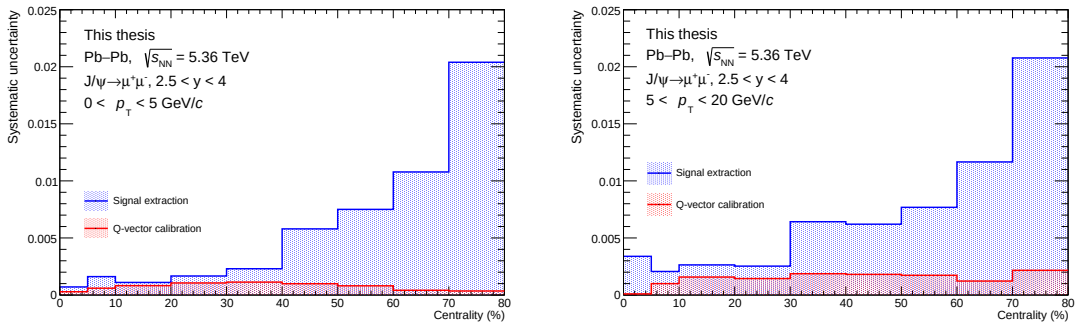

(a) 0-5 GeV/c (b) 5-20 GeV/c

Figure 4.27: Systematic uncertainties as a function of centrality for two different p_{T} classes: 0-5 GeV/c and 5-20 GeV/c.

A possible additional source of systematic uncertainty is related to muon reconstruction efficiency. In the case of a strong dependence of the muon reconstruction efficiency on the local detector occupancy, hence local track multiplicity, the presence of bulk flow could induce a flow-like signal for J/ψ . This could not be tested for the Run 3 dataset yet due to lack of embedding Monte&Carlo simulated quarkonium signals. However, such effect is important for R_{AA} and cross section measurements, it was proven to be not significant for the measurement of correlation as v_2 from with dedicated studies in the previous Run 2 analysis [263].

4.6 Results and discussions

In this section, the final results of the first Run 3 measurement of inclusive J/ψ v_2 at forward rapidity in Pb–Pb collisions at $\sqrt{s_{\mathrm{NN}}} = 5.36$ TeV will be discussed including the results from SP, EP and cumulants methods. The results were presented at Quark Matter 2025 (Goethe University, Frankfurt) with the corresponding proceedings [264]. The p_{T} -differential J/ψ v_2 measurements shall be reviewed first place, followed by a discussion of the corresponding centrality-differential results. At the same time, a comparison gathering other relevant preliminary quarkonium and open-heavy flavor flow measurements will be discussed. Finally, we shall conclude this section with the first measurement of J/ψ flow fluctuation measurement.

4.6.1 . p_{T} -differential J/ψ v_2 measurements

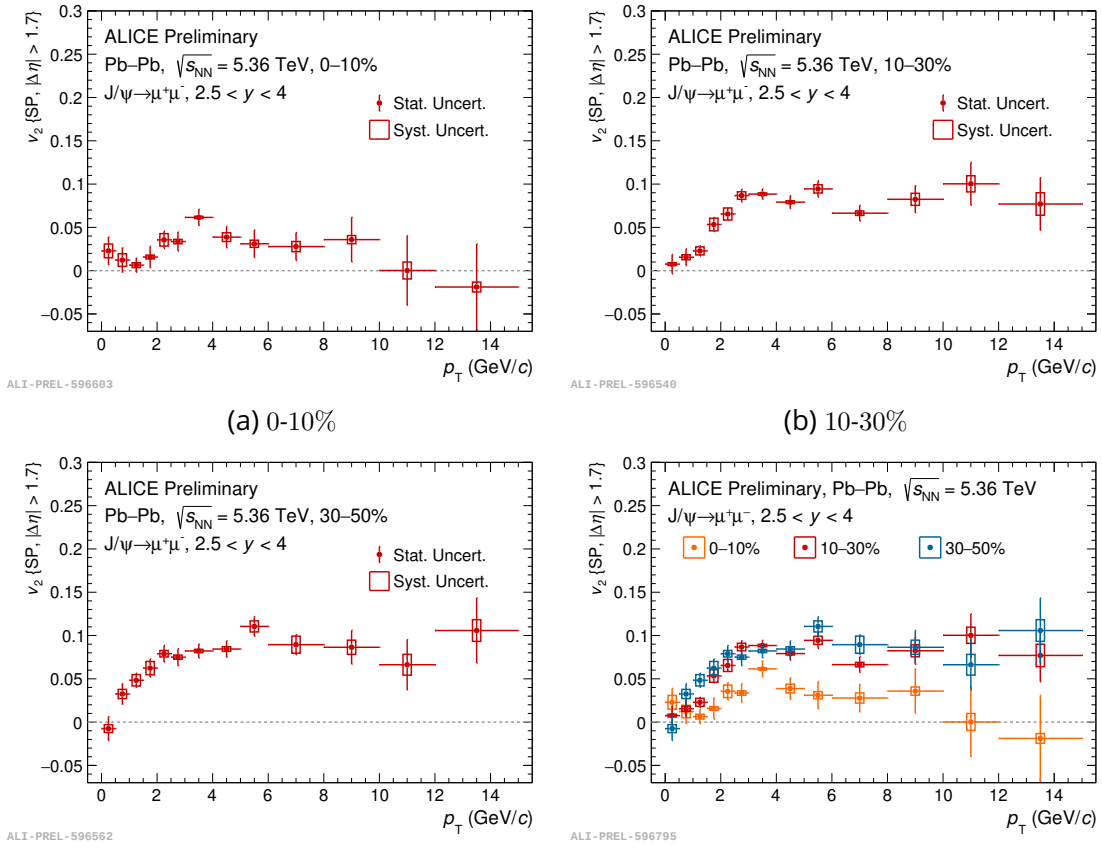

(a) 0-10%

(b) 10-30%

(c) 30-50%

(d) All centrality classes

Figure 4.28: Result of p_{T} -differential J/ψ v_2 at forward rapidity within three different centrality classes (0-10%, 10-30%, 30-50%).

In Fig. 4.28, the results of inclusive J/ψ v_2 at forward rapidity as a function of p_{T} within different centrality classes (0-10%, 10-30%, 30-50%) are presented together with a comparison of all centrality classes in a same plot.

For central collisions, the v_2 signal is slightly positive, although compatible with zero at very-low and high p_{T} . More precisely, the v_2 signal increases from zero at low p_{T} , reaching a maximum around 3-4 GeV/c, then decreasing back toward zero at high p_{T} . Instead, in non-central collisions, a positive v_2 signal across a large p_{T} range is observed together with a smooth increasing trend in the low-p_{T} region, which is attributed to the hydrodynamic expansion of the QGP. There, a linear hydrodynamic response between eccentricity and flow coefficients ($n = 2$) is expected, leading to a maximum at around $4\ \mathrm{GeV}/c$ for both 10-30% and 30-50% centrality classes.

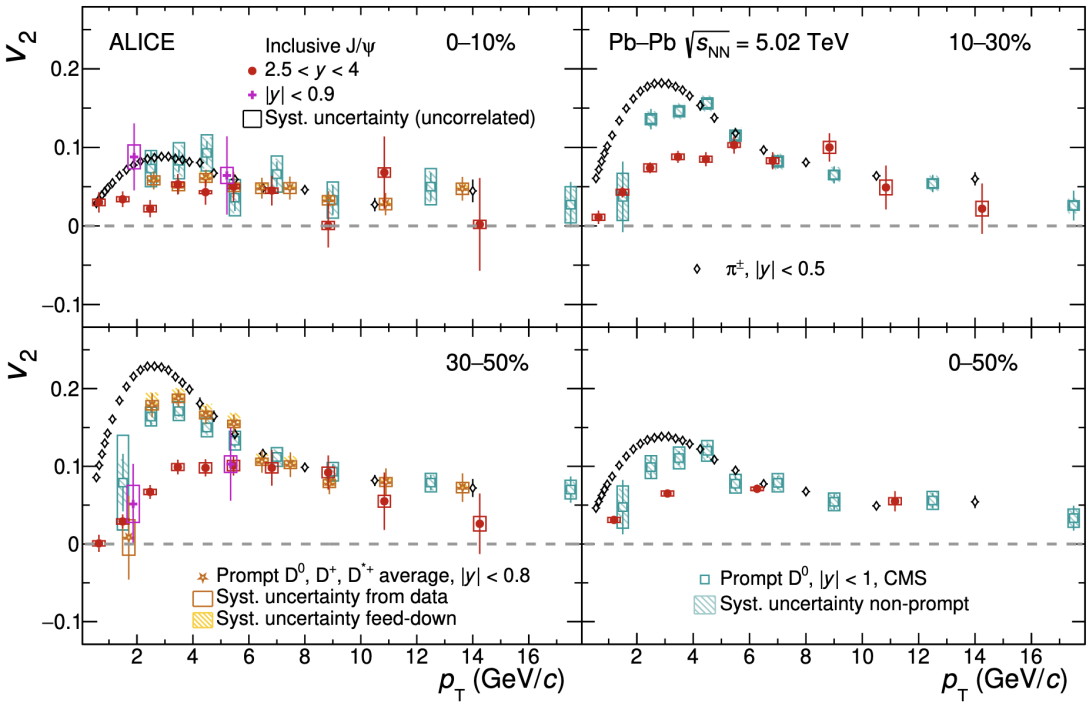

Figure 4.29: Result of p_{T} -differential J/ψ v_2 measurements within different centrality ranges compared to D^0 meson [265, 266] and charged pions [267] v_2 [268].

However, toward the high-p_{T} region in non-central collisions, the v_2 does not exhibit a dropping trend in contrast to central collisions (a similar trend is also observed in EP result). The tendency toward high-p_{T} region in non-central collisions, despite large systematic and statistical uncertainties, displays an improved significance across all high-p_{T} bins with respect to zero compared to Run 2 results [268] shown in Fig. 4.29.

Although this preliminary result still needs to be finalized, a possible interpretation related to the observed saturation instead of dropping out would point to a possible path-length-dependent energy-loss. High-p_{T} J/ψ (primordial but also non-prompt J/ψ from b hadron decays) traveling in in- and out-plane direction will exhibit an anisotropy from different path-lengths crossed. In current transport model implementations [176, 200, 201, 208], only the path-length dependence of the survival probability for primordial J/ψ and feed-down from transported b quarks (giving rise to a non-prompt contribution) are considered. In the typical transport model as TAMU, the Langevin formalism for low to intermediate p_{T} region becomes no longer valid at high p_{T} region where the energy-loss, including elastic and radiative contribution with smooth interpolation from perturbative to nonperturbative region, is accounted into the dissociation rate term Γ_{diss} in the Rate equation.

In addition, the comparison of all three centrality classes is shown in Fig. 4.28 (d). The overall magnitude of v_2 signal increases as the system anisotropy grows up from central to non-central collisions. Moreover, the two non-central cases agree with each other toward high-p_{T} region starting from $4\ \mathrm{GeV}/c$ within current uncertainties, and a slightly stepper trend of result within 30-50% at low-p_{T} region compared to 10-30% appears to be consistent with a higher system anisotropy.

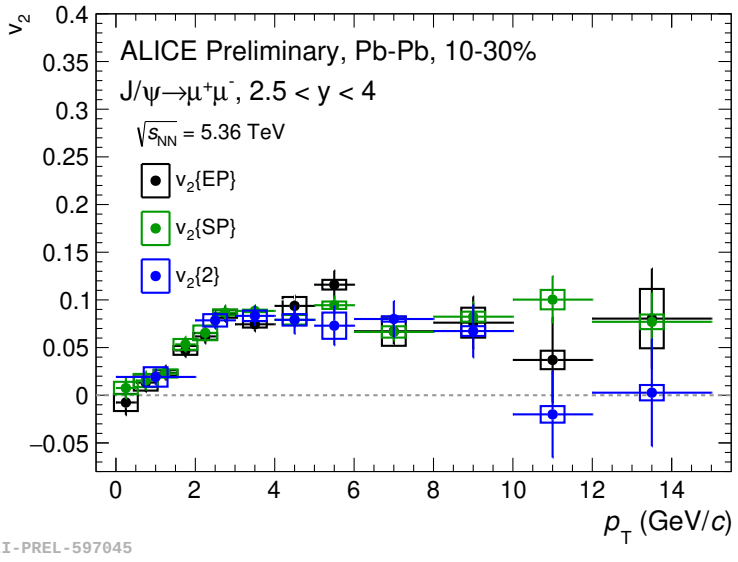

Figure 4.30: A consistency check of J/ψ v_2 with results from three measurement methods (SP, EP and cumulants) within 10-30% centrality.

Figure. 4.30 shows, as a cross check, a comparison of the results from the three different methods implemented in this analysis. A good consistency between the three methods is confirmed across a large p_{T} region from 0 to $10\ \mathrm{GeV}/c$. However, as the method of multiparticle correlation becomes limited by low particle multiplicities at higher p_{T} , the

statistical uncertainties of $v_2\{2\}$ for the cumulants method are much larger than for the SP method and the observed discrepancy is yet to be confirmed with a larger dataset, although the results are still in agreement within current uncertainties.

To conclude the discussion of p_{T} -differential v_2 measurements, the result of $v_2\{4\}$ from the cumulant method is also reported below in Fig. 4.31. For the $v_2\{4\}$ measurement, a larger binning was utilized in order to compensate for the insufficient particle multiplicity for higher-order correlation, especially toward high p_{T} . As the first Run 3 measurement of J/ψ v_2 at forward rapidity, this preliminary result is fairly consistent since the magnitude of $v_2\{4\}$ is expected to be smaller than $v_2\{2\}$.

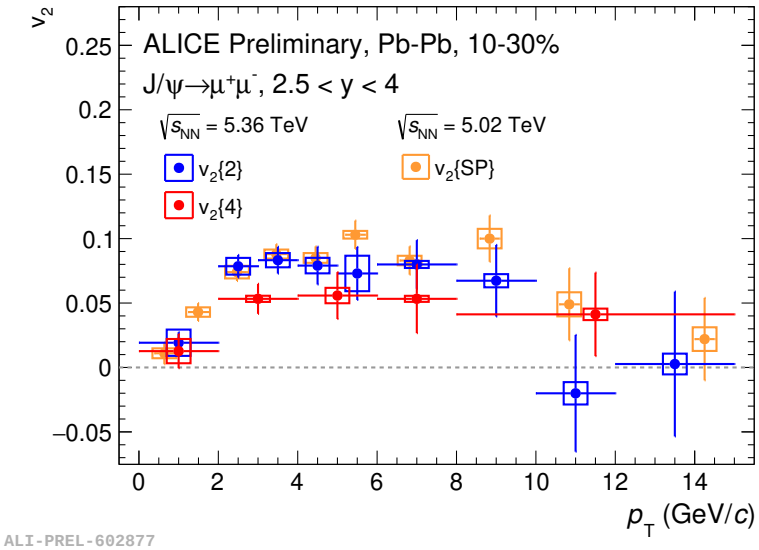

Figure 4.31: The result of J/ψ $v_2\{2\}$ and $v_2\{4\}$ within 10-30% as a function of p_{T} compared to Run 2 result [268].

Indeed, following the first-order approximation of flow fluctuations, the difference is expected to come essentially from the variance of flow coefficient, as discussed in Sec. 4.2.3, because the nonflow contribution is already strongly suppressed with the natural η-gap ($|\Delta\eta| > 1.7$) between POI and RFP and autocorrelation is removed analytically by construction in the cumulant method. The result of the cumulant method is also observed to be consistent with Run 2 data [268], and this is actually a necessary step toward the measurement of flow fluctuations, which shall be discussed in the following section.

4.6.2 . Centrality-differential J/ψ v_2 measurements

The result of centrality-differential J/ψ v_2 measurement at forward rapidity is presented below in Fig. 4.32 for two different p_{T} ranges (0-5 GeV/c and 5-20 GeV/c). In the low-p_{T} region (0-5 GeV/c), the main contribution to the observed v_2 signal is from the in-medium regenerated J/ψ mesons from (partially) thermalized charm quarks. This

mechanism is implemented in many transport models and is necessary for describing J/ψ v_2 in the low-p_T region. The regenerated J/ψ mesons inherit collective flow from in-medium (partially) thermalized charm quarks, the latter with the strong charm-medium (QGP) coupling follows the system anisotropy as the system centrality goes up. However this anisotropy gets counterbalanced toward peripheral collisions as the system energy density and lifetime decrease with smaller overlap region. On the other side, in the high-p_T region (5-20 GeV/c) the primordial production of J/ψ becomes dominant together with expected contribution from non-prompt J/ψ from feed-down of b hadrons.

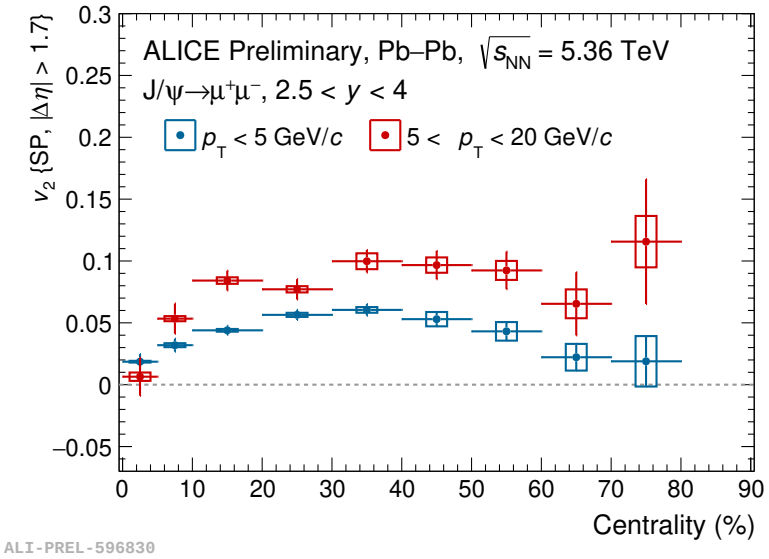

Figure 4.32: Result of centrality-differential J/ψ v_2 measurements in two different p_T ranges (0-5 GeV/c and 5-20 GeV/c).

Since primordial J/ψ mesons are more likely to survive in less-dense regions, a positive v_2 signal starts to develop from central to semi-central collisions as the system anisotropy gets more significant and their in- and out-plane distributions will be modified differently by path-length dependent effects, hence mimicking a flow-like behavior. The same mechanism applies as well to the case of flow contribution from non-prompt J/ψ . The v_2 signal then reaches a maximum at around 20-30%, and tend to get stabilized toward peripheral collisions.

The overall v_2 magnitude in the high-p_T region is slightly higher than in the low-p_T region with about 3σ. In Run 2, this saturation-like behavior at high p_T seems to occur also for other v_2 analysis, including heavy-flavor particles, leading to a picture of a common underlying mechanism, which might be understood in terms of a path-length dependent effect, possibly energy-loss.

4.6.3 . Comparison to heavy-flavor v_2 measurements in Run 3

A comparison of all preliminary heavy-flavor particle v_2 measurements is presented below in Fig. 4.33, where quarkonium v_2 are measured at forward rapidity and D mesons (prompt and non-prompt) are measured at midrapidity.

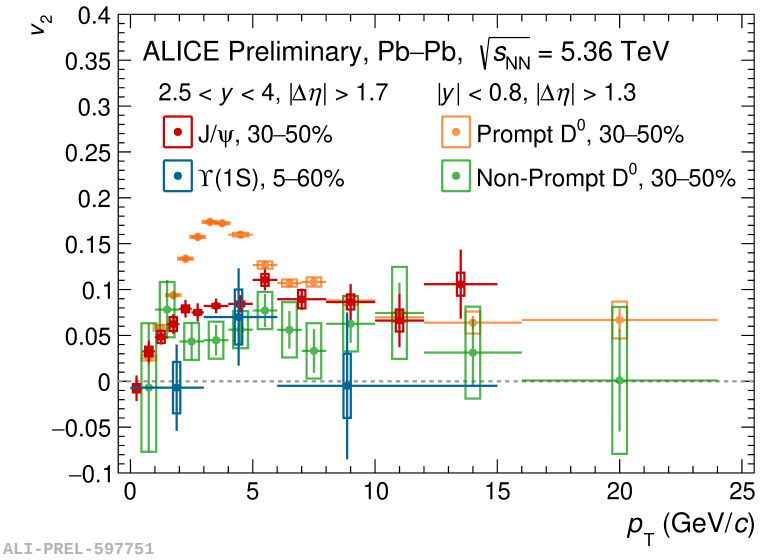

Figure 4.33: A summary of Run 3 heavy-flow v_2 measurement in Pb–Pb collisions at $\sqrt{s_{\rm NN}} = 5.36$ TeV, including inclusive quarkonia v_2 from J/ψ and $\Upsilon(1S)$ at forward rapidity as well as prompt and non-prompt D_0 v_2 at midrapidity.

Comparing inclusive J/ψ v_2 and prompt D^0 v_2 (no B decay contribution) within the same centrality class (30-50%), the measured prompt D^0 v_2 at very low $p_{\rm T}$ (0-3 GeV/c) was found to be consistent with the inclusive J/ψ v_2 . Then J/ψ v_2 shows smaller magnitude at intermediate $p_{\rm T}$ region (3-8 GeV/c)) as J/ψ meson (two charm quarks) requires more energy density to acquire flow compared to open-heavy flavor (one charm and one light quark). While, at the same time, they tend to saturate at the same level of magnitude toward the high-$p_{\rm T}$ region, the latter is likely due to path-length dependent energy-loss. In addition, to investigate the beauty quark behavior, one can also compare $\Upsilon(1S)$ v_2 with non-prompt D^0 v_2 , however the current uncertainties for $\Upsilon(1S)$ v_2 , which are also affected by a more limited reconstruction performance than J/ψ , seems not good enough to draw any conclusion of the flow signal as it appears still compatible to zero across a large range of $p_{\rm T}$.

4.6.4 . First J/ψ flow fluctuation measurement

To conclude the discussion, the first measurement of J/ψ flow fluctuations was carried out in this analysis and shown below in Fig. 4.34. The study of event-by-event flow fluctuations of the J/ψ meson provides crucial insight into the microscopic dynamics of heavy quarks and the mechanisms of charmonium production in the medium. While the

average v_2 reflects the anisotropy of (partially) thermalized charm quarks and the degree of charm–medium coupling (featuring how strongly the charm quarks interact with surrounding QGP medium, usually probed via charm transport coefficients), its event-by-event fluctuations encode the response of charmonia to fluctuations in the initial geometry and to the stochastic nature of charm-quark transport and recombination.

If J/ψ production at low and intermediate p_{T} is dominated by regeneration from (partially) thermalized $c\bar{c}$ pairs, its v_2 fluctuations are expected to correlate strongly with those of the bulk medium, reflecting the same initial-state eccentricity fluctuations. Conversely, if primordial production dominates, the v_2 distribution should exhibit weaker fluctuations and weaker correlation with the bulk flow. The J/ψ flow fluctuations measurement through $\sigma/\langle v_2 \rangle$ provides sensitive constraints on charm-quark thermalization, the relative contribution of regeneration versus primordial components, and the heavy-quark transport properties of the QGP.

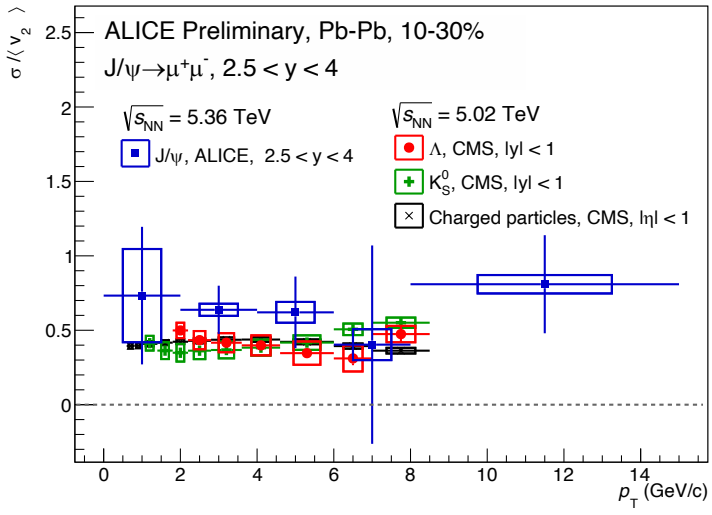

Figure 4.34: Result of inclusive J/ψ flow fluctuations in Pb–Pb collisions within $10\text{-}30\%$ compared with results from CMS [269].

As already discussed in Sec. 4.2.3, the flow fluctuations are extracted by:

$$\frac{\sigma}{\langle v \rangle} = \sqrt{\frac{v_n\{2\}^2 - v_n\{4\}^2}{v_n\{2\}^2 + v_n\{4\}^2}} \tag{4.49}$$

where in this analysis, similar to the measurements done by CMS, for the $v_2\{2\}$ we will use the results from the SP method, which is in principle equivalent to the 2-particle correlation and yet has better performance in terms of statistical uncertainty compared to genuine $v_2\{2\}$ from the cumulant method. In Fig. 4.34, the extracted J/ψ flow fluctuations

at forward rapidity are compared to results for charged-particles and K^0_S mesons, both from CMS [269]. The observed ratio shows a significance with respect to zero of about 2.7σ. The result within current uncertainties is compatible with the charged-particle flow fluctuations at midrapidity. The latter observation suggests a strong charm-medium correlation (supporting the charm thermalization scenario) with the flow of bulk medium and exhibits no significant p_T -dependence with the current uncertainty level. Therefore, the possible non-zero flow fluctuations across a large p_T range is possibly attributed to the fluctuations in the initial geometry.

Chapter 5

Conclusion and outlook

In this thesis, the first ALICE Run 3 measurements of inclusive J/ψ v_2 at forward rapidity in Pb–Pb collisions at $\sqrt{s_{\mathrm{NN}}} = 5.36$ TeV at the LHC were performed with three flow analysis methods including Event-Plane (EP), Scalar Product (SP) and cumulants methods. The analysis was conducted using the Pb–Pb dataset from 2023, and the general results across all three methods were found to be consistent. With the increased size of the dataset of Run 3 giving rise to increased number of J/ψ mesons for the correlation measurements, our analysis was able to be pushed to better precision with finer binning in both p_{T} and centrality compared to Run 2 results, the the resulting smoother trends in differential measurement enabled a detailed look into the mechanism of charm flow development involving competing mechanism from regeneration and suppression. Moreover, with the increased dataset size, higher-order correlations for quarkonium flow measurements became possible, leading to the first ALICE inclusive J/ψ $v_2\{4\}$ and therefore the first look at the inclusive J/ψ flow fluctuations at forward rapidity. The latter provided complementary aspects in quarkonium collectivity studies, and demonstrated the possibility of studying charm-medium coupling and the connection between quarkonium flow and initial geometry.

For p_{T} -differential measurements, our results were found to be consistent with Run 2 measurements across different centrality ranges (0-10%, 10-30% and 30-50%). For non-central collisions, the significant positive v_2 signal at low-p_{T} region confirmed the regeneration description. In addition, with the improved binning in the low-p_{T} region (< 4 GeV/c) for semi-central collisions, the trend of J/ψ v_2 became smoother, allowing more detailed check for the contribution of regenerated J/ψ from recombination of in-medium (partially) thermalized charm quarks. Moreover, the new v_2 Run 3 at high p_{T} (> 6 GeV/c) in non-central collisions showed v_2 signal with better significance with respect to zero, signaling possibly a stronger contribution from path-length dependent effect, but meaningful interpretation should be drawn after a finalization of the current analysis. The corresponding p_{T} -differential J/ψ $v_2\{2\}$ and $v_2\{4\}$ were also presented together with comparison of $v_2\{2\}$ to the EP and SP results as well as the result from Run 2. The $v_2\{2\}$ was found to be consistent following the cross checks, and $v_2\{4\}$ with smaller values compared to

$v_2\{2\}$ was consistent with the prescription of flow fluctuations following the first-order approximation. For centrality-differential measurements, the low- (0-5 GeV/c) and high-p_T ((5-20 GeV/c))) classes are measured respectively. The results also provide improved binning with smoother trends. For the low-p_T class in semi-central collisions the evolution was understood as a combined effect from the regeneration and system anisotropy (also constrained by system size toward peripheral collisions) giving rise to a maximum around 20-30%. For the high-p_T region, the contribution is mostly dominated by path-length difference of primordial J/ψ that survived in low-density system and non-prompt J/ψ which starts to grow around $\sim 5\ \mathrm{GeV}/c$.

The Run 3 J/ψ v_2 result is also compared to other new Run 3 heavy-flavor v_2 measurements in Pb–Pb collisions, including inclusive $\Upsilon(1S)$ at forward rapidity and prompt/non-prompt D^0 at midrapidity. The prompt D^0 v_2 at very low p_T was found to be very close to the inclusive J/ψ v_2 , probably suggesting that the overall energy level was not enough for both particles to fully develop flow. At intermediate p_T , the smaller v_2 of J/ψ compared to prompt D^0 is consistent with a charm thermalized picture following the regeneration description. On the other side, the comparison between $\Upsilon(1S)$ and non-prompt D^0 v_2 suggests that beauty quarks are not thermalized in the medium given the current poor significance of observed v_2 signal with respect to zero.

In addition, the first ALICE Run 3 measurement of inclusive J/ψ flow fluctuations as a function of p_T in Pb–Pb collisions at $\sqrt{s_\mathrm{NN}} = 5.36\ \mathrm{TeV}$ was also presented. Despite the limitation from insufficient data (number of extracted J/ψ mesons) for high-order correlations leading to the poor statistical precision for $v_2\{4\}$, the observed J/ψ flow fluctuations demonstrated a small hint ($\sim 2.7\sigma$) of positive signal with no clear p_T dependence and found to be consistent with charged-particle flow fluctuations from the CMS collaboration, the latter suggests a possible strong charm-medium coupling.

The current results can be still largely improved by including new Pb–Pb data-taking during 2024. At the same time, the full study of systematic uncertainties including track reconstruction efficiency should become soon possible with the incoming finalized Monte Carlo simulation facilities in Run 3.

Appendix A

Residual and derivatives in local picture

In the local picture where the starting point is the invariant local coordinates, we have from 3.2.1:

$$r(p+\Delta p, q+\Delta q) = \underbrace{\Delta R^{-1}\cdot\left[R^{-1}\cdot(q_{\mathrm{glo}}(q+\Delta q)-T)-\Delta T\right]}_{f^{\mathrm{loc}}(p+\Delta p, q+\Delta q)} - m_{loc} \tag{A.1}$$

where in this picture, the delta-transformation ΔR and ΔT are the transformations with respect to the local frame of detection element. Taking the same ordering convention for rotation matrix, the above expression can be then expanded as:

$$\begin{aligned} r(p+\Delta p, q+\Delta q) &= (\mathbb{1}-\Delta)\cdot\left[R^{-1}\cdot(q_{\mathrm{glo}}+\Delta q_{\mathrm{glo}}-T)-\Delta T\right] - R^{-1}(m_{\mathrm{glo}}-T) \\ &= R^{-1}(q_{\mathrm{glo}}-m_{\mathrm{glo}}) + R^{-1}\cdot\Delta q_{\mathrm{glo}} - \Delta\cdot R^{-1}\cdot q_{\mathrm{glo}} - \Delta T \end{aligned} \tag{A.2}$$

then the new linearized equation reads:

$$R^{-1}(q_{\mathrm{glo}}-m_{\mathrm{glo}}) = -R^{-1}\cdot\Delta q_{\mathrm{glo}} + \Delta\cdot R^{-1}\cdot q_{\mathrm{glo}} + \Delta T \tag{A.3}$$

Once again, the z position in the track parametrization has to be calculated using propagation to the misaligned detection element.

Then the resulting alignment parameters evaluated in the local picture can be converted back to global picture via:

$$\begin{aligned} p\cdot\Delta p &= p\cdot\Delta p\cdot p^{-1}p \\ &= \underbrace{\begin{pmatrix} R\cdot\Delta R\cdot R^{-1} & T-R\cdot\Delta R\cdot T-R\cdot\Delta T \\ 0 & 1 \end{pmatrix}}_{\text{Global }\Delta p}\cdot p \end{aligned} \tag{A.4}$$

This local picture possesses particular advantages in constraining the variation of alignment parameters, as the latter reflects directly the proper corrections in contrast to the global frame where the shifts in transverse plane might get huge values in the ALICE frame. Therefore, the convergence of algorithm is better controlled.

Appendix B

Cumulants with weighted Q-vector

The weighted Q-vectors for RFP ($Q_{n,k}$) and POI ($p_{n,k}$) follow:

$$Q_{n,k} = \sum_{i=1}^{M} w_i^k e^{in\phi_i} \quad p_{n,k} = \sum_{i=1}^{m_p} w_i^k e^{in\psi_i}. \tag{B.1}$$

and the quantities relevant for weighted sums are also introduced:

$$\begin{aligned} S_{p,k} &\equiv \left[\sum_{i=1}^{M} w_i^k\right]^p \\ \mathcal{M}_{abcd\ldots} &\equiv \sum_{i\neq j\neq k\neq l}^{M} w_i^a w_j^b w_k^c w_l^d \cdots \\ \mathcal{M}'_{abcd\ldots} &\equiv \sum_{i}^{m_p} \sum_{j\neq k\neq l}^{M} w_i^a w_j^b w_k^c w_l^d \cdots \end{aligned} \tag{B.2}$$

We also introduce weighted single-event 2- and 4-particle correlations for POI and RFP:

$$\begin{aligned} \langle 2\rangle &\equiv \frac{1}{\mathcal{M}_{11}} \sum_{i,j=1}^{M}{}' w_i w_j \, e^{in(\phi_i-\phi_j)} \\ &= \frac{|Q_{n,1}|^2 - S_{1,2}}{S_{2,1} - S_{1,2}} \\ \langle 4\rangle &\equiv \frac{1}{\mathcal{M}_{1111}} \sum_{i,j,k,l=1}^{M}{}' w_i w_j w_k w_l \, e^{in(\phi_i+\phi_j-\phi_k-\phi_l)} \\ &= \left[|Q_{n,1}|^4 + |Q_{2n,2}|^2 - 2\cdot\Re\left[Q_{2n,2}Q_{n,1}^* Q_{n,1}\right]\right. \\ &\quad \left. + 8\cdot\Re\left[Q_{n,3}Q_{n,1}^*\right] - 4\cdot S_{1,2}|Q_{n,1}|^2 - 6\cdot S_{1,4} - 2\cdot S_{2,2}\right]/\mathcal{M}_{1111} \end{aligned} \tag{B.3}$$

$$
\begin{aligned}
\langle 2' \rangle &\equiv \frac{1}{\mathcal{M}'_{01}} \sum_{i=1}^{m_p} \sum_{j=1}^{M} {}' w_j \, e^{in(\psi_i - \phi_j)} \\
&= \frac{p_{n,0} Q^*_{n,1}}{m_p S_{1,1}} \\
\langle 4' \rangle &\equiv \frac{1}{\mathcal{M}'_{0111}} \sum_{i=1}^{m_p} \sum_{j,k,l=1}^{M} {}' w_j w_k w_l \, e^{in(\psi_i + \phi_j - \phi_k - \phi_l)} \\
&= \big[p_{n,0} Q_{n,1} Q^*_{n,1} Q^*_{n,1} - p_{n,0} Q_{n,1} Q^*_{2n,2} - 2 \cdot S_{1,2} p_{n,0} Q^*_{n,1} \\
&+ 2 \cdot p_{n,0} Q^*_{n,3} \big] / \mathcal{M}'_{0111}
\end{aligned}
\tag{B.4}
$$

And the corresponding event-averaged correlations read:

$$
\begin{aligned}
\langle\langle 2 \rangle\rangle &= \frac{\sum_{i=1}^{N} (\mathcal{M}_{11})_i \langle 2 \rangle_i}{\sum_{i=1}^{N} (\mathcal{M}_{11})_i} \\
\mathcal{M}_{11} &\equiv \sum_{i,j=1}^{M} {}' w_i w_j = S_{2,1} - S_{1,2}
\end{aligned}
\tag{B.5}
$$

$$
\begin{aligned}
\langle\langle 4 \rangle\rangle &= \frac{\sum_{i=1}^{N} (\mathcal{M}_{1111})_i \langle 4 \rangle_i}{\sum_{i=1}^{N} (\mathcal{M}_{1111})_i} \\
\mathcal{M}_{1111} &\equiv \sum_{i,j,k,l=1}^{M} {}' w_i w_j w_k w_l \\
&= S_{4,1} - 6 \cdot S_{1,2} S_{2,1} + 8 \cdot S_{1,3} S_{1,1} + 3 \cdot S_{2,2} - 6 \cdot S_{1,4}
\end{aligned}
\tag{B.6}
$$

$$
\begin{aligned}
\langle\langle 2' \rangle\rangle &= \frac{\sum_{i=1}^{N} (\mathcal{M}'_{01})_i \langle 2' \rangle_i}{\sum_{i=1}^{N} (\mathcal{M}'_{01})_i} \\
\mathcal{M}'_{01} &\equiv \sum_{i=1}^{m_p} \sum_{j=1}^{M} {}' w_j \\
&= m_p S_{1,1}
\end{aligned}
\tag{B.7}
$$

$$
\begin{aligned}
\langle\langle 4' \rangle\rangle &= \frac{\sum_{i=1}^{N} (\mathcal{M}'_{0111})_i \langle 4' \rangle_i}{\sum_{i=1}^{N} (\mathcal{M}'_{0111})_i} \\
\mathcal{M}'_{0111} &\equiv \sum_{i=1}^{m_p} \sum_{j,k,l=1}^{M} {}' w_j w_k w_l \\
&= m_p \big[S_{3,1} - 3 \cdot S_{1,1} S_{1,2} + 2 \cdot S_{1,3} \big]
\end{aligned}
\tag{B.8}
$$

Appendix C

Run list for dataset used in the analysis

The data sample periods used for this analysis are: **LHC23zzf**, **LHC23zzg**, **LHC23zzh**, **LHC23zzi**, **LHC23zzk**, **LHC23zzl**, **LHC23zzm**, **LHC23zzn**, **LHC23zzo** for a total of 90 runs. The following Quality Control flags are checked and are requested to follow the **CBT_muon** criteria defined for the 2024 data-taking period:

1. FT0, ITS, MCH, MID detectors with `Good` or `Limited Acceptance and MC reproducible`
2. TPC with `Good` or `Limited Acceptance and MC reproducible` or `Bad PID`

The list of the corresponding runs, grouped by data-taking periods, is reported in below:

Period	Runlist
LHC23zzf	544013
LHC23zzg	544028, 544032
LHC23zzh	544091, 544095, 544098, 544116, 544121, 544122, 544123, 544124
LHC23zzi	544184, 544185, 544389, 544390, 544391, 544392
LHC23zzk	544454, 544474, 544475, 544476, 544477, 544490, 544491, 544492, 544508, 544510, 544511, 544512
LHC23zzl	544548, 544549, 544550, 544551, 544564, 544565, 544567, 544568, 544580, 544582, 544583, 544585
LHC23zzm	544614, 544652, 544653, 544672, 544674, 544692, 544693, 544694, 544696, 544739, 544742, 544754, 544767
LHC23zzn	544795, 544813
LHC23zzo	544868, 544887, 544917, 544931, 544961, 544963, 544964, 544968, 545004, 545008, 545009, 545041, 545044, 545047, 545060, 545062, 545063, 545086, 545103, 545117, 545184, 545185, 545210, 545222, 545223, 545246, 545249, 545262, 545289, 545291, 545295, 545311, 545312, 545345

Appendix D

Functions used for signal extraction

D.1 Signal shapes

D.1.1 . Double-Sided Crystal Ball (CB2) function

$$f(x; N, \bar{x}, \sigma, \alpha_L, \alpha_R, n_L, n_R) = N \cdot \begin{cases} A \cdot (B - t)^{-n_L} & , t \leq \alpha_L \\ \exp\left(-\frac{1}{2}t^2\right) & , \alpha_L < t < \alpha_R \\ C \cdot (D + t)^{-n_R} & , t \geq \alpha_R \end{cases} \tag{D.1}$$

where

$$\begin{aligned} t &= \frac{x - \bar{x}}{\sigma} \\ A &= \left(\frac{n_L}{|\alpha_L|}\right)^{n_L} \cdot \exp\left(-\frac{|\alpha_L|^2}{2}\right) \\ B &= \frac{n_L}{|\alpha_L|} - |\alpha_L| \\ C &= \left(\frac{n_R}{|\alpha_R|}\right)^{n_R} \cdot \exp\left(-\frac{|\alpha_R|^2}{2}\right) \\ D &= \frac{n_R}{|\alpha_R|} - |\alpha_R| \end{aligned}$$

D.1.2 . NA60 function

$$f(x; N, \bar{x}, \sigma, t_1, t_2, p_1, p_2, p_3, p_4, p_5, p_6) = N \cdot \exp\left(-\frac{1}{2}\left(\frac{t}{t_0}\right)^2\right) \tag{D.2}$$

where

$$t = \frac{x - \bar{x}}{\sigma}$$

and

$$t_0 = \begin{cases} 1 + (p_1(t_1 - t))^{p_2 - p_3\sqrt{t_1 - t}} & , t \leq t_1 \\ 1 & , t_1 < t < t_2 \\ 1 + (p_4(t - t_2))^{p_5 - p_6\sqrt{t - t_2}} & , t \geq t_2 \end{cases}$$

D.2 Background shapes

D.2.1 . Variable-Width Gaussian (VWG) function

D.2.2 . Chebyshev polynomials

Chebyshev polynomials of the first kind can be defined recurrently using the first two polynomials:

$$\begin{aligned} T_0(x) &= 1 \\ T_1(x) &= x \\ T_{n+1}(x) &= 2x\,T_n(x) - T_{n-1}(x) \end{aligned} \tag{D.3}$$

from where the first 6 polynomials read:

$$\begin{aligned} T_0(x) &= 1, \\ T_1(x) &= x, \\ T_2(x) &= 2x^2 - 1, \\ T_3(x) &= 4x^3 - 3x, \\ T_4(x) &= 8x^4 - 8x^2 + 1, \\ T_5(x) &= 16x^5 - 20x^3 + 5x \end{aligned} \tag{D.4}$$

An arbitrary parametrization up to order n using Chebyshev polynomials can be written as:

$$f(x) = \sum_{i=0}^{n} a_i \cdot T_i(x) \tag{D.5}$$

Résumé en français

Cette thèse est consacrée à l'étude expérimentale de la collectivité du quarkonium dans les collisions Pb–Pb ultra-relativistes au LHC avec une énergie dans le centre de masse $\sqrt{s_{\mathrm{NN}}} = 5.36\ \mathrm{TeV}$, dans le cadre du Run 3. Les quarkonia, et en particulier le J/ψ , constituent des sondes privilégiées du QGP, car leur production et leur évolution dynamique sont fortement sensibles aux propriétés du milieu chaud et dense créé dans les collisions d'ions lourds.

Après une introduction générale aux fondements théoriques de la chromodynamique quantique pour l'interaction forte, à la formation du QGP et à la dynamique des collisions d'ions lourds, le manuscrit présente les principales signatures expérimentales de ce nouvel état de la matière, en mettant l'accent sur le flot anisotropique. Le flot elliptique, caractérisé par le coefficient v_2 , constitue une observable clé permettant de sonder la réponse collective du milieu aux anisotropies géométriques initiales et permet d'évaluer le degré de thermalisation des particules produites. Dans le cas des quarkonia, la mesure d'un v_2 non nul apporte des informations essentielles sur les mécanismes de suppression, de régénération (par recombinaison de quarks) et de transport des paires quark–antiquark lourdes dans le QGP.

Une partie substantielle du travail de thèse décrit ici est dédiée à la description de l'appareillage expérimental, et plus particulièrement du spectromètre à muons de ALICE. Dans le contexte du Run 3, marqué par des améliorations majeures du détecteur et du système d'acquisition, une étape cruciale du travail a consisté en l'alignement précis du système de trajectographie du spectromètre à muons. Une méthode d'alignement basée sur les traces, reposant sur l'algorithme `MillePedeII`, a été mise en oeuvre, et validée par le contrôle des paramètres d'alignement. L'impact de cet alignement dans le cadre du Run 3 sur la performance de reconstruction a été étudié en détail, notamment à travers l'amélioration de la résolution en masse invariante du J/ψ et la stabilité des paramètres de reconstruction. Ce travail d'instrumentation constitue un préalable indispensable à l'analyse physique présentée dans la suite du manuscrit.

L'analyse du flot elliptique du J/ψ est réalisée dans le canal de désintégration dimuon à rapidité vers l'avant. Plusieurs méthodes complémentaires sont employées afin d'extraire le coefficient v_2 : la méthode du plan d'événement, la méthode du produit scalaire et les

méthodes par cumulants multi-particules. Une attention particulière est portée à la calibration des vecteurs Q, aux corrections d'acceptance non-uniforme, ainsi qu'à l'estimation rigoureuse des incertitudes systématiques. Les différentes méthodes sont comparées entre elles afin d'évaluer la robustesse des résultats et de contrôler les biais méthodologiques.

Les mesures du flot elliptique du J/ψ obtenues dans cette analyse mettent en évidence, avec des granularités améliorées grâce au Run 3 par rapport au Run 2, un coefficient v_2 significativement différent de zéro dans une large plage de centralité et d'impulsion transverse, en particulier à bas et intermédiaire p_{T} . Ce comportement est difficilement conciliable avec un scénario de production purement primordiale suivi uniquement d'une suppression dans le milieu, et indique donc une contribution non négligeable du mécanisme de régénération par recombinaison des quarks charm (partiellement) thermalisés dans le QGP. La dépendance en p_{T} du v_2 , caractérisée par une augmentation à bas p_{T} suivie d'une atténuation aux p_{T} plus élevés, suggère que la composante régénérée hérite partiellement de l'anisotropie collective du milieu, tandis que la composante primordiale reste faiblement couplée à la dynamique collective. La comparaison avec les mesures de flot des mésons à saveur lourde ouverte et des hadrons légers montre que l'amplitude du v_2 du J/ψ est inférieure à celle des particules légères, mais du même ordre de grandeur que celle des hadrons contenant un quark charm, ce qui est compatible avec une thermalisation partielle des quarks charm dans le QGP. Par ailleurs, la dépendance en centralité du v_2 reflète la compétition entre l'anisotropie géométrique initiale et la dilution de l'effet de régénération dans les collisions les plus centrales. Enfin, l'étude exploratoire des fluctuations du flot du J/ψ indique que l'anisotropie mesurée est sensible aux fluctuations événement par événement de la géométrie initiale, fournissant ainsi une contrainte nouvelle sur les modèles de transport couplant production du quarkonium et évolution hydrodynamique du milieu.

En conclusion, ce travail combine des contributions essentielles à l'instrumentation, au développement méthodologique et à l'analyse physique, et s'inscrit pleinement dans le programme de physique du Run 3 du LHC. Les perspectives ouvertes par l'augmentation de la statistique et par les améliorations expérimentales laissent entrevoir des études encore plus précises de la collectivité des quarkonia dans les années à venir.

Acronyms

ALICE A Large Ion Collider Experiment.

ALPIDE ALICE Pixel Detector.

AOT Analysis Objects and Tools.

ATLAS A Toroidal LHC Apparatus.

BC Bunch Crossing.

BCS theory Bardeen–Cooper–Schrieffer theory.

CB2 Double-Sided Crystal Ball.

CCDB Condition and Calibration Data Base.

CE Canonical Ensemble.

CEM Color-Evaporation Model.

CERN Conseil européen pour la recherche nucléaire.

CGC Color-Glass Condensate.

CIM Comover Interaction Model.

CMS Compact Muon Solenoid.

CNM Cold Nuclear Matter.

COM Color-Octet Model.

CPC Cathode Pad Chamber.

CRU Common Readout Unit.

CSM Color-Singlet Model.

CTF Compressed Time-Frame.

DCA Distance of the Closest Approach.

DF Data Frame.

DIS Deep Inelastic Scattering.

DPG Data Preparation Group.

DRM Dual Resonance Model.

EKT Effective Kinetic Theory.

EoS Equation of State.

EP Event-Plane.

ESE Event-Shape Engineering.

FCC Future Circular Collider.

FDD Forward Diffractive Detector.

FGMRES Flexible Generalized Minimal Residual Method.

FIT Fast Interaction Trigger.

FONLL Fixed-Order plus Next-to-Leading Logarithms.

FRG Functional Renormalization Group.

FTo Fast Timing and Trigger.

FVo Fast Vo.

GCE Grand Canonical Ensemble.

GEM Gas Electron Multipliers.

GMRES Generalized Minimal Residual Method.

GMS Geometrical Monitoring System.

HB HeartBeat.

HERA Hadron Elektron Ring Anlage.

HL-LHC High-Luminosity LHC.

HTL Hard-Thermal Loop.

IB Inner Barrel.

IP Interaction Point.

IR Infra-red.

ISR Intersecting Storage Ring.

ITS Inner Tracking System.

ITSAMS ITS Alignment Monitoring System.

LBT Linear Boltzmann Transport.

LDMEs Long-Distance Matrix Elements.

LEP Large Electron–Positron Collider.

LHC Large Hadron Collider.

LHCb Large Hadron Collider beauty.

LO Leading-Order.

LS Long-Shutdown.

LSSs Long straight sections.

LYZ Lee-Yang Zero.

MAPS Monolithic Active Pixel Sensors.

MCH Muon Chambers.

MCP-PMT Micro-Channel Plate Photomultiplier.

MCS Multiple Coulomb Scattering.

MFT Muon Forward Tracker.

MGF Moment Generating Function.

MID Muon Identifier.

MINRES Minimal Residual Method.

MLEM Maximum-Likelihood-Expectation Maximization.

MWPC Multi Wire Proportional Chamber.

NBD Negative Binominal Distribution.

NCQ Number of Constituent Quarks.

NLO Next to Leading Order.

NRQCD Non-Relativistic Quantum chromodynamics.

NUA Non-Uniform Acceptance.

NUE Non-Uniform Efficiency.

O2 Online-Offline.

OB Outer Barrel.

PDF Parton Distribution Function.

PDG Particle Data Group.

POI Particle of Interest.

PV Primary Vertex.

QC Quality Control.

QCD Quantum Chromodynamics.

QED Quantum Electrodynamics.

QGP Quark-Gluon Plasma.

RFP Reference Particle.

RHIC Relativistic Heavy Ion Collider.

RMS Root Mean Square.

ROF ReadOut Frame.

RPC Resistive Plate Chambers.

RRM Resonance Recombination Model.

SAMPA Scalable Amplifier and ADC.

SDCs Short-Distance Coefficients.

SHM Statistical Hadronization Model.

SiPM Silicon Photomultiplier.

SLAC Stanford Linear Accelerator Center.

SM Standard Model.

SMCs Space-Momentum Correlations.

SNR Signal-to-Noise Ratio.

SP Scalar Product.

SPS Super Proton Synchrotron.

SSB Spontaneous Symmetry Breaking.

TF Time-Frame.

TPC Time Projection Chamber.

TRENTo Transport-Relativistic Events iNiTial cOnditions.

TS Technical Stop.

UV Ultra-violet.

VEV Vacuum Expectation Value.

VWG Variable-Width Gaussian.

WLCG The Worldwide LHC Computing Grid.

ZDC Zero-Degree Calorimeter.

Bibliography

[1] R. P. Feynman. "The behavior of hadron collisions at extreme energies". In: *Conf. Proc. C* 690905 (1969), pp. 237–258.

[2] Murray Gell-Mann. "The Eightfold Way: A Theory of strong interaction symmetry". In: (Mar. 1961). doi: 10.2172/4008239.

[3] Wikimedia Commons. *The physicists Paul Dirac, Wolfgang Pauli and Rudolf Peierls, c 1953. (9660575591).jpg — Wikimedia Commons*. 2024. url: https://commons.wikimedia.org/w/index.php?title=File:The_physicists_Paul_Dirac,_Wolfgang_Pauli_and_Rudolf_Peierls,_c_1953._(9660575591).jpg&oldid=895702798.

[4] Paul A. M. Dirac. "The quantum theory of the electron". In: *Proc. Roy. Soc. Lond. A* 117 (1928), pp. 610–624. doi: 10.1098/rspa.1928.0023.

[5] H. A. Bethe. "The Electromagnetic shift of energy levels". In: *Phys. Rev.* 72 (1947), pp. 339–341. doi: 10.1103/PhysRev.72.339.

[6] S. Tomonaga. "On a relativistically invariant formulation of the quantum theory of wave fields". In: *Prog. Theor. Phys.* 1 (1946), pp. 27–42. doi: 10.1143/PTP.1.27.

[7] Julian S. Schwinger. "Quantum electrodynamics. I A covariant formulation". In: *Phys. Rev.* 74 (1948). Ed. by K. A. Milton, p. 1439. doi: 10.1103/PhysRev.74.1439.

[8] R. P. Feynman. "Space - time approach to quantum electrodynamics". In: *Phys. Rev.* 76 (1949). Ed. by L. M. Brown, pp. 769–789. doi: 10.1103/PhysRev.76.769.

[9] F. J. Dyson. "The Radiation theories of Tomonaga, Schwinger, and Feynman". In: *Phys. Rev.* 75 (1949), pp. 486–502. doi: 10.1103/PhysRev.75.486.

[10] Y. Aharonov and D. Bohm. "Significance of Electromagnetic Potentials in the Quantum Theory". In: *Phys. Rev.* 115 (3 Aug. 1959), pp. 485–491. doi: 10.1103/PhysRev.115.485. url: https://link.aps.org/doi/10.1103/PhysRev.115.485.

[11] H. Weyl. *The Theory of Groups and Quantum Mechanics*. New York: Dover Publishing Company Inc., 1950.

[12] Wolfgang Pauli. *Wissenschaftlicher Briefwechsel*. Ed. by Karl von Meyenn. Vol. IV. Part II. Berlin, Heidelberg: Springer-Verlag, 1999.

[13] Chen-Ning Yang and Robert L. Mills. "Conservation of Isotopic Spin and Isotopic Gauge Invariance". In: *Phys. Rev.* 96 (1954). Ed. by Jong-Ping Hsu and D. Fine, pp. 191–195. doi: 10.1103/PhysRev.96.191.

[14] Tai Tsun Wu and Chen Ning Yang. "Concept of nonintegrable phase factors and global formulation of gauge fields". In: *Phys. Rev. D* 12 (12 Dec. 1975), pp. 3845–3857. doi: 10.1103/PhysRevD.12.3845. url: https://link.aps.org/doi/10.1103/PhysRevD.12.3845.

[15] Wikimedia Commons. *Standard Model of Elementary Particles.svg — Wikimedia Commons*. 2025. url: https://commons.wikimedia.org/w/index.php?title=File:Standard_Model_of_Elementary_Particles.svg&oldid=1062088276.

[16] C. S. Wu et al. "Experimental Test of Parity Conservation in Beta Decay". In: *Phys. Rev.* 105 (4 Feb. 1957), pp. 1413–1415. doi: 10.1103/PhysRev.105.1413. url: https://link.aps.org/doi/10.1103/PhysRev.105.1413.

[17] Yoichiro Nambu. "Quasi-Particles and Gauge Invariance in the Theory of Superconductivity". In: *Phys. Rev.* 117 (3 Feb. 1960), pp. 648–663. doi: 10.1103/PhysRev.117.648. url: https://link.aps.org/doi/10.1103/PhysRev.117.648.

[18] J. Goldstone. "Field Theories with Superconductor Solutions". In: *Nuovo Cim.* 19 (1961), pp. 154–164. doi: 10.1007/BF02812722.

[19] S. Elitzur. "Impossibility of spontaneously breaking local symmetries". In: *Phys. Rev. D* 12 (12 Dec. 1975), pp. 3978–3982. doi: 10.1103/PhysRevD.12.3978. url: https://link.aps.org/doi/10.1103/PhysRevD.12.3978.

[20] M. Gell-Mann. "A schematic model of baryons and mesons". In: *Physics Letters* 8.3 (1964), pp. 214–215. issn: 0031-9163. doi: https://doi.org/10.1016/S0031-9163(64)92001-3. url: https://www.sciencedirect.com/science/article/pii/S0031916364920013.

[21] G. Zweig. "An SU(3) model for strong interaction symmetry and its breaking. Version 1". In: (Jan. 1964). doi: 10.17181/CERN-TH-401.

[22] Wikipedia contributors. *Eightfold way (physics) — Wikipedia, The Free Encyclopedia*. https://en.wikipedia.org/w/index.php?title=Eightfold_way_(physics)&oldid=1303187496. [Online; accessed 29-September-2025]. 2025.

[23] H. Fritzsch, Murray Gell-Mann, and H. Leutwyler. "Advantages of the Color Octet Gluon Picture". In: *Phys. Lett. B* 47 (1973), pp. 365–368. doi: 10.1016/0370-2693(73)90625-4.

[24] John Collins. *Foundations of Perturbative QCD*. Vol. 32. Cambridge University Press, 2011. isbn: 978-1-009-40184-5, 978-1-009-40183-8, 978-1-009-40182-1. doi: 10.1017/9781009401845.

[25] R. P. Feynman. "Space-time approach to nonrelativistic quantum mechanics". In: *Rev. Mod. Phys.* 20 (1948), pp. 367–387. doi: 10.1103/RevModPhys.20.367.

[26] L.D. Faddeev and V.N. Popov. "Feynman diagrams for the Yang-Mills field". In: *Physics Letters B* 25.1 (1967), pp. 29–30. issn: 0370-2693. doi: https://doi.org/10.1016/0370-2693(67)90067-6. url: https://www.sciencedirect.com/science/article/pii/0370269367900676.

[27] C. Becchi, A. Rouet, and R. Stora. "The abelian Higgs Kibble model, unitarity of the S-operator". In: *Physics Letters B* 52.3 (1974), pp. 344–346. issn: 0370-2693. doi: https://doi.org/10.1016/0370-2693(74)90058-6. url: https://www.sciencedirect.com/science/article/pii/0370269374900586.

[28] I. V. Tyutin. *Gauge Invariance in Field Theory and Statistical Physics in Operator Formalism*. 2008. arXiv: 0812.0580 [hep-th]. url: https://arxiv.org/abs/0812.0580.

[29] T. Kinoshita and A. Ukawa. "Mass Singularities of Feynman Amplitudes". In: *Lect. Notes Phys.* 39 (1975). Ed. by Huzihiro Araki, pp. 55–58. doi: 10.1007/BFb0013300.

[30] T. D. Lee and M. Nauenberg. "Degenerate Systems and Mass Singularities". In: *Phys. Rev.* 133 (6B Mar. 1964), B1549–B1562. doi: 10.1103/PhysRev.133.B1549. url: https://link.aps.org/doi/10.1103/PhysRev.133.B1549.

[31] Curtis G. Callan. "Broken Scale Invariance in Scalar Field Theory". In: *Phys. Rev. D* 2 (8 Oct. 1970), pp. 1541–1547. doi: 10.1103/PhysRevD.2.1541. url: https://link.aps.org/doi/10.1103/PhysRevD.2.1541.

[32] K. Symanzik. "Small distance behavior in field theory and power counting". In: *Commun. Math. Phys.* 18 (1970), pp. 227–246. doi: 10.1007/BF01649434.

[33] K. Symanzik. "Small distance behavior analysis and Wilson expansion". In: *Commun. Math. Phys.* 23 (1971), pp. 49–86. doi: 10.1007/BF01877596.

[34] J. I. Kapusta and Charles Gale. *Finite-temperature field theory: Principles and applications*. Cambridge Monographs on Mathematical Physics. Cambridge University Press, 2011. isbn: 978-0-521-17322-3, 978-0-521-82082-0, 978-0-511-22280-1. doi: 10.1017/CBO9780511535130.

[35] David d'Enterria et al. *High-precision α_s measurements from LHC to FCC-ee*. 2015. arXiv: 1512.05194 [hep-ph]. url: https://arxiv.org/abs/1512.05194.

[36] S. Navas et al. “Review of Particle Physics”. In: *Phys. Rev. D* 110 (3 Aug. 2024), p. 030001. doi: 10.1103/PhysRevD.110.030001. url: https://link.aps.org/doi/10.1103/PhysRevD.110.030001.

[37] Kenneth G. Wilson. “Confinement of quarks”. In: *Phys. Rev. D* 10 (8 Oct. 1974), pp. 2445–2459. doi: 10.1103/PhysRevD.10.2445. url: https://link.aps.org/doi/10.1103/PhysRevD.10.2445.

[38] A.M. Polyakov. “Compact gauge fields and the infrared catastrophe”. In: *Physics Letters B* 59.1 (1975), pp. 82–84. issn: 0370-2693. doi: https://doi.org/10.1016/0370-2693(75)90162-8. url: https://www.sciencedirect.com/science/article/pii/0370269375901628.

[39] K. Johnson. “The M.I.T. Bag Model”. In: *Acta Phys. Polon. B* 6 (1975), p. 865.

[40] Michael E. Peskin and Daniel V. Schroeder. *An Introduction to quantum field theory*. Reading, USA: Addison-Wesley, 1995. isbn: 978-0-201-50397-5, 978-0-429-50355-9, 978-0-429-49417-8. doi: 10.1201/9780429503559.

[41] Slavo Kratochvila and Philippe de Forcrand. “Observing string breaking with Wilson loops”. In: *Nuclear Physics B* 671 (Nov. 2003), pp. 103–132. issn: 0550-3213. doi: 10.1016/j.nuclphysb.2003.08.014. url: http://dx.doi.org/10.1016/j.nuclphysb.2003.08.014.

[42] T. Regge. “Introduction to complex orbital momenta”. In: *Nuovo Cim.* 14 (1959), p. 951. doi: 10.1007/BF02728177.

[43] G. Veneziano. “Construction of a crossing - symmetric, Regge behaved amplitude for linearly rising trajectories”. In: *Nuovo Cim. A* 57 (1968), pp. 190–197. doi: 10.1007/BF02824451.

[44] E V Shuryak. “Theory of hadron plasma”. In: *Sov. Phys. - JETP (Engl. Transl.); (United States)* 47:2 (Jan. 1978). issn: ISSN SPHJA. url: https://www.osti.gov/biblio/6583653.

[45] John Bardeen, L. N. Cooper, and J. R. Schrieffer. “Theory of superconductivity”. In: *Phys. Rev.* 108 (1957), pp. 1175–1204. doi: 10.1103/PhysRev.108.1175.

[46] Murray Gell-Mann, R. J. Oakes, and B. Renner. “Behavior of current divergences under SU(3) x SU(3)”. In: *Phys. Rev.* 175 (1968), pp. 2195–2199. doi: 10.1103/PhysRev.175.2195.

[47] Roman W. Jackiw. “Axial anomaly”. In: *Int. J. Mod. Phys. A* 25 (2010), pp. 659–667. doi: 10.1142/S0217751X10048391.

[48] J. S. Bell and R. Jackiw. “A PCAC puzzle: $\pi^0 \to \gamma\gamma$ in the σ model”. In: *Nuovo Cim. A* 60 (1969), pp. 47–61. doi: 10.1007/BF02823296.

[49] Y. Nambu and G. Jona-Lasinio. “Dynamical Model of Elementary Particles Based on an Analogy with Superconductivity. I”. In: *Phys. Rev.* 122 (1 Apr. 1961), pp. 345–358. doi: 10.1103/PhysRev.122.345. url: https://link.aps.org/doi/10.1103/PhysRev.122.345.

[50] Chun Shen et al. “The iEBE-VISHNU code package for relativistic heavy-ion collisions”. In: *Comput. Phys. Commun.* 199 (2016), pp. 61–85. doi: 10.1016/j.cpc.2015.08.039. arXiv: 1409.8164 [nucl-th].

[51] H. G. Pugh. “SEARCH FOR THE QUARK - GLUON PLASMA (1989): THE NA35 EXPERIMENT AT THE CERN SPS”. In: *Phys. Scripta T* 32 (1990), pp. 208–217. doi: 10.1088/0031-8949/1990/T32/035.

[52] I. Arsene et al. “Quark gluon plasma and color glass condensate at RHIC? The Perspective from the BRAHMS experiment”. In: *Nucl. Phys. A* 757 (2005), pp. 1–27. doi: 10.1016/j.nuclphysa.2005.02.130. arXiv: nucl-ex/0410020.

[53] B. B. Back et al. “The PHOBOS perspective on discoveries at RHIC”. In: *Nucl. Phys. A* 757 (2005), pp. 28–101. doi: 10.1016/j.nuclphysa.2005.03.084. arXiv: nucl-ex/0410022.

[54] K. Adcox et al. “Formation of dense partonic matter in relativistic nucleus-nucleus collisions at RHIC: Experimental evaluation by the PHENIX collaboration”. In: *Nucl. Phys. A* 757 (2005), pp. 184–283. doi: 10.1016/j.nuclphysa.2005.03.086. arXiv: nucl-ex/0410003.

[55] John Adams et al. “Experimental and theoretical challenges in the search for the quark gluon plasma: The STAR Collaboration’s critical assessment of the evidence from RHIC collisions”. In: *Nucl. Phys. A* 757 (2005), pp. 102–183. doi: 10.1016/j.nuclphysa.2005.03.085. arXiv: nucl-ex/0501009.

[56] Michael L. Miller et al. “Glauber Modeling in High-Energy Nuclear Collisions”. In: *Annual Review of Nuclear and Particle Science* 57.1 (Nov. 2007), pp. 205–243. issn: 1545-4134. doi: 10.1146/annurev.nucl.57.090506.123020. url: http://dx.doi.org/10.1146/annurev.nucl.57.090506.123020.

[57] R. J. Glauber. “High Energy Collision Theory”. In: *Lectures in Theoretical Physics*. Ed. by W. E. Brittin and L. G. Dunham. Vol. 1. New York: Interscience, 1959, p. 315.

[58] LHCb collaboration et al. *Centrality determination in heavy-ion collisions with the LHCb detector*. 2021. arXiv: 2111.01607 [nucl-ex]. url: https://arxiv.org/abs/2111.01607.

[59] J. D. Bjorken. “Highly Relativistic Nucleus-Nucleus Collisions: The Central Rapidity Region”. In: *Phys. Rev. D* 27 (1983), pp. 140–151. doi: 10.1103/PhysRevD.27.140.

[60] L. D. Landau. “On the multiparticle production in high-energy collisions”. In: *Izv. Akad. Nauk SSSR Ser. Fiz.* 17 (1953), p. 51.

[61] S. Z. Belenkij and L. D. Landau. "Hydrodynamic theory of multiple production of particles". In: *Usp. Fiz. Nauk* 56 (1955), p. 309. doi: 10.1007/BF02745507.

[62] J. Scott Moreland, Jonah E. Bernhard, and Steffen A. Bass. "Alternative ansatz to wounded nucleon and binary collision scaling in high-energy nuclear collisions". In: *Phys. Rev. C* 92 (1 July 2015), p. 011901. doi: 10.1103/PhysRevC.92.011901. url: https://link.aps.org/doi/10.1103/PhysRevC.92.011901.

[63] G. Altarelli and G. Parisi. "Asymptotic freedom in parton language". In: *Nuclear Physics B* 126.2 (1977), pp. 298–318. issn: 0550-3213. doi: https://doi.org/10.1016/0550-3213(77)90384-4. url: https://www.sciencedirect.com/science/article/pii/0550321377903844.

[64] Yuri L. Dokshitzer. "Calculation of the Structure Functions for Deep Inelastic Scattering and e+ e- Annihilation by Perturbation Theory in Quantum Chromodynamics." In: *Sov. Phys. JETP* 46 (1977), pp. 641–653.

[65] V. N. Gribov and L. N. Lipatov. "Deep inelastic e p scattering in perturbation theory". In: *Sov. J. Nucl. Phys.* 15 (1972), pp. 438–450.

[66] E. A. Kuraev, L. N. Lipatov, and Victor S. Fadin. "The Pomeranchuk singularity in nonabelian gauge theories". In: *Sov. Phys. JETP* 45 (1977), pp. 199–204.

[67] I. I. Balitsky and L. N. Lipatov. "The Pomeranchuk Singularity in Quantum Chromodynamics". In: *Sov. J. Nucl. Phys.* 28 (1978), pp. 822–829.

[68] J. Scott Moreland, Jonah E. Bernhard, and Steffen A. Bass. "Alternative ansatz to wounded nucleon and binary collision scaling in high-energy nuclear collisions". In: *Physical Review C* 92.1 (July 2015). issn: 1089-490X. doi: 10.1103/physrevc.92.011901. url: http://dx.doi.org/10.1103/PhysRevC.92.011901.

[69] Larry McLerran and Raju Venugopalan. "Computing quark and gluon distribution functions for very large nuclei". In: *Phys. Rev. D* 49 (5 Mar. 1994), pp. 2233–2241. doi: 10.1103/PhysRevD.49.2233. url: https://link.aps.org/doi/10.1103/PhysRevD.49.2233.

[70] Larry McLerran and Raju Venugopalan. "Gluon distribution functions for very large nuclei at small transverse momentum". In: *Phys. Rev. D* 49 (7 Apr. 1994), pp. 3352–3355. doi: 10.1103/PhysRevD.49.3352. url: https://link.aps.org/doi/10.1103/PhysRevD.49.3352.

[71] Larry McLerran and Raju Venugopalan. "Green's function in the color field of a large nucleus". In: *Physical Review D* 50.3 (Aug. 1994), pp. 2225–2233. issn: 0556-2821. doi: 10.1103/physrevd.50.2225. url: http://dx.doi.org/10.1103/PhysRevD.50.2225.

[72] I. Balitsky. "Operator expansion for high-energy scattering". In: *Nuclear Physics B* 463.1 (Mar. 1996), pp. 99–157. issn: 0550-3213. doi: 10.1016/0550-3213(95)00638-9. url: http://dx.doi.org/10.1016/0550-3213(95)00638-9.

[73] Yuri V. Kovchegov. "Small x F(2) structure function of a nucleus including multiple pomeron exchanges". In: *Phys. Rev. D* 60 (1999), p. 034008. doi: 10.1103/PhysRevD.60.034008. arXiv: hep-ph/9901281.

[74] Yuri V. Kovchegov. "Unitarization of the BFKL pomeron on a nucleus". In: *Phys. Rev. D* 61 (2000), p. 074018. doi: 10.1103/PhysRevD.61.074018. arXiv: hep-ph/9905214.

[75] Jamal Jalilian-Marian et al. "Wilson renormalization group for lowxphysics: Towards the high density regime". In: *Physical Review D* 59.1 (Nov. 1998). issn: 1089-4918. doi: 10.1103/physrevd.59.014014. url: http://dx.doi.org/10.1103/PhysRevD.59.014014.

[76] Heribert Weigert. "Unitarity at small Bjorken x". In: *Nuclear Physics A* 703.3–4 (June 2002), pp. 823–860. issn: 0375-9474. doi: 10.1016/s0375-9474(01)01668-2. url: http://dx.doi.org/10.1016/S0375-9474(01)01668-2.

[77] Edmond Iancu, Andrei Leonidov, and Larry McLerran. "Nonlinear gluon evolution in the color glass condensate: I". In: *Nuclear Physics A* 692.3–4 (Sept. 2001), pp. 583–645. issn: 0375-9474. doi: 10.1016/s0375-9474(01)00642-x. url: http://dx.doi.org/10.1016/S0375-9474(01)00642-X.

[78] G. Watt and H. Kowalski. "Impact parameter dependent color glass condensate dipole model". In: *Physical Review D* 78.1 (July 2008). issn: 1550-2368. doi: 10.1103/physrevd.78.014016. url: http://dx.doi.org/10.1103/PhysRevD.78.014016.

[79] H. Kowalski, L. Motyka, and G. Watt. "Exclusive diffractive processes at HERA within the dipole picture". In: *Physical Review D* 74.7 (Oct. 2006). issn: 1550-2368. doi: 10.1103/physrevd.74.074016. url: http://dx.doi.org/10.1103/PhysRevD.74.074016.

[80] Bjoern Schenke, Prithwish Tribedy, and Raju Venugopalan. "Fluctuating Glasma initial conditions and flow in heavy ion collisions". In: *Phys. Rev. Lett.* 108 (2012), p. 252301. doi: 10.1103/PhysRevLett.108.252301. arXiv: 1202.6646 [nucl-th].

[81] Aleksi Kurkela. "Initial state of Heavy-Ion Collisions: Isotropization and thermalization". In: *Nuclear Physics A* 956 (Dec. 2016), pp. 136–143. issn: 0375-9474. doi: 10.1016/j.nuclphysa.2016.01.069. url: http://dx.doi.org/10.1016/j.nuclphysa.2016.01.069.

[82] P. K. Kovtun, D. T. Son, and A. O. Starinets. "Viscosity in Strongly Interacting Quantum Field Theories from Black Hole Physics". In: *Phys. Rev. Lett.* 94 (11 Mar. 2005), p. 111601. doi: 10.1103/PhysRevLett.94.111601. url: https://link.aps.org/doi/10.1103/PhysRevLett.94.111601.

[83] Romuald A. Janik and Robi Peschanski. "Asymptotic perfect fluid dynamics as a consequence of AdS/CFT correspondence". In: *Phys. Rev. D* 73 (4 Feb. 2006), p. 045013. doi: 10.1103/PhysRevD.73.045013. url: https://link.aps.org/doi/10.1103/PhysRevD.73.045013.

[84] Jorge Casalderrey-Solana et al. *Gauge/String Duality, Hot QCD and Heavy Ion Collisions*. Cambridge University Press, 2014.

[85] Dam T. Son and Andrei O. Starinets. "Viscosity, Black Holes, and Quantum Field Theory". In: *Ann. Rev. Nucl. Part. Sci.* 57 (2007), pp. 95–118.

[86] Francois Gelis et al. "The Color Glass Condensate". In: *Annual Review of Nuclear and Particle Science* 60.1 (Nov. 2010), pp. 463–489. issn: 1545-4134. doi: 10.1146/annurev.nucl.010909.083629. url: http://dx.doi.org/10.1146/annurev.nucl.010909.083629.

[87] Peter B Arnold, Guy D Moore, and Laurence G Yaffe. "Effective kinetic theory for high temperature gauge theories". In: *Journal of High Energy Physics* 2003.01 (Jan. 2003), pp. 030–030. issn: 1029-8479. doi: 10.1088/1126-6708/2003/01/030. url: http://dx.doi.org/10.1088/1126-6708/2003/01/030.

[88] Mark C. Abraao York et al. "UV cascade in classical Yang-Mills theory via kinetic theory". In: *Physical Review D* 89.7 (Apr. 2014). issn: 1550-2368. doi: 10.1103/physrevd.89.074036. url: http://dx.doi.org/10.1103/PhysRevD.89.074036.

[89] Aleksi Kurkela and Yan Zhu. "Isotropization and Hydrodynamization in Weakly Coupled Heavy-Ion Collisions". In: *Phys. Rev. Lett.* 115 (18 Oct. 2015), p. 182301. doi: 10.1103/PhysRevLett.115.182301. url: https://link.aps.org/doi/10.1103/PhysRevLett.115.182301.

[90] Aleksas Mazeliauskas and Jürgen Berges. "Prescaling and Far-from-Equilibrium Hydrodynamics in the Quark-Gluon Plasma". In: *Phys. Rev. Lett.* 122 (12 Mar. 2019), p. 122301. doi: 10.1103/PhysRevLett.122.122301. url: https://link.aps.org/doi/10.1103/PhysRevLett.122.122301.

[91] Michal P. Heller and Michał Spali ński. "Hydrodynamics Beyond the Gradient Expansion: Resurgence and Resummation". In: *Phys. Rev. Lett.* 115 (7 Aug. 2015), p. 072501. doi: 10.1103/PhysRevLett.115.072501. url: https://link.aps.org/doi/10.1103/PhysRevLett.115.072501.

[92] Michal P. Heller, Romuald A. Janik, and Przemysław Witaszczyk. "Characteristics of Thermalization of Boost-Invariant Plasma from Holography". In: *Phys. Rev. Lett.* 108 (20 May 2012), p. 201602. doi: 10.1103/PhysRevLett.108.201602. url: https://link.aps.org/doi/10.1103/PhysRevLett.108.201602.

[93] Christof Wetterich. "Exact evolution equation for the effective potential". In: *Physics Letters B* 301.1 (Feb. 1993), pp. 90–94. issn: 0370-2693. doi: 10.1016/0370-2693(93)90726-x. url: http://dx.doi.org/10.1016/0370-2693(93)90726-X.

[94] JÜRGEN BERGES and JULIEN SERREAU. "PROGRESS IN NONEQUILIBRIUM QUANTUM FIELD THEORY". In: *Strong and Electroweak Matter 2002*. WORLD SCIENTIFIC, June 2003, pp. 111–126. doi: 10.1142/9789812704498_0011. url: http://dx.doi.org/10.1142/9789812704498_0011.

[95] Hans-Joachim Drescher and Yasushi Nara. "Eccentricity fluctuations from the color glass condensate in ultrarelativistic heavy ion collisions". In: *Physical Review C* 76.4 (Oct. 2007). issn: 1089-490X. doi: 10.1103/physrevc.76.041903. url: http://dx.doi.org/10.1103/PhysRevC.76.041903.

[96] Dmitri Kharzeev and Eugene Levin. "Manifestations of high density QCD in the first RHIC data". In: *Physics Letters B* 523.1–2 (Dec. 2001), pp. 79–87. issn: 0370-2693. doi: 10.1016/s0370-2693(01)01309-0. url: http://dx.doi.org/10.1016/S0370-2693(01)01309-0.

[97] Dmitri Kharzeev, Eugene Levin, and Marzia Nardi. "Erratum to: "QCD saturation and deuteron–nucleus collisions" [Nucl. Phys. A 730 (2004) 448]". In: *Nuclear Physics A* 743.4 (Nov. 2004), pp. 329–331. issn: 0375-9474. doi: 10.1016/j.nuclphysa.2004.06.022. url: http://dx.doi.org/10.1016/j.nuclphysa.2004.06.022.

[98] Rudolf Baier et al. "Relativistic viscous hydrodynamics, conformal invariance, and holography". In: *Journal of High Energy Physics* 2008.04 (Apr. 2008), pp. 100–100. issn: 1029-8479. doi: 10.1088/1126-6708/2008/04/100. url: http://dx.doi.org/10.1088/1126-6708/2008/04/100.

[99] G. S. Denicol et al. "Derivation of transient relativistic fluid dynamics from the Boltzmann equation". In: *Physical Review D* 85.11 (June 2012). issn: 1550-2368. doi: 10.1103/physrevd.85.114047. url: http://dx.doi.org/10.1103/PhysRevD.85.114047.

[100] M. Strickland. "Anisotropic Hydrodynamics: Three Lectures". In: *Acta Physica Polonica B* 45.12 (2014), p. 2355. issn: 1509-5770. doi: 10.5506/aphyspolb.45.2355. url: http://dx.doi.org/10.5506/APhysPolB.45.2355.

[101] Mubarak Alqahtani, Mohammad Nopoush, and Michael Strickland. "Quasiparticle equation of state for anisotropic hydrodynamics". In: *Physical Review C* 92.5 (Nov. 2015). issn: 1089-490X. doi: 10.1103/physrevc.92.054910. url: http://dx.doi.org/10.1103/PhysRevC.92.054910.

[102] A. Andronic, P. Braun-Munzinger, and J. Stachel. "Hadron production in central nucleus–nucleus collisions at chemical freeze-out". In: *Nuclear Physics A* 772.3–4 (June 2006), pp. 167–199. issn: 0375-9474. doi: 10.1016/j.nuclphysa.2006.03.012. url: http://dx.doi.org/10.1016/j.nuclphysa.2006.03.012.

[103] J. Cleymans and K. Redlich. "Chemical and thermal freeze-out parameters from $1A$ to $200A$ GeV". In: *Phys. Rev. C* 60 (5 Oct. 1999), p. 054908. doi: 10.1103/PhysRevC.60.054908. url: https://link.aps.org/doi/10.1103/PhysRevC.60.054908.

[104] Fred Cooper and Graham Frye. "Comment on the Single Particle Distribution in the Hydrodynamic and Statistical Thermodynamic Models of Multiparticle Production". In: *Phys. Rev. D* 10 (1974), p. 186. doi: 10.1103/PhysRevD.10.186.

[105] Cs. Anderlik et al. "Non-negative particle spectra from freeze-out surfaces". In: *Phys. Rev. C* 59 (1999), pp. 3309–3316.

[106] Chun Shen et al. *The iEBE-VISHNU code package for relativistic heavy-ion collisions*. 2015. arXiv: 1409.8164 [nucl-th]. url: https://arxiv.org/abs/1409.8164.

[107] S.A. Bass et al. "Microscopic models for ultrarelativistic heavy ion collisions". In: *Prog. Part. Nucl. Phys.* 41 (1998), pp. 255–369. arXiv: nucl-th/9803035.

[108] M. Bleicher et al. "Relativistic hadron-hadron collisions in the ultrarelativistic regime". In: *J. Phys. G* 25 (1999), pp. 1859–1896. arXiv: hep-ph/9909407.

[109] Chun Shen et al. "The VISHNU hybrid model for viscous QCD matter at RHIC and LHC". In: *Phys. Rev. C* 84 (2011), p. 044903. arXiv: 1105.3226 [nucl-th].

[110] Francesco Becattini et al. "Hadron Formation in Relativistic Nuclear Collisions and the QCD Phase Diagram". In: *Physical Review Letters* 111.8 (Aug. 2013). issn: 1079-7114. doi: 10.1103/physrevlett.111.082302. url: http://dx.doi.org/10.1103/PhysRevLett.111.082302.

[111] Peter Braun-Munzinger and Johanna Stachel. "Dynamics of ultra-relativistic nuclear collisions with heavy beams: An experimental overview". In: *Nuclear Physics A* 638.1 (1998). Quark Matter '97, pp. 3c–18c. issn: 0375-9474. doi: https://doi.org/10.1016/S0375-9474(98)00342-X. url: https://www.sciencedirect.com/science/article/pii/S037594749800342X.

[112] Bo Andersson et al. "Parton Fragmentation and String Dynamics". In: *Phys. Rept.* 97 (1983), pp. 31–145. doi: 10.1016/0370-1573(83)90080-7.

[113] Torbjorn Sjostrand. "The Lund Monte Carlo for Jet Fragmentation and e+ e- Physics: Jetset Version 6.2". In: *Comput. Phys. Commun.* 39 (1986), pp. 347–407. doi: 10.1016/0010-4655(86)90096-2.

[114] Torbjorn Sjostrand and Mats Bengtsson. "The Lund Monte Carlo for Jet Fragmentation and e+ e- Physics. Jetset Version 6.3: An Update". In: *Comput. Phys. Commun.* 43 (1987), p. 367. doi: 10.1016/0010-4655(87)90054-3.

[115] Torbjorn Sjostrand. "High-energy physics event generation with PYTHIA 5.7 and JETSET 7.4". In: *Comput. Phys. Commun.* 82 (1994), pp. 74–90. doi: 10.1016/0010-4655(94)90132-5.

[116] Christian Bierlich et al. "A comprehensive guide to the physics and usage of PYTHIA 8.3". In: *SciPost Phys. Codebases* 8 (2022), p. 8. arXiv: 2203.11601 [hep-ph].

[117] Torbjörn Sjöstrand, Stephen Mrenna, and Peter Skands. "An Introduction to PYTHIA 8.2". In: *Comput. Phys. Commun.* 191 (2015), pp. 159–177. arXiv: 1410.3012 [hep-ph].

[118] Torbjörn Sjöstrand. "PYTHIA 5.7 and JETSET 7.4: Physics and Manual". In: *Comput. Phys. Commun.* 82 (1994), pp. 74–90. arXiv: hep-ph/9508391 [hep-ph].

[119] G. Marchesini and B.R. Webber. "Simulation of QCD jets including soft gluon interference". In: *Nuclear Physics B* 238.1 (1984), pp. 1–29. issn: 0550-3213. doi: https://doi.org/10.1016/0550-3213(84)90463-2. url: https://www.sciencedirect.com/science/article/pii/0550321384904632.

[120] B. R. Webber. "A QCD Model for Jet Fragmentation Including Soft Gluon Interference". In: *Nucl. Phys. B* 238 (1984), pp. 492–528. doi: 10.1016/0550-3213(84)90333-X.

[121] G. Marchesini and B. R. Webber. "Monte Carlo Simulation of General Hard Processes with Coherent QCD Radiation". In: *Nucl. Phys. B* 310 (1988), pp. 461–526. doi: 10.1016/0550-3213(88)90089-2.

[122] G. Marchesini et al. "HERWIG: A Monte Carlo event generator for simulating hadron emission reactions with interfering gluons. Version 5.1 - April 1991". In: *Comput. Phys. Commun.* 67 (1992), pp. 465–508. doi: 10.1016/0010-4655(92)90055-4.

[123] G. Marchesini et al. "Herwig version 5.9". In: (July 1996). arXiv: hep-ph/9607393.

[124] P. Braun-Munzinger, I. Heppe, and J. Stachel. "Chemical equilibration in Pb+Pb collisions at the SPS". In: *Phys. Lett. B* 465 (1999), pp. 15–20. arXiv: nucl-th/9903010.

[125] P. Braun-Munzinger and J. Stachel. "Particle ratios, equilibration, and the QCD phase boundary". In: *J. Phys. G* 28 (2002), pp. 1971–1976. arXiv: nucl-th/0112051.

[126] A. Andronic, P. Braun-Munzinger, and J. Stachel. "Thermal hadron production in relativistic nuclear collisions". In: *Acta Phys. Polon. B* 40 (2009), pp. 1005–1012. arXiv: 0804.4132 [nucl-th].

[127] Anton Andronic et al. "Decoding the phase structure of QCD via particle production at high energy". In: *Nature* 561.7723 (Sept. 2018), pp. 321–330. issn: 1476-4687. doi: 10.1038/s41586-018-0491-6. url: http://dx.doi.org/10.1038/s41586-018-0491-6.

[128] F. Becattini. *Universality of thermal hadron production in pp, p-$\bar{p}$ and e+e- collisions*. 1997. arXiv: hep-ph/9701275 [hep-ph]. url: https://arxiv.org/abs/hep-ph/9701275.

[129] R. J. Fries et al. "Hadronization in Heavy-Ion Collisions: Recombination and Fragmentation of Partons". In: *Physical Review Letters* 90.20 (May 2003). issn: 1079-7114. doi: 10.1103/physrevlett.90.202303. url: http://dx.doi.org/10.1103/PhysRevLett.90.202303.

[130] R. J. Fries et al. "Hadron production in heavy ion collisions: Fragmentation and recombination from a dense parton phase". In: *Physical Review C* 68.4 (Oct. 2003). issn: 1089-490X. doi: 10.1103/physrevc.68.044902. url: http://dx.doi.org/10.1103/PhysRevC.68.044902.

[131] R.J. Fries, V. Greco, and P. Sorensen. "Coalescence Models For Hadron Formation". In: *Ann. Rev. Nucl. Part. Sci.* 58 (2008), pp. 177–205. arXiv: 0807.4939 [nucl-th].

[132] L. Ravagli and R. Rapp. "Quark coalescence based on a transport equation". In: *Phys. Rev. C* 76 (2007), p. 054905.

[133] Min He, R. J. Fries, and R. Rapp. "Heavy-Quark Diffusion and Hadronization in Quark-Gluon Plasma". In: *Phys. Rev. C* 86 (2012), p. 014903.

[134] Shanshan Cao, Guang-You Qin, and Steffen A. Bass. "Energy loss, hadronization and hadronic interactions of heavy flavors". In: *Phys. Rev. C* 92 (2015), p. 024907.

[135] J. Weil, J. Staudenmaier, and H. Petersen. "Particle production and equilibrium properties within a new hadron transport approach for heavy-ion collisions". In: *Phys. Rev. C* 94 (2016), p. 054905. arXiv: 1606.06642 [nucl-th].

[136] Alessandro Sciarra and Hannah Elfner. "SMASH as an event generator for heavy-ion collisions". In: *Front. Phys.* 12 (2024), p. 1502621. arXiv: 2309.04567 [nucl-th].

[137] Z. W. Lin et al. "A multi-phase transport model for relativistic heavy ion collisions". In: *Phys. Rev. C* 72 (2005), p. 064901. arXiv: nucl-th/0411110.

[138] B. Zhang et al. "Multiphase transport model for high energy heavy ion collisions". In: *Phys. Rev. C* 61 (2000), p. 067901. arXiv: nucl-th/0501068.

[139] Yifeng He, Guo-Liang Ma, and Z. W. Lin. “Probing the initial conditions and quark–gluon phase transition of heavy–ion collisions using a multi-phase transport model”. In: *Phys. Rev. C* 96 (2017), p. 014910. arXiv: 1701.04450.

[140] R. Nouicer. “New state of nuclear matter: Nearly perfect fluid of quarks and gluons in heavy-ion collisions at RHIC energies: From charged particle density to jet quenching”. In: *The European Physical Journal Plus* 131.3 (Mar. 2016). issn: 2190-5444. doi: 10.1140/epjp/i2016-16070-2. url: http://dx.doi.org/10.1140/epjp/i2016-16070-2.

[141] Jean-Yves Ollitrault. “Anisotropy as a signature of transverse collective flow”. In: *Phys. Rev. D* 46 (1 July 1992), pp. 229–245. doi: 10.1103/PhysRevD.46.229. url: https://link.aps.org/doi/10.1103/PhysRevD.46.229.

[142] Derek Teaney and Li Yan. “Non linear flow response and reaction plane correlations”. In: *Phys. Rev. C* 86 (2012), p. 044908. arXiv: 1206.1905 [nucl-th].

[143] Li Yan and Jean-Yves Ollitrault. “Universal fluctuations and the evolution of collective flow”. In: *Phys. Rev. Lett.* 112 (2014), p. 082301. arXiv: 1312.6555 [nucl-th].

[144] D. Teaney. “Effect of shear viscosity on spectra, elliptic flow, and Hanbury Brown–Twiss radii”. In: *Phys. Rev. C* 68 (2003), p. 034913. eprint: nucl-th/0301099.

[145] Björn Schenke, Sangyong Jeon, and Charles Gale. “Elliptic and triangular flow in event-by-event viscous hydrodynamics”. In: *Phys. Rev. Lett.* 106 (2011), p. 042301.

[146] Barbara V. Jacak and Berndt Müller. “The Exploration of Hot Nuclear Matter”. In: *Science* 337.6092 (2012), pp. 310–314. doi: 10.1126/science.1215901. eprint: https://www.science.org/doi/pdf/10.1126/science.1215901. url: https://www.science.org/doi/abs/10.1126/science.1215901.

[147] A. M. Poskanzer and S. A. Voloshin. “Methods for analyzing anisotropic flow in relativistic nuclear collisions”. In: *Physical Review C* 58.3 (Sept. 1998), pp. 1671–1678. issn: 1089-490X. doi: 10.1103/physrevc.58.1671. url: http://dx.doi.org/10.1103/PhysRevC.58.1671.

[148] S. Voloshin and Y. Zhang. “Flow study in relativistic nuclear collisions by Fourier expansion of azimuthal particle distributions”. In: *Zeitschrift fur Physik C Particles and Fields* 70.4 (May 1996), pp. 665–671. issn: 1431-5858. doi: 10.1007/s002880050141. url: http://dx.doi.org/10.1007/s002880050141.

[149] Nicolas Borghini, Phuong Mai Dinh, and Jean-Yves Ollitrault. “Flow analysis from multiparticle azimuthal correlations”. In: *Physical Review C* 64.5 (Sept. 2001). issn: 1089-490X. doi: 10.1103/physrevc.64.054901. url: http://dx.doi.org/10.1103/PhysRevC.64.054901.

[150] C. N. Yang and T. D. Lee. "Statistical Theory of Equations of State and Phase Transitions. I. Theory of Condensation". In: *Phys. Rev.* 87 (3 Aug. 1952), pp. 404–409. doi: 10.1103/PhysRev.87.404. url: https://link.aps.org/doi/10.1103/PhysRev.87.404.

[151] G. Aad et al. "Measurement of event-plane correlations in $\sqrt{s_{NN}} = 2.76$ TeV lead-lead collisions with the ATLAS detector". In: *Phys. Rev. C* 90 (2 Aug. 2014), p. 024905. doi: 10.1103/PhysRevC.90.024905. url: https://link.aps.org/doi/10.1103/PhysRevC.90.024905.

[152] Vardan Khachatryan et al. "Pseudorapidity dependence of long-range two-particle correlations in pPb collisions at $\sqrt{s_{NN}} = 5.02$ TeV". In: *Phys. Rev. C* 96.1 (2017), p. 014915. doi: 10.1103/PhysRevC.96.014915. arXiv: 1604.05347 [nucl-ex].

[153] J. Adam et al. "Beam energy dependence of net-Λ fluctuations measured by the STAR experiment at the BNL Relativistic Heavy Ion Collider". In: *Phys. Rev. C* 102 (2 Aug. 2020), p. 024903. doi: 10.1103/PhysRevC.102.024903. url: https://link.aps.org/doi/10.1103/PhysRevC.102.024903.

[154] Michelangelo L. Mangano, Paolo Nason, and Giovanni Ridolfi. "Heavy-quark correlations in hadron collisions at next-to-leading order". In: *Nuclear Physics B* 373.2 (1992), pp. 295–345. issn: 0550-3213. doi: https://doi.org/10.1016/0550-3213(92)90435-E. url: https://www.sciencedirect.com/science/article/pii/055032139290435E.

[155] R. Vogt. "Physic of the nucleon sea quark distributions". In: *Progress in Particle and Nuclear Physics* 45 (Jan. 2000), S105–S169. issn: 0146-6410. doi: 10.1016/s0146-6410(00)90012-7. url: http://dx.doi.org/10.1016/S0146-6410(00)90012-7.

[156] Yuri L. Dokshitzer, Valery A. Khoze, and S. I. Troian. "On specific QCD properties of heavy quark fragmentation ('dead cone')". In: *J. Phys. G* 17 (1991), pp. 1602–1604. doi: 10.1088/0954-3899/17/10/023.

[157] John C. Collins, Davison E. Soper, and George Sterman. *Factorization of Hard Processes in QCD*. 2004. arXiv: hep-ph/0409313 [hep-ph]. url: https://arxiv.org/abs/hep-ph/0409313.

[158] Jiaxing Zhao et al. *Heavy flavors under extreme conditions in high energy nuclear collisions*. 2020. arXiv: 2005.08277 [nucl-th]. url: https://arxiv.org/abs/2005.08277.

[159] Matteo Cacciari, Mario Greco, and Paolo Nason. "The p(T) spectrum in heavy flavor hadroproduction". In: *JHEP* 05 (1998), p. 007. arXiv: hep-ph/9803400.

[160] R. Vogt. "Cold nuclear matter effects on J/ψ and Υ production at energies available at the CERN Large Hadron Collider (LHC)". In: *Phys. Rev. C* 81 (4 Apr. 2010), p. 044903. doi: 10.1103/PhysRevC.81.044903. url: https://link.aps.org/doi/10.1103/PhysRevC.81.044903.

[161] J.J. Aubert et al. "The ratio of the nucleon structure functions F2N for iron and deuterium". In: *Physics Letters B* 123.3 (1983), pp. 275–278. issn: 0370-2693. doi: https://doi.org/10.1016/0370-2693(83)90437-9. url: https://www.sciencedirect.com/science/article/pii/0370269383904379.

[162] J. W. Cronin et al. "Production of hadrons with large transverse momentum at 200, 300, and 400 GeV". In: *Phys. Rev. D* 11 (1975). Ed. by J. R. Smith, pp. 3105–3123. doi: 10.1103/PhysRevD.11.3105.

[163] S. R. De Groot. *Relativistic Kinetic Theory. Principles and Applications*. Ed. by W. A. Van Leeuwen and C. G. Van Weert. 1980.

[164] RALF RAPP and HENDRIK VAN HEES. "HEAVY QUARKS IN THE QUARK-GLUON PLASMA". In: *Quark-Gluon Plasma 4*. WORLD SCIENTIFIC, Feb. 2010, pp. 111–206. isbn: 9789814293297. doi: 10.1142/9789814293297_0003. url: http://dx.doi.org/10.1142/9789814293297_0003.

[165] A Capella et al. "J/ψ and ψ' suppression in heavy ion collisions". In: *Physics Letters B* 393.3 (1997), pp. 431–436. issn: 0370-2693. doi: https://doi.org/10.1016/S0370-2693(96)01650-4. url: https://www.sciencedirect.com/science/article/pii/S0370269396016504.

[166] N. Armesto and A. Capella. "A quantitative reanalysis of charmonium suppression in nuclear collisions". In: *Physics Letters B* 430.1–2 (June 1998), pp. 23–31. issn: 0370-2693. doi: 10.1016/s0370-2693(98)00487-0. url: http://dx.doi.org/10.1016/S0370-2693(98)00487-0.

[167] N. Armesto, A. Capella, and E. G. Ferreiro. "Charmonium suppression in lead-lead collisions: Is there a break in the J/ψ cross section?" In: *Phys. Rev. C* 59 (1 Jan. 1999), pp. 395–404. doi: 10.1103/PhysRevC.59.395. url: https://link.aps.org/doi/10.1103/PhysRevC.59.395.

[168] A. Capella, E. G. Ferreiro, and A. B. Kaidalov. "Nonsaturation of the J/ψ Suppression at Large Transverse Energy in the Comovers Approach". In: *Phys. Rev. Lett.* 85 (10 Sept. 2000), pp. 2080–2083. doi: 10.1103/PhysRevLett.85.2080. url: https://link.aps.org/doi/10.1103/PhysRevLett.85.2080.

[169] A. Capella and E. G. Ferreiro. "J/ψ suppression at $\sqrt{s} = 200$ GeVin the comovers' interaction model". In: *The European Physical Journal C* 42.4 (Aug. 2005), pp. 419–424. issn: 1434-6052. doi: 10.1140/epjc/s2005-02348-0. url: http://dx.doi.org/10.1140/epjc/s2005-02348-0.

[170] A. Capella et al. “Charmonium dissociation and recombination at RHIC and LHC”. In: *The European Physical Journal C* 58.3 (Oct. 2008), pp. 437–444. issn: 1434-6052. doi: 10.1140/epjc/s10052-008-0772-6. url: http://dx.doi.org/10.1140/epjc/s10052-008-0772-6.

[171] E. G. Ferreiro. *Excited charmonium suppression in proton-nucleus collisions as a consequence of comovers*. 2015. arXiv: 1411.0549 [hep-ph]. url: https://arxiv.org/abs/1411.0549.

[172] Guy D. Moore and Derek Teaney. “How much do heavy quarks thermalize in a heavy ion collision?” In: *Physical Review C* 71.6 (June 2005). issn: 1089-490X. doi: 10.1103/physrevc.71.064904. url: http://dx.doi.org/10.1103/PhysRevC.71.064904.

[173] Hendrik van Hees and Ralf Rapp. “Thermalization of heavy quarks in the quark-gluon plasma”. In: *Physical Review C* 71.3 (Mar. 2005). issn: 1089-490X. doi: 10.1103/physrevc.71.034907. url: http://dx.doi.org/10.1103/PhysRevC.71.034907.

[174] Shanshan Cao et al. “Linearized Boltzmann transport model for jet propagation in the quark-gluon plasma: Heavy quark evolution”. In: *Physical Review C* 94.1 (July 2016). issn: 2469-9993. doi: 10.1103/physrevc.94.014909. url: http://dx.doi.org/10.1103/PhysRevC.94.014909.

[175] R. Rapp et al. “Extraction of heavy-flavor transport coefficients in QCD matter”. In: *Nuclear Physics A* 979 (Nov. 2018), pp. 21–86. issn: 0375-9474. doi: 10.1016/j.nuclphysa.2018.09.002. url: http://dx.doi.org/10.1016/j.nuclphysa.2018.09.002.

[176] Min He and Ralf Rapp. “Hadronization and Charm-Hadron Ratios in Heavy-Ion Collisions”. In: *Phys. Rev. Lett.* 124 (4 Jan. 2020), p. 042301. doi: 10.1103/PhysRevLett.124.042301. url: https://link.aps.org/doi/10.1103/PhysRevLett.124.042301.

[177] M.B. Voloshin. “Charmonium”. In: *Progress in Particle and Nuclear Physics* 61.2 (2008), pp. 455–511. issn: 0146-6410. doi: https://doi.org/10.1016/j.ppnp.2008.02.001. url: https://www.sciencedirect.com/science/article/pii/S0146641008000239.

[178] CHRISTIAN OSWALD and TODD K. PEDLAR. “RESULTS IN Bs PHYSICS AND BOTTOMONIUM SPECTROSCOPY USING THE BELLE $\Upsilon(5S)$ DATA”. In: *Modern Physics Letters A* 28.39 (2013), p. 1330036. doi: 10.1142/S021773231330036X. eprint: https://doi.org/10.1142/S021773231330036X. url: https://doi.org/10.1142/S021773231330036X.

[179] Harald Fritzsch. “Producing Heavy Quark Flavors in Hadronic Collisions: A Test of Quantum Chromodynamics”. In: *Phys. Lett. B* 67 (1977), pp. 217–221. doi: 10.1016/0370-2693(77)90108-3.

[180] F. Halzen. "Cvc for Gluons and Hadroproduction of Quark Flavors". In: *Phys. Lett. B* 69 (1977), pp. 105–108. doi: 10.1016/0370-2693(77)90144-7.

[181] Chao-Hsi Chang. "Hadronic Production of J/ψ Associated With a Gluon". In: *Nucl. Phys. B* 172 (1980), pp. 425–434. doi: 10.1016/0550-3213(80)90175-3.

[182] R. Baier and R. Ruckl. "Hadronic Production of J/ψ and Υ: Transverse Momentum Distributions". In: *Phys. Lett. B* 102 (1981), pp. 364–370. doi: 10.1016/0370-2693(81)90636-5.

[183] P. Artoisenet, J.P. Lansberg, and F. Maltoni. "Hadroproduction of J/ψ and Υ in association with a heavy-quark pair". In: *Physics Letters B* 653.1 (2007), pp. 60–66. issn: 0370-2693. doi: https://doi.org/10.1016/j.physletb.2007.04.031. url: https://www.sciencedirect.com/science/article/pii/S037026930700487X.

[184] Geoffrey T. Bodwin, Eric Braaten, and G. Peter Lepage. "Rigorous QCD analysis of inclusive annihilation and production of heavy quarkonium". In: *Phys. Rev. D* 51 (1995). [Erratum: Phys.Rev.D 55, 5853 (1997)], pp. 1125–1171. doi: 10.1103/PhysRevD.55.5853. arXiv: hep-ph/9407339.

[185] Eric Braaten and Sean Fleming. "Color-Octet Fragmentation and the ψ' Surplus at the Fermilab Tevatron". In: *Phys. Rev. Lett.* 74 (17 Apr. 1995), pp. 3327–3330. doi: 10.1103/PhysRevLett.74.3327. url: https://link.aps.org/doi/10.1103/PhysRevLett.74.3327.

[186] E. Eichten et al. "Charmonium: The model". In: *Phys. Rev. D* 17 (11 June 1978), pp. 3090–3117. doi: 10.1103/PhysRevD.17.3090. url: https://link.aps.org/doi/10.1103/PhysRevD.17.3090.

[187] T. Matsui and H. Satz. "J/ψ Suppression by Quark-Gluon Plasma Formation". In: *Phys. Lett. B* 178 (1986), pp. 416–422. doi: 10.1016/0370-2693(86)91404-8.

[188] Raphael Granier de Cassagnac. "Quarkonia Production in Hot and Cold Matters". In: *J. Phys. G* 35 (2008). Ed. by Jan-e Alam et al., p. 104023. doi: 10.1088/0954-3899/35/10/104023. arXiv: 0806.0046 [hep-ph].

[189] Eric Braaten and Markus H. Thoma. "Energy loss of a heavy quark in the quark-gluon plasma". In: *Phys. Rev. D* 44 (9 Nov. 1991), R2625–R2630. doi: 10.1103/PhysRevD.44.R2625. url: https://link.aps.org/doi/10.1103/PhysRevD.44.R2625.

[190] R. Baier et al. "Radiative energy loss and $p_\perp$-broadening of high energy partons in nuclei". In: *Nuclear Physics B* 484.1–2 (Jan. 1997), pp. 265–282. issn: 0550-3213. doi: 10.1016/s0550-3213(96)00581-0. url: http://dx.doi.org/10.1016/S0550-3213(96)00581-0.

[191] Yu.L Dokshitzer and D.E Kharzeev. "Heavy-quark colorimetry of QCD matter". In: *Physics Letters B* 519.3–4 (Nov. 2001), pp. 199–206. issn: 0370-2693. doi: 10.1016/s0370-2693(01)01130-3. url: http://dx.doi.org/10.1016/S0370-2693(01)01130-3.

[192] Shanshan Cao et al. "Linearized Boltzmann transport model for jet propagation in the quark-gluon plasma: Heavy quark evolution". In: *Phys. Rev. C* 94 (1 July 2016), p. 014909. doi: 10.1103/PhysRevC.94.014909. url: https://link.aps.org/doi/10.1103/PhysRevC.94.014909.

[193] Tan Luo et al. "Linear Boltzmann transport for jet propagation in the quark-gluon plasma: Inelastic processes and jet modification". In: *Physical Review C* 109.3 (Mar. 2024). issn: 2469-9993. doi: 10.1103/physrevc.109.034919. url: http://dx.doi.org/10.1103/PhysRevC.109.034919.

[194] Shanshan Cao et al. "Toward the determination of heavy-quark transport coefficients in quark-gluon plasma". In: *Phys. Rev. C* 99 (5 May 2019), p. 054907. doi: 10.1103/PhysRevC.99.054907. url: https://link.aps.org/doi/10.1103/PhysRevC.99.054907.

[195] Weiyao Ke, Yingru Xu, and Steffen A. Bass. "Linearized Boltzmann-Langevin model for heavy quark transport in hot and dense QCD matter". In: *Phys. Rev. C* 98 (6 Dec. 2018), p. 064901. doi: 10.1103/PhysRevC.98.064901. url: https://link.aps.org/doi/10.1103/PhysRevC.98.064901.

[196] Shuang Li et al. "Probing the transport properties of quark-gluon plasma via heavy-flavor Boltzmann and Langevin dynamics". In: *Phys. Rev. C* 99 (5 May 2019), p. 054909. doi: 10.1103/PhysRevC.99.054909. url: https://link.aps.org/doi/10.1103/PhysRevC.99.054909.

[197] Xiaojun Yao et al. "Coupled Boltzmann transport equations of heavy quarks and quarkonia in quark-gluon plasma". In: *Journal of High Energy Physics* 2021.1 (Jan. 2021). issn: 1029-8479. doi: 10.1007/jhep01(2021)046. url: http://dx.doi.org/10.1007/JHEP01(2021)046.

[198] Min He, Rainer J. Fries, and Ralf Rapp. "Heavy-Quark Diffusion and Hadronization in Quark-Gluon Plasma". In: *Phys. Rev. C* 86 (2012), p. 014903. doi: 10.1103/PhysRevC.86.014903. arXiv: 1106.6006 [nucl-th].

[199] Min He, Rainer J. Fries, and Ralf Rapp. "Heavy Flavor at the Large Hadron Collider in a Strong Coupling Approach". In: *Phys. Lett. B* 735 (2014), pp. 445–450. doi: 10.1016/j.physletb.2014.05.050. arXiv: 1401.3817 [nucl-th].

[200] Xiaojian Du and Ralf Rapp. "Sequential Regeneration of Charmonia in Heavy-Ion Collisions". In: *Nucl. Phys. A* 943 (2015), pp. 147–158. doi: 10.1016/j.nuclphysa.2015.09.006. arXiv: 1504.00670 [hep-ph].

[201] Min He, Biaogang Wu, and Ralf Rapp. "Collectivity of J/ψ Mesons in Heavy-Ion Collisions". In: *Phys. Rev. Lett.* 128 (16 Apr. 2022), p. 162301. doi: 10.1103/PhysRevLett.128.162301. url: https://link.aps.org/doi/10.1103/PhysRevLett.128.162301.

[202] Francesco Scardina et al. "Estimating the charm quark diffusion coefficient and thermalization time from D meson spectra at energies available at the BNL Relativistic Heavy Ion Collider and the CERN Large Hadron Collider". In: *Phys. Rev. C* 96.4 (2017), p. 044905. doi: 10.1103/PhysRevC.96.044905. arXiv: 1707.05452 [nucl-th].

[203] Vincenzo Minissale, Francesco Scardina, and Vincenzo Greco. "Hadrons from coalescence plus fragmentation in AA collisions at energies available at the BNL Relativistic Heavy Ion Collider to the CERN Large Hadron Collider". In: *Phys. Rev. C* 92.5 (2015), p. 054904. doi: 10.1103/PhysRevC.92.054904. arXiv: 1502.06213 [nucl-th].

[204] A. Beraudo et al. "Heavy flavors in heavy-ion collisions: quenching, flow and correlations". In: *The European Physical Journal C* 75.3 (Mar. 2015). issn: 1434-6052. doi: 10.1140/epjc/s10052-015-3336-6. url: http://dx.doi.org/10.1140/epjc/s10052-015-3336-6.

[205] Andrea Beraudo et al. "Development of heavy-flavour flow-harmonics in high-energy nuclear collisions". In: *Journal of High Energy Physics* 2018.2 (Feb. 2018). issn: 1029-8479. doi: 10.1007/jhep02(2018)043. url: http://dx.doi.org/10.1007/JHEP02(2018)043.

[206] Xingbo Zhao and Ralf Rapp. "Medium modifications and production of charmonia at LHC". In: *Nuclear Physics A* 859.1 (June 2011), pp. 114–125. issn: 0375-9474. doi: 10.1016/j.nuclphysa.2011.05.001. url: http://dx.doi.org/10.1016/j.nuclphysa.2011.05.001.

[207] Xiaojian Du, Min He, and Ralf Rapp. "In-Medium Bottomonium Production in Heavy-Ion Collisions". In: *Nuclear Physics A* 967 (Nov. 2017), pp. 904–907. issn: 0375-9474. doi: 10.1016/j.nuclphysa.2017.05.079. url: http://dx.doi.org/10.1016/j.nuclphysa.2017.05.079.

[208] X. Du, M. He, and R. Rapp. "Color screening and regeneration of bottomonia in high-energy heavy-ion collisions". In: *Phys. Rev. C* 96 (5 Nov. 2017), p. 054901. doi: 10.1103/PhysRevC.96.054901. url: https://link.aps.org/doi/10.1103/PhysRevC.96.054901.

[209] Biaogang Wu and Ralf Rapp. "Charmonium Transport in Heavy-Ion Collisions at the LHC". In: *Universe* 10.6 (2024). issn: 2218-1997. doi: 10.3390/universe10060244. url: https://www.mdpi.com/2218-1997/10/6/244.

[210] Yun-peng Liu et al. "J/psi Transverse Momentum Distribution in High Energy Nuclear Collisions at RHIC". In: *Phys. Lett. B* 678 (2009), pp. 72–76. doi: 10.1016/j.physletb.2009.06.006. arXiv: 0901.2757 [nucl-th].

[211] Yunpeng Liu et al. "Υ Production as a Probe for Early State Dynamics in High Energy Nuclear Collisions at RHIC". In: *Phys. Lett. B* 697 (2011), pp. 32–36. doi: 10.1016/j.physletb.2011.01.026. arXiv: 1009.2585 [nucl-th].

[212] E. G. Ferreiro. "Charmonium dissociation and recombination at LHC: Revisiting comovers". In: *Phys. Lett. B* 731 (2014), pp. 57–63. doi: 10.1016/j.physletb.2014.02.011. arXiv: 1210.3209 [hep-ph].

[213] E. G. Ferreiro and J. P. Lansberg. "Is bottomonium suppression in proton-nucleus and nucleus-nucleus collisions at LHC energies due to the same effects?" In: *Journal of High Energy Physics* 2018.10 (Oct. 2018). issn: 1029-8479. doi: 10.1007/jhep10(2018)094. url: http://dx.doi.org/10.1007/JHEP10(2018)094.

[214] Klaus Werner, Fu-Ming Liu, and Tanguy Pierog. "Parton ladder splitting and the rapidity dependence of transverse momentum spectra in deuteron-gold collisions at the BNL Relativistic Heavy Ion Collider". In: *Phys. Rev. C* 74 (4 Oct. 2006), p. 044902. doi: 10.1103/PhysRevC.74.044902. url: https://link.aps.org/doi/10.1103/PhysRevC.74.044902.

[215] Klaus Werner. "Revealing a deep connection between factorization and saturation: New insight into modeling high-energy proton-proton and nucleus-nucleus scattering in the EPOS4 framework". In: *Phys. Rev. C* 108.6 (2023), p. 064903. doi: 10.1103/PhysRevC.108.064903. arXiv: 2301.12517 [hep-ph].

[216] K. Werner and B. Guiot. "Perturbative QCD concerning light and heavy flavor in the EPOS4 framework". In: *Phys. Rev. C* 108 (3 Sept. 2023), p. 034904. doi: 10.1103/PhysRevC.108.034904. url: https://link.aps.org/doi/10.1103/PhysRevC.108.034904.

[217] Denys Yen Arrebato Villar et al. "New microscopic model for J/ψ production in heavy ion collisions". In: *Phys. Rev. C* 107 (5 May 2023), p. 054913. doi: 10.1103/PhysRevC.107.054913. url: https://link.aps.org/doi/10.1103/PhysRevC.107.054913.

[218] Taesoo Song et al. "Bottomonium production in pp and heavy-ion collisions". In: *Phys. Rev. C* 108.5 (2023), p. 054908. doi: 10.1103/PhysRevC.108.054908. arXiv: 2305.10750 [nucl-th].

[219] L. Adamczyk et al. "Measurement of J/ψ Azimuthal Anisotropy in $\mathrm{Au}+\mathrm{Au}$ Collisions at $\sqrt{s_{NN}}=200\ \mathrm{GeV}$". In: *Phys. Rev. Lett.* 111 (5 Aug. 2013), p. 052301. doi: 10.1103/PhysRevLett.111.052301. url: https://link.aps.org/doi/10.1103/PhysRevLett.111.052301.

[220] E. Abbas et al. "J/ψ Elliptic Flow in Pb-Pb Collisions at $\sqrt{s_{NN}} = 2.76\ \mathrm{TeV}$". In: *Phys. Rev. Lett.* 111 (16 Oct. 2013), p. 162301. doi: 10.1103/PhysRevLett.111.162301. url: https://link.aps.org/doi/10.1103/PhysRevLett.111.162301.

[221] S. Acharya et al. "J/ψ Elliptic Flow in Pb-Pb Collisions at $\sqrt{s_{NN}} = 5.02$ TeV". In: *Phys. Rev. Lett.* 119 (24 Dec. 2017), p. 242301. doi: 10.1103/PhysRevLett.119.242301. url: https://link.aps.org/doi/10.1103/PhysRevLett.119.242301.

[222] Vardan Khachatryan et al. "Suppression and azimuthal anisotropy of prompt and nonprompt J/ψ production in PbPb collisions at $\sqrt{s_{\mathrm{NN}}} = 2.76$ TeV". In: *Eur. Phys. J. C* 77.4 (2017), p. 252. doi: 10.1140/epjc/s10052-017-4781-1. arXiv: 1610.00613 [nucl-ex].

[223] J. Adam et al. "Event-shape engineering for inclusive spectra and elliptic flow in Pb-Pb collisions at $\sqrt{s_{NN}} = 2.76$ TeV". In: *Phys. Rev. C* 93 (3 Mar. 2016), p. 034916. doi: 10.1103/PhysRevC.93.034916. url: https://link.aps.org/doi/10.1103/PhysRevC.93.034916.

[224] "Measurement of the elliptic flow of $\Upsilon(1\mathrm{S})$ and $\Upsilon(2\mathrm{S})$ mesons in PbPb collisions at $\sqrt{\mathrm{s_{NN}}} = 5.02$ TeV". In: (2019).

[225] S. Acharya et al. "Measurement of $\Upsilon(1S)$ Elliptic Flow at Forward Rapidity in Pb-Pb Collisions at $\sqrt{s_{NN}} = 5.02$ TeV". In: *Phys. Rev. Lett.* 123 (19 Nov. 2019), p. 192301. doi: 10.1103/PhysRevLett.123.192301. url: https://link.aps.org/doi/10.1103/PhysRevLett.123.192301.

[226] S. Rende. *Accelerator Report: LHC Run 3 achieves record-breaking integrated luminosity*. 2024. url: https://home.cern/news/news/accelerators/accelerator-report-lhc-run-3-achieves-record-breaking-integrated-luminosity.

[227] CERN. *Accelerator Report: We reached 100!* https://home.cern/news/news/accelerators/accelerator-report-we-reached-100. Accessed: 2025-11-04. Oct. 2025.

[228] Georges Aad et al. "Observation of a new particle in the search for the Standard Model Higgs boson with the ATLAS detector at the LHC". In: *Phys. Lett. B* 716 (2012), pp. 1–29. doi: 10.1016/j.physletb.2012.08.020. arXiv: 1207.7214 [hep-ex].

[229] Serguei Chatrchyan et al. "Observation of a New Boson at a Mass of 125 GeV with the CMS Experiment at the LHC". In: *Phys. Lett. B* 716 (2012), pp. 30–61. doi: 10.1016/j.physletb.2012.08.021. arXiv: 1207.7235 [hep-ex].

[230] E. Mobs. "The CERN accelerator complex". In: (2016). General Photo. url: https://cds.cern.ch/record/2197559.

[231] B. Maximilien. "View of an open LHC interconnection". 2005. url: https://cds.cern.ch/record/905940.

[232] ATLAS Collaboration. *ATLAS Public Results - Run 3 Luminosity*. https://twiki.cern.ch/twiki/bin/view/AtlasPublic/LuminosityPublicResultsRun3. Accessed: 2025-11-04. 2025.

[233] CMS Collaboration. *CMS Public Results – Run 3 Luminosity: 2025 Proton-Proton Collisions*. https://twiki.cern.ch/twiki/bin/view/CMSPublic/LumiPublicResults. Accessed: 2025-11-04. 2025.

[234] CERN. *Accelerator Report: Preparing for 2025 LHC Operation and Setting Goals*. Accessed: 7 October 2025. CERN News. Jan. 2025. url: https://home.cern/news/news/accelerators/accelerator-report-preparing-2025-lhc-operation-and-setting-goals?utm_source=chatgpt.com (visited on 10/07/2025).

[235] CERN. *Accelerator report: When plans meet reality*. https://home.cern/news/news/accelerators/accelerator-report-when-plans-meet-reality. Accessed: 2025-11-04. Oct. 2025.

[236] J. Wenninger. "Machine Protection and Operation for LHC". In: (2016). Comments: 25 pages, contribution to the 2014 Joint International Accelerator School: Beam Loss and Accelerator Protection, Newport Beach, CA, USA , 5-14 Nov 2014, pp. 377–401. doi: 10.5170/CERN-2016-002.377. arXiv: 1608.03113. url: https://cds.cern.ch/record/2207176.

[237] Julien Ordan. "ALICE empty structure after modules removal, during LS2". In: (2019). General Photo. url: https://cds.cern.ch/record/2653650.

[238] B Abelev et al. "Upgrade of the ALICE Experiment: Letter Of Intent". In: *J. Phys. G* 41 (2014), p. 087001. doi: 10.1088/0954-3899/41/8/087001.

[239] Arturo Tauro. "ALICE Schematics". General Photo. 2017. url: https://cds.cern.ch/record/2263642.

[240] L. Valencia Palomo. "The ALICE experiment upgrades for LHC Run 3 and beyond: contributions from mexican groups". In: *Journal of Physics: Conference Series* 912.1 (Oct. 2017), p. 012023. doi: 10.1088/1742-6596/912/1/012023. url: https://doi.org/10.1088/1742-6596/912/1/012023.

[241] Nicolo' Valle. "Performance of the ALICE Inner Tracking System 2". In: *Nucl. Instrum. Meth. A* 1079 (2025), p. 170596. doi: 10.1016/j.nima.2025.170596. arXiv: 2503.17233 [physics.ins-det].

[242] Adam Laszlo Gera. *Upgrade of the ALICE Time Projection Chamber for the LHC Run 3*. 2020. arXiv: 2004.10520 [physics.ins-det]. url: https://arxiv.org/abs/2004.10520.

[243] MFT Collaboration ALICE. "ALICE Muon Forward Tracker (MFT)". In: (2020). General Photo. url: https://cds.cern.ch/record/2748310.

[244] ALICE Collaboration. *ALICE Muon Spectrometer*. Accessed: 7 October 2025. ALICE Collaboration. n.d. url: https://alice-collaboration.web.cern.ch/menu_proj_items/Muon-Spect (visited on 10/07/2025).

[245] Livia Terlizzi. *Operation and performance of the ALICE Muon IDentifier RPCs during LHC Run3*. 2025. arXiv: 2502.13602 [hep-ex]. url: https://arxiv.org/abs/2502.13602.

[246] Livia Terlizzi et al. *Studies on environment-friendly gas mixtures for the Resistive Plate Chambers of the ALICE Muon Identifier*. Tech. rep. Proceedings of 10th International Conference on New Frontiers in Physics (ICNFP 2021), 2021-08-23 to 2021-09-02. 2022. arXiv: 2202.13968. url: https://cds.cern.ch/record/2803350.

[247] Andreas Molander. "The new ALICE Fast Interaction Trigger in LHC Run 3". In: *PoS* LHCP2023 (2024), p. 268. doi: 10.22323/1.450.0268. url: https://cds.cern.ch/record/2918954.

[248] P Buncic, M Krzewicki, and P Vande Vyvre. *Technical Design Report for the Upgrade of the Online-Offline Computing System*. Tech. rep. 2015. url: https://cds.cern.ch/record/2011297.

[249] E. Mathieson. "Cathode Charge Distributions in Multiwire Chambers. 4: Empirical Formula for Small Anode - Cathode Separation". In: *Nucl. Instrum. Meth. A* 270 (1988), pp. 602–603. doi: 10.1016/0168-9002(88)90736-X.

[250] A. Zinchenko et al. "Development of algorithms for cluster finding and track reconstruction in the forward muon spectrometer of ALICE experiment". In: *14th International Conference on Computing in High-Energy and Nuclear Physics*. 2005, pp. 276–279.

[251] R. E. Kalman. "A New Approach to Linear Filtering and Prediction Problems". In: *J. Fluids Eng.* 82.1 (1960), pp. 35–45. doi: 10.1115/1.3662552.

[252] Pierre Billoir and S. Qian. "Simultaneous pattern recognition and track fitting by the Kalman filtering method". In: *Nucl. Instrum. Meth. A* 294 (1990), pp. 219–228. doi: 10.1016/0168-9002(90)91835-Y.

[253] R. Fruhwirth. "Application of Kalman filtering to track and vertex fitting". In: *Nucl. Instrum. Meth. A* 262 (1987), pp. 444–450. doi: 10.1016/0168-9002(87)90887-4.

[254] V. Blobel. "Software alignment for tracking detectors". In: *Nucl. Instrum. Meth. A* 566 (2006). Ed. by R. Bernhard et al., pp. 5–13. doi: 10.1016/j.nima.2006.05.157.

[255] Volker Blobel and Claus Kleinwort. "A New method for the high precision alignment of track detectors". In: *Conference on Advanced Statistical Techniques in Particle Physics*. June 2002. arXiv: hep-ex/0208021.

[256] Ryogo Kubo. "Generalized Cumulant Expansion Method". In: *J. Phys. Soc. Jap.* 17.7 (1962), pp. 1100–1120. doi: 10.1143/jpsj.17.1100.

[257] Ante Bilandzic et al. “Generic framework for anisotropic flow analyses with multiparticle azimuthal correlations”. In: *Physical Review C* 89.6 (June 2014). issn: 1089-490X. doi: 10.1103/physrevc.89.064904. url: http://dx.doi.org/10.1103/PhysRevC.89.064904.

[258] Ilya Selyuzhenkov and Sergei Voloshin. “Effects of non-uniform acceptance in anisotropic flow measurement”. In: *Phys. Rev. C* 77 (2008), p. 034904. doi: 10.1103/PhysRevC.77.034904. arXiv: 0707.4672 [nucl-th].

[259] Jaroslav Adam et al. “Anisotropic flow of charged particles in Pb-Pb collisions at $\sqrt{s_{\rm NN}} = 5.02$ TeV”. In: *Phys. Rev. Lett.* 116.13 (2016), p. 132302. doi: 10.1103/PhysRevLett.116.132302. arXiv: 1602.01119 [nucl-ex].

[260] S. Navas et al. “Review of particle physics”. In: *Phys. Rev. D* 110.3 (2024), p. 030001. doi: 10.1103/PhysRevD.110.030001.

[261] Shreyasi Acharya et al. “Measurement of ψ(2S) production as a function of charged-particle pseudorapidity density in pp collisions at $\sqrt{s}$ = 13 TeV and p-Pb collisions at $\sqrt{s_{\rm NN}}$ = 8.16 TeV with ALICE at the LHC”. In: *JHEP* 06 (2023), p. 147. doi: 10.1007/JHEP06(2023)147. arXiv: 2204.10253 [nucl-ex].

[262] Shreyasi Acharya et al. “Study of J/ψ azimuthal anisotropy at forward rapidity in Pb-Pb collisions at $\sqrt{s_{\rm NN}} = 5.02$ TeV”. In: *JHEP* 02 (2019), p. 012. doi: 10.1007/JHEP02(2019)012. arXiv: 1811.12727 [nucl-ex].

[263] ALICE Collaboration. *Analysis note no. 950*. https://alice-notes.web.cern.ch/node/950. Accessed: January 15, 2026.

[264] Chi Zhang. “Quarkonia collectivity in large collision systems with ALICE”. In: *31st International Conference on Ultra-relativistic Nucleus-Nucleus Collisions*. Sept. 2025. arXiv: 2509.06240 [nucl-ex].

[265] Albert M Sirunyan et al. “Measurement of prompt D^0 meson azimuthal anisotropy in Pb-Pb collisions at $\sqrt{s_{NN}}$ = 5.02 TeV”. In: *Phys. Rev. Lett.* 120.20 (2018), p. 202301. doi: 10.1103/PhysRevLett.120.202301. arXiv: 1708.03497 [nucl-ex].

[266] Shreyasi Acharya et al. “Transverse-momentum and event-shape dependence of D-meson flow harmonics in Pb–Pb collisions at $\sqrt{s_{NN}}$ = 5.02 TeV”. In: *Phys. Lett. B* 813 (2021), p. 136054. doi: 10.1016/j.physletb.2020.136054. arXiv: 2005.11131 [nucl-ex].

[267] S. Acharya et al. “Anisotropic flow of identified particles in Pb-Pb collisions at $\sqrt{s_{\rm NN}} = 5.02$ TeV”. In: *JHEP* 09 (2018), p. 006. doi: 10.1007/JHEP09(2018)006. arXiv: 1805.04390 [nucl-ex].

[268] Shreyasi Acharya et al. “J/ψ elliptic and triangular flow in Pb-Pb collisions at $\sqrt{s_{\rm NN}}$ = 5.02 TeV”. In: *JHEP* 10 (2020), p. 141. doi: 10.1007/JHEP10(2020)141. arXiv: 2005.14518 [nucl-ex].

[269] Armen Tumasyan et al. “Strange hadron collectivity in pPb and PbPb collisions”. In: *JHEP* 05 (2023), p. 007. doi: 10.1007/JHEP05(2023)007. arXiv: 2205.00080 [nucl-ex].